Charles University
Faculty of Science

Inorganic Chemistry

Mgr. Jan Blahut

Dynamics of paramagnetic complexes observed by Nuclear Magnetic Resonance

Dynamika paramagnetických komplexů a její studium pomocí jaderné magnetické rezonance

Ph.D. Thesis

Supervisor:
prof. RNDr. Petr Hermann, Ph.D.

Advisor:
RNDr. Zdeněk Tošner, Ph.D.

Prague, 2017

Prohlášení:

Prohlašuji, že jsem závěrečnou práci zpracoval samostatně a že jsem uvedl všechny použité informační zdroje a literaturu. Tato práce ani její podstatná část nebyly předloženy k získání jiného nebo stejného akademického titulu.

Declaration:

Hereby I declare that this Thesis is my original work and that I have properly cited all the information resources. This work has not been submitted either for any other or for the same academic degree.

In Prague 6th December 2017 Jan Blahut

Acknowledgements

My thanks certainly belong to my brilliant supervisor Petr Hermann for a myriad of ideas and for opening of the World of Science for me. At the same time, I express my sincere gratitudes to Zdeněk Tošner, Honza Kotek and Carlos Platas-Iglesias for moving me forward in this fantastic World. Furthermore, thanks to the group from MFF and IKEM for a fruitful collaboration and pleasant free-time moments. Thanks to Danutu Kruk and her group for the measurement of ^{19}F-NMRD profile and Jakub Hraníček for the AAS measurements.

I would also like to thank all the people who supported me and admire their patience with my hasty behaviour and my doses of laziness. I especially thank my parents and the whole family, my friends and colleagues from The Lab and from the Budeč dormitory. It would definitely be a lengthy list if I named all of these excellent personalities which have been forming my social bubble. Nevertheless, my special thanks belongs to Vojta Duchoslav for showing me a way of critical thinking and to Terka Krchová for making the world less serious.

Last, but definitely not least, let me highlight, that without a deep and sincere love, this work would never see the light of day.

Díky vám všem...

Abstract

In this Thesis, structure and dynamics of paramagnetic complexes for medical application are studied by Nuclear Magnetic Resonance (NMR). It focuses mainly on development of contrast agents (CA) for Magnetic Resonance Imaging (MRI) which is one of the most effective radiodiagnostic method nowadays. Most of the MRI CAs contains paramagnetic complexes of *d*- and *f*-metal ions.

The presence of unpaired electron in proximity of NMR active nuclei has two main effects: paramagnetically induced shift and paramagnetically induced relaxation. Both processes can dramatically change the NMR spectrum and often make it unobservable at all. Nevertheless, in many cases, acquisition of such spectra is possible and sometimes even less time-consuming than observation of diamagnetic molecules. Enhanced T_1 relaxation allows faster pulse sequence repetition and increased chemical shift dispersion may lead to resolution of originally overlapped signals. Moreover, the analysis of paramagnetic effects can provide useful information about the structure and dynamics of the studied system. Theoretical background of these effects is described in the Introduction of the Thesis.

In the first part of Discussion in the Thesis, a new class of contrast agents for ^{19}F-MRI based on nickel(II) and cobalt(II/III) ions is introduced and discussed. Structure and dynamics of their complexes with fluorinated ligands is discussed together with formation, dissociation and isomerism of these complexes. A huge difference in the kinetic inertness of nickel(II) complexes was observed. The complex of the ligand with with acetate pendant arms withstand days in 12 M aqueous HCl at 80 °C, while its analogue with 2-aminoethyl pendant arms dissociates after a few hours in neutral water at room temperature.

Strong relaxation enhancement of ^{19}F nucleus in proximity of nickel(II) was observed and it is associated with dipole-dipole interaction between ^{19}F and slowly relaxing unpaired electrons of nickel(II). Smaller, but still reasonable relaxation enhancement was observed in cobalt(II) complexes as well. Analysis of the ^{19}F-NMRD profile for one of the nickel(II) complexes showed that relaxation of the

nickel(II) electrons is magnetic field-dependent and it is modulated by transient zero-field-splitting mechanism.

Significant increase of ^{19}F-MRI CA efficiency was described for these compounds when the complexes are detected by fast MRI pulse sequences.

Internal (TSAP↔SAP) dynamics of Ln^{3+} complexes with H_4**dota** and H_5**do3ap** ligands is the subject of the second part of the Thesis Discussion. The NMR pulse sequence and data analysis were optimised to determine precise exchange rates and activation parameters of both the arm rotation and the macrocyclic ethylene ring inversion. The results were compared with detailed DFT calculations which were done in order to reveal mechanism of the exchange. Unexpected intermediate with bidentate phosphonate group was shown to be involved in the arm rotation process of $[\mathrm{Eu}(\textbf{do3ap})(\mathrm{H_2O})]^{2-}$ complex.

Beside the description of the important process in widely studied complexes with DOTA-like ligands, the developed methodology can be generally applied in many dynamic paramagnetic systems such as proteins with open-shell ions or in battery materials.

Abstrakt

Předložená práce se zaměřuje především na vývoj nových kontrastních látek pro zobrazování jadernou magnetickou rezonancí (MRI). Většina těchto látek je založena na koordinačních sloučeninách přechodných a vnitřně přechodných kovů. Studium struktury a dynamiky těchto komplexů pomocí jaderné magnetické resonance (NMR) je tedy hlavním spojujícím prvkem celé této práce.

Přítomnost nepárových elektronů paramagnetického iontu kovu v blízkosti sledovaného jádra má zásadní vliv na jeho vlastnosti z pohledu NMR. Hlavními efekty jsou výrazné rozšíření škály chemických posunů a zrychlení relaxačních procesů. Tyto efekty znesnadňují měření často až to té míry, že není možné detekovat žádné spektrum NMR. Na druhou stranu mohou tyto paramagnetické efekty měření urychlit díky rychlému ustavování rovnováhy zrychlenou podélnou relaxací. Případně může přítomnost paramagnetika přinést nové informace o studované látce, mimo jiné díky odstranění náhodných překryvů signálů ve spektru. Teoretické aspekty studia paramagnetických molekul pomocí NMR jsou diskutovány v úvodu práce.

První část diskuze této práce je zaměřena přímo na vývoj nových kontrastních látek pro MRI využívající jádra ^{19}F. Tyto látky jsou založené na nikelnatých, kobaltnatých a kobaltitých komplexech ligandů obsahujících fluorové atomy.

V práci je diskutována syntéza těchto látek, jejich stabilita a isomerie. Mimo jiné byly popsány výrazné rozdíly v kinetické inertnosti získaných nikelnatých komplexů. Zatímco komplex ligandu s karboxylovými pendantními raménky se rozkládá ve 12 M vodné HCl až po několikadenním zahřívání na 80 °C, komplex ligandu s 2-aminoethylovými pendantními raménky je hydrolyzován již za několik hodin i v neutrální vodě při 25 °C.

Pozorováno bylo výrazné zrychlení relaxačních rychlostí fluorového jádra vlivem dipol-dipolové interakce s elektrony nikelnatého iontu, stejně tak jako podobné, avšak menší, zrychlení relaxace vlivem elektronů kobaltnatého iontu. Studium ^{19}F-NMRD profilu jednoho z nikelnatých komplexů ukázalo, že elektronová relaxační

rychlost je závislá na intenzitě magnetického pole. Mechanismem vyvolávajícím tuto relaxaci je „transient zero-field splitting“. Byl prokázán nárůst efektivity kontrastních látek pro ^{19}F-MRI vlivem těchto změn relaxačního času.

Druhá část práce je zaměřena na studium přeměny TSAP↔SAP isomerů koordinačních sloučenin trojmocných lanthanoidů s ligandem H_4**dota** a jeho analogem obsahujícím fosfonátovou skupinu (H_5**do3ap**). Pro tento účel byla využita NMR pulzní sekvence upravené podle nároků konkrétního paramagnetického kovu. Stejně tak byla zdokonalena analýza získaných dat. Díky tomu byly získány přesné kinetické a termodynamické parametry pohybu pendantních ramen a překlopení ethylenových můstků cyklu. Ty byly následně využity jako srovnávací kritéria pro vyhodnocení teoretických (DFT) výpočtů. Tímto způsobem byl objasněn také mechanismus studovaných procesů. Mimo jiné byl popsán neobvyklý mechanismus pohybu pendantních ramen, jež prochází intermediátní strukturou s bidentátně koordinovanou fosfonátovou skupinou, který nebyl doposud v literatuře popsán. Kromě toho, že se podařilo detailně popsat chování těchto komplexů důležitých pro praxi, podařilo se také vyvinout obecnou metodu pro sledování rychlých pohybů v přítomnosti paramagnetického centra. Ta může být dále využita například při studiu bílkovin, či při vývoji baterií.

Contents

Thesis objectives

The presented Thesis is focussed on development of new contrast agents (CA) for Magnetic Resonance Imaging (MRI). The central topic is the Nuclear Magnetic Resonance spectroscopy of paramagnetic systems (pNMR).

Two main topics are followed. The first one is related to the development of a new class of CA for MRI of fluorine, i.e. ^{19}F-MRI. These new CAs are based on complexes of paramagnetic *d*-metal ions with fluorine containing ligands. The other topic is related to experimental and theoretical study of conformational dynamics of lanthanide(III) complexes with DOTA(i) and structurally related compounds. The Thesis objectives in these two topics are:

1. Description of formation, dissociation and rearrangement of the complexes.
2. Development and optimisation of methodology for observation of fast dynamic processes in presence of paramagnetic centre. Comparison of the results with theoretical models.
3. Determination of relaxation properties of prepared compounds and description of dynamic processes which are inducing the nuclear relaxation. Because the nuclear relaxation in the presence of unpaired electrons is critical for the efficiency of CAs.

Main aim of the Thesis is to choose and properly apply NMR techniques to observe these dynamic processes in the paramagnetic complexes of macrocyclic ligands. Character of the paramagnetic centre and time-scales of studied process are critical parameters that decide on method and its application.

(i) DOTA = 1,4,8,10-tetraazacyclotetradecane-1,4,8,10-tetrakis(methylcarboxylic) acid

Part I

Theoretical background

Chapter 1

Dynamic processes

World around us is changing. Dynamics of nature can be followed on wide range of time-scale points. The shortest measured time-scale (attoseconds i.e. $1 \times 10^{-18}\,\mathrm{s}$) [1] is characteristic for very fast electron processes like photoemission and the longest can be associated with the age of the universe ($13.8 \times 10^{9}\,\mathrm{y}$).[i] From chemistry and physical chemistry point of view, the most relevant time-scales are associated with the electron processes and with the movement of nuclei within molecules. These processes are usually treated separately and independently thanks to different time-scales of both processes. Simplification which allows us to treat electron processes in fixed geometry of the nuclei and to describe nuclear motion influenced only by infinitely fast redistributing electron cloud is called Born-Oppenheimer approximation. This Thesis is focused mainly on the molecular motions which means changes of mutual position of nuclei.

NMR is a unique spectroscopic technique that allows studying of molecular systems in equilibrium. Nuclear magnetic properties such as the nuclear magnetic moment, do not interfere with structure or dynamic processes. On the other hand, the spectroscopic outcome can be strongly influenced by the molecular dynamics. In this sense, nuclear spins represent an ideal probe for observation of molecular movements.

1.1 Dynamic processes in NMR

In the Introduction, the dynamic processes are analysed from two closely related points of view, that are illustrated in Figure 1.1. Firstly, it is the mechanism of different movements and their time-scales (the upper part of Figure 1.1). After

---

[i] See row Age/Gyr, last column, Table 4 in Ref. 2 for age in giga years

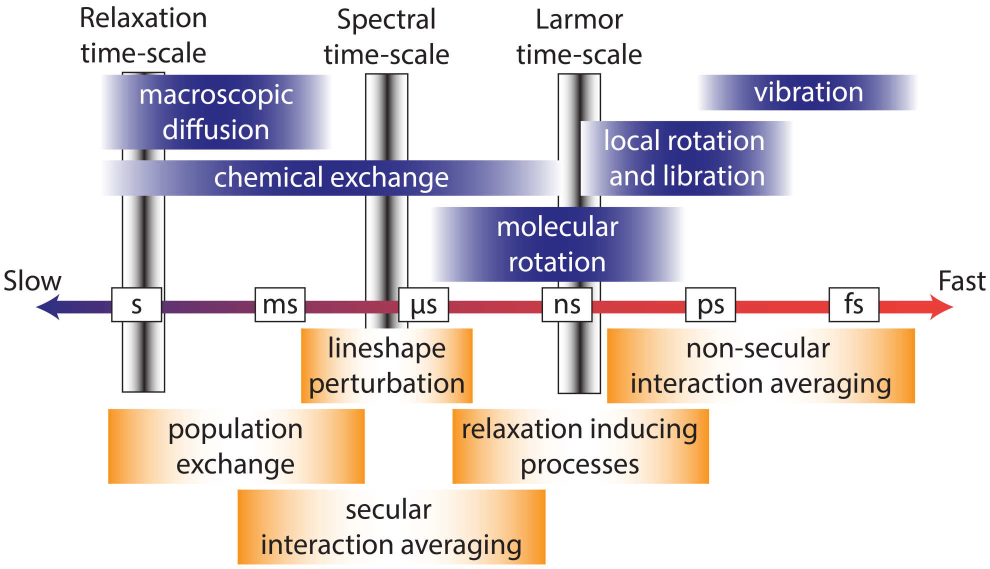

Figure 1.1: Schematic time-ranges of molecular movements (blue), their effects on NMR outcome (orange) and characteristic frequencies of three NMR time-scales (black). Adapted from Ref. 3.

that, effects of these dynamic processes on NMR spectral and relaxation properties will be summarised (the lower part of Figure 1.1).

Effects of dynamic processes on liquid-state NMR of paramagnetic systems are only discussed in this Thesis. For solid-state NMR, the reader is referred to literature, see e.g. Ref. 4.

1.1.1 Time-scales

The fastest processes are usually vibrations (from $1 \times 10^{-14}\,\mathrm{s}$ to $1 \times 10^{-12}\,\mathrm{s}$). If a light group is bonded to a a heavier group, the light one can undergo a pseudo-rotational motion with axis perpendicular to the bond. This strictly local process with characteristic time about $1 \times 10^{-13}\,\mathrm{s}$ is called libration.[5]. An example is waving of hydrogen atoms of water molecule coordinated to a metal ion, See Figure 1.2.

Local rotation of molecular groups along their bond (e.g. rotation of terminal methyl groups) occurs in the range of $1 \times 10^{-12}\,\mathrm{s}$. This process can be much slower (microseconds or milliseconds) when the rotation is hindered by steric restriction or by presence of partially double amide bond.ii)

---

ii)It should be noted that border between libration and rotation of the group is mostly formal

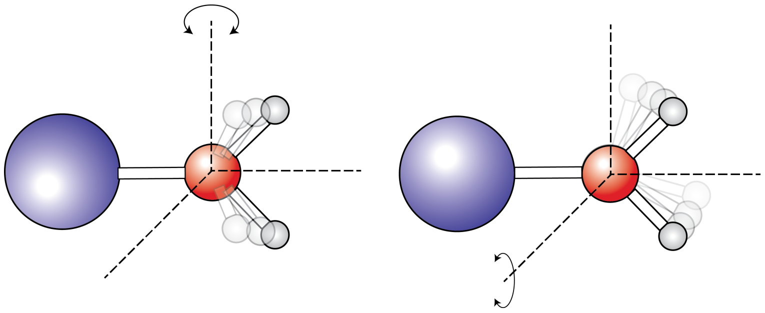

Figure 1.2: Example of libration motion of a coordinated water molecule. Blue – metal ion, red – oxygen, grey – hydrogen.

Rotation of the whole molecule is typically slower than the vibrations of its parts and depends mainly on viscosity of the solvent and the size and shape of the molecule. If the shape can be approximated by a sphere, the characteristic time of the rotation, called rotation correlation time (τ_R), is described by Stokes´s law:

$$\tau_R = \frac{\eta M_m}{\rho_V N_A k_B T}, \tag{1.1}$$

where η is viscosity, M_m is molar mass, ρ_V is solvent density, k_B is Boltzmann constant, N_A is Avogadro constant and T is thermodynamic temperature. Value of τ_R ranges from 1×10^{-11} s for small hexaaqua metal complexes to 1×10^{-8} for cca 10 kDa proteins or even over 1×10^{-6} s for huge systems over 1 MDa.

Another dynamic process is translation. It is either concurrent, i.e. convection (flow), or random, i.e. diffusion. Convection is of little importance for chemist as the samples are usually static.[iii)] On the other hand, molecular diffusion brings information about molecular shape and mass. It can be observed by NMR employing static magnetic field gradients.

In the dynamic processes mentioned above, the chemical structure of the compound was preserved. Nevertheless, an extensive family of dynamic processes involves changes of chemical identity of the compound and are referred to as chemical exchange. They occur on a very wide range of time-scales, from nanoseconds to many seconds or longer.

In this Thesis, processes related to coordination chemistry will be discussed, focussing on the coordination compound formation, dissociation and stereoisomers exchange. The time-scale, in this case, goes from ms to hours and days.

[iii)] In fact, dynamics of fluid liquids is important in angiography MRI, see e.g. Ref. 6

1.1.2 Dynamic effects in NMR

According to effect on results of NMR experiments, three time-scales of dynamic processes are important. The fastest is the time-scale where the rate of the dynamics is comparable to the nuclear Larmor frequency (ν_0), i.e. time-scale of $1 \times 10^{-7} - 1 \times 10^{-9}$ s. The second one is so called spectral time-scale which matches a frequency difference between resonances in a spectrum ($\Delta\nu_0$). It can range from a fraction of a second, in the case of almost equivalent nuclei, to microseconds when strong paramagnetically induced shift is present. The last regime is the relaxation rate time-scale which is usually on the order of seconds for diamagnetic systems but it is much faster (often below 1×10^{-3} s) in the case of paramagnetics.

The very fast dynamics (from fs to μs) directly averages spin-spin interactions. The dynamic processes which are faster than Larmor frequency, lead to motional averaging of the full interaction Hamiltonian before application of secular approximation. It means before neglecting of elements which do not commute with the Zeeman Hamiltonian. On the other hand, the slower processes average the spin Hamiltonian after the secular approximation. This distinction is important, because NMR spectrum is determined by the secular Hamiltonian while relaxation is caused by the non-secular therms.[3]

For example, assume motional averaging of direct ^{1}H$\cdots$^{13}C dipole-dipole interaction in C–H group. Corrections of interaction strength for very fast movements, like libration, must be considered for both solid-state spectra and relaxation treatment. However, correction for processes slower than ν_0, such as methyl group rotation, is included for calculation of spectral features only. The effect of methyl group rotation on relaxation cannot be described by the change of coupling strength but it influences the spectral density function.

Dynamic processes evolving in the spectral time-scale, typically chemical exchange or hindered rotation of a functional group, present itself mainly by changing the line-shape of resonances involved in this dynamics. Processes within this time-scale can induce population exchange as well. It can be followed by EXchange SpectroscopY (EXSY) techniques. Application of this technique for paramagnetic complexes of lanthanide(III) ions will be discussed in Chapter 4.

There are different approaches how to the describe phenomenons of line perturbation and population exchange. They are ranging from more or less phenomenological treatment of macroscopic magnetisation via Bloch equations to general build up of Liouville space algebra which contains the exchange directly in the Liouville superoperator and can describe evolution of any spin-density matrix under any exchange scheme.[7]

An interesting phenomenon is that, spectral features are affected even though the chemical structure of the observed molecule remains unchanged during the exchange process. A typical example is the exchange of amide hydrogen atoms in acetamide. Rotation is hindered by a partial double bond character of the amide bond, see Figure 1.3. The chemical structure of an acetamide molecule is the same although the site of nucleus $\mathrm{H_A}$ and $\mathrm{H_B}$ has been exchanged.

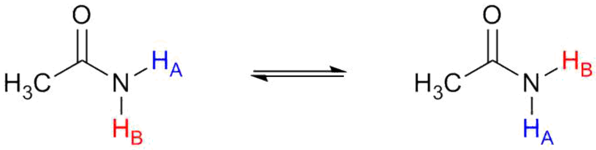

Figure 1.3: Rotation of amide group as an example of dynamic process which does not influence molecular structure

In this simple system with symmetric two-site exchange, five different regimes of ^{1}H spectra perturbation can be distinguished. See Figure 1.4 for simple simulation using analytical solution from Ref. 8.

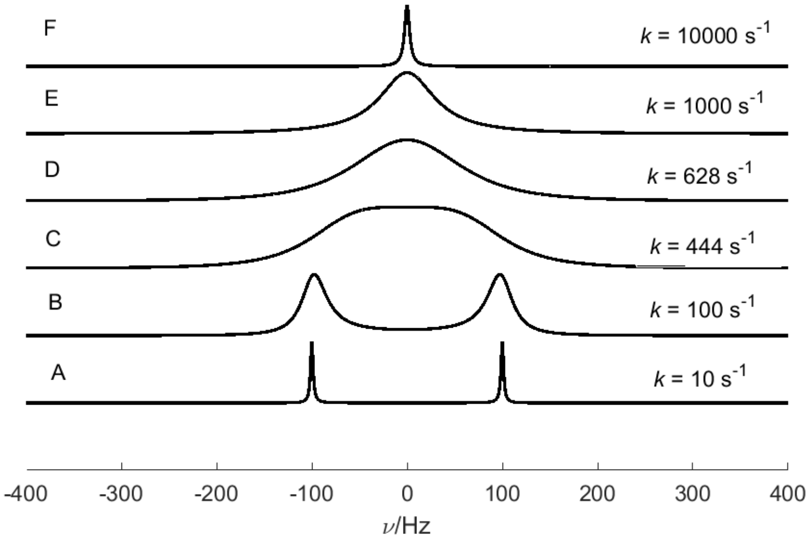

Figure 1.4: Simulated spectra of symmetric two-site exchange with various exchange rates k for $\Delta\nu = 200\,\mathrm{Hz}$ and zero transversal relaxation rate. Scaled to the same intensity

- The exchange rate k is much lower than the difference in resonance frequencies, i.e. $k \ll \Delta\nu_0$. In this case, so called slow motion regime, two isolated Lorentzian curves are observed. (Spectrum A in Figure 1.4)
- The exchange rate is still small, but comparable to $\Delta\nu_0\pi$. Two motionally broadened Lorentzian signals are observed in the spectra. (Spectrum B in Figure 1.4)
- The case when $k = \Delta\nu_0\pi$ is called crossover point. (Spectrum D in Figure 1.4) It is close to coalescence point where the two resonances merge into one which has zero first and second derivatives in the middle. (Spectrum C in Figure 1.4) If the transversal relaxation rate is smaller than k, the exchange rate in coalescence is $k_{\mathrm{coalescence}} = \pi\Delta\nu_0/\sqrt{2}$ which can be used for estimation of $k_{\mathrm{coalescence}}$ value from known $\Delta\nu_0$.
- A fast intermediate regime is characterised by the exchange which is faster but comparable to $\Delta\nu_0\pi$. In this case a broad signal is observed at average frequency. (Spectrum E in Figure 1.4)
- With the increasing exchange rate the spectrum contains only one sharp resonance. (Spectrum F in Figure 1.4)

When the exchange scheme is more complex, the the situation is considerably more complicated. But even in that case, the involved exchange rates can often be determined by non-linear fitting of the line-shapes using, for example, script published by Římal.[8] The line-shape analysis provides most accurate results for exchange rates near coalescence (Figure. 1.4 B–E). For slower rates (i.e. Figure. 1.4 A) EXSY techniques are often more reliable. If the exchange is much faster then $k_{\mathrm{coalescence}}$ (Figure. 1.4 F), it can still be determined by the relaxation dispersion method.

Chapter 2

NMR of paramagnetic molecules

Although the basic physical concepts behind NMR spectroscopy have been described many times in excellent books and reviews[i)] much better than author of this Thesis can manage to compose, some short introduction will be set up here to introduce the reader into the language used in this Thesis.

Most of the NMR techniques are designed for observation of diamagnetic systems. Pulse sequences applicable to paramagnetic systems must deal with an enlarged spectral width. Sometimes this paramagnetically induced shift is more than a thousand ppm in ^{1}H-NMR. Another complication is a significant relaxation enhancement, which broadens spectral lines. Nevertheless, for many pulse sequences, it is sufficient to set parameters properly and paramagnetic effects can bring additional information about studied system.

The negative consequences of enlarged spectral width cannot be often avoided just by a simple expansion of the acquisition window. Limited width of RF pulses and their excitation profile must be considered, especially when more complex pulse sequence is used, or if quantitative information is required. This will be discussed in more detail in Chapter 4.4.1. Decoupling efficiency decreases as well, if the resonance of decoupled nucleus are spread over wide range of frequencies. On the other hand, acquisition of ^{13}C{^{1}H} spectra using narrow-band decoupling with various offset offers a simple way to gain information about C–H connectivity when HSQC experiments are not available because of very fast T_2 relaxation (see e.g. Ref. 11).

At the same time, the paramagnetically induced shift is a source of interesting information about molecular structure, see Chapter 2.2.1 for detailed treatment.

[i)] For NMR in general, book of Levitt is recommended.[3] Relaxation theory, mainly for liquid diamagnetic systems, is comprehensively introduced in book of Kowalewski.[9]. Information about NMR in paramagnetic systems are given in a book of Bertini, Luchinat, Parigi and Ravera.[10]

Paramagnetically induced shift has an important consequences for the NMR of dynamic systems as well. Because the coalescence occurs when the exchange rate is equal to the frequency difference of the involved resonances, paramagnetically shifted signals enable observation of faster processes in the slow motion regime.

The other effect of the unpaired electrons in proximity of the observed nucleus is the relaxation enhancement. In general, both longitudinal and transversal relaxations are influenced. For detail treatment, see Chapter 2.2.2.

The transversal relaxation, labelled as T_2, describes the decrease of x, y components of magnetisation, while longitudinal (T_1) is associated with the recovering of equilibrium magnetisation in z direction.(ii) The T_2 relaxation in principle governs an attenuation of free-induction decay (FID) in pulse-NMR. In addition, the presence of microscopic and/or macroscopic inhomogeneities of magnetic field in the sample induces magnetisation dephasing and enhances the decay. After Fourier transformation of FID, both of these effects result in finite width of spectral lines. The T_2^* relaxation time is usually defined for rate of such attenuation and it can be calculated as $T_2^* = \frac{1}{\nu_{1/2}\pi}$, where $\nu_{1/2}$ is the signal width at half maximum in Hz. In paramagnetic systems, the T_2 relaxation is usually dominant contribution to this spectral line broadening. From practical point of view, it is often meaningless to spend time with thoughtful magnetic field homogenisation (shimming) of a paramagnetic sample.

Practically, the duration of the NMR experiment performed on fast relaxing sample can be reduced by shortening of delay before pulse sequence run (relaxation delay) and duration of FID detection (acquisition time). The modifications of these experimental parameters enable fast sequence repetition and, therefore, complex phase-cycles for desired magnetisation selection can be used without substantial prolongation of the measurement, see Chapter 4.4.1. On the other hand, application of magnetic field gradient pulses or long soft-pulses can be impractical due to the relaxation during them. All these complications must be taken into account not only for NMR, but also for MRI experiment setup.

(ii) In more accurate, spin density matrix description, T_2 relaxation is associated with decay of coherence and T_1 with recovering of equilibrium population according Boltzmann law.

2.1 Physical principles

2.1.1 Magnetic moments in magnetic field

In order to understand NMR of paramagnetic compounds, it is crucial to describe properties of electrons and nuclei and their interactions in an external magnetic field.

Each electron as well as each NMR-active nucleus has spin angular momentum (operators $\boldsymbol{S}$ and $\boldsymbol{I}$, respectively). Wave functions describing these particles are usually derived as eigenfunctions of two mutually commutating operators: square of the angular momentum magnitude (S^2 and I^2), and angular momentum projection to the z axis (S_z and I_z). Eigenvalues of these operators are the following:

$$S^2|S, M_S\rangle = S(S+1)|S, M_S\rangle \tag{2.1}$$

$$I^2|I, M_I\rangle = I(I+1)|I, M_I\rangle \tag{2.2}$$

$$S_z|S, M_S\rangle = M_S|S, M_S\rangle \tag{2.3}$$

$$I_z|I, M_I\rangle = M_I|I, M_I\rangle. \tag{2.4}$$

Here S and I are usually called as spin quantum numbers, while M_S and M_I as magnetic spin quantum numbers. Eigen functions of S^2, S_z and I^2, I_z are $|S, M_S\rangle$ and $|I, I_S\rangle$.

Angular momentum of an elementary particle is closely related to its magnetic momentum ($\boldsymbol{\mu}_S$ and $\boldsymbol{\mu}_I$) through the so called gyromagnetic ratio, γ_S and γ_I for electron and nucleus, respectively. The relations are the following:

$$\boldsymbol{\mu}_{\boldsymbol{S}} = \gamma_S \hbar \boldsymbol{S} \tag{2.5}$$

$$\boldsymbol{\mu}_{\boldsymbol{I}} = \gamma_I \hbar \boldsymbol{I}. \tag{2.6}$$

Sometimes, it is more convenient to write these relations using free-electron and nuclear g factors (g_e and g_I respectively). Then $\gamma_S = -\frac{g_e \mu_B}{\hbar}$ and $\gamma_I = \frac{g_I \mu_N}{\hbar}$ where $\mu_B = 9.2740 \times 10^{-24}\,\mathrm{J\,T^{-1}}$ and $\mu_N = 5.0508 \times 10^{-27}\,\mathrm{J\,T^{-1}}$ are Bohr and nuclear magneton respectively. The magnitude of free-electron magnetic momentum is 652.2 times higher than that of free proton and it has significant consequences for theory and practical experimental set-up.[10] For γ_I of the selected nuclei, see Table 2.1

Table 2.1: NMR properties of selected nuclei

isotope	spin	abundance/%	g_I	$\gamma_I/\mathrm{rad\,s^{-1}\,T^{-1}}$	sensitivity
^{1}H	1/2	99.98	5.59	2.68×10^8	1
^{2}H	1	1.56×10^{-2}	0.857	4.11×10^7	1.45×10^{-6}
^{13}C	1/2	1.108	1.40	6.73×10^7	1.76×10^{-4}
^{17}O	5/2	3.7×10^{-2}	-0.758	-3.63×10^7	1.08×10^{-5}
^{19}F	1/2	100	5.28	2.52×10^8	0.83
^{31}P	1/2	100	2.26	1.08×10^8	0.0663

For nuclei in an external magnetic field ($\boldsymbol{B}_0$) the energy is given by Zeeman Hamiltonian:

$$H = -g_I \mu_N \boldsymbol{I} \cdot \boldsymbol{B_0}. \tag{2.7}$$

Now, if the z axis is defined along $\boldsymbol{B_0}$, the nuclear spins in equilibrium have a non-zero projection along z, whereas they are generally averaged to zero in the xy plane. Therefore, we can write:

$$H = -g_I \mu_N I_z B_0. \tag{2.8}$$

Since application of I_z on wave the function $|I, M_I\rangle$ gives M_I, the energy difference between two-levels with $\Delta M_I = 1$ (e.g. transition in two level system with $S = 1/2$) is

$$\Delta E = g_I \mu_N B_0 [M_I - (M_I - 1)] = g_I \mu_N B_0. \tag{2.9}$$

The situation is similar for electron magnetic moment as long as there is only one unpaired electron occupying s orbital, i.e. without spin-spin or spin-orbit interactions. Hamiltonian of this system in field $\boldsymbol{B_0}$ is

$$H = g_e \mu_B \boldsymbol{S} \cdot \boldsymbol{B_0} \tag{2.10}$$

and, after similar consideration as in case of Eq. 2.8, it leadsy to:

$$H = g_e \mu_B M_S B_0. \tag{2.11}$$

However, many complications appear when *orbital* angular momentum ($\boldsymbol{L}$) is involved. For each orbital, its angular moment can be defined. For lighter elements (i.e. transition metals of the 4th period), where spin-orbit coupling can be treated as a perturbation, the overall orbital angular momentum ($\boldsymbol{L}$) can be calculated by combination of individual orbital moments.[iii]

Similar relations as those in Eq. 2.1 and 2.2 are valid for orbital momentum:

$$L^2|L, M_L\rangle = L(L+1)|L, M_L\rangle \tag{2.12}$$

$$M_L|L, M_L\rangle = M_L|L, M_L\rangle. \tag{2.13}$$

In a molecule, the ligand field defines internal direction (internal axis) in which the angular momentum is preferentially aligned, while the other orientations are energetically less favourable. When the molecule is in magnetic field $\boldsymbol{B_0}$, the interaction energy of the overall orbital momentum is described by Zeeman Hamiltonian

$$H = -\boldsymbol{\mu_L} \cdot \boldsymbol{B_0} = \mu_B \boldsymbol{L} \cdot \boldsymbol{B_0} \tag{2.14}$$

where $\boldsymbol{\mu_L}$ is operator of orbital magnetic moment.

This interaction tends to disalign $\boldsymbol{L}$ from internal axes. Therefore, energy is orientation dependent and changes when the molecule rotates with respect to $\boldsymbol{B_0}$. The total energy Hamiltonian containing overall orbital and electron spin contributions can be written as

$$H = \mu_B(\boldsymbol{L} + g_e\boldsymbol{S}) \cdot \boldsymbol{B_0}. \tag{2.15}$$

Very useful concept of so-called *spin Hamiltonian* can be introduced:

$$\boldsymbol{S} \cdot \boldsymbol{g} = \boldsymbol{L} + g_e\boldsymbol{S}. \tag{2.16}$$

In this formalism, laborious calculation of electronic structure effectively reduces to treating the energy Hamiltonian and system energy as being orientation dependent via $\boldsymbol{g}$ tensor:

$$H = \mu_B \boldsymbol{S} \cdot \boldsymbol{g} \cdot \boldsymbol{B_0} \tag{2.17}$$

$$E = \mu_B M_S g_{kk} B_0, \tag{2.18}$$

where g_{kk} is a projection of $\boldsymbol{g}$ tensor into $\boldsymbol{B_0}$ direction in molecular frame.

[iii] For heavier elements, where strong spin-orbit coupling appears (e.g. lanthanides), a formalism of jj-coupling is involved, establishing the total angular momentum J as a sole "good" quantum number. In this case, overall orbital and spin electron angular momentum cannot be separated. This case will not be treated here.

When the molecule under the investigation rotates, the energy fluctuates within interval ΔE. If this spreading is much smaller, than the inverse of rotation correlation time τ_R^{-1}, i.e. ($\Delta E/\hbar < \tau_R^{-1}$), then the $\boldsymbol{g}$ tensor is averaged into its isotropic value $\overline{g}$, which is typically different from g_e.

However, the spin-orbit interaction does not affect the energy of Zeemen levels only. Even at zero magnetic field energy levels with different M_S values are splitted by spin-orbit and spin-spin coupling (for $S > 1/2$). In the spin-Hamitonian formalism, the zero-field-splitting (ZFS) is indicated as:

$$H_{\mathrm{ZFS}} = \boldsymbol{S} \cdot \boldsymbol{D} \cdot \boldsymbol{S}, \tag{2.19}$$

where $\boldsymbol{D}$ is a ZFS tensor. For half-integer S, a degeneracy of levels with $M_S = \pm n/2$ is preserved (so-called Kramers dublets) whereas, for an integer spin, all degeneracy is removed.

The ZFS tensor $\boldsymbol{D}$ is traceless and, therefore, it is averaged to zero by a rapid molecular rotation. The ZFS tensor has axial ($D = D_{zz} - 1/2(D_{xx} + D_{yy})$) and rhombic ($E = 1/2(D_{xx} - D_{yy})$) components which reflect the overall symmetry of the system. For coordination compounds with cubic symmetry (typically $\mathcal{O}_h$) there is no ZFS, whereas for systems with cylindrical symmetry there is no ZFS rhombicity. The size of ZFS is usually referred to as $\Delta^2 = 2/3D^2 + 2E^2$. See Figure 2.1 for schematic splitting of electron energy levels in systems with various S.

It should be noted that even in highly symmetric systems the so called transient[iv)] ZFS can appear due to vibrations of molecule and its collisions with solvent molecules. Modulation of electron energy levels by transient ZFS is one of the mechanisms of electron relaxation.[12,13] See Chapter 2.2.2 for further discussion of NMR-relaxation in the presence of transient ZFS.

2.1.2 Populations and magnetic susceptibility

In the previous section, it was stated that a system with spin and/or orbital magnetic dipole moment occupies various energy levels E_i. An exclusive population of one single state can be reached only at $T = 0\,\mathrm{K}$. At non-zero temperature, the population P_i of a i-th level is described by Boltzmann distribution:

[iv)] permanent ZFS is sometimes called static

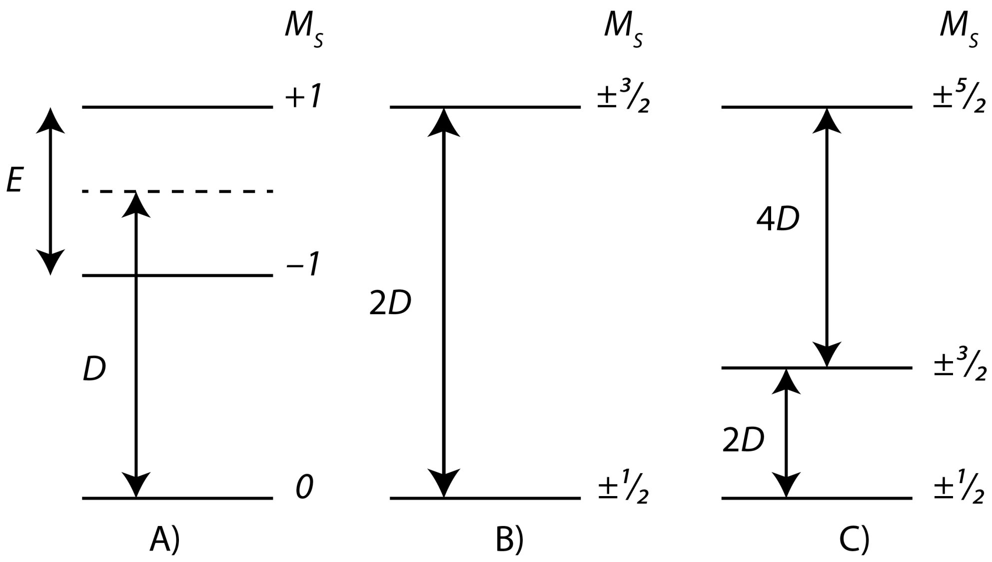

Figure 2.1: Splitting of A) $S = 1$ B) $S = 3/2$ and C) $S = 5/2$ electron manifolds in zero magnetic field due to A) fully asymmetric ZFS and B), C) cylindrically symmetric ZFS. Quantities D and E indicate axial and rhombic ZFS tensor components. Adapted from Ref 10.

$$P_i = \frac{e^{-E_i/(k_BT)}}{\sum\limits_i e^{-E_i/(k_BT)}} \tag{2.20}$$

The splitting of different electron M_S levels is only about $1\,\mathrm{cm}^{-1}$ at $1\,\mathrm{T}$ and even 658× smaller for nuclear M_I. At temperature of 300 K $k_BT = 208\,\mathrm{cm}^{-1}$, the population of the levels is almost equal. Nevertheless, there is a tiny difference which creates induced magnetic moment μ_{ind}. From the macroscopic point of view, it results in induced magnetisation M of the system, defined per unit volume V.

$$M = \frac{\mu_{\mathrm{ind}}}{V}. \tag{2.21}$$

The magnetisation M is found to be proportional to the applied magnetic field through magnetic susceptibility per unit volume χ_V. For all systems except the ferromagnetic ones, it holds that $\chi_V \ll 1$ and we get:

$$\chi_V = \frac{M\mu_0}{B_0}, \tag{2.22}$$

where μ_0 is the vacuum permeability. One can define molar magnetic susceptibility $\chi_M = V_M\chi_V$ as well, where V_M is molar volume. Average induced magnetic moment per particle $\langle\mu\rangle$ can be defined as

$$\langle\mu\rangle = \frac{\chi_M}{\mu_0 N_A} B_0. \tag{2.23}$$

From the classical point of view, the energy of the system with N_A particles in the magnetic field can be described using induced magnetic moment per particle $\langle\mu\rangle$ as well,

$$E = -\langle\mu\rangle N_A B_0. \tag{2.24}$$

These quantities are experimentally accessible via magnetometric measurement of bulk material. However, how do they reflect the electronic structure of the paramagnetic centre?

Let us have a look on S manifold in magnetic field in absence of any spin-orbit coupling, i.e. no orbital contribution and no ZFS. Without any difference in population, the energy E of the system with N_A particles is zero:

$$E = g_e \mu_B B_0 \sum_{M_S=-S}^{S} M_S = 0. \tag{2.25}$$

Nevertheless, due to the Boltzmann population distribution (Eq. 2.20), recalling that $M_S = \langle S, M_S|S_z|S, M_S\rangle$, we get:

$$E = N_A g_e \mu_B B_0 \frac{\sum\langle S, M_S|S_z|S, M_S\rangle e^{-g_e\mu_B B_0 M_S/(k_B T)}}{\sum e^{-g_e\mu_B B_0 M_S/(k_B T)}} = N_A g_e \mu_B B_0 \langle S_z\rangle, \tag{2.26}$$

where $\langle S_z\rangle$ is the expectation value of S_z operator, i.e. result of S_z opperating on each $|S, M_S\rangle$ level considering its population. Because of $g_e\mu_B B_0 M_S \ll k_B T$, it can be approximated $e^{-g_e\mu_B B_0 M_S/(k_B T)} \approx 1 - g_e\mu_B B_0 M_S/(k_B T)$ and, after some rearrangement, the energy of the system is:

$$E = -N_A g_e^2 \mu_B^2 \frac{S(S+1)B_0^2}{3k_B T} \tag{2.27}$$

and related S_z expectation value is:

$$\langle S_z\rangle = -\frac{g_e\mu_B S(S+1)B_0}{3k_B T}. \tag{2.28}$$

By comparison of Eq. 2.24 and 2.27, we get the induced magnetic moment:

$$\langle\mu\rangle = g_e^2 \mu_B^2 \frac{S(S+1)}{3k_B T} B_0. \tag{2.29}$$

The molar magnetic susceptibility can be calculated as:

$$\chi_M = \mu_0 N_A \mu_B^2 g_e^2 \frac{S(S+1)}{3k_B T}, \tag{2.30}$$

which, by the way, demonstrates the Curie law, i.e. dependence of χ_M on inverse temperature.

If there is a spin-obit coupling effecting simple S manifold, the energy of the system in magnetic field is orientation dependent. In the spin Hamiltonian formalism, this dependency is treated by introducing the $\boldsymbol{g}$ tensor instead of g_e. Therefore, the molar magnetic susceptibility is orientation dependent as well and must be treated as a tensor of molar magnetic susceptibility $\boldsymbol{\chi}_M$.

When all the excited states are well separated from the ground state, the kk element of $\boldsymbol{\chi}_M$ is

$$\chi_{M_{kk}} = \mu_0 N_A \mu_B^2 g_{kk} \frac{S(S+1)}{3k_B T} \tag{2.31}$$

The average induced magnetic moment is not parallel with external magnetic field any more, unless it is oriented along one of the main direction of $\boldsymbol{\chi}_M$. The dependence of the induced magnetic moment on external magnetic field is

$$\langle \boldsymbol{\mu} \rangle = \frac{\boldsymbol{\chi}_M \cdot \boldsymbol{B}_0}{N_A \mu_0}. \tag{2.32}$$

It should be noted that, if the excited states are close to the ground state, their populations and related effect on $\boldsymbol{\chi}_M$ cannot be neglected and simple Eq. 2.31 is not valid any more. More complex Van Vleck equation must be used instead (see Ref. 10).

The paramagnetically induced shift depends on the induced electron magnetic dipole $\langle \boldsymbol{\mu} \rangle$ and relaxation is partially induced by time fluctuations of interaction between $\langle \boldsymbol{\mu} \rangle$ and the observed nucleus. Therefore, proper description of the induced magnetic moment as well as its field and orientation dependence are of fundamental importance for treating paramagnetic effects in NMR.

As a footnote it should be noted, that in coordination chemistry literature, the effective magnetic dipole moment μ_{eff} is introduced by assumption of the Curie law:

$$\chi_M = \mu_{\text{eff}}^2 \frac{N_A \mu_0}{3k_B T}. \tag{2.33}$$

This quantity reflects the number of unpaired electrons. In spin-only formula approximation $(\mu_{\text{eff}}^{\text{spin-only}})^2 = g_e^2 S(S+1)\mu_B^2$ and deviation from this value indicate orbital contribution, spin-orbit coupling and/or low-lying excited states. Ranges of μ_{eff} for each metal and electron configuration are tabulated.[14] This value must not be confused with the induced magnetic dipole moment $\langle \boldsymbol{\mu} \rangle$ or its size $\langle \mu \rangle$.

2.2 Paramagnetic effects in NMR

2.2.1 Paramagnetically induced shift

Chemical shift of the NMR active nucleus in a paramagnetic molecule consists of diamagnetic contribution which is, in practice, approximated by chemical shift of a diamagnetic analogue (e.g. different lanthanide or *d*-element in a different oxidation number can be utilised), and of a paramagnetic contribution.[v)] Paramagnetically induced shift (sometimes called hyperfine shift) is the result of interaction between the time-averaged induced magnetic moment of the electron and the NMR active nucleus. In practice, this interaction is usually divided into two terms. The first is related to the local unpaired electron density in the position of the nucleus and usually referred to as contact, or Fermi contact, shift. The other contribution is induced by dipole-dipole interaction of the observed nucleus with induced magnetic moment $\langle \boldsymbol{\mu} \rangle$ through space. It is usually referred to as pseudocontact shift.

Fermi contact contribution

In quantum mechanical therms, the energy of Fermi contact interaction is determined by the following Hamiltonian:

$$\boldsymbol{H} = A\boldsymbol{I} \cdot \boldsymbol{S}, \tag{2.34}$$

where A is the contact coupling constant. The nuclear spin is always aligned with external magnetic field as well as the electron spin at high-field limit ($g_e \mu_B B_0 \gg A$) and in absence of strong-spin orbit coupling. The energy of the interaction can be calculated as $E^{\text{con}} = AM_I \langle S_z \rangle$.

The contact shift can be obtained by dividing E^{con} by Zeeman energy ($\hbar \gamma_I M_I B_0$).

$$\delta^{\text{con}} = \frac{A}{\hbar \gamma_I B_0} \langle S_z \rangle \tag{2.35}$$

[v)] Chemical shift contribution due to bulk magnetic susceptibility (BMS) of the sample effects all nucleus in the same way. Therefore, it is cancelled by chemical scale referencing via internal reference compound. Nevertheless, it is useful method for magnetic susceptibility measurement by so called Evans method.[15]

Recalling the equation 2.28 for $\langle S_z \rangle$, δ^{con} is:

$$\delta^{\text{con}} = \frac{A}{\hbar} \frac{g_e \mu_B S(S+1)}{3\gamma_I k_B T} \tag{2.36}$$

Obtained contact shifts is a dimensionless numbers. In order to get contribution to chemical shift in ppm, δ^{con} must by multiplied by 10^6. The hyperfine coupling constant A is closely related to the unpaired electron density ρ in the nuclear position. In a general case, it is the sum of all contributions from all molecular orbitals (MO) containing unpaired electron density. It should be highlighted that, because of spin polarisation, the unpaired spin density arises not only from a single occupied MO, but also from double occupied orbitals. The result of spin polarisation is that an unpaired electron in p orbital can induce contact shift in spite of its zero probability in the position of the nucleus. In this case, the interaction is mediated by polarisation of low-laying fully-occupied s orbitals. Nowadays, the hyperfine coupling constant is usually determined by *ab-initio* or DFT calculations.[16]

The contact contribution has a dominant effect on the nuclei directly bound to the paramagnetic centre and its effect decreases with an increasing number of bonds between the paramagnetic centre and the observed nucleus.

Pseudocontact shift

As the pseudocontact shift is induced by dipole-dipole interaction, let us recall the classical relation for the interaction between two dipoles $\boldsymbol{\mu_1}$ and $\boldsymbol{\mu_2}$ with mutual orientation described by vector $\boldsymbol{r}$ (where r is the length of $\boldsymbol{r}$):

$$E^{\text{dip}} = -\frac{\mu_0}{4\pi} \left[\frac{3(\boldsymbol{\mu_1} \cdot \boldsymbol{r})(\boldsymbol{\mu_2} \cdot \boldsymbol{r})}{r^5} - \frac{\boldsymbol{\mu_1} \cdot \boldsymbol{\mu_2}}{r^3} \right]. \tag{2.37}$$

At this point, point-dipole approximation (PDA) is introduced, i.e. it is assumed that an electron dipole can be described as a point-dipole localised at the coordinates of the paramagnetic centre (metal-centered PDA). This is often true for $4f$ elements since the unpaired electrons are localised in low-laying shells, whereas for $3d$ elements minimal distance for validity of this approximation is estimated to 7 Å.[17] In metal-centred PDA applied in the equation 2.37, $\boldsymbol{\mu_1}$ is nuclear dipole ($\boldsymbol{\mu_1} = \hbar\gamma_I \boldsymbol{I}$) and $\boldsymbol{\mu_2}$ is averaged induced electron magnetic moment ($\boldsymbol{\mu_2} = \langle \boldsymbol{\mu} \rangle$). Then we get:

$$E^{\text{dip}} = -\frac{\mu_0}{4\pi} \left[\frac{3(\hbar\gamma_I \boldsymbol{I} \cdot \boldsymbol{r})(\langle \boldsymbol{\mu} \rangle \cdot \boldsymbol{r})}{r^5} - \frac{\hbar\gamma_I \boldsymbol{I} \cdot \langle \boldsymbol{\mu} \rangle}{r^3} \right]. \tag{2.38}$$

Recalling the relationship between induced magnetic moment and magnetic susceptibility tensor (Eq. 2.32) and defining the external magnetic field direction being $\boldsymbol{\kappa}$, it can be stated that:

$$E^{\text{dip}} = -\frac{\hbar\gamma_I B_0}{4\pi r^5} M_I \boldsymbol{\kappa} \cdot \left[3\boldsymbol{r}(\boldsymbol{r} \cdot \boldsymbol{\chi}) - r^2 \boldsymbol{\chi}\right] \cdot \boldsymbol{\kappa}. \tag{2.39}$$

Magnetic susceptibility tensor $\boldsymbol{\chi}$ in Eq. 2.39 is typically anisotropic due to the orbital contribution. Then the dipolar shift (dimensionless) can be obtained by division of the dipol-dipol interaction energy in two states differing by $\Delta M_I = \pm 1$ from Eq. 2.39 by Zeeman energy ($\hbar\gamma_I B_0$)

$$\delta^{\text{dip}} = \frac{\Delta E^{\text{dip}}}{\hbar\gamma_I B_0}. \tag{2.40}$$

In liquids this dipolar shift is averaged by fast molecular motion giving isotropic pseudocontact shift, δ^{pcs}.[vi)] In any reference frame with the metal in the origin, where x, y, z are nuclear coordinates, δ^{pcs} can be calculated as:

$$\delta^{\text{pcs}} = \frac{1}{12\pi r^5} \text{Tr}\left[\begin{pmatrix} (3x^2 - r^2) & 3xy & 3xz \\ 3xy & (3y^2 - r^2) & 3yz \\ 3xz & 3yz & (3z^2 - r^2) \end{pmatrix} \begin{pmatrix} \chi_{xx} & \chi_{xy} & \chi_{xz} \\ \chi_{xy} & \chi_{yy} & \chi_{yz} \\ \chi_{xz} & \chi_{yz} & \chi_{zz} \end{pmatrix}\right]. \tag{2.41}$$

It should be highlighted that the axial symmetry of $\boldsymbol{\chi}$ tensor can significantly simplify the equation 2.41. See Chapter 2.2.2 in Ref. 10 for further details and equations for δ^{dip} in various coordinate systems.

Important consequence of Eq. 2.41 is that nuclear coordinates cannot be generally calculated from experimental pseudocontact shifts as there are 6 elements of $\boldsymbol{\chi}$ and 3 coordinates. Nevertheless, an iterative solution is possible when coordinates of a few nuclei are known.[19] Pseudocontact shifts are dimensionless numbers. In order to get contribution to chemical shift in ppm, δ^{pcs} must by multiplied by 10^6.

2.2.2 Paramagnetically induced relaxation

This Chapter was adapted from Chapter 4 in Ref. 10 where the topic is explained in an excellent, didactic way. The NMR relaxation is generally a process of equilibrium recovery in spin-system after some perturbation. The perturbation usually means the application of radio frequency pulses during NMR experiment or just

---

[vi)] In the solid state without fast reorientation, significantly larger anisotropic, orientation dependent, dipole shift is observed as well.[18]

a simple changing of external magnetic field, i.e. putting the sample into NMR spectrometer.

In equilibrium at a finite temperature, populations of spin-states are described by the Boltzmann distribution (Eq. 2.20) and there are no coherences. From the macroscopic point of view, magnetisation is observed in z direction only (see Eq. 2.22).

The NMR relaxation is induced by random dynamic processes which occur in the time-scale of Larmor precession and which are changing strength of magnetic interactions of the observed nucleus with its surroundings. Availability of these processes at frequency $\omega(\mathrm{rad\ s^{-1}})$ is described by their *spectral density* function $\mathcal{J}(\omega)$. It is a Fourier transform of autocorrelation function of these interactions strength. If mono-exponential decay of the autocorrelation function is assumed (correlation time τ_c), spectral density gets the form of Lorentzian curve:

$$\mathcal{J}(\omega, \tau_c) = \frac{\tau_c}{1 + \omega^2 \tau_c^2}. \tag{2.42}$$

If the correlation time is much smaller than $1/\omega$, the so called fast-motion limit, then $\mathcal{J}(\omega, \tau_c) \approx \tau_c$. On the contrary, if $\tau_c \gg 1/\omega$, Eq. 2.42 is reduced to $\mathcal{J}(\omega, \tau_c) \approx \frac{1}{\omega^2 \tau_c}$. This is called the slow-motion regime. The dispersion of $\mathcal{J}$ occurs when $\tau_c \approx 1/\omega$.

It should be highlighted that, in contrast to chemical shift, the NMR relaxation is not determined by the mean value of the interaction energy but by the mean square of it $\langle E_{\mathrm{int}}^2 \rangle$. Therefore, many of interactions are not averaged by dynamic processes (e.g. direct dipole-dipole interactions). Finally, it can be generally stated that the relaxation rate R is proportional to the interaction strength and its spectral density function:

$$R \propto \langle E_{\mathrm{int}}^2 \rangle \mathcal{J}(\omega, \tau_c). \tag{2.43}$$

In paramagnetic systems, the main interaction which mediates the relaxation is interaction of the observed nucleus with unpaired electron through space i.e. dipole-dipole interaction, or directly by effect of unpaired spin density in the position of the nucleus, i.e. contact interaction. The main dynamic processes which cause the nuclear relaxation in paramagnetic systems are (see Figure 2.2):

- Electron relaxation, i.e. random flipping of electronic spin between states with different M_S. See Figure (2.2.a). It is usually labelled as T_e
- Random rotation of the molecule which leads to change in mutual orientation of electron and nuclear dipole moments. Electron dipole moment can be

either the actual magnetic moment ($\boldsymbol{\mu_S}$) or the averaged induced magnetic moment ($\langle\boldsymbol{\mu}\rangle$) caused by different population of Zeeman levels. The latter case is usually referred to as Curie, or magnetic susceptibility relaxation. This reorientation does not influence the contact relaxation mechanism, as the molecule rotates as a whole. The random rotation, sometimes called thumbing, is usually described by the rotation correlation time τ_R. See Figure 2.2.b.

- Attachment and detachment of a moiety containing the observed nucleus to the paramagnetic centre (i.e. chemical exchange) cause fluctuation of the local magnetic field as well. Typical example is the exchange of coordinated water in metal ion aqua-complexes. Extreme example of this process is an outer-sphere relaxation where water molecule changes position between proximity of paramagnetic centre and bulk solvent but there is no direct bond between the molecule and the paramagnetic centre in any moment. The exchange process is usually described by the exchange time τ_M. See Figure 2.2.c

When more processes occur, their rates are summed, and overall correlation times for dipole-dipole mechanism $(\tau_c)^{\text{dip}}$ and contact mechanism $(\tau_c)^{\text{con}}$ are:[vii)]

$$(\tau_c^{-1})^{\text{dip}} = T_e^{-1} + \tau_R^{-1} + \tau_M^{-1} \tag{2.44}$$

$$(\tau_c^{-1})^{\text{con}} = T_e^{-1} + \tau_M^{-1} \tag{2.45}$$

As the reciprocal of τ_c is a sum of reciprocals, the fastest process, i.e. the *smallest* correlation time, determines overall correlation time. For typical ranges see Fig. 2.3.

From the discussion above, it arises, that the relationship between correlation times and electron relaxation is of high importance for NMR relaxation. Let us assume two paramagnetic ($S = 1/2$) coordination compounds, one with $T_e = 1 \times 10^{-8}\,\text{s}$ and the other with $T_e = 1 \times 10^{-12}\,\text{s}$. The size of both molecules is the same and, therefore, their rotation correlation times are the same as well ($\tau_R = 1 \times 10^{-10}\,\text{s}$). Let us have similar strength of the interaction which evokes relaxation in both systems as well. For the system with higher T_e, total correlation time is $\tau_c \approx \tau_R = 1 \times 10^{-10}\,\text{s}$ and relaxation depends on the rotation of the molecule. In

---

[vii)] Sometimes τ_{c1} and τ_{c2} are distinguished for T_{1e} and T_{2e}, respectively, but the meaning of electron T_{2e} transversal relaxation in NMR is ambiguous.

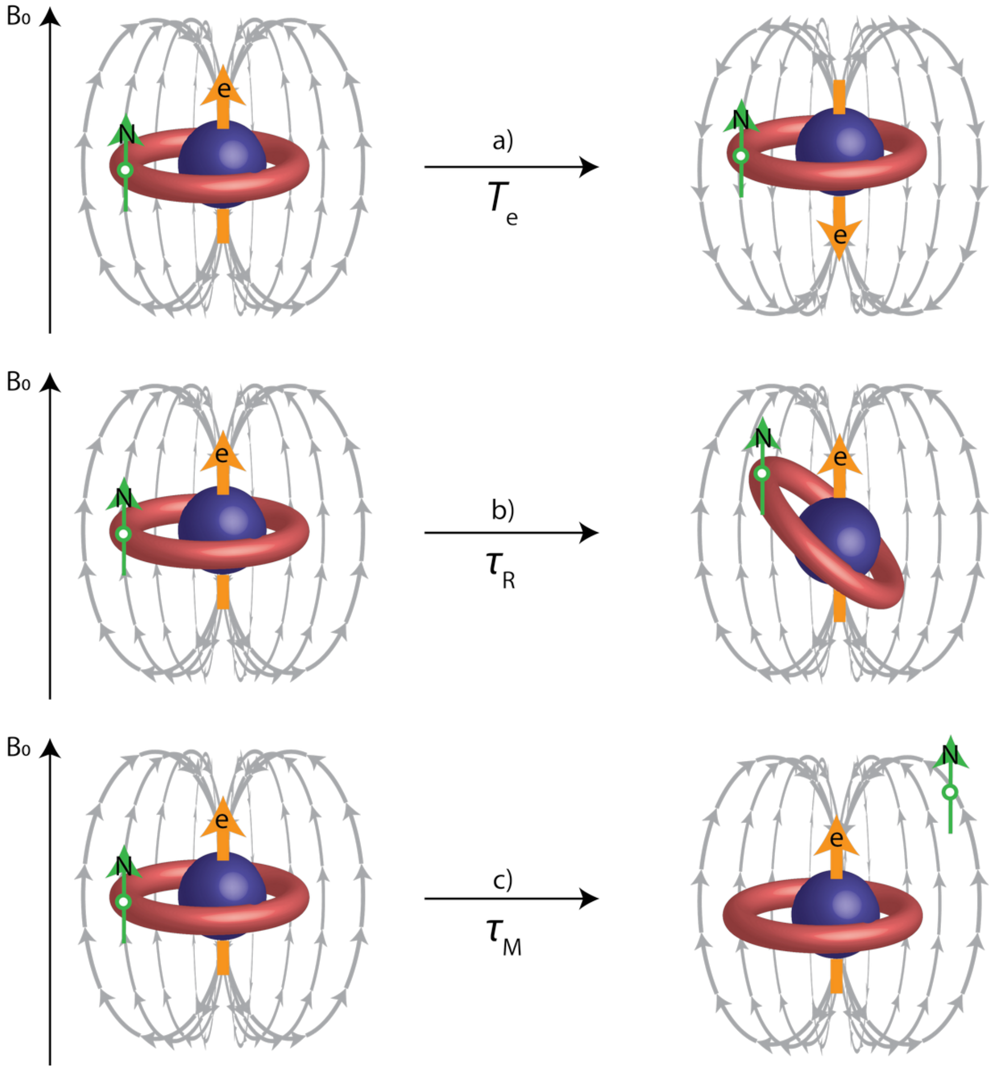

Figure 2.2: Schematic representation of dynamic processes responsible for nuclear (N) relaxation in the presence of electron magnetic dipole moment (e): a) electron relaxation (T_e); b) molecular reorientation (τ_R) c) chemical exchange (τ_M). Adapted from Ref 10

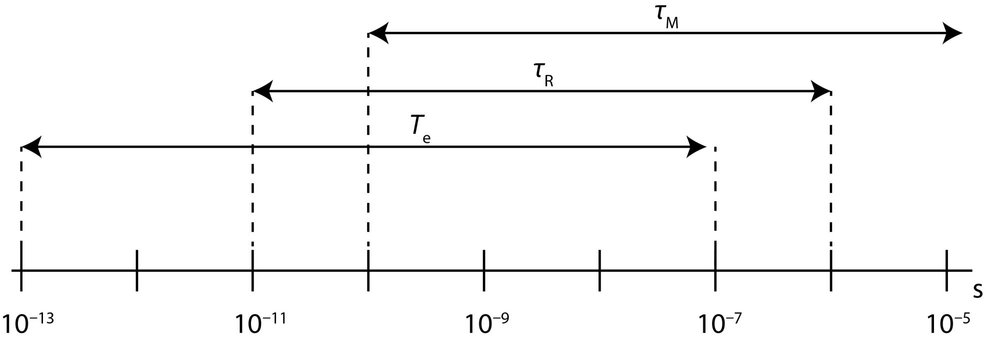

Figure 2.3: Typical ranges of correlation times present in paramagnetic systems. Adapted from Ref. 10

the other case, where $\tau_c \approx T_e = 1 \times 10^{-12}$ s, relaxation is independent of molecular rotation. Because the spectral density in fast-motion limit is approximately equal to τ_c, the relaxation is faster in the first case. It means that when the rotation mechanism determines the correlation time, the relaxation is too fast to observe reasonably resolved spectra. As a practical consequence for NMR, it can be stated that NMR is successfully applicable in systems where relaxation is determined by electron relaxation.

Detection of reasonable NMR data is possible even in systems with slowly relaxing paramagnetic electron, but the observed moiety must be in fast exchange between paramagnetic and diamagnetic site. For electronic relaxation rates of selected metal ions, see Table 2.2. Some values of electronic relaxation times are reported at zero magnetic field, as the electronic relaxation time can be strongly field-dependent (see next Chapter).

According to the Table 2.2, compounds suitable for NMR experiments are lanthanides(III) (except gadolinium(III)), low-spin (LS) iron(III) and high-spin (HS) iron(II), nickel(II)(especially in tetrahedral environment), six-coordinated (HS) cobalt(II) and chromium(II). On the other hand, the presence of chromium(III), manganese(II), copper(II) or gadolinium(III) is not compatible with the NMR of proximate nuclei.

Electronic relaxation

There are more mechanisms responsible for electron relaxation. The following description is limited only to those important for the systems studied in this Thesis.

A modulation of $\boldsymbol{g}$ tensor or/and hypefine-coupling tensor $\boldsymbol{A}$ by the rotation of the molecule or the molecular distorsion (e.g. through dynamic Jahn-Teller effect)

Table 2.2: Electronic relaxation times T_{1e} of some metal ions. Adopted from Ref. 10

ion	el. conf.	S	T_e/s
Ti^{3+}	d^1	1/2	10^{-10}–10^{-11}
VO^{2+}	d^1	1/2	$\approx 10^{-11}$[a]
V^{3+}	d^2	1	$\approx 10^{-11}$
Cr^{3+}	d^3	3/2	5×10^{-9}–5×10^{-10}
Cr^{2+}	d^4	2	10^{-11}–10^{-12}
Mn^{2+}	d^5	5/2	10^{-8}[b]
Fe^{3+}	d^5 HS	5/2	10^{-9}–10^{-10}[c]
Fe^{3+}	d^5 LS	1/2	10^{-11}–10^{-13}
Fe^{2+}	d^6 HS 5–6 coord.	2	10^{-12}–10^{-13}
Fe^{2+}	d^6 HS 4 coord.	2	$\approx 10^{-11}$
Co^{2+}	d^7 HS 5–6 coord.	3/2	10^{-12}–10^{-13}
Co^{2+}	d^7 HS 4 coord.	3/2	$\approx 10^{-11}$
Co^{2+}	d^7 LS.	1/2	10^{-9}–10^{-11}
Ni^{2+}	d^8 5–6 coord.	1	$\approx 10^{-10}$[d]
Ni^{2+}	d^8 4 coord.	1	$\approx 10^{-12}$
Cu^{2+}	d^9	1/2	$(1–5) \times 10^{-9}$
Gd^{3+}	f^7	7/2	10^{-8}–10^{-9}[e]
Ln^{3+} except Gd^{3+}, La^{3+}, Lu^{3+}			10^{-12}–10^{-14}

[a] T_e is field dependent; $T_{1e(0)}$(i.e. T_{1e} at zero magn. field) values of 5×10^{-10} s were reported.

[b] T_e is field dependent; $T_{1e(0)}$ values from 10^{-9}–10^{-10} s were reported.

[c] T_e is field dependent; $T_{1e(0)}$ values from 10^{-9} to less than 10^{-11} s were reported.

[d] T_e is field dependent; $T_{1e(0)}$ values from 10^{-11} to 10^{-12} s were reported.

[e] T_e is field dependent; $T_{1e(0)}$ values from 10^{-8} to 4×10^{-10} s were reported.

are the least effective relaxation mechanisms. They typically induce T_{1e} in the order of 1×10^{-9} s. Typical examples are Cu^{2+} or VO^{2+} aqua ions.

Other mechanism is the modulation of ZFS which induces T_{1e} approximately from 10^{-8} to 10^{-11}s, typically with a strong field dependence. If the static ZFS is present (complexes with lower than octahedral symmetry), electron relaxation is possible due to modulation of static ZFS by molecular rotation (τ_R) . At the same time, the electron energy levels are influenced by static ZFS. In highly symmetric metal complexes, i.e. without static ZFS, the relaxation is caused by transient ZFS. It is induced by vibrations and solvent collisions (correlation time τ_ν). The electron relaxation through transient ZFS is therefore independent on molecular rotation. Symmetry and fluctionality of the coordination sphere are therefore crucial parameters for the electronic relaxation. This mechanism is typical for fluctional octahedral complexes (e.g aqua ions) of Mn^{2+}, high-spin Fe^{3+}, Cr^{3+}, Ni^{2+} and Gd^{3+}.

Exact description of relaxation mechanism by ZFS modulation is an extremely tough task. If the Redfield limit is not satisfied (i.e. the stochastic process which induces electron relaxation is slower than the electron relaxation) it is not possible to define the electron relaxation time and the electron relaxation may not be described as exponential. This problem was theoretically solved by treating the electron as a part of generalised lattice, strongly coupled with the observed nucleus. This theory is described and compared with other theories in Ref. 20. Within the Redfield limit and expecting only transient ZFS modulation of electron relaxation time and $S = 1$, the electron relaxations are described by Equation 2.46 exactly. The same equations are approximately valid for $S = 3/2$ and 5/2 as well.[10]

$$T_{1e}^{-1} = \frac{2\Delta_t^2}{50}[4S(S+1)-3](\mathcal{J}(\omega_s,\tau_v)+4\mathcal{J}(2\omega_s,\tau_v)) \tag{2.46}$$

$$T_{2e}^{-1} = \frac{\Delta_t^2}{50}[4S(S+1)-3](3\tau_v+5\mathcal{J}(\omega_s,\tau_v)+2\mathcal{J}(2\omega_s,\tau_v)), \tag{2.47}$$

where Δ_v^2 is the mean square fluctuation of transient ZFS.

The process which makes the electronic relaxation faster then 1×10^{-11} s is so called Orbach process. During this process, an excitation from electronic ground state with given M_S to electronic excited state occurs through interaction with the thermal motion of the lattice.[viii] Subsequently, the second interaction leads to de-

---

[viii] The Orbach mechanism was first postulated as an interaction with phonones in solids, however similar processes can occure in liquid as well.

excitation back to the electronic ground state but with different M_S.[ix] This process requires a low-laying excited state, either due to strong spin-orbit coupling (all paramagnetic lanthanides(III) ions except Gd^{3+}) or nearly double or triple degenerated ground state due to the ligand-field splitting (idealized E or T symmetry). The later one is typical for Ti^{3+}, low-spin Fe^{3+} and for systems with $S > 1/2$: pseudo-octahedral Co^{2+}, pseudo-tetrahedral Ni^{2+} or high-spin pseudo-octahedral Fe^{2+}. In pseudo-tetrahedral Co^{2+} and pseudo-octahedral Ni^{2+}, the excited states are relatively high in energy and, therefore, Orbach and Raman mechanisms are not as effective as ZFS modulation. This variability of the electron relaxation mechanisms as well as diversity of coordination modes was an important reason to study the nickel(II) and cobalt(II/III) complexes in this Thesis.

Finally, it should be noted that the magnetic coupling in multi-nuclear complexes can have a considerable effect on the electron relaxation of the metal ion. For example, a significant shortening of copper(II) T_e enables observation of the PARACEST effect in its multinuclear complexes.[21]

Electron-nuclear dipole-dipole relaxation

The Solomon theory describes relaxation rates due to point dipole-dipole interaction between electron and nuclear spin.[10] The rates ($R_{1,2} = T_{1,2}^{-1}$) are:

$$R_1 = \frac{1}{15}K(2\mathcal{J}(\omega_I - \omega_S, \tau_c) + 6\mathcal{J}(\omega_I, \tau_c) + 12\mathcal{J}(\omega_I + \omega_S, \tau_c)), \tag{2.48}$$

$$R_2 = \frac{1}{15}K(4\mathcal{J}(0, \tau_c) + \mathcal{J}(\omega_I - \omega_S, \tau_c) + 3\mathcal{J}(\omega_I, \tau_c) + 6\mathcal{J}(\omega_I + \omega_S, \tau_c) + 6\mathcal{J}(\omega_S, \tau_c)), \tag{2.49}$$

where K is proportional to the average of square of dipole-dipole interaction:

$$K = \left(\frac{\mu_0}{4\pi}\right)^2 \frac{\gamma_I^2 g_e^2 \mu_B^2 S(S+1)}{r^6}, \tag{2.50}$$

and where $\mathcal{J}$ refers to the spectral density as defined in equation 2.42.
The main difference between longitudinal and transversal dipole-dipole relaxation is that R_2 depends on $\mathcal{J}(0, \tau_c)$ as well. This term is equal to τ_c and it reflects random processes with characteristic frequencies near zero.

[ix] A Raman process can be involved as well. The excitation occurs to virtual excited states in this case.

In practice, it is possible to approximated: $\omega_I + \omega_S \approx \omega_I - \omega_S \approx \omega_S$ and therefore:

$$R_1 = \frac{1}{15} K(14\mathcal{J}(\omega_S, \tau_c) + 6\mathcal{J}(\omega_I, \tau_c)), \tag{2.51}$$

$$R_2 = \frac{1}{15} K(4\mathcal{J}(0, \tau_c) + 13\mathcal{J}(\omega_S, \tau_c) + 3\mathcal{J}(\omega_I, \tau_c)). \tag{2.52}$$

$$\tag{2.53}$$

In the fast-motion limit, where $\tau_c^{-1} \gg \omega_S > \omega_I$ is valid, relaxation rates are:

$$R_1 = R_2 = \frac{4}{3} K \tau_c. \tag{2.54}$$

Figure 2.4 shows dependence of $R_{1,2}$ on external magnetic field. The first relaxation dispersion occurs at the field where $\omega_S = \tau_c^{-1}$. In this point, longitudinal relaxation rate drops down to 3/10 and transveral to 7/20 of their maximal value. If the field is further increased, another dispersion can be observed at $\omega_I = \tau_c^{-1}$. After this, R_1 is effectively zero and R_2 drops down to 4/20 of its maximal value.

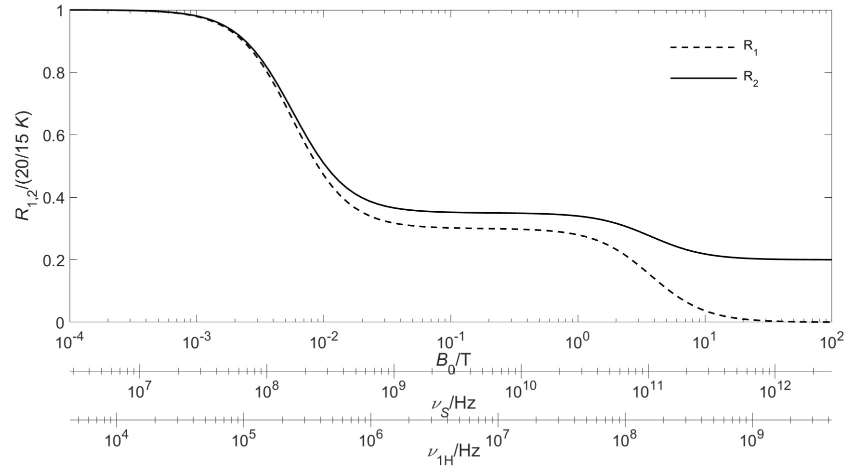

Figure 2.4: Simulated ^{1}H-NMRD profiles with relaxation induced by dipole-dipole mechanism only. Total correlation time is field independent with value of $\tau_c = \tau_R = 1 \times 10^{-9}$ s. The electron relaxation is neglected. The τ_R corresponds to molecular mass ≈ 1 kDa according Stokes´s law (e.g. small peptide with coordinated Cu^{2+}).

It should be highlighted that in Equations 2.48 and 2.49, the dipole-dipole interaction is approximated by interaction of two point dipoles. This can be safely done for nuclear spin, but electrons are delocalised, at least in metal ion valence orbitals. For this reason, this approximation fails if the metal–nucleus distance is below

3–4 Å. For example, in metal ion aqua complexes, metal–^{17}O distance determined by a relaxation measurement under point-dipole approximation is significantly shorter than its real crystallographic value. For $[\mathrm{Ni(H_2O)_6}]^{2+}$, the distances are 1.749 Å and 2.061 Å respectively.[10,22]

Relaxation due to contact coupling

A mechanism of relaxation caused by the presence of the unpaired electron density in the position of the observed nucleus is often called contact mechanism. The contact coupling constant A does not change its value as the molecule rotates and, therefore, the overall correlation time for contact mechanism (τ_c^{con}) is determined by electron relaxation only. In some rare cases the chemical exchange is involved as well.

$$(\tau_c^{-1})^{\mathrm{con}} = T_e^{-1} + \tau_{\mathrm{M}}^{-1}. \tag{2.55}$$

If $T_e^{-1} \gg \tau_{\mathrm{M}}^{-1}$, it can be stated:

$$R_1^{\mathrm{con}} = \frac{2}{3} S(S+1) \left(\frac{A}{\hbar}\right)^2 \mathcal{J}(\omega_S, T_{2e}) \tag{2.56}$$

$$R_2^{\mathrm{con}} = \frac{1}{3} S(S+1) \left(\frac{A}{\hbar}\right)^2 (\mathcal{J}(0, T_{1e}) + \mathcal{J}(\omega_S, T_{2e})). \tag{2.57}$$

The term $S(S+1)(A/\hbar)^2$ is proportional to the square of the coupling energy between electron and the nuclear spin vector and it is described in Chapter 2.2.1. In fast motion, limit the previous equations are reduced to:

$$R_1^{\mathrm{con}} = R_2^{\mathrm{con}} = \frac{2}{3} S(S+1) \left(\frac{A}{\hbar}\right)^2 T_{1e} \tag{2.58}$$

Curie nuclear spin relaxation

When the difference in electron M_S level populations is relatively high, the magnetic moment induced by this difference cannot be neglected. For simple case, it can be calculated by Eq. 2.28: $\langle S_z \rangle = \frac{g_e \mu_B S(S+1) B_0}{3 k_B T}$. Interaction of this induced dipole moment modulated by molecular reorientation and/or chemical exchange results in nuclear relaxation. As this mechanism is closely related to magnetic susceptibility, it is sometimes called magnetic susceptibility relaxation. The dipolar contribution to R_1 and R_2 by this mechanism are:

$$
\begin{aligned}
R_1 = \frac{1}{5}\left(\frac{\mu_0}{4\pi}\right)^2 \frac{\gamma_I^2 g_e^2 \mu_B^2}{r^6}\langle S_z\rangle^2 6\mathcal{J}(\omega_I, \tau_R^{\text{curie}}) \\
= \frac{1}{5}\left(\frac{\mu_0}{4\pi}\right)^2 \frac{\omega_I^2 g_e^4 \mu_B^4 S^2(S+1)^2}{(3k_BT)^2 r^6} 6\mathcal{J}(\omega_I, \tau_R^{\text{curie}}) \quad (2.59)
\end{aligned}
$$

$$
\begin{aligned}
R_2 = \frac{1}{5}\left(\frac{\mu_0}{4\pi}\right)^2 \frac{\gamma_I^2 g_e^2 \mu_B^2}{r^6}\langle S_z\rangle^2 (4\mathcal{J}(0, \tau_R^{\text{curie}}) + 3\mathcal{J}(\omega_I, \tau_R^{\text{curie}})) \\
= \frac{1}{5}\left(\frac{\mu_0}{4\pi}\right)^2 \frac{\omega_I^2 g_e^4 \mu_B^4 S^2(S+1)^2}{(3k_BT)^2 r^6} (4\mathcal{J}(0, \tau_R^{\text{curie}}) + 3\mathcal{J}(\omega_I, \tau_R^{\text{curie}})) \quad (2.60)
\end{aligned}
$$

In a presence of fast exchange, the correlation time (τ_R^{curie}) in previous equations can include an exchange contribution. The electron relaxation does not infuence τ_R^{curie} because the electron level population is in principle time averaged.

The Curie-type relaxation can contribute to contact relaxation mechanism as well. This mechanism is modulation by exchange only. Although the term $\langle S_z\rangle^2$ is much smaller than $S(S+1)/3$ for direct dipole-dipole relaxation, the Curie-type relaxation can be significant or even dominant mechanism if the direct dipole-dipole mechanism is modulated by the fast electron relaxation – typical situation for lanthanides(III) (except Gd^{3+}). This is the case especially at high magnetic field as the Curie relaxation rate grows with B_0^2. Effects of Curie R_2 relaxation can be observed for macromolecules as well especially at high magnetic field.

Notes for lanthanides

In the case of relaxation in presence of paramagnetic lanthanide(III) ions, equations for dipole-dipole, contact and Curie relaxation mechanism are valid, but the overall quantum number J obtained by jj coupling must be used instead of electron spin quantum number S. Electron g-factor g_e must be replaced by g_J. Moreover, the effective value $\langle J_z\rangle$ must be employed instead of effective value $\langle S_z\rangle$. Sometimes experimental effective μ_{eff} can be used instead of $g_J^2\mu_B^2 J(J+1)$. Dominant electron relaxation mechanism for all lanthanide(III) ions is the Orbach one except lanthanide(III) ions with f^7configuration (Gd^{3+} and Eu^{2+}). Effective Raman process was described as well.

Part II

Results and discussion

Chapter 3

Paramagnetic ^{19}F-MRI contrast agents

This part of the Thesis is focused on further discussion of the following articles (See full texts in Appendices A and B):

- J. Blahut, P. Hermann, A. Gálisová, V. Herynek, I. Císařová, Z. Tošner, J. Kotek, *Dalton Trans.* 2016, **45**, 474–8.
- J. Blahut, K. Bernášek, A. Gálisová, V. Herynek, I. Císařová, J. Kotek, J. Lang, S. Matějková, P. Hermann, *Inorg. Chem.* 2017, **56**, 13337–48.

Details of the nickel(II) complexes synthesis, properties, applications and literature background are thoroughly discussed in the articles. Therefore, discussion in this Chapter is mainly focused on pNMR properties of the prepared complexes and their dynamics. In addition unpublished results, description and analysis of their low-field ^{19}F-NMRD profile and pNMR study of cobalt(II/III) complexes are discussed here as well.

3.1 Magnetic resonance imaging

Nowadays, Magnetic Resonance Imaging (MRI) is one of the most commonly used diagnostic technique. Contrast agent (CA) is often used to enhance contrasts of target tissue. The most relevant principles of MRI and requirements on contrast agents are discussed here. References 23 and 24 are recommended for further reading.

A crucial quantity for efficiency of MRI-CA is signal-to-noise ratio between the targeted tissue and the background (SNR). The SNR depends on experimental time, CA concentration, pulse sequence used for measurement and relaxation properties of the CA. Because of the safety requirements, the experimental time and the

CA concentration may not exceed certain values. The main attention is therefore focused on the pulse sequence and the CA properties.

The most important group of contrast agents are complexes of Gd^{3+} with one coordinated water molecule. This water is in exchange with the bulk water and is responsible for the enhancement of its relaxation rate. For efficiency of this class of CAs, it is crucial to find optimal balance between rotation correlation time and water exchange dynamics. A lot of effort has been made to optimise these parameters[23]. Among others, the internal dynamics of the ligand skeleton is important and is deeply discussed in Chapter 4.

Increase of hardware performance enabled observation of different molecules than water. One way is to observe different signal than water, but still in the ^{1}H channel.[25] Spectral width, in this case, is usually enhanced by a paramagnetic shift agent. In the other approach, channel of different nucleus is observed. Typical nuclei are ^{31}P (e.g. Ref. 11) or ^{19}F (e.g. Ref. 26,27). The ^{19}F-MRI is the central topic of this Chapter.

3.2 ^{19}F-MRI: advantages and requirements

Among other nuclei detectable using MRI, fluorine ^{19}F nucleus has important advantages:

- 100% natural abundance, nuclear spin 1/2 and high gyromagnetic ratio $\gamma_{19F} = 40.052\,\mathrm{MHz\,T^{-1}}$ result in sensitivity comparable to ^{1}H.
- Routinely used MRI hardware can be used for ^{19}F imaging after some minor modification.[28]
- No natural background ensures high signal-to-noise ratio (SNR), as only the CA is observed. Simultaneous ^{1}H-MRI anatomical image is often required to localize fluorine "hot-spot" image.

The pulse sequence and the properties of the CA (especially its NMR relaxation) should be tuned synchronously in order to obtain optimal SNR and, therefore, minimize detection limits and/or detection time. Fast pulse sequences discussed below often require extreme hardware performance, its limitations (RF coils, gradient coils and amplifiers characteristics) must be considered.

3.2.1 Simultaneous optimisation of the pulse sequence and the contrast agent

The repetition time of pulse sequence TR should be roughly 5×T_1 of the CA. For organic perfluorinated compounds with T_1 relaxation times higher than 1 s it would lead to unbearably long measurement using standard spin-echo (SE) or gradient-echo (GE) pulse sequences. (e.g. T_1 = 1.7 s for PFOB, see Figure 3.1)[29]. One possibility to overcome this limitations is to employ fast version of the pulse sequences with small flipping angle, e.g. FLASH or turbo-SE.[28] If the T_2 relaxation time is long enough, more rows in k-space can be detected during one pulse sequence run, like in the RARE pulse sequence.[30]

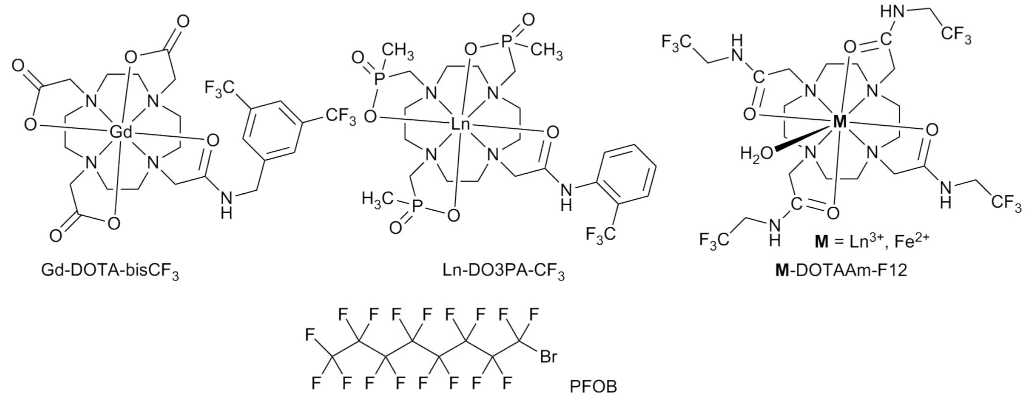

Figure 3.1: ^{19}F-MRI contras agents discussed in the text. Examples of lanthanide(III) (Ln) complexes of DOTA-like ligands are taken from ref. 31.

The other way is to increase the T_1 relaxation rate. It can be achieved by addition of a paramagnetic centre near ^{19}F nucleus. But the paramagnetic centre influences T_2 relaxation as well.

Limitations of various pulse sequences must be considered when the CA is developed. Spin-echo pulse sequence includes 180° refocusation pulse and phase encoding which are time-consuming and, therefore, it cannot be effectively used for CAs with T_2 shorter than ca. 10 ms. Gradient echo sequence, where two opposite field gradients are used, is faster but more sensitive to field inhomogeneity. The fastest pulse sequences do not use echoes, but direct FID detection after 90° pulse. Space encoding is then achieved by modulated gradient-pulses during acquisition which does not require delay for phase encoding, e.g. by radial sampling technique. Zero-time echo (ZTE) or ultra-time echo (UTE) are examples of such pulse sequences tested for paramagnetic ^{19}F-MRI CA.[32–34] In conclusion, the critical value for CA evaluation is T_2^*/T_1 ratio which should be as close to one as possible.

Apart the proper relaxation times, a CA for ^{19}F-MRI should have following properties:

- A high amount of fluorine atoms in the molecule contributing to a single ^{19}F signal, i.e. being chemically equivalent or, at least, almost equivalent.[35] Small inequivalence or splitting by J-coupling can be smoothed out by selection of proper acquisition and pulse bandwidths.[29]
- The CA must be well soluble in water. That is the reason why highly fluorinated compounds are often used in a form of micelles solubilized in water. There have been some attempts to modify relaxation rates of such micelles with Gd^{3+} complexes on surface of the micelles but the T_2^*/T_1 ratio was far from optimal. However, recent experiments with Fe^{3+} complexes dissolved inside the micelles have shown remarkable improvement.[36]
- The CA must be non-toxic even in relatively high doses. For example, Gd^{3+} **dota** complex dose of 0.1 mmol/kg is usually applied. High kinetic inertness and thermodynamic stability of the complex are therefore an essential requirement.

Different approaches toward design of optimal ^{19}F-MRI CAs were described in the review of Tirotta.[35] There are not many examples with paramagnetic metal centre. Most of them are utilising lanthanide(III) ions, as those presented in Figure 3.1. Although transition metal ions can modify relaxation rate with the same efficiency, there are only a few examples described in literature.[37] Some works have been focused on the transition metal ions as an on/off centre which turns the CA from visible to invisible (eventually the opposite) mode by redox process[38,39], enzymatic cleavage[40] or by a coordination of paramagnetic Mn^{2+} from a tissue[41]. This gap is surprising as the transition metal ion complexes can form much more stable, therefore much less toxic, complexes. Some transition metal are bio-compatible in form of a free ion as well.

As described in Chapter 2.2.2, nickel(II) and cobalt(II/III) were chosen in this work, as they ensure a broad range of induced relaxation rates that can be modified by the ligand environment. Responsive CAs are accessible as well. In the case of cobalt, a responsive CA can be based on the change of oxidation states as well.

3.3 Complexes design, synthesis and stability

According to the literature[42] and the author's previous experience, derivatives of 1,4,8,11-tetraazacyclotetradecane (cyclam) form kinetically inert and thermodynamically stable complexes with first-row transition metal ions. For this reason, the cyclam was chosen as the basic skeleton of the desired ligands. The 2,2,2-trifluorethyl group was introduced on cyclam nitrogen atoms in order to bring the highest possible number of ^{19}F atoms localised close to the central metal. Synthetic troubles with introducing of this strong electron withdrawing group are described in Appendix A and the author's diploma thesis[43] which is entirely dedicated to organic synthesis. Only the final procedure is indicated here (Figure 3.2). Details are described in Appendix A.

Unfortunately, the ligand with four trifluorethyl pendants, i.e. with 12 equivalent fluorine atoms, appeared to be very insoluble in water. When there are only two trifluorethyl groups on the cyclam skeleton (**te2f**), such compound is water-soluble in the form of hydrochloride.

It was found that in the presence of a chloride anion, *cis*-[Ni(**te2f**)Cl$_2$]$^{2+}$ is formed, but it is again insoluble in water. When the presence of Cl$^-$ was avoided, a blue solution of [Ni(**te2f**)(H$_2$O)$_2$]$^{2+}$ with an unknown coordination geometry was obtained. In the presence of very high amount of the NaClO$_4$, nickel(II) complex of **te2f** crystallized as a red *trans*-[Ni(**te2f**)](ClO$_4$)$_2$. The isomerisation of *trans*-[Ni(**te2f**)]$^{2+}$ cation in aqueous solution was followed by time-resolved NMR. The intermediate of this dynamic process is expected to be *trans*-[Ni(**te2f**)(H$_2$O)$_2$]$^{2+}$, taking in account the isomerism of metal ion-cyclam complexes.[44] Finally, this intermediate is transformed into a blue solution having the same ^{19}F spectra as the initial [Ni(**te2f**)(H$_2$O)$_2$]$^{2+}$. According to the literature, the only possible complex conformation different from *trans* is *cis*-[Ni(**te2f**)(H$_2$O)$_2$]$^{2+}$. It should be highlighted that the *cis* geometry of more stable isomer was confirmed by UV-VIS spectroscopy as well. (See Appendix A.)

The fluctionality of nickel(II) complexes with **te2f** ligand has consequences for its stability as well. Although the *cis*-[Ni(**te2f**)(H$_2$O)$_2$]$^{2+}$ is stable against acidic hydrolysis ($\tau_{1/2} = 8\,\mathrm{h}$ in 1 M aq. HCl at 37 °C), instantaneous complex decomposition was observed in the presence of aqueous ammonia. To avoid such a ligand exchange, the axial coordination group must be connected with the cyclam ring. Therefore, designed ligands with four different coordinating pendant arms were designed. The structure of these compounds and schematic synthetic approach are presented in Figure 3.2.

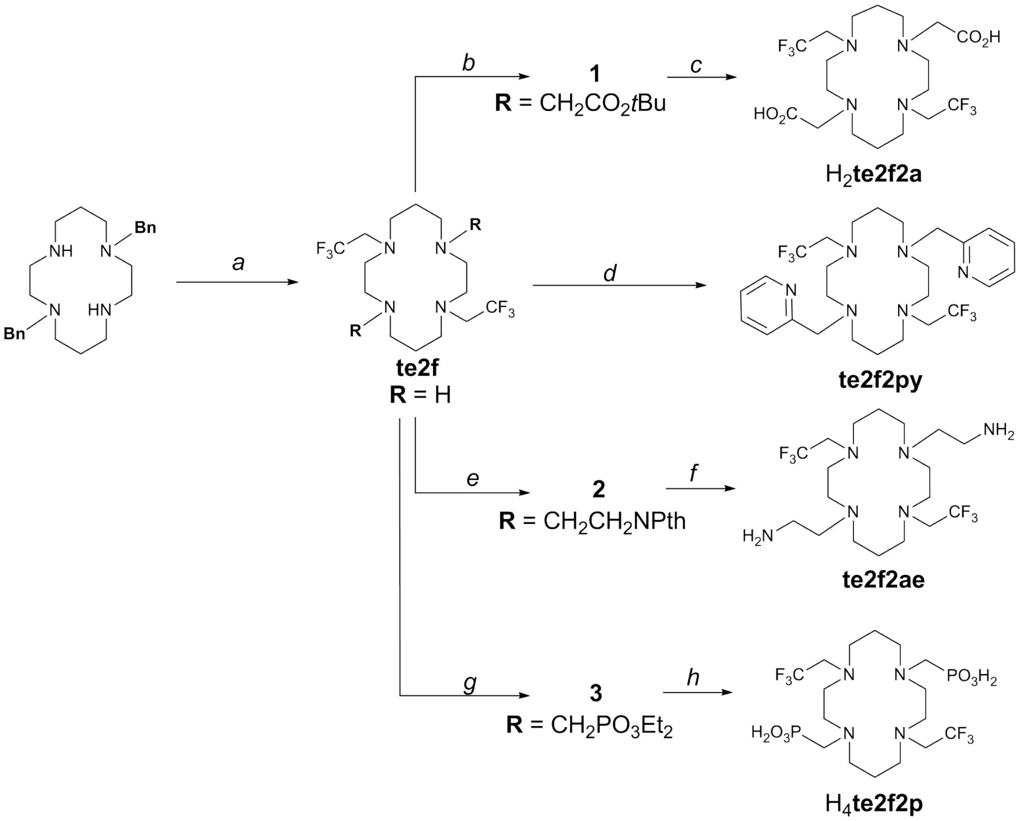

Figure 3.2: Structure and synthesis of ligands discussed in this work: (*a*) (*1*) trifluoroacetic anhydride (5 eq.), dry $CHCl_3$, room temperature, 3 h; (*2*) $NaBH_4$ (30 eq.), $BF_3{\cdot}Et_2O$ (10 eq.), anhydrous diglyme, 100 °C, 12 h; (*3*) 10 % Pd/C, H_2 (balloon), AcOH/EtOH/H2O (1/5/4, v/v/v), 40 °C, 24 h; (*b*) $BrCH_2CO_2tBu$, K_2CO_3,CH_3CN, room temperature (RT), 12 h; (*c*)TFA,$CHCl_3$, room temperature, 12 h; (*d*) 2-(chloromethyl)pyridine hydrochloride, K_2CO_3, CH_3CN, 60 °C, 12 h; (*e*) *N*-(2-bromoethyl)phthalimide, K_2CO_3,CH_3CN, 60 °C, 4 days; (*f*) (*1*) N_2H_4, EtOH/H_2O, 90 °C, 12 h, (*2*) NaOH, EtOH/H_2O, 90 °C, 12 h; (*g*) neat $P(OEt)_3$, $(CH_2O)_n$, 70 °C, 12 h; (*h*) (*1*) trimethylsilylbromide (20 eq.), dry acetonitrile, RT, 12 h; (*2*) H_2O excess, RT.

Ligands with carboxylic (H_2**te2f2a**), 2-aminoethyl (**te2f2ae**) and (pyridin-2-yl)methyl (**te2f2py**) pendant arms were prepared by alkylation of the **te2f2** with a proper alkylation agent and subsequent deprotection. The phoshonomethyl pendant arm was introduced by Mannich-type reaction with formaldehyde and $P(OEt)_3$. Ethyl groups were then hydrolysed to give the H_4**te2f2p**.

Although the ligands are structurally related, stability of their nickel(II) complexes is different and it is reflected in a rates of complexation and acid-assisted hydrolysis. The most inert complex is the *trans*-[Ni(**te2f2a**)], which is one of the most inert nickel(II) complexes observed to date ($\tau_{1/2}$ = 14 d in ≈12 M HCl at 80 °C). Actually, this process is so slow that single-crystals of free ligand suitable for diffraction studies were formed during the complex dissociation experiment. Unfortunately, this complex is not enough soluble in water and, therefore, it can hardly be used for any practical application. The second most stable complex, *trans*-[Ni(**te2f2p**)]$^{2-}$, possessing $\tau_{1/2}$ = 4.54 h in 1 M aqueous HCl at 80 °C is negatively charged and, therefore, well soluble in water above pH 6.5. For this reason, it was chosen for further ^{19}F-MRI experiments. Complex of the ligand with pyridine groups, *trans*-[Ni(**te2f2py**)]$^{2+}$, has reasonable inertness as well ($\tau_{1/2}$ = 3.3 h in 1 M aq. HCl at 80 °C) but is hardly soluble in water. Finally, the *trans*-[Ni(**te2f2ae**)]$^{2+}$ complex is very unstable – it dissociates with $\tau_{1/2}$ = 2.8 h at 25 °C even in water buffered to pH 7.8. This complex, at the same time, can be formed only under anhydrous conditions from water-free nickel(II) salt, here from $[Ni(EtOH)_4](ClO_4)_2$.

The time-resolved NMR proved to be very useful for observation of complex formation and dissociation processes. Observation of complex signal integral values at different times was used for determination of acid assisted dissociation half-times. The intermediates during the formation of the *trans*-[Ni(**te2f2a**)] and the *trans*-[Ni(**te2f2p**)]$^{2-}$ were detected as well.

3.4 Complexes of $Co^{2+/3+}$

Complexes of cobalt in oxidation states II and III with selected ligands were synthesized as well. These results have not been published yet and experimental details on the synthesis and description of NMR experiments are given in Appendix D.

For the synthesis of cobalt(II) complexes with H_2**te2f2a** and H_4**te2f2p** ligands, $[Co(NH_3)_6]Cl_2$ was chosen as a source of the metal ion. Due to the sensitivity of cobalt(II) compounds to oxidation to kinetically inert cobalt(III) complexes, the preparations of [Co(**te2f2p**)]$^{2-}$ and [Co(**te2f2a**)] were performed under inert atmosphere but the methodology is, in principle, the same as that for nickel(II). The *trans* coordination geometry was confirmed by X-ray for both Co^{2+} and Co^{3+} complexes of **te2f2a** and **te2f2p** (except [Co(**te2f2a**)]$^+$ where this geometry is expected per analogy with *trans*-[Co(**te2f2p**)]$^-$). Unlike the starting $[Co(NH_3)_6]Cl_2$, the final complexes are not sensitive to oxidation by air oxygen and, therefore, *meta*-chloroperoxybenzoic acid was used as oxidants. Such resistance against oxidation has already been reported for some macrocyclic complexes of Co^{2+}.[45] It should be noted that decomposition of the **te2f2p** ligand was observed if the oxidation was carried out by hydrogen peroxide. Cleavage of N–C–P bonds has been reported under these conditions.[46]

3.5 NMR properties

Although the solubility of the complexes (except those with H_4**te2f2p** and **te2f**) in water is relatively low, the concentrations were sufficient for measurement of their ^{19}F-NMR relaxation rates. For those of the discussed ligands and their nickel(II), cobalt(II) and cobalt(III) complexes, see Table 3.2, 3.1 and 3.4 respectively.

3.5.1 Nickel(II) complexes

For Ni^{2+} complexes, a strong relaxation enhancement was observed. The T_1 is more than two orders of magnitude faster compared to free ligands. It implicates that diamagnetic contribution to the relaxation rates can be neglected for further analysis of the relaxation times at high fields.

For all nickel(II) complexes, the T_1 relaxation time is shorter, i.e. relaxation faster, with increasing B_0. Assuming the Solomon-Bloembergen-Morgan-Redfield theory (SBMR), this faster relaxation can be explained by dependence of nickel(II) electron relaxation time on B_0. At the same time, decrease of relaxation rate can appear at very high field due to dispersion at $\omega_{19F} \approx \tau_R^{-1}$. However, it was not fully confirmed for any of the nickel complexes measured at B_0 field as high as 20 T. It indicates, that the rotation correlation times (τ_R) of the molecules is smaller than $\approx 1 \times 10^{-9}\,$s which is in qualitative agreement with that approximated by the Stokes´s law ($\tau_R = 2.1 \times 10^{-10}\,$s for *trans*-[Ni(**te2f2p**)]$^{2-}$ complex according Eq. 1.1 Chapter 1.1.1).

Table 3.1: ^{19}F-NMR relaxation times of the discussed nickel(II) complexes. (25 °C)

	T_1/ms				T_2^*/ms
B_0	0.94 T	7.0 T	9.4 T	20.0 T	7.0 T
trans-[Ni(**te2f2a**)]	12.5(4)	2.4(6)	1.5(2)	1.27(9)	1.03
trans-[Ni(**te2f2ae**)]$^{2+}$	6(2)	1.8(2)	1.2(1)	1.3(1)	0.83
trans-[Ni(**te2f2py**)]$^{2+}$	18(4)	1.8(1)	1.4(2)	1.37(1)	0.76
trans-[Ni(**te2f2p**)]$^{2-}$	28(9)	2.8(7)	1.82(7)	1.265(5)	0.9
cis-[Ni(**te2f**)(H_2O)$_2$]$^{2+}$	5(3)	1.72(1)	1.66(9)	1.60(2)	0.82

Table 3.2: ^{19}F-NMR relaxation times of the discussed ligands (25 °C)

	T_1/ms			
B_0	0.94 T	7.0 T	9.4 T	20.0 T
H_2**te2f2a**	810(40)	620(20)	540(3)	245(1)
te2f2ae	730(30)	710(20)	507(6)	232(2)
te2f2py	710(60)	530(10)	456(8)	218(2)
H_4**te2f2p**	500(20)	820(10)	375(6)	202(2)
te2f	1060(20)	1100(20)	715(5)	304(2)

In order to understand the dependence of the ^{19}F relaxation rates on B_0, the whole ^{19}F-NMRD profile was measured at fields ranging from 1.5×10^{-4} T to 20 T. Unfortunately, due to limited experimental time on ^{19}F field-cycling relaxometer (Olsztyn, Poland) and low solubility of the other complexes, the ^{19}F-NMRD was measured only for [Ni(**te2f2p**)]$^{-2}$.

Table 3.3: Relaxation related parameters of *trans*-[Ni(**te2f2p**)]$^{2-}$ complex obtained by non-linear fit of ^{19}F-NMRD data via SBMR theory

parameters	value	error[a]
r/Å	5.25	0.07
τ_R/s	2.4×10^{-10}	0.5×10^{-10}
τ_v/s	7.0×10^{-12}	0.2×10^{-12}
Δ_T/cm^{-1}	4.6	0.2

[a] Standard deviation of the parameters obtained by the fit repeated 100× using data with random 10% error.

The acquired data were analysed employing the dipole-dipole relaxation mechanism according to Eq. 2.51 given in Chapter 2.2.2, see Figure 3.3. For final parameters of the fit, see Table 3.3. The Curie relaxation mechanism can be neglected as it does not contribute significantly at external magnetic fields $B_0 < 20$ T,

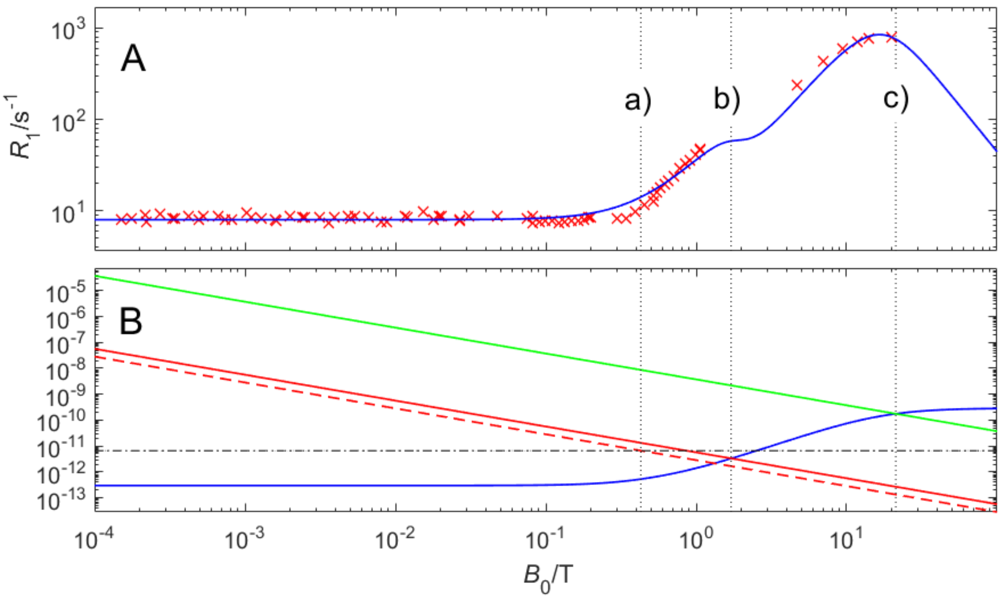

Figure 3.3: Plot A: Experimental R_1 ^{19}F-NMRD profile (red ×) fitted by Equation 2.51, Chapter 2.2.2, describing longitudinal relaxation due to dipole-dipole interaction. Plot B: External magnetic field dependence of overall correlation time τ_c (blue line), electron Larmor precession time ω_s^{-1} (red line), twice electron Larmor precession time $(2\omega_s)^{-1}$ (red dashed line), transient ZFS correlation time τ_v (black dashed line) and ^{19}F Larmor precession time $(\omega_{19\mathrm{F}})^{-1}$ (green line). Vertical black dotted lines indicate dispersion regions due to equality of a) $(2\omega_s)^{-1} = \tau_v$ b) $\omega_s^{-1} = \tau_c$ and c) $(\omega_{19\mathrm{F}})^{-1} = \tau_c$.

see Figure 3.4 for the estimation. Contact mechanism was neglected as there are four bonds between the fluorine atoms and the nickel(II) ion.

According to this fit, the electron relaxation rate in this model occurs via transient ZFS, described by Equation 2.46 in Chapter 2.2.2. At low field, T_e is extremely fast $\approx 3 \times 10^{-13}$ s, but after its dispersion at $2\omega_\mathrm{s}^{-1} \approx \tau_v$, it slows down to $\approx 4 \times 10^{-10}$ s at 20 T and ^{19}F relaxation is modulated by the molecule rotation ($\tau_R = 2.4 \times 10^{-10}$ s) at higher fields. As mentioned above, the value of τ_R is in agreement with the Stokes´s law (Eq. 1.1).

The data indicate other two dispersions – one at very high field (20 T) where ^{19}F Larmor frequency $\omega_{19\mathrm{F}} = \tau_c^{-1}$ and the other when electron Larmor frequency $\omega_\mathrm{s} = \tau_c^{-1}$, i.e. at $B_0 \approx 2$ T. High relative error of the fitted τ_R (21%) is caused by the absence of data points in regions with these dispersions due to inaccessibility of NMR spectrometers with the a proper field.

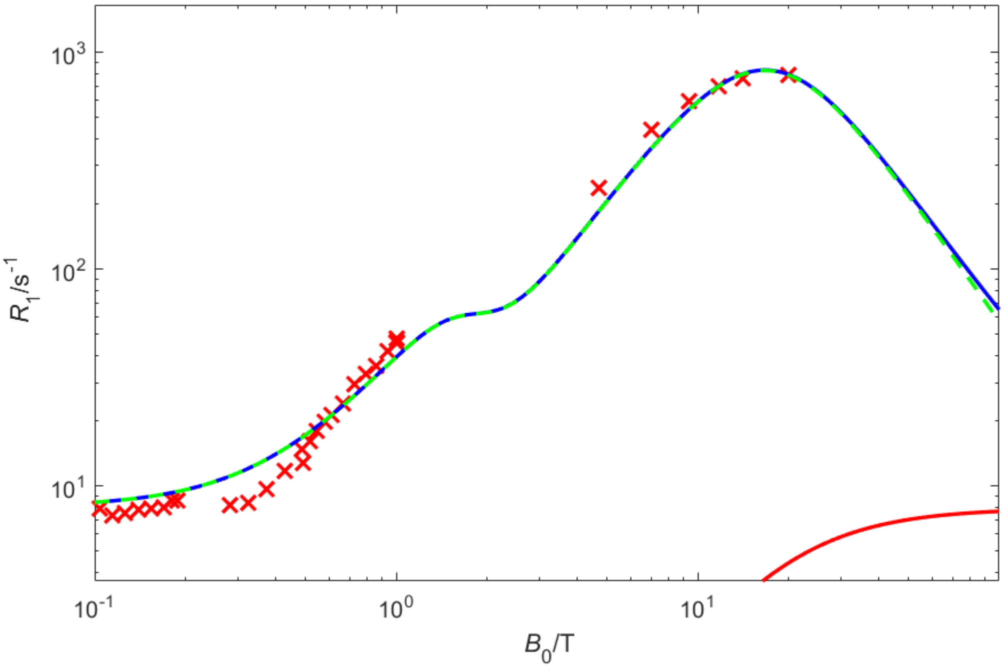

Figure 3.4: Medium- and high-field regions of the ^{19}F-NMRD data (red ×) with distinguished contribution of relaxation via Curie (red line) a dipole-dipole (green dashed line) to the overall fit (blue line).

It should be highlighted that the application of SBMR theory is slightly controversial in this case. First of all, the Redfield limit is disturbed. The electron relaxation rate at low fields is higher than the rate of stochastic process by which it is modulated, i.e. by transient ZFS induced by vibrations ($\tau_v = 7.0 \times 10^{-12}$ s) of the ligand skeleton and perhaps also by fast collisions with solvent. Secondly, the tensorial character of ZFS is not reflected by SBMR model at all. Especially at low field the rhombicity of ZFS and non-coincidency of the dipole-dipole and ZFS principal axis can have a large effect.[13] On the other hand, $\mathrm{Ni}^{2+} \cdots \mathrm{F}$ distance from the fit (5.25 Å) is in a good agreement with the average distance obtained from the X-ray diffraction (5.23 Å) (Appendix A).

For exact description of these effects, more advanced slow-motion theory must be applied.[47] Unfortunately, implementation of this theory is complicated without comprehensive experiences with operator algebra and deep quantum-mechanic knowledge. Among other features, the slow-motion theory does not provide analytical expression for the magnetic field dependency of R_1.

Another method, that can be used for analysis of such data have been suggested as well, like a spin-dynamic simulation or various multi-parameter models beyond Solomon-Bloembergen-Morgan-Redfield theory.[48]

Despite the limits of SBMR theory, this study has shown the importance of dynamic processes for development of ^{19}F-MRI CAs. It is not only the rotation of complex as a whole, but also its internal dynamics which disturbs coordination polyhedron symmetry and induces the electron relaxation. One of the crucial advantages of these complexes as CAs for MRI is that (in contrast to routinely used Gd^{3+}-based CAs) the relaxation rate is increasing with increasing B_0 in the region of clinically used tomographs. It would be effectively applicable in the future MRI systems approaching main field strength of 10 T.

3.5.2 Cobalt complexes

The effect of oxidation state on NMR relaxation and chemical shift was studied in complexes of cobalt(II) and cobalt(III). Similar geometry of the complexes in both oxidation states enables comparison of the paramagnetic compounds with their closest diamagnetic analogues. The *trans* geometry was proved by x-ray diffraction of both complexes with H_4**te2p** ligand. The same geometry was observed in $[Co^{II}$(**te2f2a**)] complex and *per analogiam* it is highly probable for $[Co^{III}$(**te2f2a**)$]^+$complex as well. For the observed relaxation rates and chemical shifts, see Table 3.4.

Complexes of cobalt(III), i.e. configuration d^6, with oxygen/nitrogen coordination sphere typically has diamagnetic low-spin configuration because of t_{2g}^6 configuration stabilisation. Configuration of the central ion in complexes of cobalt(II) was proved by the bulk magnetic susceptibility measurement.[49] The effective dipole moment of cobalt(II) in *trans*-$[Co^{II}$(**te2f2p**)$]^{2-}$ is $\mu_{\text{eff}} = 4.9(2)\mu_B$. As the magnetic dipole moment within spin-only-formula limit is $\mu_{\text{eff}}^{\text{spin-only}} = \sqrt{4S(S+1)}\mu_B = 3.87\mu_B$, the orbital contribution due to the spin-orbit coupling is important in this system. Nevertheless, the determined effective magnetic dipole moment confirms the high-spin d^7 configuration, as it is within the published range 4.1–5.2 μ_B.[14,45]

For this electron configuration, the electron relaxation time is $T_e = 10^{-12}$–10^{-13}s^{-1} (see Table 2.2). It is referred to be induced mainly by the Orbach electron relaxation mechanism employing low-lying excited states in distorted octahedron geometry.[10] This distortion was confirmed by X-ray diffraction as well (see Table 3.5 for selected geometry parameters found in crystal structures of the $Co^{2+/3+}$

complexes). The geometry of *trans*-[Co(**te2f2p**]$^{2-}$ is almost the same as that of *trans*-[Ni(**te2f2p**]$^{2-}$ described in Appendixes A and B. The average metal-fluorine distance is the same in complexes of both metal ions.

A strong paramagnetically induced relaxation was observed on T_1 and T_2^* relaxation times. Cobalt(II) induces approximately 40-times faster longitudinal ^{19}F-NMR relaxation than diamagnetic cobalt(III). This effect is slightly higher for the complex with H_4**te2f2p** than that with H_2**te2f2a**.

On the other hand, the ^{19}F T_1 relaxation times at high field are much higher than those of nickel complexes (1.82(7) ms and 12(1) ms for *trans*-[Ni(**te2f2p**)]$^{2-}$ and *trans*-[Co^{II}(**te2f2p**)]$^{2-}$ at 9.4 T, respectively). In addition, T_1 is not field dependent within experimental errors for the cobalt(II) complexes. (See Table 3.4 and 3.1.) This is another proof of different electron relaxation mechanism.

Similar trends were observed for the nickel(II) and cobalt(II) complexes of H_2**te2f2a** but, in this case, solubility of *trans*-[Co(**te2f2a**] is not sufficient to perform a reliable bulk magnetic susceptibility measurement in solution.

Fluorine chemical shifts of Co^{3+} complexes differ from those of free ligands by approximately $\Delta\delta \approx -10$ ppm (shifts of free H_4**te2f2p** and H_2**te2f2a** are $\delta = -68.9$ and $\delta = -68.3$ ppm, respectively, at 9.4 T). This ^{19}F-NMR shift change is not reflecting the type of the ligand at all.

Strong paramagnetically induced NMR shift was observed in presence of Co^{2+} and it is slightly affected by the ligand type. For *trans*-[Co^{II}(**te2f2p**)]$^{2-}$, the shift is slightly larger that for *trans*-[Co^{II}(**te2f2a**)], see Table 3.4.

Table 3.4: ^{19}F-NMR relaxation times of the discussed Co$^{2+/3+}$ complexes (at 25°C). For comparison with the parameters of free ligand, see Table 3.2

	T_1/ms		T_2^*/ms		δ_{19F}/ppm	
B_0	7.0 T	9.4 T	7.0 T	9.4 T	7.0 T	9.4 T
[Co^{II}(**te2f2p**)]$^{2-}$	12(5)	12(1)	9.62	8.93	-23.00	-22.94
[Co^{II}(**te2f2a**)]	16(2)	15.5(9)	11.0	10.4	-25.37	-25.20
[Co^{III}(**te2f2p**)]$^{-}$	600(20)	500(19)	360(90)^a	321(100)^a	-59.23	-59.23
[Co^{III}(**te2f2a**)]$^{+}$	660(50)	573(31)	540(130)^a	460(150)^a	-59.43	-59.47

[a] The T_2^* is not well defined for *J*-splitted signals, T_2 are listed instead.

3.6 Chapter conclusions

Novel class of ^{19}F-MRI contrast agents was investigated. Paramagnetic complexes of nickel(II) and cobalt(II) and diamagnetic complexes of cobalt(III) were synthesized and thoroughly studied.

Table 3.5: Selected geometry parameters found in crystal structures of the $Co^{2+/3+}$ complexes.

avg. distance/Å	$[Co^{II}(\mathbf{te2f2p})]^{2-}$	$[Co^{II}(\mathbf{te2f2a})]$	$[Co^{III}(\mathbf{te2f2p})]^{-}$
∅ ($Co–N^{tfe}$)[a]	2.25	2.25	2.13
∅ ($Co–N^{pend}$)[b]	2.14	2.12	2.01
∅ (Co–O)	2.09	2.05	1.90
∅ ($Co\cdots F$)	5.24	5.26	5.14

[a] Ring nitrogen atom bearing trifluorethyl group

[b] Ring nitrogen atom bearing coordinated pendant arm.

Critical parameter for application of CAs in MRI is their T_2^*/T_1 ratio. The nickel(II) complexes exhibit T_2^*/T_1 ratio in the range from 0.32 to 0.48. Complexes of cobalt(II) are slightly better, i.e. 0.69 and 0.80 for H_2**te2a** and H_4**te2p** complex, respectively, but the absolute value of T_1 relaxation is higher. These ratios are lower than those reported for Gd-DOTA-bisCF_3 (see Figure 3.1) which has $T_2^*/T_1 = 1.0 \pm 0.4$,[32] but comparable to those of M-DOTAAm-F12 (the ratio between 0.07 and 0.18 for M = Ln^{3+} and 0.57 for M = Fe^{2+}).[37]

Discussed systems show higher T_2^*/T_1 ratio than the recently published micelles of fluorinated poly-ethers with dissolved paramagnetic complexes (0.31 and 0.05 for Fe^{2+} and Gd^{3+}, respectively).[36]

NMR relaxation properties of *trans*-$[Ni^{II}(\mathbf{te2f2p})]^{2-}$ were studied in detail and the system was used for ^{19}F-MRI experiments as well. High SNR enhancement was obtained compared to the diamagnetic reference. Mouse mesenchymal stem cells were successfully labelled with this compound and visualised using UTE pulse sequence. These results are presented in the paper in Appendix B. The presented study was published in two papers, enclosed in Appendixes A and B.

Chapter 4

Study of conformational dynamics in lanthanide(III) complexes of DOTA-like ligands

This part of the Thesis is focused on discussion of the following article. (See Appendix C for the full text.):

- J. Blahut, P. Hermann, Z. Tošner, C. Platas-Iglesias, *Phys. Chem. Chem. Phys.* 2017, **19**, 26662–71. (2017 PCCP HOT Articles Collection)

4.1 Description of studied systems

This Chapter is focused on dynamic NMR of azamacrocylic complexes of trivalent lanthanides (mainly Eu^{3+} and Yb^{3+}). The employed ligands are H_4**dota** and an analogous ligand bearing one phosphonic acid pendant arm (H_5**do3ap**), see Figure 4.1 for the structure of complexes [Eu(**dota**)(H_2O)]$^-$ and [Eu(H**do3ap**)(H_2O)]$^-$.

The central ion in the complexes of dota-like ligands is coordinated between N_4 plane of the cycle and O_4 plane of oxygen atoms in the pendant arms. A water molecule can occupy the ninth coordination position above the O_4 plane. Presence or absence of the water strongly depends on the structure of the ligand and on the central metal ion.[50]

Relative torsion between N_4 and O_4 planes defines two possible orientations of the pendant arms, Δ for clockwise torsion and Λ for the anti-clockwise one. The ethylene bridges of cyclen ring can adopt geometry deformed by positive or negative torsion as well, which results in $\delta\delta\delta\delta$ or $\lambda\lambda\lambda\lambda$ geometry of the cycle respectively. As result, four possible conformation isomers are observed as two enantiomeric pairs. The isomer which has opposite sense of pendant and cycle torsion (i.e. $\Lambda\delta\delta\delta\delta$ or $\Delta\lambda\lambda\lambda\lambda$) adopts square antiprismatic geometry which is commonly

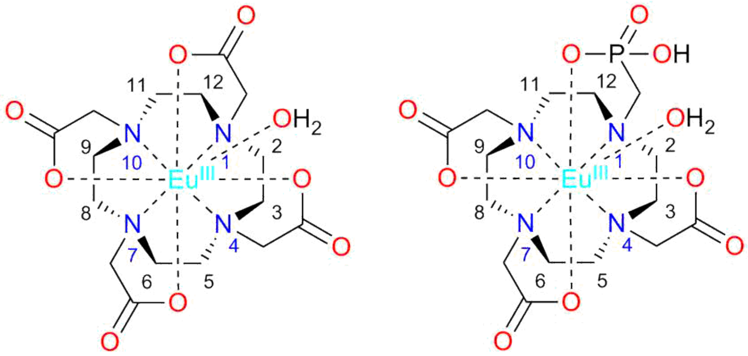

[Eu(**dota**)(H_2O)]$^-$ [Eu(H**do3ap**)(H_2O)]$^-$

Figure 4.1: Structure of the complexes discussed in this work with an atom numbering scheme. The TSAP isomers are depicted in both cases.

denoted as SAP. The other diastereomer ($\Delta\delta\delta\delta\delta$ or $\Lambda\lambda\lambda\lambda\lambda$) is denoted as TSAP (twisted square antiprismatic). The exchange between those diastereomers occurs via arm rotation or ring inversion, while combination of both motions results in enantiomer exchange.[51] See Figure 4.2 for pictorial representation of this dynamics in [Eu(**do3ap**)(H_2O)]$^{2-}$ complex.

Despite the fact that this isomerisation is known to affect applicability of the complex as a MRI contrast agent[52–54] or as a paramagnetic probe for protein study,[55] detail studies are rare in the literature. Especially, determination of the exchange rates has been seldom reported with sufficient accuracy.[56,57]

Internal dynamics of complexes with DOTA-like ligands can be studied by quantum chemistry theoretical calculations as well. These calculations can bring insight into the mechanism of the exchange, but they are much more reliable if they are compared with the experiment.[58]

4.2 Lineshape analysis

Various complexes with diamagnetic lanthanides(III) ions have been studied in the literature by quantification of changes in NMR spectra at different temperatures.[59–64] In analogy with these works the VT-analysis was applied to ^{31}P spectra of [Eu(**do3ap**)(D_2O)]$^{2-}$ (D_2O/d^4-MeOH mixture; v/v=1/1). The temperature dependence of chemical shifts of both isomers without exchange was extrapolated from chemical shift at low temperature (from −40 to 25 °C). The ^{31}P T_2^* in absence of exchange was estimated from low-temperature spectra (average between

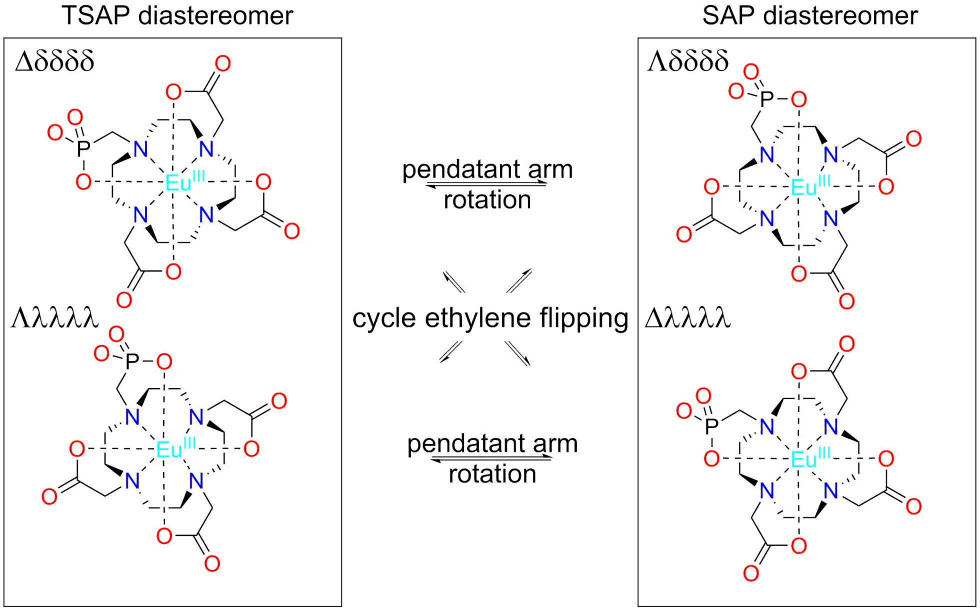

Figure 4.2: Schematic representation of TSAP/SAP structure and possible interconversion pathways demonstrated on $[Eu(\textbf{do3ap})(H_2O)]^{2-}$. The water molecule above the O_4 plane was omitted for clarity.

−5 and 0 °C) to be 5.8 and 6.5 ms for the SAP and the TSAP isomers, respectively. Interestingly, the line-width increased at lower temperature, which can be associated with the presence of other kind of isomerism at low temperature. Another possible explanation is decrease of T_2. Short T_2 can be induced by increase of solvent viscosity and substantial increase of relaxation rate through Curie mechanism. This relaxation mechanism is dominant here and the rate depends on T^{-3}.[10] For VT-^{31}P-NMR spectra see Figure 4.3. Spectra were analysed using Asymexfit Matlab package, provided by Římal.[8] Results are listed in Table 4.1 and compared with activation parameters of TSAP pendant flipping determined from 1D-EXSY discussed in Chapter 4.4. For temperature dependence of fitted rate constants, see plot in Figure 4.4.

Table 4.1: Comparison of activation parameters determined by variable-temperature analysis and 1D-EXSY experiment

method	$\Delta G^{\ddagger}$(298 °C)/kJ mol^{-1}	$\Delta H^{\ddagger}$/kJ mol^{-1}	$\Delta S^{\ddagger}$/J K^{-1} mol^{-1}
VT	58(2)	80(1)	75(4)
1D-EXSY[a]	58(1)	53.4(7)	17(2)

[a] Parameters of pendant flipping in direction TSAP → SAP which is slightly favourable pathway (Appendix C)

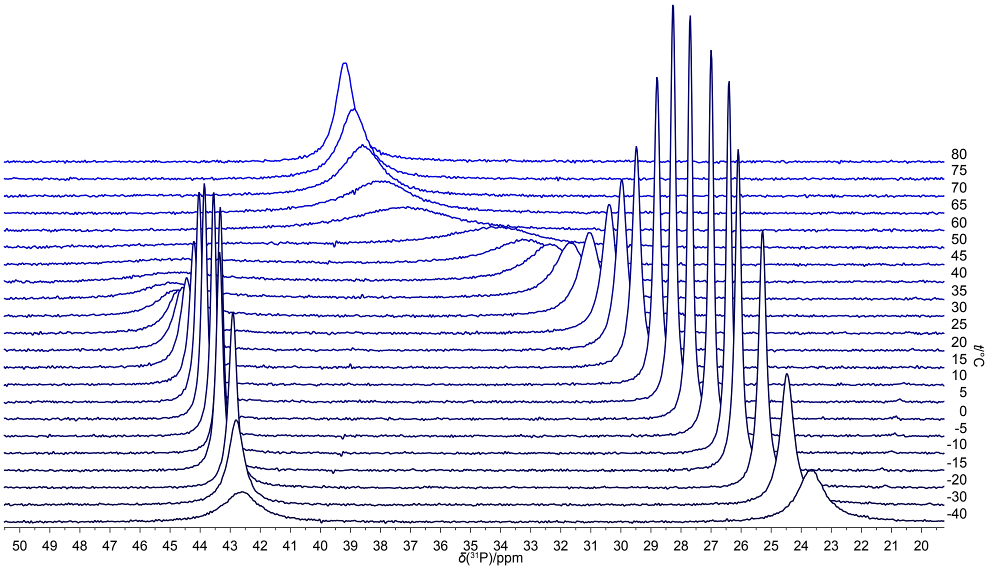

Figure 4.3: Temperature dependece of ^{31}P-NMR spectra of $[\mathrm{Eu}(\mathbf{do3ap})(\mathrm{H_2O})]^{2-}$.

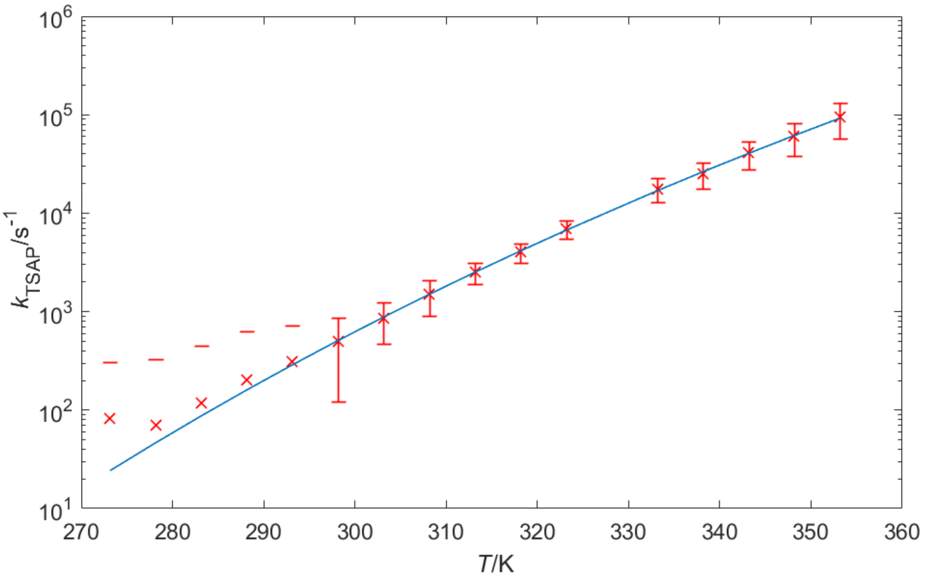

Figure 4.4: Temperature dependence of TSAP → SAP exchange rate constant of $[\mathrm{Eu}(\mathbf{do3ap})(\mathrm{H_2O})]^{2-}$ as determined by VT analysis.

Although the line-shape analysis ensures reliable results, it cannot be used for ^{1}H-NMR spectra due to a strong signal overlap and the complicated kinetic scheme. On the other hand, ^{31}P-NMR-VT analysis does not distinguish between arm rotation and ring inversion and, therefore, does not bring information about the mechanism.

4.3 2D-EXSY

Historically, the first method used to study TSAP-SAP exchange in paramagnetic lanthanide(III) complexes of DOTA-like ligands was 2D-EXSY applied on $[\mathrm{Eu}(\mathbf{dota})(\mathrm{H_2O})]^-$ complex. Although this study was a breakthrough at the time of its publication, only a limited set of data points was used and its subsequent analysis did not bring correct information about the system dynamics.[56] Data for $[\mathrm{Yb}(\mathbf{dota})(\mathrm{H_2O})]^-$ were obtained by Desreux et al.[57] and will be further discussed in the text. It was found that 2D-EXSY is useful only for qualitative description of the exchange processes because proper phase and baseline correction are not straightforward and off-diagonal signal integration does not bring reliable results.

4.4 1D-EXSY

Reliable and reproducible results can be obtained using selective 1D-EXSY pulse sequence. Although this technique is well established for diamagnetic systems,[65,66] the paramagnetic systems require extensive modification of the pulse sequence. At the same time, the paramagnetic effects must be taken into account during during evaluation of the obtained data.

4.4.1 Pulse sequence optimisation

As described in the paper (Appendix C), the required modification of standard pulse sequence is related to shortening of delay times where the system is loosing coherence due to T_2 relaxation, especially during the signal selection. For this reason, the echo time δ in the pulse sequence (4.1) must be reduced. At the same time, data obtained with very short τ_M (below $1 \times 10^{-4}\,\mathrm{s}$) are crucial for proper description of fast exchange and T_1 relaxation. Delays δ and τ_M were shortened by elimination of field gradient pulses and 180° refocusation pulse during τ_M. These elements are used for slowly relaxing systems to improve performance and precision of the method.[66] Of course, these modifications reintroduce artefacts due to pulse imperfections and dynamic effects. They can be suppressed by application of a proper phase cycle. One EXORCYCLE was used on weak 180° pulse in the centre of selection spin-echo and the other EXORCYCLE on the last read-out pulse. A two-step phase cycle was applied on the first 90° pulse in order to alternate the initial magnetisation between $\pm z$ at the beginning of τ_M part of the sequence. By addition or subtraction of FID with this alternation, the effects of T_1 relaxation can be reduced or amplified in respect to the effects of exchange. As the precise determination of exchange rates was the main goal of the work, these FIDs were subtracted, see Chapter 4.4.2 for further discussion. The result of all these modifications is the reduction of minimal accessible mixing time τ_M down to 1×10^{-5} s. The long phase cycle (32 steps) is not a problem in this case, as the paramagnetically induced relaxation enables fast sequence repetition. The resulting pulse sequence is:

$$90^\circ - \delta - 180^\circ(\text{selective}) - \delta - 90^\circ - \tau_M - 90^\circ - \text{FID}. \tag{4.1}$$

Another complication is limited pulse width. Experimental excitation profile of hard 15 µs pulse is displayed in Figure 4.5.[i] As the signals of Eu^{3+} complexes

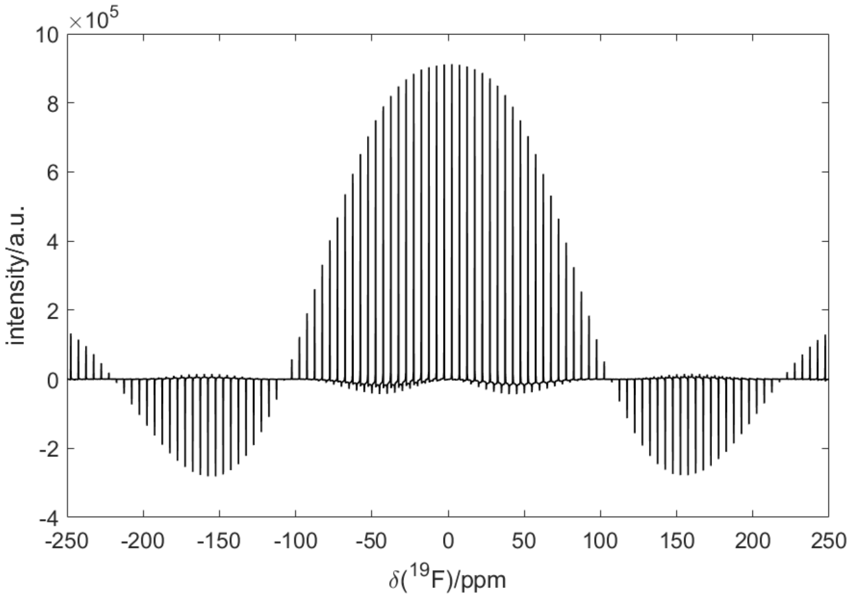

Figure 4.5: Excitation profile of hard 15 µs pulse in ^{1}H channel using 600 MHz spectrometer; after phase correction.

---

[i] For further discussion of pulse excitation profiles, see Ref. 67.

are spread between 45 and −25 ppm, the pulse can be considered as uniform. The other paramagnetic lanthanides(III) induce a much higher shift, for example [Yb(**dota**)(H$_2$O)]$^-$ complex resonances range from 150 to −95 ppm and the excitation by hard pulse is definitely not uniform. Broadband pulses, e.g. sweep-frequency chirp pulses, cannot be used, as their duration exceeds relaxation and exchange times.[68] Therefore, hard pulses with different offsets were used. The selection block ($90° - \delta - 180°(\text{selective}) - \delta - 90°$) was performed at the resonance frequency of selected nucleus and final read-out pulse at the resonance frequency of the nucleus in exchange. Data for [Yb(**dota**)(H$_2$O)]$^-$ at 5 °C were successfully obtained with this pulse sequence (See Figure 4.6) and exchange and relaxation rates were obtained by their analysis. See Table 4.3 in Section 4.4.2.

4.4.2 Data analysis

Magnetisation transfer due to the internal dynamics in **dota**$^{4-}$ and **do3ap**$^{5-}$, as discussed in Chapter 4.1, can be described by differential Equation 4.2.

$$\frac{\mathrm{d}}{\mathrm{d}t}\boldsymbol{M}(t) = -\boldsymbol{R}(\boldsymbol{M}(t) - \boldsymbol{M}_{eq}) + \boldsymbol{k}\boldsymbol{M}(t)$$

$$\frac{\mathrm{d}}{\mathrm{d}t}\boldsymbol{M}(t) - (\boldsymbol{k} - \boldsymbol{R})\boldsymbol{M}(t) = \boldsymbol{R}\boldsymbol{M}_{eq}. \tag{4.2}$$

$$\boldsymbol{k} = \begin{pmatrix} -k_{\text{PendSAP}} - k_{\text{CycleSAP}} & 0 & k_{\text{PendTSAP}} & k_{\text{CycleTSAP}} \\ 0 & -k_{\text{PendSAP}} - k_{\text{CycleSAP}} & k_{\text{CycleTSAP}} & k_{\text{PendTSAP}} \\ k_{\text{PendSAP}} & k_{\text{CycleSAP}} & -k_{\text{PendTSAP}} - k_{\text{CycleTSAP}} & 0 \\ k_{\text{CycleSAP}} & k_{\text{PendSAP}} & 0 & -k_{\text{PendTSAP}} - k_{\text{CycleTSAP}} \end{pmatrix}$$

where $\boldsymbol{M}(t)$ is a vector consisting of the z-magnetization of the SAP$_{\text{ax}}$, SAP$_{\text{eq}}$, TSAP$_{\text{ax}}$ and TSAP$_{\text{eq}}$ hydrogen atoms. The $\boldsymbol{M}_{eq}$ is its equilibrium value, and $\boldsymbol{R}$ is a diagonal matrix of R_1 relaxation rates at each site. The exchange matrix $\boldsymbol{k}$ describes all the exchange processes that occur in the system. Exchange rates k_{PendSAP}, k_{CycleSAP}, k_{PendTSAP} and $k_{\text{CycleTSAP}}$ describe pendant arm rotation and macrocycle inversion experienced by either the SAP or TSAP isomers.

General the solution of equation 4.2 with starting condition $\boldsymbol{M}(0) = \boldsymbol{M}_0$ is:

$$\boldsymbol{M}(t) = \frac{\boldsymbol{R}\boldsymbol{M}_{eq}}{\boldsymbol{k} - \boldsymbol{R}}(e^{(\boldsymbol{k}-\boldsymbol{R})t} - 1) + \boldsymbol{M}_0 e^{(\boldsymbol{k}-\boldsymbol{R})t}. \tag{4.3}$$

The second step of the phase cycle leads to starting condition $\boldsymbol{M}(0) = -\boldsymbol{M}_0$ and we get:

$$\boldsymbol{M}(t) = \frac{\boldsymbol{R}\boldsymbol{M}_{eq}}{\boldsymbol{k} - \boldsymbol{R}}(e^{(\boldsymbol{k}-\boldsymbol{R})t} - 1) - \boldsymbol{M}_0 e^{(\boldsymbol{k}-\boldsymbol{R})t}. \tag{4.4}$$

After subtraction of both results, we get:

$$\boldsymbol{M}(t) = 2\boldsymbol{M}_0 e^{(\boldsymbol{k}-\boldsymbol{R})t}. \tag{4.5}$$

This solution is in the same form as that of Equation 4.2 without the right side:

$$\frac{\mathrm{d}}{\mathrm{d}t}\boldsymbol{M}(t) - (\boldsymbol{k} - \boldsymbol{R})\boldsymbol{M}(t) = 0, \tag{4.6}$$

It means that, after the application of the phase cycle the system effectively relaxes to zero instead to its equilibrium magnetisation.[ii)]

At the beginning of each 1D-EXSY experiment, the vector of z magnetisations has only one non-zero element (selective excitation). e.g. M_{SAPAx}. From Equations 4.6 at $t = 0$, we get:

$$\frac{\mathrm{d}}{\mathrm{d}t}\begin{pmatrix} M_{\mathrm{SAPAx}} \\ M_{\mathrm{SAPEq}} \\ M_{\mathrm{TSAPAx}} \\ M_{\mathrm{TSAPEq}} \end{pmatrix}\Bigg|_{t=0} = \begin{pmatrix} -k_{\mathrm{PendSAP}} - k_{\mathrm{CycleSAP}} - R_{\mathrm{SAPAx}} \\ 0 \\ k_{\mathrm{PendSAP}} \\ k_{\mathrm{CycleSAP}} \end{pmatrix} M_{\mathrm{SAPAx}}(0). \tag{4.7}$$

Using this equation, exchange rates k_{PendSAP} and k_{CycleSAP} can be calculated from the slope (at $t = 0$) of the initial buil-up of the M_{TSAPAx} and M_{TSAPEq} signals, divided by $M_{\mathrm{SAPAx}}(0)$ intensity (the 2nd order polynomial was used for fitting of the magnetisation time dependence). From the slope of M_{SAPAx} and M_{SAPEq} at $t = 0$ divided by $M_{\mathrm{TSAPAx}}(0)$, the exchange rates k_{PendTSAP} and $k_{\mathrm{CycleTSAP}}$ were obtained. This approach is sometimes referred to as initial rate analysis. The results for $[\mathrm{Eu}(\textbf{dota})(\mathrm{H_2O})]^-$ at 5 °C were compared to those obtained by numerical fitting of the Equations 4.2 as described below and in Appendix C. (See Table 4.2).

[ii)] Factor 2 is not important in this case, as the magnetisation is detected in arbitrary units and only a relative value of each $\boldsymbol{M}$ element with respect to the others is important.

Table 4.2: Exchange rates of the TSAP↔SAP interchange of [Eu(**dota**)(H_2O)]$^-$ as obtained by initial-rate analysis of 1D-EXSY data at 5 °C compared to those obtained by numerical solution of Equation 4.2

Parameter	Initial-rate	Numerical fit
$k_{\mathrm{PendSAP}}/\mathrm{s}^{-1}$	4.6(2)	5.58(6)
$k_{\mathrm{CycleSAP}}/\mathrm{s}^{-1}$	10.5(2)	10.60(7)
$k_{\mathrm{PendTSAP}}/\mathrm{s}^{-1}$	24.1(9)	25.81(7)
$k_{\mathrm{CycleTSAP}}/\mathrm{s}^{-1}$	48(1)	52.30(8)

The systematic underestimation of the rates from the initial rate analysis is caused by the relaxation effects on the data points even at small τ_M which influence the slope at $t = 0$.

For this reason, data of all systems and various temperatures were analysed by non-liner fit of numerically solved Equation 4.2 using home-made Matlab script. The other advantage is that the relaxation rates (R) were obtained as well. This procedure is discussed in Appendix C.

The same approach was used to study [Yb(**dota**)(H_2O)]$^-$ at 5 °C. This compound is more challenging because of much a faster relaxation leading to a decrease of signal intensity during the selective pulse and offset problems. The results are listed in Table 4.3. Data from the literature obtained by 2D-EXSY[57] for the same system and data from Appendix C for [Eu(**dota**)H_2O]$^-$ are included for comparison. Fits of the experimental data are shown in Figure 4.6 for [Yb(**dota**)(H_2O)]$^-$ at 5 °C and in Supplementary Information in Appendix C for the other systems and temperatures.

Values obtained in this study differ from those published by Desreux et al.[57] However, there is a qualitative agreement in a sense that the exchange from SAP to TSAP is slower than the reverse process. It is confirmed by the relative abundance of these isomers in equilibrium (K_{integral}) as well.

The accuracy of parameters for [Yb(**dota**)(H_2O)]$^-$ is lower compared to the data for [Eu(**dota**)(H_2O)]$^-$. It can be concluded that the exchange proceeds preferentially from TSAP to SAP in both cases. For Eu^{3+}, it is dominated by the cycle inversion but in case of Yb^{3+}, the arm rotation is the more important process. Exchange from SAP to TSAP is slower and dominated by the cycle inversion for both complexes.

The arm rotation and ring inversion processes proceed with comparable rates for [Eu(H**do3ap**)(H_2O)]$^-$. Deprotonation of the phosphonate pendant arm does not have an important effect on the rates characterizing the ring inversion pathway;

Table 4.3: Exchange and relaxation rates of Yb^{3+} and Eu^{3+} complexes of **dota** at 5 °C in water

Parameter	[Yb(**dota**)(H_2O)]$^-$	[Yb(**dota**)(H_2O)]$^-$ [a]	[Eu(**dota**)(H_2O)]$^-$
$k_{\mathrm{PendSAP}}/\mathrm{s}^{-1}$	14(3)	1.09[b]	5.58(6)
$k_{\mathrm{CycleSAP}}/\mathrm{s}^{-1}$	18(4)	0.7[b]	10.60(7)
$k_{\mathrm{PendTSAP}}/\mathrm{s}^{-1}$	37.6(4)	8.7[b]	25.81(7)
$k_{\mathrm{CycleTSAP}}/\mathrm{s}^{-1}$	30.7(5)	18.0[b]	52.30(8)
K_{EXSY} [c]	0.5(1)	0.07	0.207(5)
K_{integral} [d]	0.15	–	0.21
$R_{\mathrm{SAPAx}}/\mathrm{s}^{-1}$	400(12)	–[e]	69.1(1)
$R_{\mathrm{SAPEq}}/\mathrm{s}^{-1}$	91(3)	–[e]	22.53(7)
$R_{\mathrm{TSAPAx}}/\mathrm{s}^{-1}$	328(1)	–[e]	47.6(2)
$R_{\mathrm{TSAPEq}}/\mathrm{s}^{-1}$	97(1)	–[e]	18.3(1)

[a] Ref. 57

[b] Extrapolated to 5 °C using Arrhenius parameters.

[c] Equlibrium constant calculated from kinetic parameters as $K_{\mathrm{EXSY}} = (k_{\mathrm{PendSAP}} + k_{\mathrm{CycleSAP}})/(k_{\mathrm{PendTSAP}} + k_{\mathrm{CycleTSAP}})$.

[d] Equlibrim constant calculated from an integral value of TSAP/SAP signals. Not available in Ref. 57 at 5 °C.

[e] Not discoussed in Ref. 57

however, it dramatically accelerates the arm rotation pathway for the TSAP→SAP interconversion (from $25.0\,\mathrm{s}^{-1}$ to $71.7\,\mathrm{s}^{-1}$), and even more for the reverse process (from $23.2\,\mathrm{s}^{-1}$ to $99.7\,\mathrm{s}^{-1}$, Table 1 in Appendix C). These differences in exchange rates are probably related to a different arm rotation mechanism proposed in Section 4.5. The results are in a good agreement with the results of ^{31}P 1D-EXSY experiments as well, where only the sum of arm rotation and ring inversion rates can be detected (see Fig. S6, S7 and Table S5, in Appendix C).

The relaxation rates induced by Yb^{3+} are evidently almost an order of magnitude higher than those induced by Eu^{3+} and, for both complexes, they are higher for axial protons which are closer to the central lanthanide(III) ions.

Activation parameters for Eu^{3+} complexes were obtained by repeating of the same analysis at different temperatures (see Table 2 in Appendix C). The arm rotation was found to be driven mainly by enthalpy factors. Consistently negative values of activation entropy were observed for the ring inversion. Based on DFT calculation, this trend was associated with a change of vibration contribution to entropy which is caused by prolongation of Eu–N bond in the transition state.(See Table 3 and S9 in Appendix C) Comparison and discussion of data obtained for [Eu(**do3ap**)(H_2O)]$^{2-}$ and [Eu(H**do3ap**)H_2O]$^-$ complexes with those of [Eu(**dota**)(H_2O)]$^-$ are thoroughly discussed in the appended article.

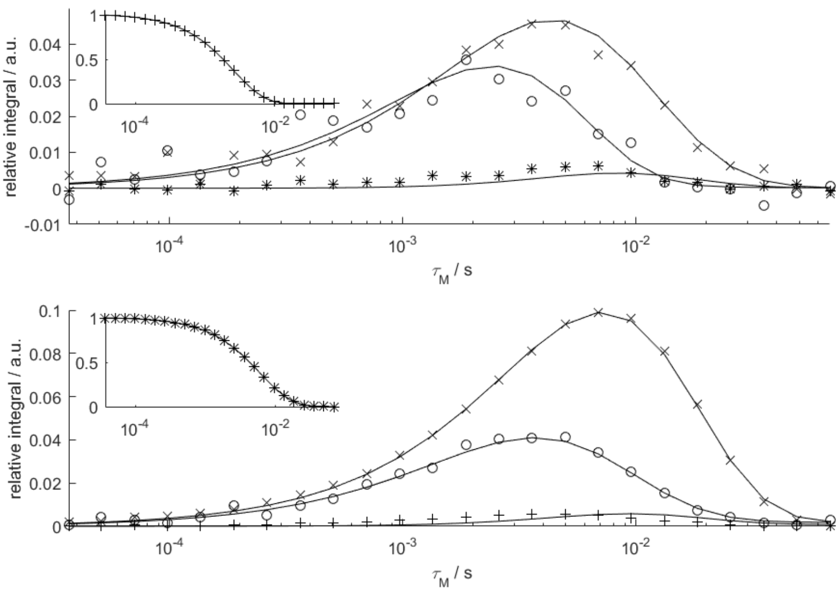

Figure 4.6: Relative areas of the signals of $[Yb(\mathbf{dota}))(H_2O)]^-$ as a function of the mixing time obtained from 1D-EXSY experiments at 5 °C with changing pulse offset as discussed in Chapter 4.4.2. The insets show the evolution of magnetization of the signal to which the refocusing selective 180° pulse was applied. Symbols: TSAPax (+), SAPeq (×), TSAPeq (*), SAPax (○). The solid lines represent the simultaneous fit of both data sets using Equation 4.2.

4.5 Quantum chemistry methods

A quantum chemical simulation was performed in order to describe mechanism of the TSAP↔SAP interchange. As the time-scale of the studied processes is between milliseconds and hundreds of milliseconds, the molecular dynamics simulation is impossible under any simplification. Instead, the mechanism was described by analysis of extreme points of potential energy surface. DFT methods, compared to post-Hartee-Fock on one side and molecular mechanics on the other side, ensure good ratio between calculation demands and accuracy. However, choice of energy functional influences the results significantly. The M06 functional was used in the calculation, because the hybrid meta-GGA DFT functionals were described to perform well for Ln^{3+} complexes with polyamino-polycarboxylate ligands[69].

Effective core potentials were used for Eu^{3+}, because proper description of lanthanide inner electrons is complicated and they do not contribute significantly to bonds with ligand. In this study, $46+4f^6$ electrons were included in the core relativistic effective pseudopotential of Dolg.[70,71] Circa 150 transition states and local minima were found [iii)].

It was found, that cyclen inversion proceeds by a stepwise mechanism, one ethylene after the other. In all three systems, several pathways are possible because different orders of ethylen inversions have similar activation energy within the common error of DFT methods. On the other hand, the arm rotation proceeds stepwise only in [Eu(**do3ap**)(H_2O)]$^{2-}$ and involves intermediates with bidentately bound phosphonate group. Up to date, this mechanism and phosphonate coordination mode were not described for phosphonic derivatives of DOTA-like complexes. The structure of the related trasition state is depicted in Figure 4.7.

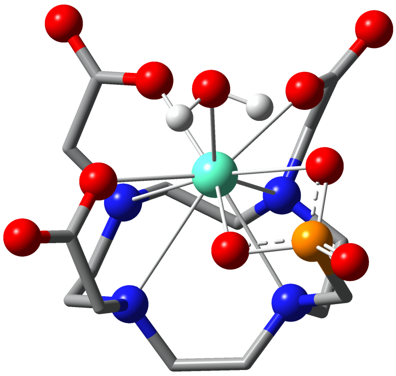

Figure 4.7: Calculated molecular structure of the [Eu(**do3ap**)(H_2O)]$^{2-}$ intermediate with the bidentate phosphonate group. Color code: black – carbon; white – hydrogen; blue – nitrogen; red – oxygen; orange – phosphorus; green – europium. Macrocycle hydrogen atoms are omitted for clarity.

In [Eu(H**do3ap**)(H_2O)]$^-$ and [Eu(**dota**)(H_2O)]$^-$, synchronous mechanism was found where all four pendant arms rotate together through a single transition state. As the character of the bonds between lanthanide(III) and DOTA-like ligands is mostly electrostatic, a proper description of solvatation is necessary. Inclusion of implicit water solvatation (polarised continuum model, PCM) leads to a better agreement with the experiment than published in the literature for [Lu(**dota**)H_2O]$^-$.[59] However, correct description of coordination geometries and reasonable agreement of experimental and calculated arm rotation barriers were reached only when explicit second-sphere water molecules were included, see Table 4.4. On the other hand, the mobility of these water molecules complicates iden-

---

[iii)] For coordinates, see Electronic Supplementary Information of article in Appendix C available on-line, DOI:10.1039/c7cp05296k tification of the transition states to such a degree that no more than two explicit second-sphere water molecules can be included.

Table 4.4: Free energy of the arm rotation ($\Delta G^{\ddagger}_{\mathrm{calc}}$/kJ mol^{-1}) calculated with n second-sphere water molecules and corresponding experimental values ($\Delta G^{\ddagger}_{\mathrm{PendSAP}}$/kJ mol^{-1}). The free energies are related to the SAP isomers

	Anion		
Parameter	**dota**$^{4-}$	(H**do3ap**)$^{4-}$	**do3ap**$^{5-}$
$\Delta G^{\ddagger}_{\mathrm{PendSAP}}$	64(1)	61(1)	57(1)
$\Delta G^{\ddagger}_{\mathrm{calc}}$ $n = 0$	71.4^{b}	85.5^{b}	42.6^{c}
$\Delta G^{\ddagger}_{\mathrm{calc}}$ $n = 2$	60.0^{b}	81.9^{b}	51.2^{c}
[Lu(**dota**)(H$_2$O)]$^{-\,d}$	82	–	–

[a] Ref. 59.

[b] Synchronous process.

[c] Rate-determining step of successive arm rotation.

[d] Without PCM.

Chapter 5

Conclusions

In this Thesis, the structure and dynamics of paramagnetic coordination compounds were studied by nuclear magnetic resonance. The main aim of these studies was to describe properties of potential contrast agents for MRI.

In order to prepare fluorinated ligand for *d*-metal ions, cyclam was derivatized with 2-trifluorethyl group. Complexes with Ni^{2+} were prepared in both *cis* and *trans* octahedral geometries as well as in the square-planar complex. Studies of kinetic inertness showed that *cis*-$[Ni(\mathbf{te2f})(H_2O)_2]^{2+}$ undergoes slow, acid-assisted hydrolysis, but it is sensitive to trans-chelatation. This process was effectively reduced by introduction of the coordinating pendant arms into the ligand structure. Five different ligands were prepared for this comparative study. It was found that the kinetic inertness qualitatively correlates with the strength of the axial ligand metal binding and/or with the axial group basicity and its ability to transfer protons onto the macrocycle amine group(s). In most cases, the kinetic inertness increased compare to *cis*-$[Ni(\mathbf{te2f})]^{2+}$ but, surprisingly, the ligand with 2-aminoethyl pendant arm forms very labile complexes. It could be suggested that this lability is induced by the high basicity of 2-aminoethyl group which facilitates the protonation of cycle amine group(s) by proton transfer. The ring amine protonation is generally considered to be the rate-determining step in the decomplexation reactions.

Strong paramagnetic relaxation enhancement was observed in all of the prepared complexes of Ni^{2+} and Co^{2+} ions. The Ni^{2+} complexes have faster relaxation than the Co^{2+} complexes. This difference is caused by slower Ni^{2+} electron relaxation which is induced by different mechanism than in the case of Co^{2+}. The relaxation enhancement is not influenced by the type of the axial coordination group.

Mechanism of fluorine relaxation in *trans*-$[Ni(\mathbf{te2f2p})]^{2-}$ was studied in details by fitting of ^{19}F-NMRD profile by SBMR theory. The relaxation is induced by the dipole-dipole coupling between ^{19}F nucleus and quickly relaxing nickel electron. The Curie contribution to the relaxation can be neglected which is an important difference from the systems based on lanthanide(III) ions.

The same complex, i.e. *trans*-[Ni(**te2f2p**)]$^{2-}$, was tested for MRI application and six-times increase of relaxation rate was observed compared to the diamagnetic analogue of the ^{19}F-MRI CA used in practice. This non-toxic complex was successfully used for cell labelling.

Although the Eu^{3+} amd Yb^{3+} complexes of the DOTA-like ligands in the Chapter 4 are well known in the scientific community and were originally intended as a model systems for development and optimisation of NMR methods, the study revealed new informations about these systems. The arm rotation and cyclen chelate ring inversion rates were determined separately by utilization of a optimised EXSY NMR pulse sequence in combination with full Bloch-McConnell-based data analysis. The rates of these processes were measured with a high accuracy. These results were compared with the exchange rates obtained by ^{31}P VT analysis, ^{31}P EXSY and ^{1}H EXSY processed using the initial rate approach. In addition, the corresponding activation barriers were reported as well. A detailed insight into the mechanisms of these motions at the molecular level was obtained using DFT calculations. The calculated activation parameters for the cyclen-inversion process are in excellent agreement with the experimental one, including the activation entropies. The activation barriers computed with DFT for the arm rotation pathway present larger deviations from the experimental values. However, we showed that it is mainly due to deficient modelling of solvent effects by PCM as the arm rotation process involves flipping of the negatively charged pendant arms. Propitiously, utilisation of a mixed cluster-continuum model that includes two explicit second-sphere water molecules results in activation parameters which are in a better agreement with the experimental one.

Author contributions

Nowadays, each scientific work relies on a broad collaboration of many people (see publication Acknowledgements). However "modern" scientometric machinery requires an explicit listing of my own contributions. The majority of work discussed in this Thesis was done solely by myself, specifically I did:

- Synthesis of all of the investigated cyclam derivatives as well as their Ni^{2+} and $Co^{2+/3+}$ complexes. As well as their characterisation by NMR, MS and UV/VIS.
- Kinetic studies of Ni^{2+} complexes formation, isomerisation and dissociation using time-resolved NMR.
- Measurement of the relaxation properties, including assistance during the measurement of ^{19}F-NMRD profile, their analysis and final interpretation.
- Assistance during the MRI experiments, especially sample preparation.
- Optimisation and performance of all NMR methods.
- Analysis of obtained data using self-written Matlab routines.
- All of the DFT calculations.

Part III

Appendices

Appendix A

Nickel(II) complexes of N-CH_2CF_3 cyclam derivatives as contrast agents for ^{19}F magnetic resonance imaging

- J. Blahut, P. Hermann, A. Gálisová, V. Herynek, I. Císařová, Z. Tošner, J. Kotek, *Dalton Trans.* 2016, **45**, 474–8.

Dalton
Transactions

COMMUNICATION

View Article Online
View Journal

Cite this: DOI: 10.1039/c5dt04138d

Received 21st October 2015,
Accepted 18th November 2015

DOI: 10.1039/c5dt04138d

www.rsc.org/dalton

Nickel(II) complexes of *N*-CH_2CF_3 cyclam derivatives as contrast agents for ^{19}F magnetic resonance imaging†

Jan Blahut,[a] Petr Hermann,[a] Andrea Gálisová,[b] Vít Herynek,[b] Ivana Císařová,[a]
Zdeněk Tošner[c] and Jan Kotek*[a]

Kinetically inert Ni(II) complexes of N^1,N^8-bis(2,2,2-trifluoroethyl) cyclams with hydrogen atoms or phosphonic acid groups in the N^4,N^{11}-positions show significant ^{19}F NMR relaxation rate enhancement useful for 19-fluorine MRI imaging.

Magnetic resonance imaging (MRI) is one of the most common techniques in molecular imaging. It is based on the detection of the NMR signal originating from water protons in a tissue. To increase its sensitivity, paramagnetic contrast agents (CAs) are often applied.[1,2] They affect mainly the longitudinal (T_1) relaxation time of the ^1H signal, which leads to an increase in the intensity of the water proton MRI signal. However, essentially all tissues contain water and, thus, the background signal compromises the detection accuracy. This problem can be solved by using non-proton MRI and the ^{19}F nucleus seems to be the most promising candidate.[3–6] Natural monoisotopic ^{19}F has an NMR resonance frequency close to that of ^1H (40.08 MHz T^{-1} for ^{19}F compared to 42.58 MHz T^{-1} for ^1H) and exhibits sensitivity comparable to ^1H (83%). Fluorine concentration in organisms is virtually zero and, therefore, the lack of background in fluorine-based images enables “hot-spot” imaging. The wider spectral range of the ^{19}F nucleus (~350 ppm) compared to ^1H (~10 ppm) is also beneficial for some applications. Moreover, only small hardware and software adjustments of standard ^1H scanners are needed for ^{19}F detection.[6] This makes the nucleus very potent for *e.g.* cellular tracking of labelled cell cultures.[7–11]

However, the ^{19}F nucleus present in organic molecules has usually a very long T_1 relaxation time requiring a long delay between excitation pulses; this prolongs the total duration of imaging experiments to unrealistic lengths. Shortening of the T_1 relaxation time can result in significant shortening of the experimental time. However, it is necessary to take into account the concomitant shortening of the transversal (T_2 or T_2^*) relaxation time, which leads to signal broadening and can result in very fast loss of signal intensity. It has been shown that the introduction of highly paramagnetic lanthanide(III) ions to the close vicinity of the fluorine atom(s) leads to significant shortening of the relaxation times,[12] and the T_2^*/T_1 ratio is in the range of 0.3–0.9, which is suitable for MRI measurements.[12c,13]

It is known that, despite the low overall electronic spin (S = 1) and magnetic momentum (μ_{eff} ~ 3 B.M.) of Ni(II), this ion can induce a large paramagnetic chemical shift and relaxation enhancement comparable to that of lanthanide(III) ions with higher S and μ.[14] Therefore, some Ni(II) complexes have been studied as MRI agents employable in the Chemical Exchange Saturation Transfer method.[15] Here, we decided to study the ^{19}F NMR relaxation properties of Ni(II) complexes. The Ni(II) ion fits perfectly in the cavity of 1,4,8,11-tetraazacyclotetradecane (cyclam) and cyclam derivatives are well-known to form Ni(II) complexes with high thermodynamic stability, especially with ligands having coordinating pendant arms enabling octahedral binding to the metal. The 2,2,2-trifluoroethyl side arm was chosen as a group containing a high number of equivalent fluorine atoms. Therefore, ligands **1** and $H_4te2p\text{-}tfe_2$ (Fig. 1)

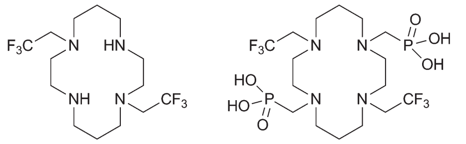

1

$H_4te2p\text{-}tfe_2$

Fig. 1 Ligands studied in this work.

---

[a] Department of Inorganic Chemistry, Faculty of Science, Charles University (Univerzita Karlova), Hlavova 2030, 128 43 Prague 2, Czech Republic. E-mail: modrej@natur.cuni.cz; Fax: +420-221951253; Tel: +420-221951261
[b] Department of Radiodiagnostic and Interventional Radiology, Magnetic Resonance Unit, Institute for Clinical and Experimental Medicine, Vídeňská 1958/9, Prague 4, 140 21 Czech Republic
[c] NMR Laboratory, Faculty of Science, Charles University (Univerzita Karlova), Hlavova 2030, 128 43 Prague 2, Czech Republic

† Electronic supplementary information (ESI) available: Synthesis of studied compounds, single-crystal RTG diffraction data, details on potentiometric study, study of acid-assisted dissociation of prepared complexes, relaxation study, $^1H/^{19}F$ MRI visualization. CCDC 1430237–1430242. For ESI and crystallographic data in CIF or other electronic format see DOI: 10.1039/c5dt04138d

were suggested for testing the ^{19}F NMR parameters of their complexes.

Acylation of 1,8-dibenzylcyclam with ethyl trifluoroacetate or trifluoroacetic anhydride yielded the corresponding bis(amide). It was followed by BH_3 reduction[16] in diglyme at elevated temperature and the benzyl protecting groups were removed by Pd/C hydrogenolysis to obtain ligand **1**. The reaction[17] of amine **1** in neat $P(OEt)_3$ with CH_2O led to the tetraethyl bis(methylenephosphonate) cyclam derivative. The ethylester groups were removed by transesterification with trimethylsilylbromide[18] followed by the silylester hydrolysis to yield H_4te2p-tfe$_2$, which was isolated in a zwitterionic form after ion exchange chromatography. Synthetic details and results of a single-crystal X-ray diffraction study of **1**·2HCl·2H_2O and H_4te2p-tfe$_2$·4HBr·0.5H_2O are given in the ESI (Fig. S5 and S6†).

Ligand **1** (in the form of a hydrochloride) reacts with Ni(II) salts in aqueous solutions to give a light greenish-blue precipitate. The structure of this compound was determined by a single-crystal X-ray study as *cis*-[Ni(**1**)(Cl)$_2$] (see ESI Fig. S7†); the central ion is surrounded by four cyclam nitrogen atoms in the *cis*-V configuration[19] with two-fold symmetry ($d_{\text{Ni–N}}$ = 2.10 and 2.26 Å for secondary and tertiary amines, respectively) and *cis*-chloride anions coordinated with $d_{\text{Ni–Cl}}$ = 2.42 Å.

However, the *cis*-[Ni(**1**)(Cl)$_2$] complex shows extremely low solubility in all solvents. Thus, the presence of chloride ions had to be avoided during the preparation of a water-soluble complex. Therefore, ligand **1** in the form of a free base and Ni(ClO$_4$)$_2$ was used for further complex preparation. The course of the reaction in the H_2O : DMSO 1 : 6.5 mixture at 50 °C was followed by ^{19}F NMR spectroscopy (Fig. S2†). Such a solvent mixture was used to keep the reaction mixture fully homogeneous right from the beginning as compound **1** is poorly soluble in water. The reaction proceeds (at 50 °C) through an intermediate (δ_F = −22.9 ppm) and is completed during 90 min to give the final complex with δ_F = −29.3 ppm (at 50 °C). On cooling to 25 °C, the signal shifts to −26.5 ppm. No further ^{19}F NMR spectral changes were observed upon heating the solution at 100 °C for several days.

To obtain an aqueous stock solution, prolonged heating (80 °C) of the suspension of ligand **1** with Ni(ClO$_4$)$_2$ in H_2O : MeOH 1 : 1 (with subsequent evaporation of MeOH) was used. It led to the formation of a light blue aqueous solution of a single product with δ_F = −26.2 ppm. When the aqueous solution of the complex prepared in H_2O : MeOH was mixed with the sample prepared in H_2O : DMSO, only one symmetric signal in ^{19}F NMR was observed revealing that the species formed in both experiments are identical complexes.

Despite a number of attempts, we were not able to crystallize this light blue product. However, red single-crystals of *trans*-[Ni(**1**)](ClO$_4$)$_2$ (Fig. 2) were obtained when the blue aqueous solution of the complex was saturated with NaClO$_4$ and was left standing for a few weeks. In this complex, the cyclam ring is coordinated in the centrosymmetric *trans*-III configuration[19] ($d_{\text{Ni–N}}$ = 1.95 and 1.99 Å for secondary and tertiary amino groups, respectively). Consistent with the red colour, only very weak axial interaction with perchlorate anions located in distant positions ($d_{\text{Ni–O}}$ = 2.83 Å) was observed.

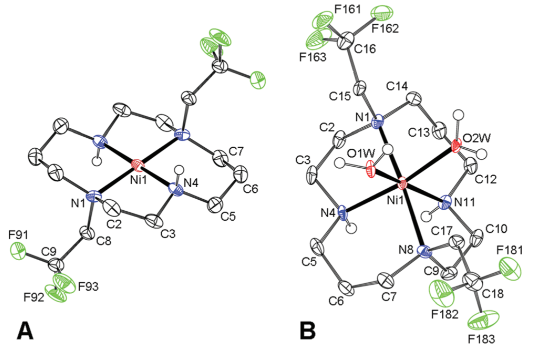

Fig. 2 Structures of (A): *trans*-[Ni(**1**)]$^{2+}$ and (B): *cis*-[Ni(**1**)(H_2O)$_2$]$^{2+}$ complex cations found in the solid state structures of *trans*-[Ni(**1**)](ClO$_4$)$_2$ and *cis*-[Ni(**1**)(H_2O)$_2$](TsO)$_2$, respectively. Carbon-bound hydrogen atoms are omitted for clarity. Thermal ellipsoids are shown at the 60% probability level.

Dissolution of the red *trans*-[Ni(**1**)](ClO$_4$)$_2$ complex in water produced a light blue solution with δ_F = −19.3 ppm and the species slowly isomerizes with first-order kinetics ($\tau_{1/2}$ ~3.5 h, 25 °C) to a species with δ_F −26.3 ppm (Fig. S3†). The final species is identical to the original Ni(II)–**1** complex, as it was confirmed by ^{19}F NMR after the addition of a standard. Taking into account the isomerism of metal ion–cyclam complexes,[19] red *trans*-[Ni(**1**)](ClO$_4$)$_2$ with the *trans*-III configuration probably forms a blue hexacoordinated *trans*-[Ni(**1**)(H_2O)$_2$]$^{2+}$ species upon dissolution, and this complex is rearranged in solution to the *cis*-[Ni(**1**)(H_2O)$_2$]$^{2+}$ species with the *cis*-V cyclam conformation.

Typically, the *trans*-III isomer of cyclam complexes is considered to be the thermodynamically most stable one,[20] and the preference of the *cis*-V cyclam conformation for the Ni(II)–**1** complex is rather surprising. However, the higher stability of the *cis*-V isomer over the *trans*-III one was supported also by the isolation of *cis*-[Ni(**1**)(H_2O)$_2$](TsO)$_2$ (Fig. 2). The structure shows Ni–N distances of 2.07 and 2.09 Å for secondary amino groups, and 2.22 and 2.25 Å for tertiary ones, respectively, with two water molecules coordinated with $d_{\text{Ni–O}}$ = 2.07 and 2.10 Å.

Based on the data presented above, one can conclude that the reaction of ligand **1** with Ni(ClO$_4$)$_2$ leads to the formation of the *cis*-[Ni(**1**)(H_2O)$_2$](ClO$_4$)$_2$ complex. The geometries of Ni(II) coordination polyhedra found in the solid state structures are compiled in Table S2† and are comparable to other [Ni(L)(H_2O)$_2$] complexes of cyclam derivatives.[21,22] The Ni–F distances found in all solid-state structures were in the range of 4.8–5.4 Å (Table S3†).

The complex of the second studied ligand, H_4te2p-tfe$_2$, was prepared by heating the ligand together with a slight excess of

$NiCl_2$ in aq. ammonia (pH 10) at 75 °C for 24 h; the excess of Ni(II) ions was removed by column chromatography. As mentioned above, the course of the reaction was followed by ^{19}F NMR (Fig. S4†), which showed a fast drop in the concentration of the free ligand (δ_F = −68.3 ppm), and the formation of an intermediate (δ_F = −41.1 ppm) and its slower rearrangement to the final product (δ_F = −26.4 ppm). The time-dependence of intensities of all three signals could be satisfactorily fitted using a monoexponential function (Fig. S4†) and showed comparable rate constants for all three processes (see the ESI†). Such behaviour points to the presence of an equilibrium between the free ligand and the intermediate with an irreversible (rate-determining) reaction step leading to the formation of the final complex.

The final product was isolated in the form of light blue crystals, which were identified as $(NH_4)\{$*trans*-[Ni(Hte2p-tfe$_2$)]$\}\cdot 3.25H_2O$ by single-crystal X-ray diffraction. Therefore, the complex species present in solution are expected to be *trans*-[Ni(H$_n$te2p-tfe$_2$)]$^{n-2}$ (n = 0, 1) depending on pH. The molecular structure of the complex anion is shown in Fig. 3, and geometric parameters of the coordination sphere of Ni(II) and Ni–F distances are listed in Tables S2 and S3.† The cyclam ring exhibits the *trans*-III configuration[19] (d_{Ni-N} are ∼2.10 and 2.11 Å for amino groups bearing the methylenephosphonate pendant arms, and 2.22 and 2.23 Å for those substituted by trifluoroethyl groups) with the oxygen atoms of phosphonate groups occupying apical positions (Ni–O distances are 2.06 and 2.10 Å, respectively). The molecules of the complex are connected *via* short hydrogen bonds between the oxygen atoms of protonated and unprotonated phosphonate pendants ($d_{O\cdots O}$ = 2.47 Å), forming infinite chains, similar to what was found for analogous complexes of cyclam-methylenephosphonate derivatives.[23,24] Bonding distances and the overall molecular structure are very similar to those of Ni(II) complexes of analogous derivatives.[22,24]

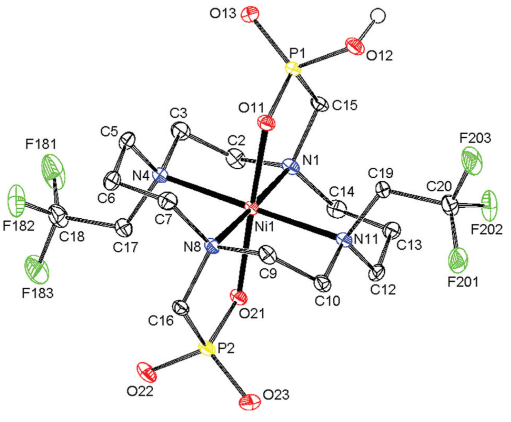

Fig. 3 Molecular structure of the *trans*-[Ni(Hte2p-tfe$_2$)]$^-$ anion found in the crystal structure of *trans*-(NH$_4$)[Ni(Hte2p-tfe$_2$)]$\cdot$3.25H$_2$O. Carbon-bound hydrogen atoms are omitted for clarity. Thermal ellipsoids are shown at the 60% probability level.

The thermodynamics of complexing properties of the phosphonate H$_4$te2p-tfe$_2$ ligand was studied by potentiometry (see the ESI and Table S4†). The comparison of ligand stepwise protonation constants (log K_{1-4} 10.86, 10.09, 5.60 and 4.73) with those of the N^1,N^8-dimethyl-N^4,N^{11}-bis(methylenephosphonate) analogue[25] (log K_{1-4} 11.47, 12.17, 7.20 and 6.33, Table S5†) points to significantly decreased ligand basicity caused by the presence of electron-withdrawing –CH_2CF_3 groups. Surprisingly, it affects not only the first two protonation constants corresponding to the ring amino groups but also those of the phosphonate moieties, probably as a result of a strong electron-withdrawing effect transferred through intramolecular hydrogen bonds, which are expected to have a geometry analogous to that found for related cyclam derivatives.[25] Equilibration of the Ni(II)–H$_4$te2p-tfe$_2$ system is relatively slow and, therefore, the out-of-cell titration method had to be used. As the complexation mechanism is not fully straightforward (see above), the samples used for the out-of-cell titration were heated at 50 °C for 2 weeks to ensure quantitative rearrangement of the intermediate to the final *trans* isomer. The time required for equilibration was checked by ^{19}F NMR of separate samples. The stability constant, log K_{NiL} = 13.28, is about 2–7 orders of magnitude lower than the constants of complexes with related ligands (Table S5†),[26,27] mainly as a consequence of the lower ligand basicity. The distribution diagram of the system (Fig. S8†) shows that full Ni(II) complexation by H$_4$te2p-tfe$_2$ is completed at pH 7 and the complex is present at this pH almost entirely in a fully deprotonated form.

For possible *in vitro*/*in vivo* utilization, kinetic inertness is a more important parameter than thermodynamic stability. Kinetic inertness is often tested in acidic solutions as acid-assisted complex dissociation. Thus, the decomposition of both studied complexes was examined in 1 M aq. HCl at 37 and 80 °C. Both complexes are decomposed relatively slowly by HCl at 37 °C ($\tau_{1/2}$ ∼8 and ∼10 h for *cis*-[Ni(**1**)(H$_2$O)$_2$]$^{2+}$ and *trans*-[Ni(H$_n$te2p-tfe$_2$)]$^{n-2}$, respectively) but the decomplexation of the *cis*-[Ni(**1**)(H$_2$O)$_2$]$^{2+}$ complex is substantially accelerated at the higher temperature (80 °C, $\tau_{1/2}$ ∼ 3 min compared to ∼5 h for *trans*-[Ni(H$_n$te2p-tfe$_2$)]$^{n-2}$, Table S6†), as the presence of apically coordinated pendant arms in the H$_4$te2p-tfe$_2$ complex enhances kinetic inertness. High inertness has been observed for several Cu(II) complexes with analogous cyclam-based ligands,[28] and highly protonated species of several Ni(II)[22,24] complexes of phosphonated cyclam derivatives have been isolated even in the solid state. These results suggest sufficient complex stability under physiological conditions and warrant the possible use of the Ni(II)–H$_4$te2p-tfe$_2$ complex in *in vitro*/*in vivo* applications.

As the *trans*-[Ni(te2p-tfe$_2$)]$^{2-}$ complex is kinetically inert and promises reasonable stability *in vivo*, its ^{19}F MRI-related parameters were investigated. Although the *cis*-[Ni(**1**)(H$_2$O)$_2$]$^{2+}$ complex is not suitable for any *in vivo* application due to its low solubility in chloride-containing media, it was studied as well for comparative purposes as there are no related data reported in the literature at all. The ^{19}F NMR relaxation measurement of both Ni(II) complexes at B_0 = 7.05 T showed extreme shortening of ^{19}F NMR T_1 relaxation times by 2–3 orders of magnitude compared with the values observed for the free ligands, **1** and H_4te2p-tfe$_2$ (Table 1).

The suitability of the *trans*-[Ni(te2p-tfe$_2$)]$^{2-}$complex for ^{19}F MRI was tested by phantom visualization at B = 4.7 T. At this magnetic field, the T_1 of the complex is very short in the millisecond range with a still convenient T_2^*/T_1 relaxation times ratio (Table 1). The observed relaxation times are even slightly shorter than those reported for studied Ln(III) complexes – in the cases of highly paramagnetic Tb(III), Dy(III) and Ho(III) complexes with the estimated Ln(III)–F distance lying in the range of 5–7 Å, the reported T_1 is typically in the range of 7–11 ms at 4.7 T and room temperature.[12c,13] The very short relaxation time of the Ni(II) complex required optimization of the fast pulse sequence – for the visualization of the complex, a fast gradient echo sequence with TE = 1.3 ms and TR = 3 ms was used. The slowly relaxing samples (containing the free ligand and trifluoroethanol used as a standard) were best measured using a long turbospin echo sequence employing TE = 40 ms and TR = 2000 ms. For localization of the samples, the ^1H MRI scan (Fig. 4A) was also acquired. Fig. 4 shows the results of the MRI visualization. The brightness of aq. solution of the Ni(II) complex compared to aq. solutions of the free ligand and trifluoroethanol is caused by its paramagnetism, which shortens the T_1 relaxation time of water protons (r_1(complex) = 0.12 mm^{-1} s^{-1}, 4.7 T, 25 °C). As each sample has a different ^{19}F NMR chemical shift (δ_F −26 ppm, −68 ppm and −77 ppm for the complex, free ligand and trifluoroethanol, respectively), each signal can be excited separately. In the case of the fast sequence, only a negligible signal of the free ligand was detected, as virtually no diamagnetic sample relaxation occurs during the sequence time-scale. On the contrary, in the experiment employing the long sequence, no signal of the paramagnetic sample was found as its magnetization relaxes before the start of acquisition.

The samples of free ligand **1** and *cis*-[Ni(**1**)(H_2O)$_2$](ClO_4)$_2$ show fully concordant behaviour (Fig. S9†).

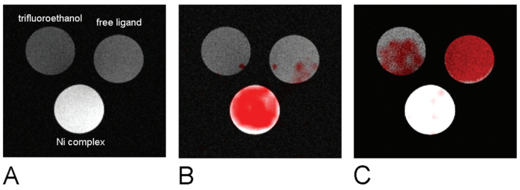

Fig. 4 MRI study of phantoms containing trifluoroethanol, free H_4te2p-tfe$_2$ and the *trans*-[Ni(te2p-tfe$_2$)]$^{2-}$ complex (c_F = 0.004 M in all samples), B = 4.7 T, 25 °C, home-made $^1H/^{19}F$ surface single loop coil. (A) ^1H MRI scan, gradient echo sequence, flip angle 30°, TE = 3.7 ms, TR = 100 ms, matrix 256 × 256. (B) Overlay of ^1H MRI with ^{19}F MRI; ^{19}F MRI was optimized for the complex; acquired at δ = −26 ppm, gradient echo sequence, TE = 1.3 ms, TR = 3 ms, matrix 32 × 32 interpolated to 256 × 256. (C) Overlay of ^1H MRI with ^{19}F MRI; ^{19}F MRI was optimized for the ligand; acquired at δ = −77 ppm, turbospin echo sequence, TE = 40 ms, TR = 2000 ms, matrix 32 × 32 interpolated to 256 × 256.

In conclusion, transition metal ion complexes of fluorine-containing ligands can be considered a new class of ^{19}F MRI contrast agents, as shown in the case of Ni(II). The presence of strongly complexing and electron donating phosphonates enhances the kinetic inertness of the studied complexes and compensates the disadvantageous coordination properties of fluorine-containing ligands. Relaxation parameters of the *trans*-[Ni(te2p-tfe$_2$)]$^{2-}$ complex with fluorine atoms located about 5 Å from the Ni(II) centre are highly suitable for ^{19}F MRI hot-spot imaging employing fast pulse sequences. As the Ni(II) complexes with coordinated water molecules exhibit useful water proton T_1-relaxivity, properly designed compounds could be potentially used as dual $^1H/^{19}F$ MRI contrast agents.[29]

The work was supported by the Czech Science Foundation (P207-11-1437) and by the project of the Ministry of Health, Czech Republic, for development of research organization IN00023001 (Institutional support, Institute for Clinical and Experimental Medicine). We thank Z. Böhmová and J. Hraníček for potentiometric and AAS measurements, respectively.

Table 1 ^{19}F NMR relaxation times[a] and ^1H relaxivity of the studied compounds (pH 7, 25 °C)

Parameter	1	*cis*-[Ni(**1**)(H_2O)$_2$]$^{2+}$	H_4te2p-tfe$_2$	*trans*-[Ni(te2p-tfe$_2$)]$^{2-}$
B_0 = 7.05 T (300 MHz for ^1H, 282 MHz for ^{19}F)				
$T_1(^{19}F)$	0.8(3) s	1.72(1) ms	0.5(1) s	2.8(7) ms
$T_2^*(^{19}F)$	≈76 ms	≈0.82 ms	≈50 ms	≈0.90 ms
$T_2^*/T_1(^{19}F)$	0.1	0.48	0.1	0.32
$r_1(^1H)$	—	0.83(3)	—	0.18(1)
B_0 = 4.70 T (200 MHz for ^1H, 188 MHz for ^{19}F)				
$T_1(^{19}F)$	0.82(1) s	1.2(1) ms	1.1(2) s	4.2(1.1) ms
$T_2^*(^{19}F)$	3.1(1) ms	0.62(1) ms	3.1(2) ms	1.1(1) ms
T_2^*/T_1	0.0038	0.52	0.0028	0.26
$r_1(^1H)$	—	0.66(4) s^{-1} mM^{-1}	—	0.12(2) s^{-1} mM^{-1}

[a] T_1 was determined using inversion recovery pulse sequence; T_2^* was determined from line-width using Lorentzian-shape fitting of the signal.

References

1 *The Chemistry of Contrast Agents in Medical Magnetic Resonance Imaging*, ed. A. Merbach, L. Helm and É. Tóth, Wiley, Hoboken, 2nd edn, 2013.

2 P. Caravan, J. J. Ellison, T. J. McMurry and R. B. Lauffer, *Chem. Rev.*, 1999, **99**, 2293–2352; P. Hermann, J. Kotek, V. Kubíček and I. Lukeš, *Dalton Trans.*, 2008, 3027–3047; C. F. G. C. Geraldes and S. Laurent, *Contrast Media Mol. Imaging*, 2009, **4**, 1–23.

3 J. Ruiz-Cabello, B. P. Barnett, P. A. Bottomley and J. W. M. Bulte, *NMR Biomed.*, 2011, **24**, 114–129.

4 J. C. Knight, P. G. Edwards and S. J. Paisey, *RSC Adv.*, 2011, **1**, 1415–1425.

5 J.-X. Yu, R. R. Hallac, S. Chiguru and R. P. Mason, *Prog. Nucl. Magn. Reson. Spectrosc.*, 2013, **70**, 25–49.

6 I. Tirotta, V. Dichiarante, C. Pigliacelli, G. Cavallo, G. Terraneo and F. B. Bombelli, *Chem. Rev.*, 2015, **115**, 1106–1129.

7 S. Temme, F. Boenner, J. Schrader and U. Floegel, *Wiley Interdiscip. Rev.: Nanomed. Nanobiotechnol.*, 2012, **4**, 329–343.

8 E. T. Ahrens and J. Zhong, *NMR Biomed.*, 2013, **26**, 860–871.

9 Y. B. Yu, *Wiley Interdiscip. Rev.: Nanomed. Nanobiotechnol.*, 2013, **5**, 646–661.

10 D. Bartusik and B. Tomanek, *Adv. Drug Delivery Rev.*, 2013, **65**, 1056–1064.

11 H. Amiri, M. Srinivas, A. Veltien, M. J. van Uden, I. J. M. de Vries and A. Heerschap, *Eur. J. Radiol.*, 2015, **25**, 726–735.

12 (*a*) P. K. Senanayake, A. M. Kenwright, D. Parker and S. K. van der Hoorn, *Chem. Commun.*, 2007, 2923–2925; (*b*) A. M. Kenwright, I. Kuprov, E. De Luca, D. Parker, S. U. Pandya, P. K. Senanayake and D. G. Smith, *Chem. Commun.*, 2008, 2514–2516; (*c*) K. H. Chalmers, E. De Luca, N. H. M. Hogg, A. M. Kenwright, I. Kuprov, D. Parker, M. Botta, J. I. Wilson and A. M. Blamire, *Chem. – Eur. J.*, 2010, **16**, 134–148; (*d*) K. H. Chalmers, M. Botta and D. Parker, *Dalton Trans.*, 2011, **40**, 904–913; (*e*) P. Harvey, I. Kuprov and D. Parker, *Eur. J. Inorg. Chem.*, 2012, 2015–2022; (*f*) P. Harvey, K. H. Chalmers, E. De Luca, A. Mishra and D. Parker, *Chem. – Eur. J.*, 2012, **18**, 8748–8757; (*g*) E. De Luca, P. Harvey, K. H. Chalmers, A. Mishra, P. K. Senanayake, J. I. Wilson, M. Botta, M. Fekete, A. M. Blamire and D. Parker, *J. Biol. Inorg. Chem.*, 2014, **19**, 215–227.

13 K. H. Chalmers, A. M. Kenwright, D. Parker and A. M. Blamire, *Magn. Reson. Med.*, 2011, **66**, 931–936.

14 E. Belorizky, P. H. Fries, L. Helm, J. Kowalewski, D. Kruk, R. R. Sharp and P.-O. Westlund, *J. Chem. Phys.*, 2008, **128**, 052315.

15 A. O. Olatunde, S. J. Dorazio, J. A. Spernyak and J. R. Morrow, *J. Am. Chem. Soc.*, 2012, **134**, 18503–18505.

16 W. Curran and R. Angier, *J. Org. Chem.*, 1966, **31**, 3867–3868.

17 X. Sun, M. Wuest, Z. Kovács, A. D. Sherry, R. Motekaitis, Z. Wang, A. E. Martell, M. J. Welch and C. J. Anderson, *J. Biol. Inorg. Chem.*, 2003, **8**, 217–225.

18 C. E. McKenna, M. T. Higa, N. H. Cheung and M.-C. McKenna, *Tetrahedron Lett.*, 1977, **18**, 155–158.

19 B. Bosnich, C. K. Poon and M. Tobe, *Inorg. Chem.*, 1965, **4**, 1102–1108.

20 (*a*) K. R. Adam, I. M. Atkinson and L. F. Lindoy, *Inorg. Chem.*, 1997, **36**, 480–481; (*b*) M. Zimmer, *Coord. Chem. Rev.*, 2001, **212**, 133–163.

21 M. A. Donnelly and M. Zimmer, *Inorg. Chem.*, 1999, **38**, 1650–1658.

22 J. Kotek, P. Vojtíšek, I. Císařová, P. Hermann and I. Lukeš, *Collect. Czech. Chem. Commun.*, 2001, **66**, 363–381.

23 J. Kotek, P. Hermann, I. Císařová, J. Rohovec and I. Lukeš, *Inorg. Chim. Acta*, 2001, **317**, 324–330.

24 J. Havlíčková, H. Medová, T. Vitha, J. Kotek, I. Císařová and P. Hermann, *Dalton Trans.*, 2008, 5378–5386.

25 J. Kotek, P. Vojtíšek, I. Císařová, P. Hermann, P. Jurečka, J. Rohovec and I. Lukeš, *Collect. Czech. Chem. Commun.*, 2000, **65**, 1289–1316.

26 I. Svobodová, J. Havlíčková, J. Plutnar, P. Lubal, J. Kotek and P. Hermann, *Eur. J. Inorg. Chem.*, 2009, 3577–3592.

27 I. Svobodová, P. Lubal, J. Plutnar, J. Havlíčková, J. Kotek, P. Hermann and I. Lukeš, *Dalton Trans.*, 2006, 5184–5197.

28 J. Kotek, P. Lubal, P. Hermann, I. Císařová, I. Lukeš, T. Godula, I. Svobodová, P. Táborský and J. Havel, *Chem. – Eur. J.*, 2003, **9**, 233–248.

29 M. Wolters, S. G. Mohades, T. M. Hackeng, M. J. Post, M. E. Kooi and W. H. Backes, *Invest. Radiol.*, 2013, **48**, 341–350.

Electronic Supplementary Material (ESI) for Dalton Transactions.

Electronic Supporting Information
for

Nickel(II) complexes of *N*–CH_2CF_3 cyclam derivatives as contrast agents for ^{19}F magnetic resonance imaging

Jan Blahut,[a] Petr Hermann,[a] Andrea Gálisová,[b] Vít Herynek,[b] Ivana Císařová,[b] Zdeněk Tošner,[c] Jan Kotek[a]*

[a] Department of Inorganic Chemistry, Faculty of Science, Charles University (Univerzita Karlova), Hlavova 2030, 128 43 Prague 2, Czech Republic. Tel.: +420-22195-1261. Fax: +420-221951253. E-mail: modrej@natur.cuni.cz.

[b] Department of Radiodiagnostic and Interventional Radiology, Magnetic Resonance Unit, Institute for Clinical and Experimental Medicine, Vídeňská 1958/9, Prague 4, 140 21 Czech Republic.

[c] NMR laboratory, Faculty of Science, Charles University (Univerzita Karlova), Hlavova 2030, 128 43 Prague 2, Czech Republic.

Contents

General experimental conditions

The 1,8-dibenzylcyclam (*trans*-Bn_2cyclam) hydrochloride was prepared by published method.[1] Paraformaldehyde was filtered from aged aqueous solutions of formaldehyde (Lachema) and was dried in a desiccator over conc. H_2SO_4. Cyclam (CheMatech) and other chemicals from commercial sources were used as received. NMR spectra were recorded on the VNMRS300, Varian^{UNITY} *INOVA* 400 or Bruker Avance III 600 spectrometers using 5-mm sample tubes. NMR chemical shifts are given in ppm and coupling constants are reported in Hz. Unless stated otherwise, all NMR spectra were collected at 25 °C. For the ^1H and $^{13}C\{^1H\}$ NMR measurements in D_2O, *t*-BuOH was used as internal standard ($\delta_H = 1.25$, $\delta_C = 30.29$). The pD in D_2O solution was calculated by +0.4 correction to reading of calibrated pH-electrode. For the measurements in $CDCl_3$, TMS was used as internal standard ($\delta_H = 0.00$, $\delta_C = 0.00$). For other solvents used for ^1H and ^{13}C NMR measurements, signals of (residual) non/semi-deuterated solvents were used.[2] For ^{31}P NMR measurements, 70 % aq. H_3PO_4 was used as external reference ($\delta_P = 0.00$). For ^{19}F NMR measurements, trifluoracetic acid (TFA, 0.1 M in D_2O, $\delta_F = -76.55$ ppm, external standard), perfluorobenzene (PFB, $\delta_F = -164.9$ ppm) or 2,2,2-trifluoroethanol (TfeOH, $\delta_F = -77.0$ ppm) were used as internal standards. Abbreviations s (singlet), t (triplet), q (quartet), m (multiplet) and b (broad) are used in order to express the signal multiplicities. All ^{13}C NMR spectra were measured using a broad-band ^1H decoupling. Longitudinal relaxation times T_1 were measured using inversion recovery sequence with spectrometer offset identical to compound signal and properly calibrated pulse length. Relaxation times T_2* were estimated from signal half-width. The positive or negative ESI-MS spectra were acquired on the Bruker ESQUIRE 3000 spectrometer with ion-trap detection. Thin-layer chromatography (TLC) was performed on TLC aluminium sheets with silica gel 60 F254 (Merck). For the detection, UV, ninhydrin spray (0.5 % in EtOH), dipping of the sheets in 5 % aq. $CuSO_4$ or I_2 vapour exposition were used. Elemental analyses were performed at the Institute of Macromolecular Chemistry (Academy of Sciences of the Czech Republic, Prague). AAS was measured employing spectrometer AAS 3 (Zeiss-Jena) with acetylene-air flame atomization. Throughout the paper, pH means –log[H^+].

Ligands syntheses

The syntheses of ligands it overviewed in Scheme S1.

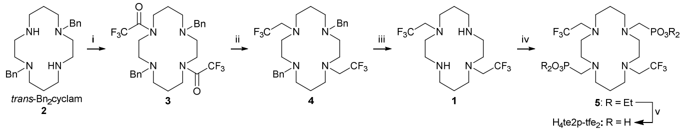

Scheme S1 (*i*) trifluoroacetic anhydride (4 eq.), Et_3N (5 eq.), dry $CHCl_3$, room temperature (RT), 3 h; (*ii*) $NaBH_4$ (10 eq.), $BF_3{\cdot}Et_2O$ (10 eq.), dry diglyme, 120 °C, 12 h; (*iii*) 10 % Pd/C, H_2 (balloon), AcOH/EtOH/H_2O (1/5/4, v/v/v), 40 °C, 24 h; (*iv*) neat $P(OEt)_3$, $(CH_2O)_n$, 70 °C, 12 h; (*v*) (1) trimethylsilylbromide (=TMSBr; 20 eq.), dry acetonitrile, RT, 12 h; (2) H_2O excess, RT.

1,8-bis(trifluoroacetyl)-4,11-dibenzyl-1,4,8,11-tetraazacyclotetradecane, 3

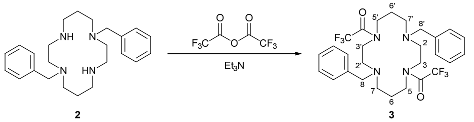

Trans-Bn_2cyclam hydrochloride (**2**·4HCl·4H_2O, 1.00 g, 1.7 mmol) was suspended in 5 % aq. NaOH (75 ml) and extracted three times with $CHCl_3$ (75 ml). The organic phases were unified and dried using anhydrous Na_2SO_4 and the solvent was removed *in vacuo*. Amine free base was dissolved in anhydrous $CHCl_3$ (50 ml) and trifluoroacetic anhydride (930 µl, 6.4 mmol, 4 eq.) and dry triethylamine (1.1 ml, 8.0 mmol, 5 eq.) were added. The mixture was stirred at room temperature for 3 h. Volatiles were evaporated *in vacuo* and product was purified by crystallization from hot EtOH yielding compound **3** as white solid (750 mg, 78 %).

NMR spectra of compound **3** at 25 °C are complicated by a relative rigidity of amide groups which results in three possible conformers. In one of them, the atom with and without apostrophe (below) are not chemically equivalent. Therefore, for each carbon atom, four signals are expected. Some of them are overlaid by random coalescence. However, measurement at elevated temperature up to 80 °C did not lead to better resolution; at this temperature, signals are very broad due to their coalescence. For VT-NMR spectra, see Figure S1.

TLC: $R_f = 0.7$ (conc. aq. NH_3/EtOH = 1/50).

NMR: ^1H (600 MHz; DMSO-d_6): 1.70–1.81 and 1.81–1.92 (2×bm, 4H, H6 and H6’); 2.40, 2.44, 2.47 (3×t, 4H, H7 and H7’, $^3J_{HH} = 6.0$, $^3J_{HH} = 6.4$, $^3J_{HH} = 6.4$); 2,59 and 2,65 (2×t, 4H, H2 and H2’); 3.46–3.60

(bm, 12H, H3, H3’, H5, H5’, H8 and H8’); 6.96–7.72 (bm, 10H, phenyl). ^{13}C (151 MHz; DMSO-d_6): 23.8, 23.9, 25.8 and 26.0 (4×s, C6 and C6’); 45.8, 45.9, 46.2-bs, 46.3, 46.4, 46.9, 47.0 (7×s and bs, C3, C3’, C5 and C5’); 50.7, 51.0, 51.2-bs, 51.47, 51.52, 51.7, 52.6 (7×s and bs, C2, C2’,C7, C7’); 59.1 59.2, 59.5, 59.6 (4×s, C8 and C8’); 116.3 (q, CF_3, $^1J_{CF}$ = 288); 127.0, 127.1, 128.1, 128.6, 128.8, 129.0 (6×s, phenyl C–H); 138.6-bs, 138.9, 139.0 (bs and 2×s, phenyl q-C); 155.4, 155.5, 155.6 (3×q, C=O and C’=O, $^2J_{FC}$ = 35). ^{19}F (282 MHz; DMSO-d_6): –78.37, –70.45, –70.48, –70.51. ^{19}F (282 MHz; DMSO-d_6; 80 °C): –70.31.

MS(+): 573.3 (calc. 573.3, [**3**+H]$^+$).

Elem. anal.: found C 58.32; H 6.17; N 9.55 (calc. for $C_{28}H_{34}N_4F_6O_2$, M_r = 572.6; C, 58.73; H, 5.99; N, 9.78).

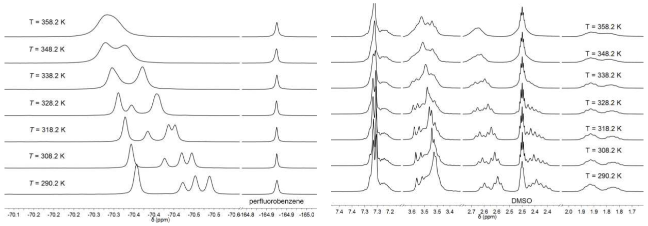

A B

Figure S1 NMR spectra of compound **3** acquired at different temperatures. (A): ^{19}F NMR. (B): ^1H NMR.

1,8-bis(2,2,2-trifluoroethyl)-4,11-dibenzyl-1,4,8,11-tetraazacyclotetradecane, 4

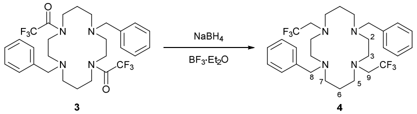

In three-necked flask, $NaBH_4$ (4.6 g, 122 mmol, 10 eq.) and **3** (7.0 g, 12.2 mmol) were suspended in anhydrous diglyme (100 ml) under Ar-atmosphere. Then, $BF_3·Et_2O$ (14 ml, 122 mmol, 10 eq.) diluted by anhydrous diglyme (100 ml) was added dropwise under gentle stream of argon. B_2H_6 in escaping gas was removed by bubbling through 5 % NaOH in 10 % aq. H_2O_2. The reaction mixture was stirred at 120 °C overnight. After cooling, 12 % aq. HCl (10 ml) was added dropwise. The volatiles were evaporated *in vacuo*. Crude product was dissolved in 5 % aq. NaOH (100 ml) and extracted into $CHCl_3$ (3×100 ml). Combined organic layers were dried using anhydrous Na_2SO_4 and evaporated and product **4** was crystallized as a white solid from hot $CHCl_3$ (5.1 g, 76 %).

TLC: R_f = 0.8 (MeOH).

NMR: ^1H (400 MHz; $CDCl_3$): 1.67 (p, 4H, H6, $^3J_{HH}$ = 6.8); 2.51 (t, 4H, H7, $^3J_{HH}$ = 7.0); 2.57 (t, 4H, H2, $^3J_{HH}$ = 6.2); 2.68 (t, 4H, H5, $^3J_{HH}$ = 6.9); 2.77 (t, 4H, H3, $^3J_{HH}$ = 6.0); 2.92 (q, 4H, H9, $^3J_{HF}$ = 9.6); 3.52 (s, 4H, H8); 7.17–7.41 (bm, 10H, phenyl). ^{13}C (151 MHz; $CDCl_3$; 25): 24.9 (s,C6); 51.2 (bs, C7 and C2); 52.2 (s, C3); 52.5 (s, C5); 55.3 (q, C9, $^2J_{CF}$ = 30); 59.5 (s, C8); 126.1 (q, CF_3, $^1J_{CF}$ = 282); 127.1, 128.3, 129.2, 140.0 (s, phenyl). ^{19}F (282 MHz; $CDCl_3$): –72.5(bs).

MS(+): 545.3 (calc. 545.3, [**4**+H]$^+$).

Elem. anal.: found C 61.50; H 7.15; N 9.98 (calc. for $C_{28}H_{38}N_4F_6$, M_r = 544.6; C, 61.75; H, 7.03; N, 10.29).

1,8-bis(2,2,2-trifluoroethyl)-1,4,8,11-tetraazacyclotetradecane, 1

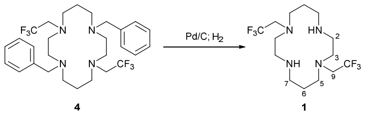

Compound **4** (4.0 g, 7.4 mmol) was dissolved in AcOH/EtOH/H_2O mixture (1/5/4 v/v, 100 ml) and 10 % Pd/C (200 mg) was added. The flask was evacuated, filled with hydrogen and the mixture was stirred under hydrogen atmosphere (balloon) at 40 °C for 24 h. The catalyst was filtered off, and the filtrate was evaporated to dryness, co-evaporated with 35 % aq. HCl (10 ml) and the residue was triturated with EtOH. Yield 2.4 g (65 %).

TLC: R_f = 0.1 (conc. aq. NH_3/EtOH = 1/50).

NMR: ^1H (600 MHz; D_2O; pD = 3.1): 1.89–2.05 (bm, 4H, H6); 2.92 (bt, 4H, H7, $^3J_{HH}$ = 5.6); 3.08 (bm, 4H, H2); 3.35 (bs, 4H, H3); 3.38 (q–partially overlapped with other signals, 4H, H9, $^3J_{HF}$ = 9.8); 3.41 (t, 4H, H5, $^3J_{HH}$ = 6.4). ^{13}C (151 MHz; D_2O; pD = 3.1): 23.7 (s, C6); 45.7 (s, C3); 47.7 (s, C5); 52.5 (s, C2); 53.5 (s, C7); 53.9 (q, C9, $^2J_{CF}$ = 30); 126.5 (q, CF_3, $^1J_{CF}$ = 282). ^{19}F (282 MHz; D_2O; pD = 3.1): –64.9 (t, $^3J_{HF}$ = 9.4).

MS(+): 365.2 (calc. 365.2, [**1**+H]$^+$).

Elem. anal.: found C 32.64; H 5.91; N 10.56; Cl 28.40 (calc. for **1**·4HCl, M_r = 473.8; C, 32.96; H, 5.93; N, 10.98; Cl, 27.79).

Single crystals of **1**·2HCl·$2H_2O$ suitable for X-ray diffraction analysis were prepared by slow evaporation of diluted aqueous solution of **1**·4HCl.

1,8-bis(diethoxyphosphorylmethyl)-4,11-bis(trifluoroethyl)-1,4,8,11-tetraazacyclotetradecane, 5

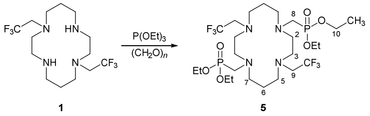

Compound **1**·4HCl (1.00 g, 2.1 mmol) was extracted from 5 % aq. NaOH (50 ml) by $CHCl_3$ (3×50 ml). Organic phases were unified, dried by anhydrous Na_2SO_4 and the solvent was evaporated. Triethyl phosphite (20 ml) and paraformaldehyde (254 mg, 13 mmol, 4 eq.) were added and the mixture in a flask closed by stopper was stirred at 70 °C for 12 h. Unreacted $(CH_2O)_n$ was filtered off and $P(OEt)_3$ was evaporated on rotary evaporator. Crude product was isolated after chromatography on strong cation exchanger (100 ml, H^+-form); impurities were washed off by EtOH (500 ml) and the product was eluted by EtOH/conc. aq. NH_3 = 5/1 mixture (v/v, 250 ml). The crude product was further purified by chromatography (SiO_2, MeOH) affording **5** as a colourless oil.

TLC: R_f = 0.8 (MeOH).

NMR: ^{1}H (300 MHz; MeOH-d_4): 1.29 (d, 12H, CH_3, $^3J_{HH}$ = 7.1); 1.62 (p, 4H, H6, $^3J_{HH}$ = 6.7); 2.72 (bm, 14H, H2, H3, H5, H7); 2.91 (d, 4H, H8, $^2J_{HP}$ = 9.8); 3.14 (q, 4H, H9, $^3J_{HF}$ = 9.9); 4.09 (pseudo-p, 8H, H10, $^3J_{HP} \sim {}^3J_{HH}$ = 7.2). ^{13}C (101 MHz; MeOH-d_4): 16.9 (d, CH_3, , $^4J_{CP}$ = 5.8); 26.0 (s, C6); 51.0 (d, C8, $^1J_{CP}$ = 159); 53.2 (s, C3); 53.6 (s, C5); 53.8 (d, C7, $^2J_{CP}$ = 7); 53.9 (d, C2, $^2J_{CP}$ = 8); 56.2 (q, C9, $^2J_{CF}$ = 30); 63.5 (d, C10, $^2J_{CP}$ = 7); 127.8 (q, CF_3, $^1J_{CF}$ = 281). ^{19}F (282 MHz; MeOH-d_4): –71.0 (t, $^3J_{HF}$ = 9.9). ^{31}P (121 MHz; MeOH-d_4): 27.2 (pseudo-p, $^2J_{HP} \sim {}^3J_{HP}$ = 8.0). ^{31}P{^{1}H} (121 MHz; MeOH-d_4): 27.2 (s).

MS(+): 665.9 (calc. 665.6, [**5**+H]$^+$); 687.9 (calc. 687.3, [**5**+Na]$^+$); 703.9 (calc. 703.3, [**5**+H]$^+$).

1,8-bis(dihydroxyphosphorylmethyl)-4,11-bis(2,2,2-trifluoroethyl)-1,4,8,11-tetraazacyclotetradecane, H_4te2p-tfe$_2$

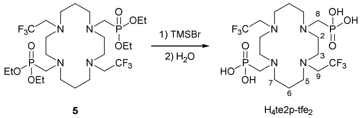

Entire amount of the crude product from the previous reaction was dried by repeated (2×) evaporation with anhydrous MeCN. Dried amine was dissolved in anhydrous MeCN (60 ml) and TMSBr (3.2 ml, 18 mmol, large excess) was added. The reaction mixture was stirred in dark at room temperature overnight. The mixture was evaporated *in vacuo* and the residue was dissolved in MeCN. The solution was added dropwise to water (25 ml). Mixture was evaporated and the residue was dissolved in MeOH and precipitated by addition of Et_2O. The solid was isolated by centrifugation. The product, H_4te2p-tfe$_2$, was isolated in the zwitterionic form after purification on strong cation exchanger (100 ml, H^+-form). Impurities were removed by water (500 ml) and the product was eluted off by 10 % aq. pyridine. Lyophilization affords 842 mg (74 % based on **5**) of white solid. X-ray quality single crystals of H_4te2p-tfe$_2$·4HBr·0.5H_2O were obtained by slow diffusion of aq. ligand solution which was layered over conc. aq. HBr.

NMR: ^{1}H (300 MHz; D_2O; pD = 6.3): 2.00 (bs, 4H, H6); 2.86 (bs, 4H, H5); 3.12 (s, 4H, H3); 3.17 (d, 4H, H8, $^2J_{HP}$ = 11.3); 3.32 (q, 4H, H9, $^3J_{HF}$ = 9.4); 3.66 (bs, 8H, H2 and H7). ^{13}C (151 MHz; D_2O; pD = 6.3): 23.3 (s, C6); 50.5 (s, C3); 53.0 (d, C8, $^1J_{CP}$ = 127); 53.5 (s, C5); 53.9 (s, C2); 54.2 (q, C9, $^2J_{CF}$ = 31); 55.3 (s, C7); 126.6 (q, CF_3, $^1J_{CF}$ = 282). ^{19}F (376 MHz; D_2O; pD = 6.3): –68.9 (t, $^3J_{HF}$ = 9.3). ^{31}P{^{1}H} (162 MHz; D_2O; pD = 6.3): 6.2 (bs).

MS(–): 550.5 (calc. 551.2, [M–H]$^-$); (+): 552.6 (calc. 553.2, [M+H]$^+$).

Elem. anal.: found C 32.46; H 5.85; N 9.52; P 10.53 (calc. for H_4te2p-tfe$_2$·2H_2O, M_r = 588.4; C, 32.66; H, 6.17; N, 9.52; P 10.53).

Complex syntheses

***cis*-[Ni(1)(Cl)$_2$]**

Ligand hydrochloride (**1**·4HCl, 50 mg, 0.1 mmol) was mixed with $Ni(ClO_4)_2$ (42 mg, 0.11 mmol, 1.1 eq) in 3 ml of water (pH adjusted to 6.9 by diluted aq. NaOH). After ca 1 d at 60 °C, a violet precipitate appeared. The mixture was heated for 6 d at the same temperature to complete the reaction.

Further heating of the undisturbed reaction mixture (in flame-sealed ampoule) at 105 °C for 7 d yielded light green single crystals of *cis*-[Ni(**1**)Cl$_2$]. The same compound was obtained also when aqueous solution of *cis*-[Ni(**1**)(H_2O)$_2$](ClO_4)$_2$ (prepared as mentioned below) was layered over 5 % aq. NaCl and the mixture was left at room temperature for 2 d.

***cis*-[Ni(1)(H$_2$O)$_2$](ClO$_4$)$_2$**

Ligand as **1**·4HCl (200 mg, 0.42 mmol) was dissolved in 5 % aq. NaOH (25 ml) and the solution was extracted with $CHCl_3$ (3×25 ml). Organic phases were combined and evaporated to dryness. Free base **1** was dissolved in MeOH (5 ml). To this solution, a solution of $Ni(ClO_4)_2$·6H_2O (115 mg, 0.31 mmol, 0.75 eq.) in water (5 ml) was added. The mixture was stirred in an opened vial placed in oil bath heated to 80 °C for 4 d; during this time, the volume was gradually reduced as MeOH evaporated, and some distilled water was added several times to keep volume of the reaction mixture ~3–5 ml. The mixture was filtered through 0.1-µm syringe filter. Absence of free Ni(II) was proved by negative reaction with 1 % dimethylglyoxime in EtOH. The solution was evaporated *in vacuo* and the residue was dissolved in water (10 ml, final pH ~7.4) and the solution was extracted with $CHCl_3$ (8×10 ml) to remove excess of free ligand (controlled by ^{19}F NMR). The complex was not isolated and its concentration in this stock aq. solution was determined by means of AAS. Any attempts to grow single crystals were unsuccessful.

TLC: decomposition (see below).

NMR: Only extremely broad signals and no signals were found in ^{1}H NMR and ^{13}C NMR spectra, respectively. ^{19}F (282 MHz, D_2O, pD = 7.62, 25 °C): –26.2, T_1 = 1.72(1) ms, $T_2^* \approx$ 820 µs.

MS(+): 210.8 (calc.211.1 $[Ni(\mathbf{1})]^{2+}$); 420.9 (calc. 421.1 $[Ni(\mathbf{1})-H]^{+}$) ; 456.9 (calc. 456.1 $[Ni(\mathbf{1})Cl]^{+}$); 520.8 (calc. 520.1 $[Ni(\mathbf{1})(ClO_4)]^{+}$).

It should be noticed that the *cis*-$[Ni(\mathbf{1})(H_2O)_2]^{2+}$ complex is easily decomposed (transchelation) in diluted aqueous ammonia, even during TLC with ammonia-containing eluents; it points out to a rather low thermodynamic and kinetic stability in ammonia solutions.

Mechanism of the complex formation was followed by ^{19}F NMR by following procedure. Ligand as $\mathbf{1}\cdot 4HCl$ (100 mg, 0.21 mmol) was dissolved in 5 % aq. NaOH (10 ml) and the solution was extracted by $CHCl_3$ (3×10 ml). Organic phases were combined and evaporated. Compound **1** was dissolved in the DMSO (2 ml) and water (1 ml) was added. Approximate concentration of **1** in stock solution (55 mM) was determined by comparison of ^{19}F-NMR signal integral intensity with that of trifluoroethanol (TfeOH) as a standard. In NMR tube, the stock solution of **1** (200 µl, 11 µmol) was mixed with DMSO-d_6 (300 µl) and TfeOH (1 µl). The mixture was heated to 50 °C and ^{19}F-NMR spectrum was measured. Then, 0.2 M aq. $Ni(ClO_4)_2$ (50 µl, 10 µmol, 0.9 equiv.) was quickly added and the reaction was followed by ^{19}F-NMR over 2 h. The spectra were phase-corrected, and 50 Hz exponential apodization and baseline correction were applied. In the NMR experiment, aq. DMSO was chosen as the solvent keeps reaction mixture fully homogeneous even at the starting point. ^{19}F NMR spectral changes during course of the reaction are shown in Figure S2.

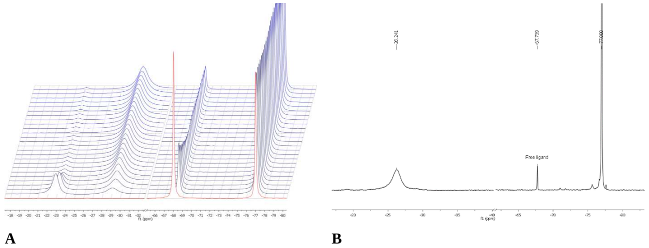

Figure S2 (**A**): Time dependence of ^{19}F NMR spectra during $Ni(ClO_4)_2$–**1** complexation in DMSO:water 6.5:1 mixture at 50 °C (blue lines); red line represents spectrum of the free ligand before $Ni(ClO_4)_2$ addition. As an internal standard, trifluoroethanol was used. (B): ^{19}F NMR spectrum of $[Ni(\mathbf{1})(H_2O)_2](ClO_4)_2$ in water (pH 7.1, 5 mM) with trifluoroethanol as internal standard (δ_F = –77 ppm).

trans-[Ni(1)](ClO₄)₂

Solution of *cis*-$[Ni(\mathbf{1})(H_2O)_2](ClO_4)_2$ (2 ml 0.2 M) was mixed with solution of 18 g $NaClO_4$ in 12 ml water, and the mixture was left for 2 weeks at room temperature. During this period, a red precipitate appeared. The precipitate was isolated by centrifugation.

Single crystals of *trans*-$[Ni(\mathbf{1})](ClO_4)_2$ were prepared by analogous procedure: 1 ml of 50 % $NaClO_4$ was layered with 0.2 ml of 0.05 M *cis*-$[Ni(\mathbf{1})(H_2O)_2](ClO_4)_2$, and the mixture was left undisturbed for 3 weeks.

Isomerization of *trans*-$[Ni(\mathbf{1})(H_2O)_2](ClO_4)_2$ to *cis*-$[Ni(\mathbf{1})(H_2O)_2](ClO_4)_2$ was studied by following way: sample of the red *trans*-$[Ni(\mathbf{1})](ClO_4)_2$ (15 mg) was dissolved in D_2O (0.5 ml) with 1 µl of trifluoroethanol, and time-evaluation of ^{19}F NMR spectra was measured (Figure S3). Consistent values of half-times for this rearrangement process were calculated from single-exponential fit of time-dependences of both signals intensities: $\tau_{½}$ = 3.6(2) h from decrease of *trans*-$[Ni(\mathbf{1})(H_2O)_2]^{2+}$ signal and $\tau_{½}$ = 3.4(1) h from increase of *cis*-$[Ni(\mathbf{1})(H_2O)_2]^{2+}$ signal.

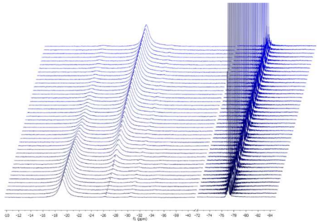

Figure S3 Time dependence of ^{19}F NMR spectra during isomerization of species after dissolution of red *trans*-[Ni(1)](ClO_4)$_2$ in water at 25 °C. As an internal standard, trifluoroethanol was used.

***cis*-[Ni(1)(H_2O)$_2$](OTs)$_2$**

To prepare single crystals of *cis*-[Ni(**1**)(H_2O)$_2$](OTs)$_2$, equimolar amounts of Ni(TsO)$_2$ (47 mg, 0.12 mmol) and free base **1** (freshly prepared from 50 mg, 0.11 mmol of its hydrochloride **1**·4HCl) were mixed in water:MeOH 1:1 mixture (2 ml, native pH 7.5). After short heating at 50 °C, a pink precipitate appeared. The suspension was flame-sealed into ampoule and the mixture was heated at 105 °C for 7 d. During this time, the pink precipitate was transformed to blue bar-like crystals, which were used for X-ray diffraction analysis.

(NH_4){*trans*-[Ni(Hte2p-tfe$_2$)]}

The ligand H_4te2p-tfe$_2$·2H_2O (100 mg, 0.16 mmol) was dissolved in water (5 ml) and $NiCl_2 \cdot 6H_2O$ (47 mg, 0.20 mmol, 1.25 eq.) was added. Solution pH was adjusted to 10 by 5 % aq. NH_3 and the mixture was stirred at 75 °C for 24 h. The complex was purified by column chromatography (SiO_2, 6×3 cm) with EtOH/conc. aq. NH_3 5/1 as mobile phase. Fractions containing pure product were combined, evaporated to dryness and the product was crystallised from minimal amount of water with a drop of 5 % aq. NH_3 by diffusion of acetone. Absence of free Ni(II) was proved by negative reaction with 1 % dimethylglyoxime in EtOH.

Yield 87 mg (75 %).

TLC: $R_f = 0.5$ (EtOH/aq. conc. NH_3 5/1).

NMR: Only extremely broad signals and no signals were found in ^{1}H NMR and ^{13}C/^{31}P NMR spectra, respectively. ^{19}F (282 MHz, D_2O, pD = 6.7, 25 °C): –20.8, $T_1 = 2.32(5)$ ms, $T_2^* \approx 1.3$ ms.

MS(+): 609.7 (calc. 609.1, [Ni{H_3te2p-tfe$_2$}]$^+$); MS(–): 607.5 (calc. 607.1, [Ni{Hte2p-tfe$_2$}]$^-$).

Elem. anal.: found C 28.03; H 5.71; N 10.15 (calc. for (NH_4){*trans*-[Ni(Hte2p-tfe$_2$)]}·3H_2O, $C_{16}H_{41}F_6N_5NiO_9P_2$, $M_r = 681.2$; C, 28.17; H, 6.06; N, 10.27).

Single crystals of (NH_4){*trans*-[Ni(Hte2p-tfe$_2$)]}·3.25H_2O were prepared by acetone vapour diffusion into aq. solution of the complex containing slight excess of ammonia.

The following procedure was used to investigate mechanism of the complex formation by ^{19}F NMR. The ligand, H_4te2p-tfe$_2$, in zwitterionic form (10.6 mg, 17.3 µmol) was dissolved in D_2O (0.5 ml) containing 0.1 % *t*-BuOH and trifluoroethanol (TfeOH, 10 µL) was added. Solution pH was adjusted to 10.0 by adding of 5 % aq. NH_3, reaction mixture was heated to 75 °C and ^{19}F NMR spectrum was measured. Then, $NiCl_2 \cdot 6H_2O$ (4.7 mg, 19.7 µmol, 1.1 eq) in D_2O (100 µL) was added and the reaction progress was followed by ^{19}F NMR over 13.5 h. The spectra were phase-corrected, and 10 Hz exponential apodization and baseline correction were applied. Time-dependence of integral values of signals at $\delta_F = -26.4$ (*trans*-[Ni(te2p-tfe2)]$^{2-}$), –41.1 (intermediate) and –68.3 ppm (te2p-tfe$_2^{4-}$) was analysed using Matlab[3] using first order kinetic equation: $I(t) = A + B \cdot \exp(-k_{obs}t)$, where $I(t)$ are integral values in time, k_{obs} is the first-order rate constant and A and B are parameters characterising initial and final integral values. The results are shown in Figure S4.

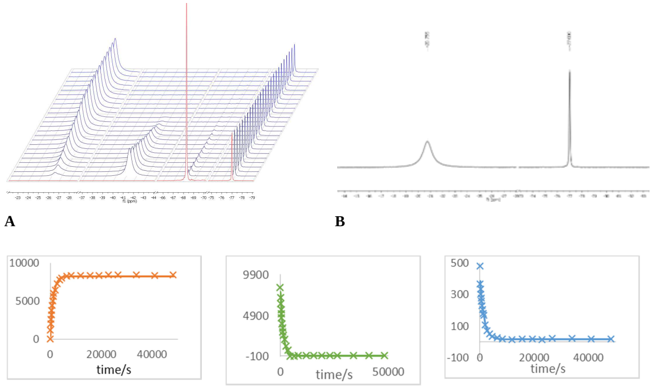

trans-[Ni(te2p-tfe$_2$)]$^{2-}$ Intermediate H_4te2p-tfe$_2$

C

Figure S4 (**A**): Time dependence of ^{19}F NMR spectra during Ni(II)–H_4te2p-tfe$_2$ complexation (blue lines); red line represents spectrum of the free ligand before $NiCl_2$ addition. As an internal standard, trifluoroethanol was used (75 °C, diluted aq. ammonia, pH ~10). (**B**): ^{19}F NMR spectrum of *trans*-[Ni(te2p-tfe$_2$)]$^{2-}$ in water (pH 7.4, 22 mM) with trifluoroethanol as internal standard (δ_F = –77 ppm) (**C**): Time dependences of ^{19}F NMR signal integral intensities (×) and fits (solid lines) using general equation $I(t) = A + B\cdot\exp(-k_{obs}t)$, where $I(t)$ are signal integral intensities at time t, k_{obs} is the first-order rate constant and A and B are scale factors characterising initial and final intensities. Values of the rate constants k_{obs} are following: decrease in concentration of the free ligand $^{lig}k_{obs} = 0.71(3)\cdot10^{-3}$ s^{-1}, decrease in concentration of the intermediate $^{int}k_{obs} = 0.85(8)\cdot10^{-3}$ s^{-1}, increase of concentration of the final product $^{cplx}k_{obs}$ = $0.89(7)\cdot10^{-3}$ s^{-1}.

X-ray diffraction

The selected crystals were mounted on a glass fibre in random orientation and the diffraction data were acquired at 150(1) K (Cryostream Cooler Oxford Cryosystem) using Mo-K_α radiation (λ = 0.71073 Å). The diffraction data were collected employing ApexII CCD diffractometer and analysed using the SAINT V8.27B (Bruker AXS Inc., 2012) program package. The structure was solved by direct methods (SHELXS97)[4] and refined by full-matrix least-squares techniques (SHELXL97)[5]. Absorption correction using Gaussian integration was applied.[6] All non-hydrogen atoms were refined anisotropically. Although hydrogen atoms were found in the electron difference map, they were fixed in original (those bound to nitrogen and oxygen atoms) or theoretical (those belonging to carbon atoms) positions using riding model with $U_{eq}(H) = 1.2\ U_{eq}(X)$ to keep a number of refined parameters low.

For compound **4**·2HCl·2H_2O, the ligand molecule lies on centre of symmetry, *i.e.* the independent unit consists from one half of formula unit. In the case of H_4te2p-tfe$_2$·4HBr·0.5H_2O, the independent unit consists from two halves of ligand molecules laying on symmetry centres and four bromide anions. In addition, a number of several low-intensity maxima in electron difference map points to a disordered solvate. It was attributed to 0.5 water molecule and squeezed off using PLATON.[7] The independent unit of *cis*-[Ni(**1**)(H_2O)$_2$](TsO)$_2$ is formed by whole molecular formula. For *cis*-[Ni(**1**)Cl_2], the molecule possess two-fold symmetry, with one half of the molecule as an independent unit. Electron map difference maxima close to fluorine atoms point to a disorder in trifluoromethyl group. This was best refined as staggered in two positions with fixed relative occupancy 95:5 and with isotropic refinement of atoms in the less-occupied positions. In the case of *trans*-[Ni(**1**)](ClO_4)$_2$, one half of centrosymmetric complex molecule and one perchlorate anion forms the independent unit. In the case of (NH_4){*trans*-[Ni(Hte2p-tfe$_2$)]}·3.25H_2O, the independent unit is formed by whole molecular formula. Water solvate molecules were best refined as disordered in several positions, making in total 3.25 molecules. Selected experimental data are listed in Table S1, and selected geometric parameters are listed in Table S2 and Table S3. Relevant data for the structures have been deposited at the Cambridge Crystallographic Data Centre.

Table S1 Experimental data for the reported crystal structures.

Parameter	$\mathbf{1}\cdot 2HCl\cdot 2H_2O$	H_4te2p-tfe$_2\cdot 4HBr\cdot 0.5H_2O$	*cis*-[Ni(**1**)(H_2O)$_2$](TsO)$_2$	*cis*-[Ni(**1**)Cl$_2$]	*trans*-[Ni(**1**)](ClO$_4$)$_2$	*trans*-(NH$_4$)[Ni(Hte2p-tfe$_2$)]$\cdot$3.25H_2O
Formula	$C_{14}H_{32}Cl_2F_6N_4O_2$	$C_{16}H_{37}Br_4F_6N_4O_{6.5}P_2$	$C_{28}H_{44}F_6N_4NiO_8S_2$	$C_{14}H_{26}Cl_2F_6N_4Ni$	$C_{14}H_{26}Cl_2F_6N_4NiO_8$	$C_{16}H_{39.5}F_6N_5NiO_{9.25}P_2$
M_r	473.34	885.08	801.50	494.00	622.00	684.68
Colour	colourless	colourless	light blue	light blue green	red	light blue
Habit	prism	prism	bar	prism	prism	bar
Crystal system	monoclinic	triclinic	orthorhombic	monoclinic	triclinic	monoclinic
Space group	$P2_1/n$	P–1	P*bca*	C2/*c*	P–1	$P2_1/n$
a [Å]	9.5863(6)	7.3372(2)	8.7262(3)	22.2787(9)	8.2589(8)	9.4281(4)
b [Å]	9.4059(7)	11.5789(3)	25.5904(15)	6.4382(3)	8.5203(7)	16.7420(7)
c [Å]	11.7418(8)	17.6946(4)	30.9247(18)	16.0685(7)	9.2443(8)	17.0428(6)
α [°]	90	85.446(1)	90	90	71.903(4)	90
β [°]	105.367(2)	88.825(1)	90	122.852(1)	68.416(3)	90.310(1)
γ [°]	90	80.982(1)	90	90	72.718(3)	90
V [Å^3]	1020.88(12)	1479.96(6)	6905.7(6)	1936.19(15)	562.54(9)	2690.09(19)
Z	2	2	8	4	1	4
$D_{calcd.}$ [g cm^{-3}]	1.540	1.986	1.542	1.695	1.836	1.691
μ [mm^{-1}]	0.390	5.625	0.768	1.341	1.200	0.938
Unique refl.	2354	6780	6742	2232	1490	6159
Obsd. refl. [$I > 2\sigma(I)$]	2157	5621	4408	1973	1080	4968
R; R' [$I > 2\sigma(I)$]	0.0324; 0.0354	0.0268; 0.0381	0.0563; 0.1029	0.0385; 0.0448	0.0498; 0.0775	0.0322; 0.0476
wR; wR' [$I > 2\sigma(I)$]	0.0787; 0.0814	0.0561; 0.0581	0.1060; 0.1212	0.0951; 0.0984	0.1168; 0.1331	0.0735; 0.0803
CCDC	1430241	1430242	1430240	1430237	1430238	1430239

Solid-state structure of $\mathbf{1\cdot 2HCl\cdot 2H_2O}$

Structure of the $(H_2\mathbf{4})^{2+}$ cation adopts common[8] conformation of diprotonated cyclam derivatives. It is stabilized by intramolecular hydrogen bond between protonated and unprotonated amino group ($d_{N\cdots N}$= 2.99 and 3.01 Å) as shown in Figure S5. The structure confirms higher basicity of secondary amino groups comparing to tertiary ones.

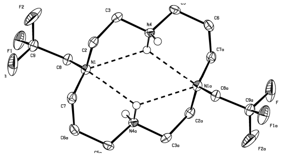

Figure S5 Molecular structure of the $(H_2\mathbf{1})^{2+}$ cation found in the crystal structure of $\mathbf{1}\cdot 2HCl\cdot 2H_2O$. Intramolecular hydrogen bonds are dashed. Carbon-bound hydrogen atoms are omitted for clarity.

Solid-state structure of $\mathbf{H_4te2p\text{-}tfe_2\cdot 4HBr\cdot 0.5H_2O}$

Fully protonated ligand molecule, $(H_8te2p\text{-}tfe_2)^{4+}$, found in the crystal structure of $H_4te2p\text{-}tfe_2\cdot 4HBr\cdot 0.5H_2O$, adopts rectangular conformation (3,4,3,4)-A[8] with nitrogen atoms in the corners (Figure S6A). It is the most frequently observed conformation of the fully protonated polyazamacrocycles.[8] The two independent ligand molecules exhibit almost identical geometric parameters of the macrocycle, but differ in orientation of pendant substituents (Figure S6B).

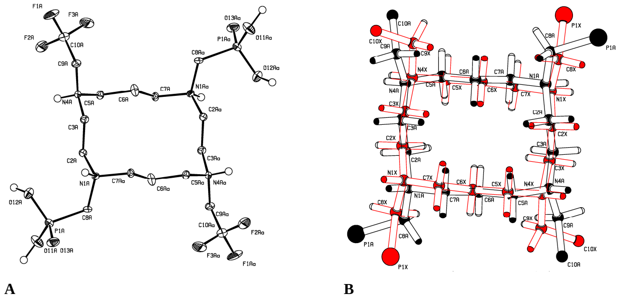

Figure S6 (A): Molecular structure of cation $(H_8te2p\text{-}tfe_2)^{4+}$ found in the crystal structure of $H_4te2p\text{-}tfe_2\cdot 4HBr\cdot 0.5H_2O$. One of two independent ligand molecules is shown. Carbon-bound hydrogen atoms are omitted for clarity. (B): Overlay of two independent ligand molecules. Only pivot atoms of pendant substituents are shown.

Solid-state structure of *cis*-[Ni(1)Cl$_2$]

Two-fold symmetric molecule of *cis*-[Ni(**1**)Cl$_2$] shows slightly distorted octahedral sphere with macrocyclic ligand in *cis*-V configuration, with central Ni(II) on laying slightly "out" of the macrocycle (angle N1-Ni-N1$^{\#}$ = 171°) (Figure S7). Coordination bonds from tertiary amino groups are significantly longer (2.26 Å) comparing to those between the central metal ion and secondary amino groups (2.10 Å).

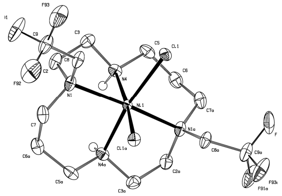

Figure S7 Molecular structure of *cis*-[Ni(**1**)Cl$_2$] found in its crystal structure. Carbon-bound hydrogen atoms are omitted for clarity.

Selected geometric parameters of Ni(II) coordination spheres found in the solid-state structures

Table S2 Coordination geometry of Ni(II) cation in the prepared complexes.

Parameter	*cis*-[Ni(**1**)(H_2O)$_2$](TsO)$_2$^{a}	*cis*-[Ni(**1**)Cl$_2$]^b	*trans*-[Ni(**1**)](ClO$_4$)$_2$^{c}	(NH$_4$){*trans*-[Ni(Hte2p-tfe$_2$)]}·3.25H_2O^{d}
		Distances (Å)		
Ni–N1	2.217(3)	2.260(2)	1.992(5)	2.108(2)
Ni–N4	2.087(3)	2.100(2)	1.946(5)	2.221(2)
Ni–N8	2.254(3)	2.260(2)$^{\#}$	1.992(5)$^{\$}$	2.093(2)
Ni–N11	2.072(3)	2.100(2)$^{\#}$	1.946(5)$^{\$}$	2.229(2)
Ni–X1	2.100(2)	2.419(1)	–	2.063(1)
Ni–X2	2.072(2)	2.419(1)	–	2.102(1)
		Angles (°)		
N1-Ni-N4	83.23(12)	82.09(9)	87.9(2)	85.35(6)
N1-Ni-N8	171.80(11)	171.32(11)$^{\#}$	180$^{\$}$	178.02(6)
N1-Ni-N11	92.25(11)	91.95(9)$^{\#}$	92.1(2)	93.98(6)
N1-Ni-X1	97.53(10)	96.75(6)	–	86.62(6)
N1-Ni-X2	90.09(11)	89.48(6)	–	95.97(6)
N4-Ni-N8	90.67(12)	91.95(9)$^{\#}$	92.1(2)$^{\$}$	93.77(6)
N4-Ni-N11	96.01(11)	93.59(12)$^{\#}$	180$^{\$}$	179.24(6)
N4-Ni-X1	92.50(10)	89.67(6)	–	91.02(6)
N4-Ni-X2	172.01(11)	171.06(7)	–	91.37(6)
N8-Ni-N11	82.91(11)	82.09(9)$^{\#}$	87.9(2)$^{\$}$	86.89(6)
N8-Ni-X1	88.17(10)	89.48(6)$^{\#}$	–	91.63(6)
N8-Ni-X2	96.38(11)	96.75(6)$^{\#}$	–	85.82(6)
N11-Ni-X1	167.73(12)	171.06(7)$^{\#}$	–	88.59(6)
N11-Ni-X2	88.60(11)	89.67(6)$^{\#}$	–	89.04(6)
X1-Ni-X2	84.01(9)	88.35(3)	–	176.61(5)

^{a}X1 = O1W, X2 = O2W. ^{b}X1 = Cl1, X2 = Cl1$^{\#}$. $^{\#}$two-fold symmetry-related atoms: N8 = N1$^{\#}$, N11 = N4$^{\#}$, # = –x+2, y, –z+1/2. ^{c} N8 = N1$^{\$}$, N11 = N4$^{\$}$, \$ = –x+1, –y+1, –z+1. ^{d}X1 = O11, X2 = O21.

Table S3 The Ni···F distances found in crystal structures of the studied Ni(II) complexes.

cis-[Ni(**1**)(H_2O)$_2$](TsO)$_2$		*cis*-[Ni(**1**)Cl$_2$]		*trans*-[Ni(**1**)](ClO$_4$)$_2$		(NH$_4$){*trans*-[Ni(Hte2p-tfe$_2$)]·3.25H_2O	
Atoms	Distances (Å)	Atoms	Distances (Å)	Atoms	Distances (Å)	Atoms	Distances (Å)
Ni···F161	5.297	Ni···F91	5.127	Ni···F91	4.872	NiF181	5.151
Ni···F162	5.045	Ni···F91A	5.086	Ni···F92	5.033	NiF182	5.113
Ni···F163	5.107	Ni···F92	5.032	Ni···F93	4.848	NiF183	5.360
Ni···F181	5.325	Ni···F92A	5.237	–	–	Ni···F201	5.126
Ni···F182	5.087	Ni···F93	5.281	–	–	Ni···F202	5.117
Ni···F183	5.114	Ni···F93A	5.105	–	–	Ni···F203	5.458

Potentiometry

Stock solution of $Ni(NO_3)_2$ was prepared by dissolution of recrystallized hydrate in water. The Ni(II) content was determined by titration with Na_2H_2edta standard solution. A standard HCl was prepared by dilution of conc. HCl (purris. grade, Aldrich). A standard NMe_4OH solution was prepared by passing an aq. NMe_4Cl solution through a Dowex 1 column in the OH^--form under argon atmosphere and using CO_2-free deionized water.[9] A carbonate-free NMe_4OH solution (~0.2 M) was standardized against potassium hydrogen phthalate, and the HCl stock solution (~0.03 M) against the NMe_4OH standardized solution. Ligand concentration in the stock solution was calculated from the weighted amount of the solid ligand, and it corresponded well with the value obtained during fitting procedure together with determination of the protonation constants. Water ion product was taken from the literature ($pK_W = 13.81$).[10] The constants with their standard deviations were calculated with the OPIUM program package.[11] The program minimises the criterion of the generalized least squares method using the calibration function $E = E_0 + S\cdot\log[H^+] + j_1\cdot[H^+] + j_2\cdot K_W/[H^+]$ where the additive term E_0 contains the standard potentials of the electrodes used and the contributions of inert ions to the liquid-junction potential, term S corresponds to the Nernstian slope, and the $j_1\cdot[H^+]$ and $j_2\cdot K_W/[H^+] = j_2\cdot[OH^-]$ terms describe contributions of the H^+ and OH^- ions to the liquid-junction potential, respectively. The calibration parameters were determined from titration of the standard HCl with the standard NMe_4OH solutions before and after each titration of ligand or ligand/metal ion mixture to give calibration-titration pairs used for calculations of the constants. Titrations were carried out in a thermostatted vessel at 25.0±0.1 °C, at constant ionic strength $I(NMe_4Cl) = 0.1$ M, using a PHM 240 pH-meter, a 2-ml ABU 900 automatic piston burette and a GK 2401B combined electrode (all Radiometer). The concentration of the ligand was approximately 0.004 M and ligand-to-metal ratio was 1:1. An inert atmosphere was ensured by a constant passage of argon saturated with the water vapours.

The measurements were taken with HCl excess added to the initial mixture, and the mixtures were titrated with stock NMe_4OH solution. In a study of protonation equilibrium of the free ligand, the systems were studied by conventional titrations in the pH range 1.8–12.0 (~40 data points per titration). The initial volume was ~5 cm^3 and four parallel titrations were carried out. The equilibrium in Ni(II)–H_4te2p-tfe$_2$ system was established slowly and, therefore, out-of-cell technique was used. Each solution as titration data point (~1 cm^3) was prepared separately in an ampoule which was flame-sealed. Two parallel sets of ampoules were equilibrated at 50 °C for 2 weeks. The ampoules were cooled down and left at room temperature for 24 h. The electrode potential at each titration point (ampoule) was determined for each titration set with freshly calibrated electrode. Titrations were done in pH range 2.4–7.0 with ~20 points per each titration set. Calculated overall protonation and stability constants are compiled in Table S4 and their comparison with published data is given in Table S5.

Table S4 Overall protonation ($\log\beta_h$) and stability ($\log\beta_{hlm}$) constants, and consecutive protonation constants of H_4te2p-tfe$_2$ and its *trans* Ni(II) complex ($I = 0.1$ M NMe_4Cl, 25 °C).

h	$\log\beta_h$	$\log K(H_hL)$	h	l	m	$\log\beta_{hlm}$	$\log K(H_hLM)$
1	10.857(5)	10.86	0	1	1	13.28(6)	–
2	20.956(5)	10.09	1	1	1	19.13(5)	5.85
3	26.557(9)	5.60	2	1	1	23.58(33)	4.4
4	31.289(8)	4.73					

$\beta_h = [H_hL]/\{[H]^h\cdot[L]\}$. $K(H_hL) = [H_hL]/\{[H]\cdot[H_{h-1}L]\}$.
$\beta_{hlm} = [H_hL_lM_m]/\{[H]^h\cdot[L]^l\cdot[M]^m\}$. $K(H_hLM) = [H_hLM]/\{[H]\cdot[H_{h-1}LM]\}$.

Table S5 Comparison of consecutive protonation constants log$K$(H_hL) and stability and protonation constants of Ni(II) complexes of H_4te2p-tfe$_2$ with related ligands.

h	H_4te2p-tfe$_2$	cyclam [12]	tmc [12]	1,8-H_4te2p-Bn$_2$ [13]	1,8-H_4te2p-Bn,Me [13]	1,8-H_4te2p-Me$_2$	1,8-H_4te2p	1,4-H_4te2p [14]
	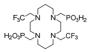	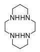	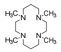	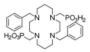	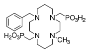	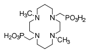	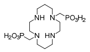	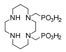
				log$K$(H_hL)				
1	10.86 ^{a}	11.4 ^{a}	9.36 ^{a}	10.53 ^{a}	10.87 ^{a}	11.47 ^{a} [13]	–	–
2	10.09 ^{a}	10.28 ^{a}	9.02 ^{a}	10.68 ^{a}	11.42 ^{a}	12.17 ^{a} [13]	26.41 $^\#$ [13]	25.72 $^\#$
3	5.60 ^{b}	1.6 ^{a}	2.54 ^{a}	7.10 ^{b}	7.24 ^{b}	7.20 ^{b} [13]	6.78 ^{b} [13]	6.56 ^{b}
4	4.73 ^{b}	2.1 ^{a}	2.25 ^{a}	6.44 ^{b}	6.38 ^{b}	6.33 ^{b} [13]	5.36 ^{b} [13]	5.19 ^{b}
5	–	–	–	–	1.60 ^{c}	1.52 ^{c} [13]	1.15 ^{c} [13]	2.30 ^{c}
6	–	–	–	–	1.0 ^{c}	0.85 ^{c} [13]	–	–
				logK_{NiL}				
	13.28	22.2	8.65	–	–	15.55 [15]	21.99 [16]	21.92
				log$K$(NiH_hL)				
1	5.85 ^{b}	–	–	–	–	7.27 ^{b} [15]	7.31 ^{b} [16]	6.14 ^{b}
2	4.4 ^{b}	–	–	–	–	5.1 ^{b} [15]	4.77 ^{b} [16]	5.12 ^{b}

^{a}Protonation of macrocycle amino group. ^{b}Protonation of phosphonate moiety to $–PO_3H^-$. ^{c}Unresolved simultaneous protonation of ring amino group and hydrogenphosphonate moiety to $–PO_3H_2$. $^\#$Overall protonation constant for two consecutive steps, log$K$(HL)+log$K$(H_2L).

Constants are defined in following way (charges are omitted for clarity):

$K(H_hL) = [H_hL] / \{[H]\cdot[H_{h-1}L]\}$

$K_{NiL} = [NiL] / \{[Ni]\cdot[L]\}$

$K(NiH_hL) = [NiH_hL] / \{[H]\cdot[NiH_{h-1}L]\}$.

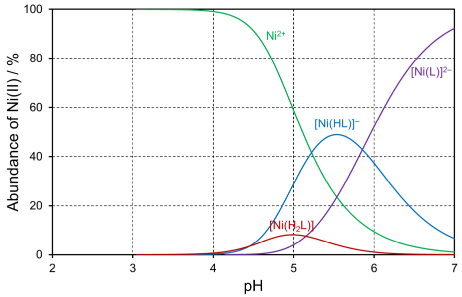

Figure S8 Distribution diagram of the Ni(II)–H_4te2p-tfe$_2$ system (c_M = c_L = 0.004 M, I = 0.1 NMe_4Cl, “frozen” equilibrium at 50 °C, measured at 25 °C).

Dissociation kinetics studies

Inertness of the *trans*-[Ni($H_n$te2p-tfe$_2$)]$^{n-2}$ (0.5 mM) and [Ni(**1**)(H_2O)$_2$]$^{2+}$ (0.8 mM) complexes against acid-assisted dissociation was studied in 1 M aq. HCl at 37 and 80 °C using UV spectroscopy at 230 nm. The rate constants were determined by regression analysis using equation for the first-order kinetics, $A_{230}(t) = a + b\cdot\exp(-k_{obs}t)$, where $A_{230}(t)$ is absorbance at 230 nm in a time, k_{obs} is first-order reaction rate constant, and a and b are parameters characterising initial and final absorbance of the sample. The values of k_{obs}, reaction half-life time ($\tau_{½}$) and time for dissociation from 99 % (τ_{99}) are compiled in Table S6.

Table S6: First-order rate constant (k_{obs}), reaction half-life ($\tau_{½}$) and 99 % reaction time (τ_{99}) for HCl-assisted dissociation of studied complexes in 1 M aq. HCl.

Parameter	Complex			
	cis-[Ni(**1**)(H_2O)$_2$]$^{2+}$		*trans*-[Ni($H_n$te2p-tfe$_2$)]$^{(n-2)}$	
t / °C	37	80	37	80
k_{obs} / $10^{-5}\cdot s^{-1}$	2.442(1)	417(2)	2.005(2)	4.24(1)
$\tau_{½}$ / h	7.883(1)	0.0462(2)	9.60(1)	4.54(1)
τ_{99} / h	52.26(1)	0.306(2)	63.67(7)	30.12(6)

^{19}F NMR/MRI

Aqueous solutions of samples 1) 10 mM *trans*-$(NH_4)_2$[Ni(te2p-tfe$_2$)] 2) 10 mM H_4te2p-tfe$_2$ and 3) 20 mM trifluoroethanol (fluorine concentration was identical in all samples) were filled into separate 1 ml glass vials.

MR Imaging was measured on 4.7-T Bruker MRI scanner equipped with a home-made ^{1}H/^{19}F surface single loop coil (diameter 40 mm), tunable to both 200 (^{1}H) and 188 (^{19}F) MHz.

Base ^{1}H images (200 MHz) were acquired using a T_1-weighted gradient echo sequence with TE = 3.715 ms and TR = 99 ms, FOV = 35×35 mm, matrix 256×256.

^{19}F MR images were obtained using a gradient echo sequence with TE = 1.3 ms and TR = 3 ms optimized for visualization of fast relaxing signals. Slowly relaxing samples were visualized using turbospin echo sequence employing TE = 40 ms and TR = 2000 ms. Field of view (FOV) was 35×35 mm, slice thickness 5 mm, matrix 32×32. The matrix was interpolated to 256×256 to match that of proton images. Acquisition times of ^{19}F MRI experiments were approx. 34 min.

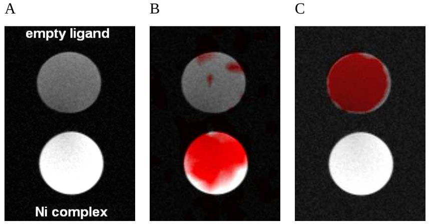

Figure S9 MRI study of phantoms containing free ligand **1** and *cis*-[Ni(**1**)$(H_2O)_2$]$(ClO_4)_2$ complex (c_F = 0.004 M in both samples), B = 4.7 T, 25 °C, home-made ^{1}H/^{19}F surface single loop coil. (**A**): ^{1}H MRI scan, gradient echo sequence, flip angle 30°, TE = 3.7 ms, TR = 100 ms, matrix 256×256. (**B**): Overlay of ^{1}H MRI with ^{19}F MRI; ^{19}F MRI was optimized for the complex; acquired at $\delta = -26$ ppm, gradient echo sequence, TE = 1.3 ms, TR = 3 ms, matrix 32×32 interpolated to 256×256. (**C**): Overlay of ^{1}H MRI with ^{19}F MRI; ^{19}F MRI was optimized for the ligand; acquired at $\delta = -70$ ppm, turbospin echo sequence, TE = 40 ms, TR = 2000 ms, matrix 32×32 interpolated to 256×256.

References

---

[1] G. Royal, V. Dahaoui-Gindrey, S. Dahaoui, A. Tabard, R. Guilard, P. Pullumbi and C. Lecomte, *Eur. J. Org. Chem.* **1998**, 1971–1975.

[2] H. E. Gottlieb, V. Kotlyar and A. Nudelman, *J. Org. Chem.*, 1997, **62**, 7512–7515.

[3] MATLAB R2014a: The MathWorks Inc., Natick, MA, **2014**.

[4] G. M. Sheldrick, SHELXS97, Program for Crystal Structure Solution from Diffraction Data: University of Göttingen, Göttingen, **1997**.

---

[5] G. M. Sheldrick, SHELXL97, Program for Crystal Structure Refinement from Diffraction Data: University of Göttingen, Göttingen, **1997**.

[6] P. Coppens, *Crystallographic Computing*, (Eds.: F. R. Ahmed, S. R. Hall, C. P. Huber), Munksgaard, Copenhagen, **1970**, pp. 255–270.

[7] A. L. Spek, PLATON, A Multipurpose Crystallographic Tool, Utrecht University, Utrecht, **2005**.

[8] M. Meyer, V. Dahaoui-Ginderey, C. Lecomte and R. Guilard, *Coord. Chem. Rev*. **1998**, *178−180*, 1313−1405.

[9] (a) P. Táborský, P. Lubal, J. Havel, J. Kotek, P. Hermann and I. Lukeš, *Collect. Czech. Chem. Commun.*, 2005, **70**, 1909–1942. (b) M. Försterová, I. Svobodová, P. Lubal, P. Táborský, J. Kotek, P. Hermann and I. Lukeš, *Dalton Trans.*, **2007**, 535–549.

[10] Baes, C. F., Jr.; Mesmer, R. E. *The Hydrolysis of Cations*; Wiley: New York, 1976.

[11] M. Kývala, I. Lukeš, *Chemometrics '95*, Abstract book p. 63. Pardubice, Czech Republic, **1995**. Full version of *OPIUM programe package* is available (free of charge) on http://www.natur.cuni.cz/~kyvala/opium.html.

[12] A. E. Martell, R. M. Smith, R. J. Motekaitis, *NIST Standard Reference Database 46 (Critically Selected Stability Constants of Metal Complexes)*, Version 7.0, Texas A&M University, TX, USA, **2003**.

[13] J. Kotek, P. Vojtíšek, I. Císařová, P. Hermann, P. Jurečka, J. Rohovec and I. Lukeš, *Collect. Czech. Chem. Commun.*, 2000, **65**, 1289–1316.

[14] J Havlíčková, H. Medová, T. Vitha, J. Kotek, I. Císařová and P. Hermann, *Dalton Trans.*, **2008**, 5378–5386.

[15] I. Svobodová, J. Havlíčková, J. Plutnar, P. Lubal, J. Kotek and P. Hermann, *Eur. J. Inorg. Chem.*, **2009**, 3577–3592.

[16] I. Svobodová, P. Lubal, J. Plutnar, J. Havlíčková, J. Kotek, P. Hermann and I. Lukeš, *Dalton Trans.*, **2006**, 5184–5197.

Appendix B

Paramagnetic ^{19}F relaxation enhancement in nickel(II) complexes of *N*-trifluoroethyl cyclam derivatives and cell labelling for ^{19}F MRI

- J. Blahut, K. Bernášek, A. Gálisová, V. Herynek, I. Císařová, J. Kotek, J. Lang, S. Matějková, P. Hermann, *Inorg. Chem.* 2017, **56**, 13337–48.

Inorganic Chemistry

Article

Cite This: Inorg. Chem. 2017, 56, 13337-13348

pubs.acs.org/IC

Paramagnetic ^{19}F Relaxation Enhancement in Nickel(II) Complexes of *N*-Trifluoroethyl Cyclam Derivatives and Cell Labeling for ^{19}F MRI

Jan Blahut,[†] Karel Bernášek,[‡] Andrea Gálisová,[§] Vít Herynek,[§] Ivana Císařová,[†] Jan Kotek,[†] Jan Lang,[‡] Stanislava Matějková,[∥] and Petr Hermann*[,†]

[†]Department of Inorganic Chemistry, Faculty of Science, Charles University (Univerzita Karlova), Hlavova 2030, 128 43 Prague 2, Czech Republic

[‡]Department of Low Temperature Physics, Faculty of Mathematics and Physics, Charles University (Univerzita Karlova), V Holešovičkách 2, 180 00 Prague 8, Czech Republic

[§]Department of Radiodiagnostic and Interventional Radiology, Magnetic Resonance Unit, Institute for Clinical and Experimental Medicine, Vídeňská 1958/9, 140 21 Prague 4, Czech Republic

[∥]Institute of Organic Chemistry and Biochemistry, Czech Academy of Sciences, Flemingovo nám. 2, 166 10 Prague, Czech Republic

Supporting Information

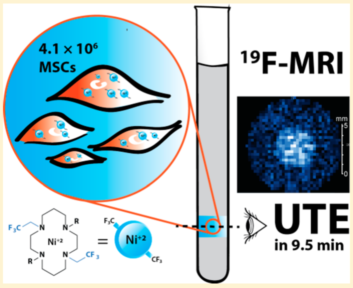

ABSTRACT: 1,8-Bis(2,2,2-trifluoroethyl)cyclam (**te2f**) derivatives with two coordinating pendant arms involving methylenecarboxylic acid (H_2**te2f2a**), methylenephosphonic acid (H_4**te2f2p**), (2-pyridyl)methyl (**te2f2py**), and 2-aminoethyl arms (**te2f2ae**) in 4,11-positions were prepared, and their nickel(II) complexes were investigated as possible ^{19}F MR tracers. The solid-state structures of several synthetic intermediates, ligands, and all complexes were confirmed by X-ray diffraction analysis. The average Ni···F distances were determined to be about 5.2 Å. All complexes exhibit a *trans*-III cyclam conformation with pendant arms bound in the apical positions. Kinetic inertness of the complexes is increased in the ligand order **te2f2ae** ≪ **te2f** < **te2f2py** ≈ H_4**te2f2p** ≪ H_2**te2f2a.** The [Ni(**te2f2a**)] complex is the most kinetically inert Ni(II) complex reported so far. Paramagnetic divalent nickel caused a shortening of ^{19}F NMR relaxation time down to the millisecond range. Solubility, stability, and cell toxicity were only satisfactory for the $[Ni(\textbf{te2f2p})]^{2-}$ complex. This complex was visualized by ^{19}F MRI utilizing an ultrashort echo time (UTE) imaging pulse sequence, which led to an increase in sensitivity gain. Mesenchymal stem cells were successfully loaded with the complex (up to 0.925/5.55 pg Ni/F per cell).^{19}F MRI using a UTE pulse sequence provided images with a good signal-to-noise ratio within the measurement time, as short as tens of minutes. The data thus proved a major sensitivity gain in ^{19}F MRI achieved by utilization of the paramagnetic (transition) metal complex as ^{19}F MR tracers coupled with the optimal fast imaging protocol.

INTRODUCTION

Magnetic resonance imaging (MRI) is a very useful method for noninvasive diagnosis of manifold human and animal diseases. Frequently, contrast agents (CAs) are used for specific tissue recognition. To be utilizable in imaging, the CAs must be nontoxic and stable under in vivo conditions and should be able to alter the MRI response of the tissues employing a proper MRI-pulse sequence. A combination of the CAs and the imaging conditions has to provide sufficient sensitivity and specificity for targeted tissue within a reasonable experimental time.

Even tougher requirements are imposed on CAs used to trace the fate of transplanted cells in vivo, considering toxicity and sensitivity. However, the development of tools for cell tracking is required because cell transplantation is a promising therapeutic procedure for various diseases and it has become an important biomedical research topic.[1] The low specificity of standard CA can be overcome by utilization of compounds with the NMR signal shifted away from that of water due to the presence of a paramagnetic center (PARASHIFT).[2,3] From another point of view, detection of NMR-active nuclei other than ^{1}H is an extension of the same approach.

Among them, the most promising emerging MRI nucleus[4] is ^{19}F with 100% natural abundance and a high gyromagnetic ratio (γ = 40.052 MHz T^{-1}) which is close to that of ^{1}H nuclei. Therefore, standard ^{1}H MRI scanners can also be used for ^{19}F imaging after a relatively simple hardware modification.[5] As there are negligible amounts of natural fluorine atoms in the human body (or in model animals), the imaging is extremely specific. In spite of the low sensitivity of ^{19}F MRI,[6] it has been used for cell labeling.[7,8] To increase sensitivity, the number of fluorine atoms present in the molecule of ^{19}F MR tracers should be as high as possible. This can be achieved mostly by the application of soft nanoparticles made from lipophilic perfluoro compounds.[7−9] Alternatively, the image quality may

Received: August 16, 2017
Published: October 19, 2017

DOI: 10.1021/acs.inorgchem.7b02119
Inorg. Chem. 2017, 56, 13337−13348

Scheme 1. Ligands Discussed in This Work[a]

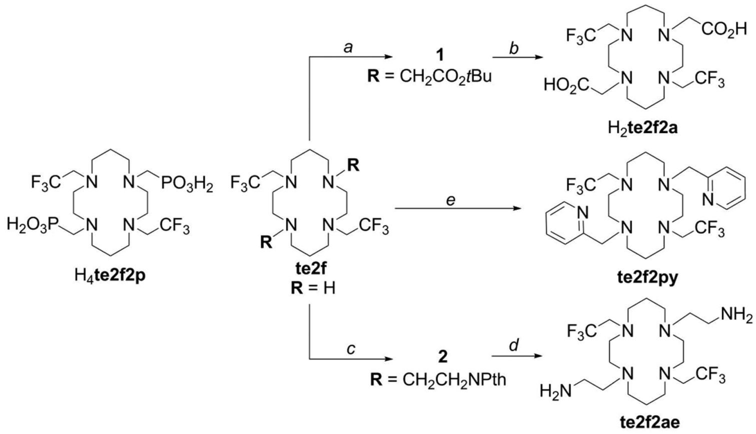

[a]Synthesis: (*a*) BrCH$_2$CO$_2$*t*Bu, K$_2$CO$_3$, CH$_3$CN, room temperature, 12 h; (*b*) TFA, CHCl$_3$, room temperature, 12 h; (*c*) *N*-(2-bromoethyl)phthalimide, K$_2$CO$_3$, CH$_3$CN, 60 °C, 4 days; (*d*) (1) N$_2$H$_4$, EtOH/H$_2$O, 90 °C, 12 h, (2) NaOH, EtOH/H$_2$O, 90 °C, 12 h; (*e*) 2-(chloromethyl)pyridine hydrochloride, K$_2$CO$_3$, CH$_3$CN, 60 °C, 12 h.

be improved by increasing the number of acquisitions. However, relaxation times of ^{19}F nuclei in routinely used ^{19}F MR tracers are very long (time scale of seconds) and, therefore, overall acquisition times are too long. To increase the number of acquisitions obtained in a realistic time, there is a demand for probes with a short relaxation time T_1 which enables quick sequence timing and usage of fast imaging sequences.[10]

For the soft-matter nanoparticle ^{19}F MR tracers, the T_1 value could be modified by an admixture of paramagnetic complexes into the nanoparticle formulations.[11] To date, mostly complexes of high-spin metal ions such as Gd(III) and Fe(III) have been utilized; however,^{19}F relaxation times ratio, T_1/T_2, of the systems was not optimal to achieve a large sensitivity improvement.

The presence of a paramagnetic center in the ^{19}F MR tracer structure is the most straightforward method for significant T_1 relaxation time shortening, and complexes of trivalent lanthanides have been utilized for such a purpose for a long time.[12−15] On the other hand, complexes of paramagnetic transition-metal ions have been used only occasionally. The transition-metal-ion complexes were used mostly in on/off mode, where the presence of paramagnetic species/ion turns off the signal of the ^{19}F MR tracers and the signal can then be re-established due to a redox process[16,17] or an enzymatic cleavage.[18] Only very recently, transition-metal ions were suggested for a relaxation enhancement of fluorine atoms in complexes of DOTA-tetraamide intended to be used as ^{19}F MR tracers.[19]

In our previous communication,[20] we studied Ni^{2+} complexes of **te2f** and H$_4$**te2f2p** (Scheme 1) containing two symmetrical trifluoroethyl moieties (i.e., six equivalent fluorine atoms). In comparison to the free ligands, the complexes show extreme shortening of both T_1 and T_2 ^{19}F nuclear relaxation times down to a millisecond range and, therefore, utilization of an ultrafast pulse sequence would be appropriate. However, real application of the ultrafast pulse sequences was not possible in that study because hardware allowing such pulse sequences was not available to us at the time. Thus, confirmation of the sensitivity enhancement due to short ^{19}F nuclear relaxation times could not be provided in the communication. Here, we wanted to get a better insight into the properties of this promising new class of ^{19}F MR tracers and confirm the MRI sensitivity gain if an appropriate technique is used. Therefore, several new ligands were synthesized having pendant arms able to induce various axial ligand fields in their complexes. They were investigated to obtain a broader knowledge of the influence of the pendant arms on ^{19}F NMR properties of the complexes. As the complexes have different charges and hydrophilicities/hydrophobicities, we also wanted to test their cell-labeling properties. Finally, we were able to show that, with the appropriate pulse sequence and the suitable complex, ^{19}F MRI sensitivity enhancement and visualization of the labeled cells are possible.

■ RESULTS AND DISCUSSION

Ligand Syntheses. As stated above, there are not enough data available to correlate the NMR relaxation properties of nickel(II) complexes with structures of ligands. Therefore, to explore the influence of ligand structure on complex properties, other pendant arms in the *trans*-bis(2,2,2-trifluoroethyl) cyclam derivatives were chosen to introduce commonly used coordinating groups—carboxylic acid (H$_2$**te2f2a**), amino (**te2f2ae**), pyridine (**te2f2py**), and previously reported phosphonate (H$_4$**te2f2p**). For synthesis of the new ligands, 1,8-bis(2,2,2-trifluoroethyl)-1,4,8,11-tetraazacyclotetradecane (**te2f**)[20] was used as the common precursor and the pendant arms were introduced by an alkylation approach (Scheme 1).

The synthesis of **te2f** from 1,8-dibenzyl cyclam was reported in our preliminary communication,[20] and now two intermediates in the synthesis, 1,8-bis(2,2,2-trifluoroacetyl)-4,11-dibenzyl-1,4,8,11-tetraazacyclotetradecane and 1,8-bis(2,2,2-trifluoroethyl)-4,11-dibenzyl-1,4,8,11-tetraazacyclotetradecane, were structurally characterized (for more information, see Figures S1−S3 in the Supporting Information). Compound **te2f** was reacted with an appropriate alkylation agent, *tert*-butyl 2-bromoacetate, *N*-(2-bromoethyl)phthalimide, or 2-(chloromethyl)pyridine, in anhydrous acetonitrile using

K_2CO_3 as a base, affording the key intermediates **1** and **2** and the targeted ligand **te2f2py**, respectively. Intermediate **1** was characterized by X-ray diffraction analysis as well (see Figures S4 and S5 in the Supporting Information). The *tert*-butyl ester groups in intermediate **1** were removed using trifluoroacetic acid (TFA). The acetic acid ligand, H_2**te2f2a**, was isolated as a tetrahydrochloride salt, which was also structurally characterized (see Figures S6 and S7 in the Supporting Information). To synthesize intermediate **2**, an excess of the alkylation agent *N*-(2-bromoethyl)phthalimide had to be added in several portions, as the compound is not fully stable under the reaction conditions and undergoes elimination of hydrobromic acid, affording *N*-vinylphthalimide. The intermediate **2** was isolated by crystallization from EtOH, and its identity was confirmed by X-ray diffraction analysis (Figure S8 in the Supporting Information). The phthaloyl protecting groups in compound **2** were removed by hydrazine. To simplify isolation of **te2f2ae**, the phthalhydrazide formed as a byproduct was further hydrolyzed using alkali hydroxide to phthalic acid. A simple extraction of the reaction mixture gave the required ligand **te2f2ae** in the $CHCl_3$ phase, leaving phthalic acid in the aqueous phase. The ligand **te2f2ae** was purified by chromatography and isolated as a hydrochloride salt. The last ligand, **te2f2py**, was isolated by chromatographic workup of the reaction mixture and stored as a hydrochloride. Its identity was also confirmed by X-ray diffraction analysis (see Figure S9 in the Supporting Information).

Syntheses of Ni(II) Complexes. Similar to the formation of the *trans*-[Ni(**te2f2p**)]$^{2-}$ complex in our preliminary communication,[20] the reaction of H_2**te2f2a** with $NiCl_2$ leading to the *trans*-[Ni(**te2f2a**)] complex in aqueous ammonia solution proceeded with the formation of an intermediate (Figure S10 in the Supporting Information). The free ligand ($\delta(^{19}F)$ −69.2 ppm) was gradually consumed, and formation of an intermediate complex with $\delta(^{19}F)$ −40 ppm was observed, which was fully rearranged into the final *trans*-[Ni(**te2f2a**)] ($\delta(^{19}F)$ −21 ppm) complex after extended heating (sealed ampule, 120 °C, 4 days). These conditions are harsher than those used previously to accomplish the rearrangement leading to the *trans* complex of the phosphonate derivative H_4**te2f2p**. The *trans* arrangement of the coordinated acetate pendant arms was confirmed by an X-ray diffraction study (see below). The complex *trans*-[Ni(**te2f2ae**)]$^{2+}$ was found to be surprisingly sensitive to water, and it cannot be formed in an aqueous solution at all. In addition, it cannot be prepared from $NiCl_2$ even under anhydrous conditions. Therefore, the complex was prepared in anhydrous MeOH starting from a carefully dried free amine, **te2f2ae**, and "$[Ni(MeOH)_4](ClO_4)_2$", which was prepared in situ by reaction of $[Ni(EtOH)_4]Cl_2$[21] with $AgClO_4$. The target complex precipitated off after the reaction mixture was stirred at an elevated temperature (60 °C, 3 h). The *trans* arrangement of the complex was confirmed by X-ray diffraction (see below). The *trans*-[Ni(**te2f2py**)]$^{2+}$ complex was prepared from **te2f2py** and $Ni(ClO_4)_2\cdot 6H_2O$. The free amine **te2f2py** was isolated from **te2f2py**$\cdot 6HCl\cdot 3H_2O$ by extraction from alkaline aqueous solution, and it is insoluble in water but slightly soluble in MeOH. The product, complex *trans*-[Ni(**te2f2py**)]$(ClO_4)_2$, is very soluble in CH_3NO_2; however, it is almost insoluble in water and MeOH. Therefore, the complexation reaction was started in a CH_3NO_2/MeOH mixture (2/1, 100 °C, 2 h) with gradual evaporation of MeOH during the course of the reaction. All complexes were soluble, at least slightly, in water to allow measurement of ^{19}F NMR and decomplexation kinetic data, but only the *trans*-[Ni(**te2f2p**)]$^{2-}$ complex was soluble enough to be used in biological experiments (see below).

Crystal Structures of Ni(II) Complexes. In the solid state, the *trans*-[Ni(**te2f2a**)] complex molecule (Figure 1) is located in the general position of the appropriate space group ($P2_1/n$) and its overall geometry is close to centrosymmetric. The metal ion is centered in a slightly distorted octahedral sphere with coordination distances of macrocycle nitrogen atoms of about 2.07 Å (those bearing pendant carboxylates) and 2.23 Å (those bearing trifluoroethyl moieties). The carboxylate oxygen atoms are coordinated at a very close distance 2.04 Å. The biggest deviation of *cis* bond angles from the theoretical value was observed for the *N*,*O*-chelate ring belonging to the pendant acetate (83°) due to a small chelate ring size. All *trans* angles are almost ideal (179°). Each ethanol solvate molecule is bound by medium-strong hydrogen bonds ($d_{O\cdots O}$ = 2.84 and 2.86 Å, respectively) to an axially coordinated oxygen atom. Relevant coordination geometric parameters are given in Table 1 and Table S1 in the Supporting Information.

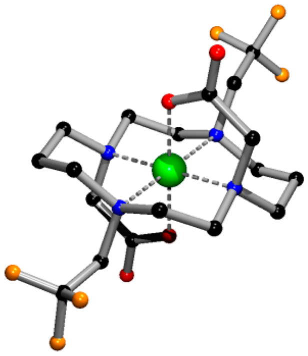

Figure 1. Molecular structure of the *trans*-[Ni(**te2f2a**)] species found in the crystal structure of *trans*-[Ni(**te2f2a**)]·2EtOH. Color code: C, black; N, blue; O, red; F, orange; Ni, green.

The complex *trans*-[Ni(**te2f2ae**)]$^{2+}$ found in the crystal structure of *trans*-[Ni(**te2f2ae**)]$(ClO_4)_2\cdot 2MeOH$ is an octahedral N_6 species with a center of symmetry enforcing *trans* angles to be 180° (Figure 2). The coordination distance of the macrocycle nitrogen atoms bearing pendant arm (2.07 Å) are shorter than those of trifluoroethyl-substituted nitrogen atoms (2.30 Å). Apical nitrogen atoms of the aminoethyl pendant arm are coordinated at a rather long distance (2.16 Å). The long axial N−Ni bonds cause large deviation of the *cis* angle (82°) of the five-membered pendant chelate ring from the theoretical value. The relevant coordination geometry is given in Table 1 and Table S1 in the Supporting Information.

In the solid-state structure of *trans*-[Ni(**te2f2py**)]$(ClO_4)_2$, two independent centrosymmetric complex units were found, both with the macrocyclic part disordered in two positions (relative occupancies 83%:17% and 85%:15%, respectively). The nondisordered parts of both molecules are formed by the trifluoroethyl groups with a corresponding macrocycle nitrogen pivot atom and the pyridine moieties. The macrocycle disorder swaps the positions of the five- and six-membered chelate rings together with the position of the pivot atom bearing the pyridine pendant arm, and thus, the less abundant unit roughly

Table 1. Selected Distances Found in the Solid-State Structures of the Studied Nickel(II) Complexes (Å)

	average distance (Å)[a]					
	trans-[Ni(**te2f2a**)]	*trans*-[Ni(H**te2f2p**)]$^{-}$ [d]	*trans*-[Ni(**te2f2py**)]$^{2+}$	*trans*-[Ni(**te2f2ae**)]$^{2+}$	*trans*-[Ni(**te2f**)(H_2O)$_2$]$^{2+}$	*cis*-[Ni(**te2f**)(H_2O)$_2$]$^{2+}$ [d]
d(Ni–N$^{\text{tfe}}$)[b]	2.23	2.23	2.22	2.30	2.19	2.24
d(Ni–N$^{\text{pend}}$)[b]	2.07	2.10	2.10	2.07	2.04	2.08
d(Ni–Ax)[c]	2.04	2.08	2.24	2.16	2.13	2.09
d(Ni···F)	5.22	5.23	5.25	5.34	5.18	5.16

[a] Average distances are based on data in Table S1 in the Supporting Information. [b] Ring nitrogen atoms. [c] Ax = axial donor atom. [d] Reference 20.

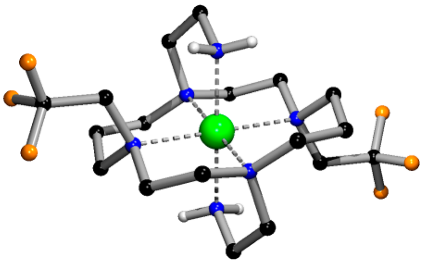

Figure 2. Molecular structure of the *trans*-[Ni(**te2f2ae**)]$^{2+}$ cation found in the crystal structure of the *trans*-[Ni(**te2f2ae**)](ClO_4)$_2$·2MeOH. Color code: C, black; N, blue; H, white; F, orange; Ni, green.

matches the pseudo-C_s symmetry of the more abundant part (Figure S11 in the Supporting Information). However, both independent units have very similar geometries (Table 1 and Table S1 in the Supporting Information), and therefore, only the more abundant part of one of them is shown in Figure 3.

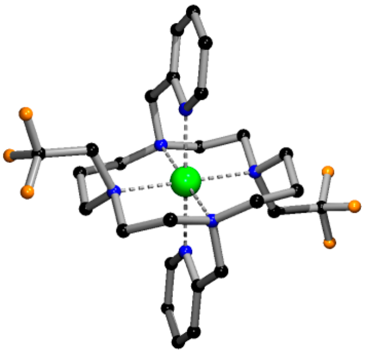

Figure 3. Molecular structure of one of two independent *trans*-[Ni(**te2f2py**)]$^{2+}$ complex units found in the crystal structure of *trans*-[Ni(**te2f2py**)](ClO_4)$_2$. Only the more abundant (83%) position of the disordered macrocycle is shown. Color code: C, black; N, blue; F, orange; Ni, green.

Generally, coordination bond distances are longer than those found in the previous structures. The bond lengths are increased from those for nitrogen atoms bearing the methylpyridine pendant arm (2.10–2.11 Å), through those of amines substituted by the trifluoroethyl group (2.21–2.22 Å), to those for apically coordinated pyridine nitrogen atoms (2.22–2.26 Å). The largest angle deviation in the nickel(II) coordination sphere is forced by a small and rigid five-membered chelate ring involving the pyridine pendant arm (~78°).

In a repeated preparation of (NH_4)[Ni(H**te2f2p**)] according to the previously reported procedure, a bulk solid corresponding to *trans*-(NH_4)[Ni(H**te2f2p**)]·3.25H_2O phase was isolated[20] and a few prismatic crystals were obtained on evaporation of the mother liquor. This phase has different crystal packing. The asymmetric unit contains two complex anions with protonated phosphonate pendants, two ammonia cations, and eight water molecules. The complex units are connected through very short hydrogen bonds between pendant oxygen atoms ($d_{\text{O}\cdots\text{O}}$ = 2.42 and 2.43 Å) into infinite chains (Figure 4) which are interconnected through a wide system of hydrogen bonds involving phosphonate oxygen atoms, ammonium counterions, and water solvate molecules (Figure S12 in the Supporting Information). Coordination spheres of both independent units do not differ much from each other, and they are very similar to that found previously in *trans*-(NH_4)[Ni(H**te2f2p**)]·3.25H_2O, where a similar intermolecular hydrogen bond between phosphonate groups was also found ($d_{\text{O}\cdots\text{O}}$ = 2.47 Å).[20] Analogous hydrogen bonds stabilize the crystal structures of complexes of other phosphonic acid cyclam derivatives.[22] Coordination lengths for the nitrogen atoms bearing the methylphoshonate pendant arm (2.09–2.10 Å), for those substituted by a trifluoroethyl group (2.22–2.23 Å), and for the apical phosphonate oxygen atoms (2.07–2.10 Å) are also similar to those observed previously. The *cis* angle of the coordinating ring involving the phosphonate pendant arm is close to the theoretical value (86–87°) as a result of a larger phosphorus atom and longer bonds around it which adequately increase the size of the five-membered chelate ring formed by the pendant arm.

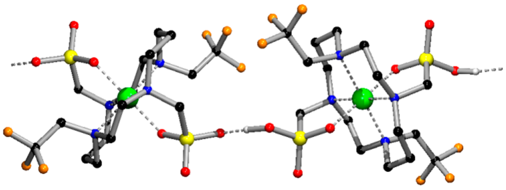

Figure 4. Asymmetric part of the infinite chain formed by {*trans*-[Ni(H**te2f2p**)]$_2$}$_n^{2n-}$ anions found in the structure of *trans*-(NH_4)-[Ni(H**te2f2p**)]·4H_2O. Color code: C, black; N, blue; O, red; H, white; F, orange; Ni, green; P, yellow.

In a previous study, we observed that the simple trifluoroethyl cyclam derivative **te2f** prefers *cis* coordination to the central Ni(II) ion and the *cis*-[Ni(**te2f**)(H_2O)$_2$]$^{2+}$ species was found to be thermodynamically more stable than the *trans* species.[20] However, when **te2f**·4HCl was reacted with Ni-

$(ClO_4)_2$, a few violet crystals were formed apart from the bulk blue-green *cis*-[Ni(**te2f**)Cl_2] complex reported previously.[20] These violet crystals were structurally characterized and were found to have *trans*-[Ni(**te2f**)$(H_2O)_2$]Cl_2 composition with unexpected *trans*-III macrocycle conformation[23] enabling *trans* apical water molecule binding (Figure 5, Table 1, and Table S1 in the Supporting Information). The coordination distances of macrocycle nitrogen atoms (2.04 Å for the secondary amino group and 2.19 Å for the nitrogen atom bearing trifluoroethyl moiety) are somewhat shorter than those found in the *cis* complex but significantly longer than those observed in the square-planar *trans*-[Ni(**te2f**)]$(ClO_4)_2$ complex reported previously (see Table S1).[20] The apical water molecules are coordinated at a distance of 2.13 Å.

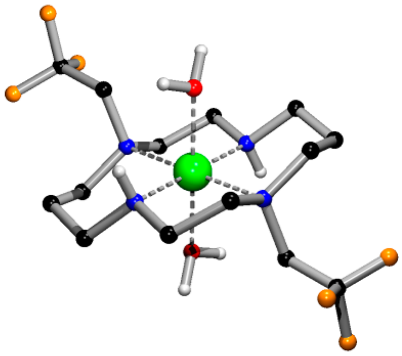

Figure 5. Molecular structure of *trans*-[Ni(**te2f**)$(H_2O)_2$]$^{2+}$ cation found in the crystal structure of *trans*-[Ni(**te2f**)$(H_2O)_2$]Cl_2. Color code: C, black; N, blue; O, red; H, white; F, orange; Ni, green.

The geometric parameters of complex coordination spheres found in crystal structures of *trans*-(NH_4)[Ni(H**te2f2p**)]·3.25H_2O, *cis*-[Ni(**te2f**)$(H_2O)_2$]$(TsO)_2$, and *trans*-[Ni(**te2f**)]$(ClO_4)_2$ reported previously[20] are given in Table 1 and Table S1 in the Supporting Information together with data obtained for complexes in the present study. All *trans* complexes adopt the equatorial *trans*-III conformation of the macrocycle ring.[23] The coordination sphere in these complexes is a distorted octahedron with prolonged bond distances between the central Ni(II) ion and nitrogen atoms bearing a trifluoroethyl group due to the strong electron-withdrawing effect of this group. These distances (2.21−2.23 Å) are comparable in almost all studied complexes with coordinated pendant arms (and also in the coordination sphere of *cis*-[Ni(**te2f**)$(H_2O)_2$]$(TsO)_2$), and the bonds are even longer (2.30 Å) in the *trans*-[Ni(**te2f2ae**)]$^{2+}$ species. In the octahedral *trans*-[Ni(**te2f**)$(H_2O)_2$]$^{2+}$ complex, these bonds are slightly shorter (2.19 Å), while in the tetracoordinated square-planar *trans*-[Ni(**te2f**)]$^{2+}$ species the distances are significantly shorter (1.99 Å). A similar trend was also found for Ni−N bond lengths of the other macrocycle nitrogen atoms, which lie in a narrow range of 2.07−2.11 Å for all structures; the only exceptions are the *trans*-[Ni(**te2f**)$(H_2O)_2$]$^{2+}$ (2.04 Å) and *trans*-[Ni(**te2f**)]$^{2+}$ (1.95 Å) cations, respectively. The shortest Ni−axial atom average distances were observed in the *trans*-[Ni(**te2f2a**)] species (2.04 Å), and those observed in the *trans*-[Ni(H**te2f2p**)]$^-$ anion were only slightly longer (2.06−2.10 Å). These short coordination distances, together with a relatively low basicity of the oxygen atoms, result in a noticeable kinetic inertness of these complexes (see below). On the other hand, the apically coordinated nitrogen donors are more distant—the longest bonds (2.22−2.26 Å) were observed in the *trans*-[Ni(**te2f2py**)]$^{2+}$ cation, where they are forced by the steric requirements of the pyridine ring (the C−N−Ni angle is 120°). As a consequence, the methylpyridine pendant arm is bent out from the axial direction with the most deformed *cis* angle of the axial chelate ring (79°) and this probably leads to the increased bond distances. For the *trans*-[Ni(**te2f2ae**)]$^{2+}$ ion, a medium-long axial bond (2.16 Å) together with a high basicity of the aminoethyl nitrogen atom leads to easy protonation (and decoordination) of the pendant arm and subsequent dissociation of the complex (see below), which occurs even in an aqueous solution with neutral pH. The coordination geometries are in good agreement with the observed kinetic inertness against acid-assisted hydrolysis, where the stability increases in the order *trans*-[Ni(**te2f2ae**)] < *trans*-[Ni(**te2f2py**)] < *trans*-[Ni(**te2f2p**)] < *trans*-[Ni(**te2f2a**)] (vide infra).

The Ni···F distances, which are relevant for the magnetic dipole−dipole relaxation of the ^{19}F nuclei as discussed below, are in the 5.0−5.4 Å range in all studied octahedral complexes but differ from the distances in the square-planar *trans*-[Ni(**te2f**)]$^{2+}$ cation, where distances of 4.8−5.0 Å were observed due to the significantly shorter Ni−N bonds (see above). However, after aquation of this complex, as expected upon its dissolution in water, the octahedral *cis* complex species is formed[20] and the Ni···F distances are in the range observed for the other complexes (Table 1 and Table S1 in the Supporting Information). In the previously investigated lanthanide(III) complexes of the DOTA-like ligands, the Ln···F distances are longer, generally about 6.5 Å.[12,19]

UV−Vis Spectra of the Ni(II) Complexes. The d^8 configuration enables simple evaluation of ligand field strength because the lowest-energy transition band $^3T_{2g} \leftarrow {}^3A_{2g}$ has energy equal to d orbital splitting (i.e., Δ or 10*Dq*). Therefore, the UV−vis spectra of the prepared Ni(II) complexes in solution were acquired. In the wavelength range λ 300−1100 nm, each of the *trans* complexes exhibits three broad d−d bands—with increasing energy, these are transitions between ground state $^3A_{2g}$ and $^3T_{2g}$, $^3T_{1g}(F)$, and $^3T_{1g}(P)$, respectively (Figure S13 and Table S2 in the Supporting Information). For the *trans*-[Ni(**te2f2py**)]$^{2+}$ complex, the highest-energy d−d band is overlapped with a base of strong pyridine ring UV absorption. In the spectra of *trans*-[Ni(**te2f2ae**)]$^{2+}$, more bands in the d−d region were found. Such a complexity of UV−vis spectra is probably associated with partially solvolyzed (aquated) species, pointing to aminoethyl pendant arm(s) decoordination and protonation.[20] Protonation constants of H_2**te2f2ae** were determined to be log K_{a1}−K_{a4} 9.64, 9.26, 5.55, and 4.85, respectively, where the most basic values are assigned to the 2-aminoethyl groups. This leads to instability of the octahedral *trans*-[Ni(**te2f2ae**)]$^{2+}$ complex species even in a neutral aqueous solution (see below). A reversible decoordination of the axial amine-containing pendant arms was described by Kaden et al. for a Ni(II) complex of 1,8-bis(2-aminoethyl)-4,11-dimethyl cyclam. The reaction in that case was also associated with simultaneous protonation of the pendant amine groups.[24] The spectrum of *cis*-[Ni(**te2f**)$(H_2O)_2$] has a pattern similar to that of *trans* complexes, but the extinction coefficients are higher due to the absence of a center of symmetry (Figure S13). In the complex series, the largest ligand-field splitting is found for *trans*-Ni(**te2f2a**)]

DOI: 10.1021/acs.inorgchem.7b02119
Inorg. Chem. 2017, 56, 13337−13348

Table 2. Acid-Assisted Decomplexation of the Title Nickel(II) Complexes

complex	t/°C	conditions	k_{obs}/h^{-1}	$\tau_{1/2}$
cis-[Ni(**te2f**)(H_2O)$_2$]$^{2+}$ [a]	80	1 M aq HCl	15.00(6)	2.77 min
trans-[Ni(**te2f2p**)]$^{2-}$ [a]	80	1 M aq HCl	0.1526(3)	4.54 h
trans-[Ni(**te2f2a**)]	80	∼12 M aq HCl	0.002(1)	14 days
trans-[Ni(**te2f2ae**)]$^{2+}$	25	pH 7.8 (HEPES)	0.25(6)	2.8 h
trans-[Ni(**te2f2py**)]$^{2+}$	80	1 M aq HCl	0.21(4)	3.3 h

[a] Reference 20.

Table 3. ^{19}F NMR Relaxation Data for Title Complexes and Ligands in Several External Magnetic Fields (Aqueous Solutions, 25 °C)[b]

	T_1/ms				T_1 of free ligand/ms		
complex	B_0 = 0.94 T	B_0 = 7.0 T	B_0 = 9.4 T	T_2*/ms B_0 = 7.0 T	B_0 = 0.94 T	B_0 = 7.0 T	B_0 = 9.4 T
trans-[Ni(**te2f2a**)]	12(3)	2.0(6)	1.5(3)	1.03	810(40)	620(20)	540(3)
trans-[Ni(**te2f2ae**)]$^{2+}$	6(2)	1.7(7)	1.2(2)	0.83	730(30)	710(20)	507(6)
trans-[Ni(**te2f2py**)]$^{2+}$	18(4)	1.8(2)	1.4(4)	0.76	710(60)	530(10)	456(8)
trans-[Ni(**te2f2p**)]$^{2-}$	28(9)	2.8(7)[b]	1.8(1)	0.90	500(20)	820(10)[b]	375(6)
cis-[Ni(**te2f**)(H_2O)$_2$]$^{2+}$	5(3)	1.72(1)[b]	1.7(2)	0.82	1060(20)	1100(20)[b]	715(5)

[a] Values in parentheses represent 95% confidence bounds of fitted parameters. [b] Reference 20.

(10Dq = 11600 cm^{-1}) followed by *trans*-[Ni(**te2f2py**)]$^{2+}$ (10Dq = 11000 cm^{-1}) and *trans*-[Ni(**te2f2p**)]$^{2-}$ (10Dq = 10790 cm^{-1}) complexes. The smallest splitting appears in *trans*-[Ni(**te2f2ae**)]$^{2+}$ (10Dq = 9430 cm^{-1}) and *cis*-[Ni(**te2f**)]$^{2+}$ (10Dq = 9520 cm^{-1}) complexes. These findings point to a change in the overall strength of coordination bonds and roughly correlates with the order of kinetic inertness of the complexes (see below). In general, the ligand-field strength induced by the title ligands is decreased in comparison with analogous cyclam derivatives bearing two coordinating pendant arms[24−26] due to the electron-withdrawing nature of the *N*-trifluoroethyl substituents.

Stability of the Ni(II) Complexes in Aqueous Solution. The title complexes exhibit remarkable differences in acid-assisted decomplexation (Table 2). To compare decomplexation rates of the complexes, the same experimental conditions as those used previously (1 M aqueous HCl, 80 °C) were employed here and the course of the reaction was followed by ^{19}F NMR (Figure S14 in the Supporting Information). The decomplexation half-life of the *trans*-[Ni(**te2f2py**)]$^{2+}$ complex is comparable with that of the *trans*-[Ni(**te2f2p**)]$^{2-}$ complex.[20] Surprisingly, the *trans*-[Ni(**te2f2ae**)]$^{2+}$ complex immediately decomposes in aqueous acidic solutions. Therefore, its demetalation at ambient temperature was followed at several pHs close to neutral (see the Experimental Section) and proceeded with half-lives of several hours: e.g. $\tau_{1/2}$ = 2.8 h at pH 7.8. The **te2f2ae** is a hexadentate ligand, and the kinetic lability of its complex is surprising, as the complex is even more labile than the complex of its parent ligand with no coordinating pendant arms, *cis*-[Ni(**te2f**)(H_2O)$_2$]$^{2+}$.[20] This behavior also explains the problems with synthesis of the complex (see above). Therefore, only simple NMR characteristics could be measured immediately after the complex was dissolved in water. On the other hand, the complex of the ligand with carboxymethyl pendant arms, *trans*-[Ni(**te2f2a**)], is so kinetically inert that acid-assisted hydrolysis had to be carried out in concentrated aqueous HCl to be observable on a reasonable time scale (full decomplexation in >100 days; 12 M aqueous HCl, 80 °C). The complex can be considered as the most kinetically inert nickel(II) complex investigated to date,[27] and the complex is one of the most kinetically inert complexes of cyclam-based ligands. The *trans*-[Ni(**te2f2p**)]$^{2-}$ complex is significantly more labile but still stable enough for any in vivo utilizations. Overall, the kinetic inertness/lability qualitatively correlates with the strength of the axial ligand metal binding and/or with the axial group basicity and its ability to transfer protons onto the macrocycle amine group(s). The protonation of the ring amine group(s) is generally considered to be a rate-determining step in the decomplexation reactions of complexes of macrocyclic ligands.[28]

^{19}F NMR Relaxation Properties. Unfortunately, the complexes *trans*-[Ni(**te2f2a**)] and *trans*-[Ni(**te2f2py**)](ClO_4)$_2$ are almost insoluble in water and, therefore, cannot be used for ^{19}F MRI imaging either in vitro or in vivo. However, the concentrations of their saturated aqueous solutions were sufficient for measurement of ^{19}F NMR spectra and relaxation times (Table 3).

The ^{19}F NMR chemical shifts of the complexes are in a narrow range, from −19 to −26 ppm, as are their relaxation times (e.g., T_1 1.5−1.8 ms at 9.4 T), and therefore, the ^{19}F NMR parameters of the complexes are not significantly altered with a change in character of the donor atom of the pendant arms. Enhancement of the ^{19}F relaxation in the complexes, on comparison to that in the free ligands, is about 500-fold at high fields. A significant decrease in T_1 relaxation time was also observed at low field (0.94 T). Such a decrease in nuclear relaxation time with an increasing magnetic field is in accordance with the Solomon−Bloemberger−Morgan theory,[29] and it is associated with prolongation of the electron spin relaxation times of the central Ni(II) ion. The more accurate theories, such as the Stockholm slow motion theory or the generalized Solomon−Bloemberger−Morgan theory, are in qualitative agreement with such an observation.[30,31] The T_1 relaxation enhancement at 9.4 T in the presented systems is higher than that reported for various lanthanide(III) complexes of macrocyclic ligands (T_1 ranging from 4 to 21 ms).[12c,13b] Very recently reported data for Fe^{2+} and Ln^{3+} complexes of a DOTA-tetraamide derivative also describe a slower longitudinal relaxation (5.7 ms for Fe^{2+} and 6.3−360 ms for various Ln^{3+}).[19] The relaxation enhancement for the nickel(II) complexes at the same magnetic field (9.4 T), in comparison with that for the Ln(III) complexes of DOTA-like ligands,[12,13]

Table 4. Data for ^{19}F MRI Phantom Samples (in Water, 25 °C, B_0 = 11.8 T)

sample	c(tracer)/mM	$c(^{19}F)$/mM	T_1/ms	T_2/ms	method	t_{exp}/min	SNR[c]	TR/ms
trans-[Ni(**te2f2p**)]$^{2-}$	16.7	100.2	1.52(3)	0.78(2)	UTE[a]	9.47	35	5.5
2,2,2-trifluoroethanol	33.1	99.3	3460(70)	2960(150)	RARE[b]	9.50	5.9	3000

[a] References 10 and 13. [b] Reference 32. [c] Signal to noise-ratio (SNR) after an acquisition time of 10 min. SNR = $[2 \times ((\text{signal})^2 - (\text{noise})^2)/(\text{noise})^2]^{1/2}$. The signal and noise values were determined from equal numbers of pixels of the corresponding areas of the images.

is not as high as might be expected when only the metal ion—fluorine atom distance is taken into account (~5.2 Å vs ~6.5 Å, respectively). This highlights the fact that both distance and electronic properties of the metal ions are important for alteration of nuclear relaxation times. From this point of view, transition-metal complexes offer a diverse range of electronic and structural parameters which can be rationally tuned.

^{19}F MRI and Cell Labeling. Specific measuring methods as well as special ^{19}F MR tracers with a very low detection limit are required for cell labeling due to the extremely low achievable in-cell concentration of a probe. Therefore, the most suitable complex, *trans*-[Ni(**te2f2p**)]$^{2-}$, was studied to determine its detection limit and signal-to-noise ratio (SNR). 2,2,2-Trifluoroethanol (TFE) was used as a diamagnetic standard. All experiments were performed at B_0 = 11.8 T and at 25 °C in water. The *trans*-[Ni(**te2f2p**)]$^{2-}$ complex is present mainly as the dianionic species (log K_1 5.85) at pH 7.5−8.1, which was used in the ^{19}F MRI experiments and during cell labeling.[20]

The ^{19}F relaxation times in the *trans*-[Ni(**te2f2p**)]$^{2-}$ complex were T_1 = 1.52(3) ms and T_2 = 0.78(2) ms, and those of TFE were T_1 = [3.46(7)] × 10^3 ms and T_2 = [2.96(15)] × 10^3 ms. The choice of imaging sequences and their settings were optimized for the very different ^{19}F relaxation properties of both compounds. For this complex, the short T_1 relaxation time enables fast acquisition with a short repetition time (TR). The short T_2 relaxation time raised the requirement of utilization of the ultrashort echo time (UTE) pulse sequence[10,13] employing the radial *k*-space sampling and direct FID detection, thus minimizing the delay between signal excitation and acquisition. Since the UTE sequence does not involve a spin echo, the echo time (TE) means the time between the middle of the excitation pulse and the start of acquisition. Conversely, for TFE with much a slower relaxation rate, a standard RARE[32] pulse sequence was used. The phantom samples of the *trans*-[Ni(**te2f2p**)]$^{2-}$ complex (pH 8.1) and TFE in glass capillaries with the same ^{19}F concentrations (100 mM) were prepared and placed into a standard 5 mm NMR tube. The images were set to the same voxel volume of 0.0256 mm^3 (a 0.08 × 0.08 mm pixel and 4 mm slice thickness). Acquisition bandwidth (BW) was optimized −25 kHz for UTE on the *trans*-[Ni(**te2f2p**)]$^{2-}$ sample and 15 kHz for RARE on the TFE sample. The results are compiled in Table 4 and Figure 6.

It can be clearly seen that, with a proper pulse sequence optimized for the fast-relaxing compounds, the measurement efficiency (as viewed by SNR) of the sample with the prepared paramagnetic complex is significantly higher in comparison to the diamagnetic standard imaged by the routinely used multiecho RARE pulse sequence. This difference in imaging efficiency can also be expressed as a detection limit—a minimal observable concentration during the chosen experimental time. Thus, the minimal required ^{19}F concentration to reach SNR = 2 in 10 min of measurement is 5.6 mM for the *trans*-[Ni(**te2f2p**)]$^{2-}$ complex (i.e., 0.93 mM complex concentration) and 33 mM for TFE (i.e., 11 mM TFE concentration). This means that detectable ^{19}F concentration with utilization of the *trans*-[Ni(**te2f2p**)]$^{2-}$ complex is about 6 times lower than that if TFE is used as a diamagnetic model compound. This is a smaller decrease of detectable ^{19}F concentration in comparison to that described for Ln(III) complexes of the fluorinated DOTA-like ligands, where up to ~25 times lower ^{19}F concentrations were recognized.[13b]

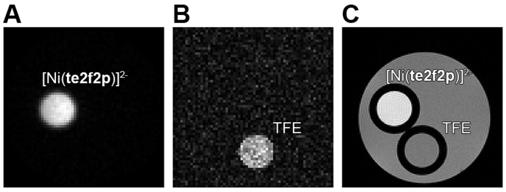

Figure 6. Image of the 1.1 mm inner diameter capillaries (25 °C, B_0 = 11.8 T) with 16.7 mM aqueous solution of the *trans*-[Ni(**te2f2p**)]$^{2-}$ complex and with 33.1 mM aqueous solution of TFE measured using (A) ^{19}F-UTE pulse sequence (TR 5.5 ms; TE 0.091 ms; BW 25 kHz; field of view 5 × 5 mm; slice thickness 4 mm; 202 projections; number of averages (NA) 512 averages; reconstruction matrix of 64 × 64 measured in 9 min and 29 s), (B) ^{19}F-RARE (TR 3000 ms; TE 7 ms; BW 15 kHz; field of view 5 × 5 mm; slice thickness 4 mm; RARE factor 64; NA 190; reconstruction matrix of 64 × 64 points; measured in 9 min and 30 s), and (C) ^{1}H-FLASH (TR 100 ms; TE 2.5 ms; BW 50 kHz field of view 5 × 5 mm; slice thickness 1 mm; number of NA 4; reconstruction matrix 128 × 128 points measured in 51.2 s).

Next, the *trans*-[Ni(**te2f2p**)]$^{2-}$ complex was tested as a cellular label on mesenchymal stem cells (MSCs) (Table 5).

Table 5. Data for Cell Labeling and MRI Experiments

$c(^{19}F)$[a] (mM)	c(tracer)[a] (mM)	viability (%)[b]	cell gain (%)	t_{exp}[c] (min)	SNR[c]
50	8.3	92	98	48	4.1
100	16.7	88	95	9.5	4.4
0[d]	0[d]	96	100		

[a] In the cell cultivation media. [b] The percentage of vital cells after labeling. [c] Horizontal slice. [d] Control experiment.

The cells (ca. 1 million cells) were incubated in the presence of the complex in the medium at four concentrations (4.2, 8.3, 16.7, and 25.0 mM). The viability of MSCs was not affected by the presence of the complex (Table S3 in the Supporting Information); however, at the highest concentration, the amount of harvested cells was substantially lower (Figure S15 in the Supporting Information). The concentration of the complex in MSCs after labeling revealed an almost linear dependence on concentration in the medium during labeling, and this indicates that the complex is probably entering the cells by passive diffusion.

For the MRI experiments, higher amounts (4.3 million) of cells were labeled with 8.3 and 16.7 mM concentration of the complex in the medium, respectively (Table 4). The amount of the complex in cells labeled with these concentrations was

0.423 and 0.925 pg Ni(II) per cell (Table S3 in the Supporting Information). The labeled cells were washed, fixed, and transferred into Shigemi tubes. The area of the cell pellet (photograph at the bottom of Figure 7) is visible in an ^{1}H-FLASH image as a hypointense signal at the bottom of the cuvette. The ^{19}F MR images of the cell sample were obtained using a UTE pulse sequence. Sufficient SNR (SNR > 4) in the horizontal slice was obtained within 48 min (6000 acquisitions) in the sample containing cells labeled in the 8.3 mM complex concentration, or within 9.5 min (1200 acquisitions) in the sample with cells labeled in the 16.7 mM complex concentration (Table 4 and Figure 7). The experimental times for the cell samples are in good agreement with the detection limits estimated from the phantom samples. Vertically oriented ^{19}F-UTE images acquired with higher SNR and resolution showed distribution of the complex in the sample. The complex was not specifically localized in the cell pellet. The membrane of the fixed cells is probably still permeable for the investigated complex (as it is a small molecule), and a partial efflux of the ^{19}F MR tracer occurred. However, despite the partial efflux, most of the image intensity is still localized in the cell pellet area.

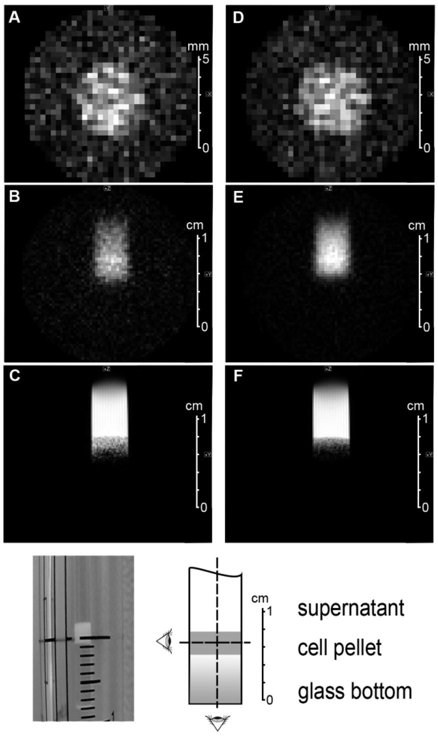

Figure 7. Fixed MSCs (4.1 × 10^6) labeled by the *trans*-[Ni(**te2f2p**)]$^{2-}$ complex (8.3 mM, (A)−(C); 16.7 mM, (D)−(F)) and placed into 5 mm Shigemi NMR tubes. The pellets were imaged by a ^{19}F UTE pulse sequence with horizontal ((A) and (D): TR = 4.5 ms, TE = 0.111 ms, NA = 6000 (A) and 1200 (D), FOV = 10 × 10 mm, 5 mm slice, matrix 34 × 34) and vertical ((B) and (E): TR = 6.5 ms, TE = 0.111 ms, NA = 20000, FOV = 20 × 20 mm, 5 mm slice, matrix 66 × 66) slices and by a ^{1}H gradient-echo pulse sequence in vertical orientation ((C) and (F): TR = 100 ms, TE = 2.1 ms, NA = 8, FOV = 20 × 20 mm, 1 mm slice, matrix 128 × 128). A photograph of the Shigemi NMR tube and a sketch of the experimental setup are shown at the bottom of the figure.

The imaging experiments proved that cell labeling with the paramagnetic ^{19}F MR tracer and detection of the cells by ^{19}F MRI is possible and, thus, advantages of the fast-relaxing ^{19}F MR tracers can be fully exploited. They provide a reasonable signal-to-noise ratio, which is achievable in short imaging times. The observed efflux of the ^{19}F MR tracer from the cells presents a complication to be solved before practical in vivo applications of this particular system. Nevertheless, it is a successful proof of principle study, introducing for the first time the nontoxic paramagnetic ^{19}F MR tracers with much better in cellulo accumulation that enables real in vivo cell tracking.

■ CONCLUSIONS

We investigated the potential of nickel(II) complexes of fluorinated cyclam derivatives as ^{19}F MR tracers. So far, mostly lanthanide(III) complexes have been used for this purpose. Several structurally related 1,8-bis(2,2,2-trifluoroethyl) cyclam derivatives (exhibiting six equivalent fluorine atoms) were designed and synthesized, and the properties of their nickel(II) complexes were investigated. In all complexes, the ligands are *trans*-hexacoordinated with two coordinating pendant arms in the apical positions. Depending on the pendant arms, the complexes exhibit significant differences in properties, such as stability, solubility, and particularly kinetic inertness. The complex with 2-aminoethyl pendant arms is highly labile while, quite surprisingly, the complex with the acetate pendants is the most kinetically inert nickel(II) complex described to date. The divalent nickel induces a paramagnetic shift of the ^{19}F resonances, as well as significant paramagnetic relaxation time enhancement, and the values of these parameters are not dependent on the donor character of the pendant arms.

The ^{19}F NMR T_1 relaxation times are in a millisecond range, and they are perfectly suitable for utilization of ultrashort MRI pulse sequences and, thus, the sensitivity can be greatly increased due to shortening of the repetition time and the possibility of acquiring many scans in a short time period. Unfortunately, only the complex of the bis(methylphosphonate) cyclam derivative is water-soluble and stable enough for practical applications. In phantoms, the complex could be detected by ^{19}F MRI in concentrations even below 1 mM at 11.8 T. For the first time, a nontoxic transition-metal ion complex was used for cell labeling. The proof of principle NMR/MRI experiments showed that fast imaging protocols can be utilized for detection of cells labeled with paramagnetic ^{19}F MR tracers. The sensitivity gain is significant due to a suitable combination of the paramagnetic ^{19}F MR tracers with the desired properties and an optimized experimental setup. The detection limits might be further decreased through better cellular uptake and/or by utilization of multimers with several paramagnetic complexes in one molecule of such ^{19}F MR tracers. The observed efflux of the ^{19}F MR tracer from the cells can be decreased or fully avoided by a suitable design of the ^{19}F MR tracers and/or their conjugation to a macromolecular or nanosized carrier. The data presented here prove that application of paramagnetic molecular ^{19}F MR tracers for cell labeling and tracking is a viable alternative to the already published protocols. In addition, our data also open doors for more routine utilization of transition-metal ion complexes as MRI contrast agents/tracers, proving that the complexes can exhibit the desired magnetic properties and, at the same time, can be fully nontoxic.

■ EXPERIMENTAL SECTION

Commercial chemicals (Fluka, Aldrich, CheMatech, Lachema) were used as obtained. Anhydrous solvents were obtained by established procedures or purchased. The compounds **te2f**·4HCl and H_2**te2f2p** and their nickel(II) complexes were prepared according to the literature.[20] Anhydrous $[Ni(EtOH)_4]Cl_2$ (prepared according to ref 21) was dissolved in anhydrous MeOH to give a 230 mM solution (the concentration was determined by chelatometric titration). The NMR spectra were recorded employing VNMRS300 (7.0 T), Varian UNITY INOVA 400 (9.4 T), Bruker Avance III 400 (9.4 T), Bruker Avance III 600 (14.3 T), and Magritech Spinsolve 43 MHz (0.94 T) spectrometers using 5 mm sample tubes. NMR chemical shifts are given in ppm, and coupling constants are reported in Hz. Unless stated otherwise, all NMR spectra were collected at 25 °C. For the ^1H and $^{13}C\{^1H\}$ NMR measurements in D_2O, *t*-BuOH was used as an internal standard ($\delta(^1H)$ 1.25 ppm, $\delta(^{13}C)$ 30.29 ppm). The pD in D_2O solutions was calculated by adding a +0.4 correction to the reading of the calibrated pH electrode. For the measurements in $CDCl_3$, TMS was used as an internal reference ($\delta(^1H)$ 0.00 ppm, $\delta(^{13}C)$ 0.00 ppm). For other solvents used for ^1H and ^{13}C NMR measurements, signals of (residual) non-/semideuterated solvents were used.[33] For ^{31}P NMR measurements, 70% aqueous H_3PO_4 was used as an external reference ($\delta(^{31}P)$ 0.00). For ^{19}F NMR measurements, trifluoroacetic acid (TFA, 0.1 M in D_2O, $\delta(^{19}F)$ −76.55 ppm, external standard), perfluorobenzene (PFB, $\delta(^{19}F)$ −164.9 ppm), or 2,2,2-trifluoroethanol (TFE, $\delta(^{19}F)$ −77.0 ppm) was used as an internal standard. The abbreviations s (singlet), t (triplet), q (quartet), m (multiplet), and b (broad) are used in order to express the signal multiplicities. All ^{13}C NMR spectra were measured using broad-band ^1H decoupling. Longitudinal relaxation times T_1 were measured using an inversion recovery sequence. Relaxation times T_2* were estimated from the signal half-width $\omega_{1/2}$ ($T_2^* = 1/(\pi\omega_{1/2})$), in Hz. Samples of the complexes or TFE for ^{19}F NMR measurements were dissolved in water (as saturated solutions for *trans*-[Ni(**te2f2a**)] and *trans*-[Ni(**te2f2py**)]$^{2+}$), and the pH was adjusted to 7.2 if necessary. The positive or negative ESI-MS spectra were acquired on a Bruker ESQUIRE 3000 spectrometer with ion-trap detection. Protonation constants of **te2f2ae** were determined by potentiometry as described.[20] Thin-layer chromatography (TLC) was performed on TLC aluminum sheets with silica gel 60 F254 (Merck). For UV detection, ninhydrin spray (0.5% in EtOH), dipping of the sheets in 5% aqueous $CuSO_4$, or I_2 vapor exposition were used. Elemental analyses were performed at the Institute of Macromolecular Chemistry (Academy of Sciences of the Czech Republic, Prague, Czech Republic). Exact concentrations of Ni(II) in stock solutions used for sample preparations were determined by AAS on an AAS 3 spectrometer (Zeiss-Jena) with acetylene/air flame atomization. Details of X-ray diffraction experimental data acquisition and fitting are given in the Supporting Information.

Synthesis of the Complexes. ***trans-[Ni(te2f2a)].*** H_2**te2f2a** (100 mg, 0.19 mmol) and $NiCl_2·6H_2O$ (91 mg, 39 mmol) were dissolved in 5% aqueous NH_3 (6 mL), and the mixture was stirred at 60 °C for 24 h. In addition to the ^{19}F NMR signal of the free ligand (δ −69 ppm, ∼10%), two new broad signals (paramagnetically induced relaxation, half-width ∼190 Hz) at δ −40 ppm (79%) and δ −21 ppm (12%) appeared. The mixture was heated to reflux for a further 2 days. After this period, the ^{19}F NMR signal of the free ligand disappeared. The intensities of two paramagnetic signals changed to 34% (δ −41 ppm) and 66% (δ −21 ppm). The reaction mixture was then sealed into a glass ampule and heated at 120 °C for 4 days, resulting in 95% abundance of the compounds with δ −21 ppm. The solution was then evaporated to dryness, and the residue was dissolved in MeOH and purified using chromatography (SiO_2, concentrated aqueous NH_3/EtOH 1/5 v/v, R_f = 0.8). The complex was isolated by precipitation on addition of Et_2O (∼20 mL) to its MeOH solution (∼5 mL) with a few drops of EtOH (∼0.5 mL), yielding 47 mg of violet powder. ^{19}F NMR (282 MHz, D_2O, pD 7.1): −21.86 (s, $\omega_{1/2}$ = 310 Hz). HR-MS: 537.1425 (calcd 537.1447, {[Ni(**te2f2a**)] + H}$^+$). Single crystals of *trans*-[Ni(**te2f2a**)]·2EtOH suitable for an X-ray diffraction study were prepared by slow vapor diffusion of Et_2O into an oversaturated solution of the complex in MeOH/EtOH (10/1), which was saturated in the boiling mixture and then carefully cooled to room temperature.

trans-[Ni(te2f2ae)](ClO$_4$)$_2$. **te2f2ae**·$4H_2O$·4HCl (∼430 mg, 0.64 mmol) was portioned between 5% aqueous NaOH (50 mL) and $CHCl_3$ (3 × 50 mL). The organic phases were combined, dried with anhydrous Na_2SO_4, and evaporated to dryness, yielding a viscous oil. The oil was dissolved in anhydrous MeOH (10 mL) to give a stock solution (64 mM) of the ligand. This solution (1 mL, 0.064 mmol of the ligand) was mixed with 278 μL (0.064 mmol) of the $[Ni(EtOH)_4](ClO_4)_2$ stock solution (prepared by reaction of the stock solution of $[Ni(EtOH)_4]Cl_2$ (0.5 mL, 0.12 mmol) with 45 mg (0.22 mmol) of $AgClO_4$; precipitated AgCl was filtered off). After the mixture was stirred at 60 °C for 3 h, a violet precipitate of the product appeared. The product was filtered off, washed with Et_2O, and dried in air on the filter to yield a fine violet powder (30 mg). ^{19}F NMR (282 MHz, D_2O, pD 9.3): −23.62 (s, $\omega_{1/2}$ = 386 Hz). HR-MS: 226.1517 (calcd 226.1526, [**te2f2ae** + 2H]$^{2+}$); 254.1117 (calcd 254.1124, [Ni**te2f2ae**]$^{2+}$); 451.2970 (calcd 451.2978, [**te2f2ae**+H]$^+$); 543.1931 (calcd 543.1942, {[Ni**te2f2ae**]$^{2+}$ + Cl^-}).

To obtain crystals suitable for X-ray analysis, the reaction was performed at ambient temperature using $[Ni(EtOH)_4]^{2+}$ with a substoichiometric amount of Cl^-. An MeOH solution containing 0.5 equiv of Cl^- was obtained from a stock solution of $[Ni(EtOH)_4]Cl_2$ (0.5 mL of the stock solution, 0.12 mmol) and $AgClO_4$ (23 mg, 0.11 mmol). This solution (130 μL) was then mixed with 1 equiv of **te2f2ae** MeOH stock solution prepared as mentioned above from 20 mg of **te2f2ae**·$4H_2O$·4HCl (30 μmol). Under these conditions, violet single crystals of *trans*-Ni(**te2f2ae**)]$(ClO_4)_2$·2MeOH appeared after approximately 5 days. The substoichiometric amount of $AgClO_4$ was crucial as, if the stoichiometric amount of $AgClO_4$ was used, the complex formation/crystallization was too fast and the product was obtained only as a microcrystalline powder.

trans-[Ni(te2f2py)](ClO$_4$)$_2$. A stock solution of $Ni(ClO_4)_2$ in MeOH was prepared by dissolution of $Ni(ClO_4)_2·6H_2O$ (419 mg, 1.15 mmol) in MeOH (50 mL). Its concentration (21.7 mM) was determined by chelatometric titration. The free ligand **te2f2py** was extracted with $CHCl_3$ (3 × 10 mL) from a solution of **te2f2py**·6HCl·$3H_2O$ (100 mg, 0.12 mmol) in 5% aqueous NaOH (10 mL). The organic phases were combined and dried over anhydrous Na_2SO_4, and the solvent was evaporated off. The solid product was dissolved in CH_3NO_2 (10 mL), and the $Ni(ClO_4)_2$ stock solution in MeOH (5.35 mL) was added. Methanol was slowly distilled off as the reaction mixture was heated to reflux for 2 h. The volatiles were evaporated in vacuo. The solid residue was dissolved in a minimal amount of CH_3NO_2 and the product was precipitated by addition of Et_2O (50 mL) and filtered off, yielding a light brown powder (67 mg) which is only slightly soluble in water. ^{19}F NMR (282 MHz, D_2O, pD 7.71): −19.55 (s, $\omega_{1/2}$ = 418 Hz). HR-MS: 302.1120 (calcd 302.1124, [Ni(**te2f2py**)]$^{2+}$); 639.1941 (calcd 639.1942, {[Ni(**te2f2py**)] + Cl}$^+$).

Crystals of *trans*-[Ni(**te2f2py**)]$(ClO_4)_2$ suitable for X-ray diffraction were obtained by a slow vapor diffusion of THF into a solution of the complex in CH_3NO_2.

Decomplexation Reactions. Decomplexation kinetics of complexes was followed by ^{19}F NMR spectroscopy. The reaction rate constants, k_{obs}, were determined from the time change of NMR signal integral value, $I(t)$, employing three-parameter exponential functions $I(t) = A + B\exp(-k_{obs}/t)$ used for data fitting, where t is time and A and B are parameters related to the initial and the final integral values. (i) A small amount (∼2 mg) of *trans*-[Ni(**te2f2a**)] was dissolved in ∼12 M aqueous HCl, and 1 drop of 2,2,2-trifluorethanol (TFE) was added as an internal reference. The solution was heated to 80 °C in a flame-sealed NMR tube. Complex dissociation was followed for 7 weeks, showing a half-time of 14 days. (ii) A 0.1 M HEPES aqueous buffer (236 mg in 10 mL of water) with pH adjusted by 5% aqueous NaOH was prepared. A small amount (∼2 mg) of the solid *trans*-

[Ni(**te2f2ae**)](ClO$_4$)$_2$ was dissolved in the buffer solution (0.5 mL) with 1 drop of TFE. Dissociation was followed using ^{19}F NMR at 25 °C, resulting in half-times of 2.8(7), 3.4(7), and 3(3) h at pH 6.8, 7.8, and 8.4, respectively. The dissociation experiment was also carried out at pD ~13 in a borate buffer (6.6 mg of H_3BO_3 in 1 mL of D_2O) at 25 °C to give a half-time of 4.8(3) h. (iii) A small amount (~2 mg) of *trans*-[Ni(**te2f2py**)](ClO$_4$)$_2$ was suspended in 1 M aqueous HCl, and the rest of the undissolved complex was filtered off. One drop of TFE was added as an internal reference. The reaction had a half-time of 3.3(6) h at 80 °C.

MRI Visualization Experiments. Experiments were performed on a Bruker Avance III HD spectrometer (Bruker Biospin, Germany) operating at 11.8 T (500 MHz for ^{1}H) equipped with a GREAT 60 triple gradient amplifier and Micro-5 microimaging probehead consisting of an *x,y,z* gradient coil (maximum gradient amplitude 300 G/cm) and ^{1}H radio frequency coil tunable to ^{19}F designed for 5 mm NMR tubes. The ^{19}F NMR resonance frequencies for the Ni(II) complexes and for TFE solutions were 470.884 and 470.858 MHz, respectively. Standard pulse sequences for UTE[10] and RARE[32] sequences from the ParaVision 6 library (Bruker Biospin, Germany) were used. The UTE was measured in FID-acquisition mode, and trajectory calibration was done on a sample of TFE with a water ratio of 1/3. One glass capillary (1.1 mm inner diameter) with a 16.7 mM aqueous solution of *trans*-[Ni(**te2f2p**)]$^{2-}$ complex and another with 33.1 mM aqueous TFE were placed together into a 5 mm glass tube. (i) The following parameters were used for the ^{19}F UTE measurement: excitation 90° pulse length 0.105 ms; TR 5.5 ms; TE 0.091 ms; BW 25 kHz; field of view 5 × 5 mm; slice thickness 4 mm; 202 projections; number of averages 512; reconstruction matrix of 64 × 64; measured in 9 min 29 s. (ii) The following parameters were used for the ^{19}F RARE: excitation 90° pulse length 2.1 ms; TR = 3000 ms; TE = 7 ms; BW 15 kHz; field of view 5 × 5 mm; slice thickness 4 mm; RARE factor 64; number of averages 190; reconstruction matrix of 64 × 64 points; measured in 9 min 30 s. (iii) The following parameters were used for the ^{1}H FLASH measurement of position of two capillaries: excitation 15° with duration 0.84 ms; TR 100 ms; TE 2.5 ms; bandwidth 50 kHz; field of view 5 × 5 mm; slice thickness 1 mm; number of averages 4; reconstruction matrix 128 × 128; measured in 51.2 s.

Cell samples were imaged using the following sequences. (i) Vertical ^{1}H MR images were obtained by a gradient echo sequence with the following parameters: TR = 100 ms, echo time TE = 2.1 ms, flip angle 90°, number of acquisitions NA = 8, field of view FOV = 20 × 20 mm, slice thickness 1 mm, matrix 128 × 128. (ii) Horizontal ^{19}F MR images were obtained using a UTE sequence with the following parameters: excitation pulse 90° (pulse shape optimized by means of the Shinnar−Le Roux algorithm implemented by Paravision 6.0 software)[34] with a duration of 0.158 ms; TR = 4.5 ms; TE = 0.111 ms; bandwidth 20 kHz, field of view 10 × 10 mm; slice thickness 5 mm; 106 projections, number of averages 6000 and 1200; reconstruction matrix of 34 × 34 points; measured in 48 and 9.5 min for cell samples labeled in medium containing 50 and 100 mM of ^{19}F, respectively. (iii) The following parameters were used for ^{19}F UTE in the vertical direction: excitation pulse 90° (pulse shape optimized by means of the Shinnar−Le Roux algorithm implemented by Paravision 6.0 software)[34] with a duration of 0.158 ms; TR = 6.5 ms; TE = 0.111 ms; bandwidth 20 kHz; field of view 20 × 20 mm; slice thickness 5 mm; 208 projections; number of averages 20000; reconstruction matrix of 66 × 66 points; measured in 7 h 30 min.

Toxicity Studies. Rat mesenchymal stem cells (MSCs) from Lewis rats were used for cell labeling experiments. MSCs were isolated from the visceral adipose tissue of donor Brown−Norway rats according to a standard protocol.[35] Briefly, the tissue was digested by collagenase, filtered, overlayered on 5 mL of Ficoll 1077 g/mL (Ficoll-Paque Premium, GE Healthcare Bio Science AB, Sweden) and spun. The cells in the interphase were collected and seeded into a tissue flask. The cells were passaged to reach the sufficient amount. Then, the cells were redistributed into flasks (1 × 10^6 cells per 5 mL/25 cm^2 flask) and labeled by addition of an aqueous solution of the Na$^+$ salt of *trans*-[Ni(**te2f2p**)]$^{2-}$ to the culture medium at four concentrations: 4.2, 8.3, 16.7, and 25.0 mM. Cells cultured in the medium without the complex served as control samples. After 24 h of incubation (37 °C, 5% CO_2 atmosphere), the cells were washed three times with PBS (5 mL per flask). The medium removed from the flasks was collected and examined for the presence of nonadherent cells. The medium collected from all samples contained only a negligible amount of cells. The cells were detached from the flask by addition of trypsin (2 mL, 0.05%). After incubation for 5 min, trypsinization was stopped by adding 10% fetal bovine serum (5 mL). The cells were collected and centrifuged at 1500 rpm for 5 min. The pellet was resuspended in PBS (5 mL) and centrifuged once more to remove any remains of the complex from the cultured medium. Then, the cell pellet was resuspended in PBS (0.5 mL), and the cells were manually counted in the Burker chamber under a light microscope. Cell viability was determined by using the Trypan blue (Sigma-Aldrich) exclusion test.[36] Cell viability was expressed as a ratio of viable (unstained) cells to all cells. The viability of the labeled MSCs varied between 98% (the lowest complex concentration) to 94% (the highest concentration). The control samples reached viabilities of 98 and 99%. To express possible differences in adherence and proliferation of cells incubated in the presence of the tracer, we also calculated the cell gain as a ratio of number of viable harvested labeled cells and number of viable harvested cells in a control sample (given as a percentage). The ratio reflects not only the cell viability but also the cell proliferation and/or loss of the nonadherent cells during washing and other steps of the protocol. The gain reached 98% (labeling at 8.3 mM) and 95% (labeling at 16.7 mM).

For the MR experiments, concentrations of 8.3 and 16.7 mM of the *trans*-[Ni(**te2f2p**)]$^{2-}$ complex were chosen for labeling. A procedure similar to that described above was used. Flasks with a larger volume (30 mL/180 cm^2) were used to reach 4.3 × 10^6 cells per sample. After labeling and washings (i.e., removal of remaining complex from medium outside the cells), the cells were fixed using 4% aqueous formaldehyde, transferred into Shigemi tubes, and used for the MR imaging.

In-Cell Nickel Content Determination. The nickel concentration in the cell culture suspension samples was determined by the ETV-ICP-OES (electrothermal vaporization inductively coupled plasma optical emission spectrometry) technique. Using this method, the individual samples are heated in a graphite oven and evaporated. The dry aerosol formed is transported into the plasma, atomized, and excited, and the time-dependent emitted characteristic light signal is processed by the spectrometer.

The whole amount of the individual suspension sample (cells and the surrounding liquid) was quantitatively transferred into a graphite boat and dried. The boats were heated under an optimized temperature program in the electrothermal vaporization device ETV 4000c (Spectral Systems Peter Perzl, Germany). The emitted radiation was analyzed by a Spectro Arcos SOP ICP-OES spectrometer (Spectro A.I., Germany). The method was calibrated and validated using certified solid and aqueous standards at several wavelengths to cover the quantification range 0−1.2 μg of Ni abs.

■ ASSOCIATED CONTENT

Ⓢ Supporting Information

The Supporting Information is available free of charge on the ACS Publications website at DOI: 10.1021/acs.inorgchem.7b02119.

> Additional experimental data, all experimental crystallographic data, ligand syntheses, and additional figures and tables as described in the text (PDF)

Accession Codes

CCDC 1558410−1558419 and 1558786 contain the supplementary crystallographic data for this paper. These data can be obtained free of charge via www.ccdc.cam.ac.uk/data_request/cif, or by emailing data_request@ccdc.cam.ac.uk, or by contacting The Cambridge Crystallographic Data Centre, 12 Union Road, Cambridge CB2 1EZ, UK; fax: +44 1223 336033.

AUTHOR INFORMATION

Corresponding Author

*P.H.: tel, +420-221951263; fax, +420-221951253; e-mail, petrh@natur.cuni.cz.

ORCID

Jan Kotek: 0000-0003-1777-729X

Petr Hermann: 0000-0001-6250-5125

Notes

The authors declare no competing financial interest.

ACKNOWLEDGMENTS

The authors thank J. Englich for discussions regarding image signal-to-noise ratio, Z. Böhmová for potentiometric data, and J. Hraníček for AAS measurement. The study was supported by the Ministry of Health of the Czech Republic (Institute for Clinical and Experimental Medicine-IKEM, Project IN 00023001 to A.G. and V.H.), the Ministry of Education of the Czech Republic (MŠMT Inter-COST, no. LTC17067 to P.H., J.L., J.B., and J.K.), and the Czech Science Foundation (GACR P205-16-03156S to J.B., J.K., A.G., and V.H.). The 11.8 T NMR spectrometer was purchased within Project CZ.2.16/3.1.00/21566 funded by the Operational Programme Prague-Competitiveness. The work was carried out within the framework of CA15209 COST Action.

REFERENCES

(1) Watt, F. M.; Driskell, R. R. The therapeutic potential of stem cells. *Philos. Trans. R. Soc., B* **2010**, *365*, 155−163.

(2) Schmidt, R.; Nippe, N.; Strobel, K.; Masthoff, M.; Reifschneider, O.; Castelli, D. D.; Höltke, C.; Aime, S.; Karst, U.; Sunderkötter, C.; Bremer, C. Faber C. Highly shifted proton MR imaging: Cell tracking by using direct detection of paramagnetic compounds. *Radiology* **2014**, *272*, 785−795.

(3) (a) Harvey, P.; Blamire, A. M.; Wilson, J. I.; Finney, K.-L. N. A.; Funk, A. M.; Senanayake, P. K.; Parker, D. Moving the goal posts: enhancing the sensitivity of PARASHIFT proton magnetic resonance imaging and spectroscopy. *Chem. Sci.* **2013**, *4*, 4251−4258. (b) Senanayake, P. K.; Rogers, N. J.; Finney, K.-L. N. A.; Harvey, P.; Funk, A. M.; Wilson, J. I.; O'Hogain, D.; Maxwell, R.; Parker, D.; Blamire, A. M. A new paramagnetically shifted imaging probe for MRI. *Magn. Reson. Med.* **2017**, *77*, 1307−1317. (c) Mason, K.; Rogers, N. J.; Suturina, E. A.; Kuprov, I.; Aguilar, J. A.; Batsanov, A. S.; Yufit, D. S. Parker D. PARASHIFT probes: solution NMR and X-ray structural studies of macrocyclic ytterbium and yttrium complexes. *Inorg. Chem.* **2017**, *56*, 4028−4038.

(4) *Fluorine Magnetic Resonance Imaging*; Flogel, U., Ahrens, E., Eds.; CRC Press: Boca Raton, FL, 2016.

(5) Amiri, H.; Sriniva, M.; Veltien, A.; van Uden, M. J.; de Vries, I. J.; Heerschap, A. Cell tracking using ^{19}F magnetic resonance imaging: technical aspects and challenges towards clinical applications. *Eur. Radiol.* **2015**, *25*, 726−735.

(6) (a) Ruiz-Cabello, J.; Barnett, B. P.; Bottomley, P. A.; Bulte, J. W. Fluorine (^{19}F) MRS and MRI in biomedicine. *NMR Biomed.* **2011**, *24*, 114−129. (b) Knight, J. C.; Edwards, P. G.; Paisey, S. J. Fluorinated contrast agents for magnetic resonance imaging; a review of recent developments. *RSC Adv.* **2011**, *1*, 1415−1425. (c) Yu, J.-X.; Hallac, R. R.; Chiguru, S.; Mason, R. P. New frontiers and developing applications in ^{19}F NMR. *Prog. Nucl. Magn. Reson. Spectrosc.* **2013**, *70*, 25−49. (d) Tirotta, I.; Dichiarante, V.; Pigliacelli, C.; Cavallo, G.; Terraneo, G.; Bombelli, F. B. ^{19}F Magnetic resonance imaging (MRI): From design of materials to clinical applications. *Chem. Rev.* **2015**, *115*, 1106−1129.

(7) Ahrens, E. T.; Flores, R.; Xu, H.; Morel, P. A. *In vivo* imaging platform for tracking immunotherapeutic cells. *Nat. Biotechnol.* **2005**, *23*, 983−987.

(8) (a) Srinivas, M.; Heerschap, A.; Ahrens, E. T.; Figdor, C. G.; de Vries, I. J. M. ^{19}F MRI for quantitative *in vivo* cell tracking. *Trends Biotechnol.* **2010**, *28*, 363−370. (b) Boehm-Sturm, P.; Mengler, L.; Wecker, S.; Hoehn, M.; Kallur, T. *In vivo* tracking of human neural stem cells with ^{19}F magnetic resonance imaging. *PLoS One* **2011**, *6*, e29040. (c) Srinivas, M.; Boehm-Sturm, P.; Figdor, C. G.; de Vries, I. J.; Hoehn, M. Labeling cells for *in vivo* tracking using ^{19}F MRI. *Biomaterials* **2012**, *33*, 8830−8840. (d) Temme, S.; Boenner, F.; Schrader, J.; Floegel, U. ^{19}F magnetic resonance imaging of endogenous macrophages in inflammation. *Wiley Interdiscip. Rev.: Nanomed. Nanobiotechnol.* **2012**, *4*, 329−343. (e) Ahrens, E. T.; Zhong, J. *In vivo* MRI cell tracking using perfluorocarbon probes and fluorine-19 detection. *NMR Biomed.* **2013**, *26*, 860−871. (f) Yu, Y. B. Fluorinated dendrimers as imaging agents for ^{19}F MRI. *Wiley Interdiscip. Rev.: Nanomed. Nanobiotechnol.* **2013**, *5*, 646−661.

(9) (a) Partlow, K. C.; Chen, J.; Brant, J. A.; Neubauer, A. M.; Meyerrose, T. E.; Creer, M. H.; Nolta, J. A.; Caruthers, S. D.; Lanza, G. M.; Wickline, S. A. ^{19}F magnetic resonance imaging for stem/progenitor cell tracking with multiple unique perfluorocarbon nanobeacons. *FASEB J.* **2007**, *21*, 1647−1654. (b) Ahrens, E. T.; Helfer, B. M.; O'Hanlon, C. F.; Schirda, C. Clinical cell therapy imaging using a perfluorocarbon tracer and fluorine-19 MRI. *Magn. Reson. Med.* **2014**, *72*, 1696−1701. (c) Gaudet, J. M.; Ribot, E. J.; Chen, Y.; Gilbert, K. M.; Foster, P. J. Tracking the fate of stem cell implants with fluorine-19 MRI. *PLoS One* **2015**, *10*, e0118544. (d) Vu-Quang, H.; Vinding, M. S.; Xia, D.; Nielsen, T.; Ullisch, M. G.; Dong, M. D.; Nielsen, N. C.; Kjems, J. Chitosan-coated poly(lactic-co-glycolic acid) perfluorooctyl bromidenanoparticles for cell labeling in ^{19}F magnetic resonance imaging. *Carbohydr. Polym.* **2016**, *136*, 936−944. (e) Gonzales, C.; Yoshihara, H. A. I.; Dilek, N.; Leignadier, J.; Irving, M.; Mieville, P.; Helm, L.; Michielin, O.; Schwitter, J. *In-Vivo* detection and tracking of T cells in various organs in a melanoma tumor model by ^{19}F-fluorine MRS/MRI. *PLoS One* **2016**, *11*, e0164557. (f) Makela, A. V.; Gaudet, J. M.; Foster, P. J. Quantifying tumor associated macrophages in breast cancer: a comparison of iron and fluorine-based MRI cell tracking. *Sci. Rep.* **2017**, *7*, 42109.

(10) Robson, M. D.; Gatehouse, M. D.; Bydder, M.; Bydder, G. M. Magnetic resonance: an introduction to ultrashort TE (UTE) imaging. *J. Comp. Assist. Tomogr.* **2003**, *27*, 825−846.

(11) (a) Kok, M. B.; de Vries, A.; Abdurrachim, D.; Prompers, J. J.; Grull, H.; Nicolay, K.; Strijkers, G. J. Quantitative ^{1}H MRI^{19}F MRI, and ^{19}F MRS of cell-internalized perfluorocarbon paramagnetic nanoparticles. *Contrast Media Mol. Imaging* **2011**, *6*, 19−27. (b) Hu, L.; Zhang, L.; Chen, J.; Lanza, G. M.; Wickline, S. A. Diffusional mechanisms augment the fluorine MR relaxation in paramagnetic perfluorocarbon nanoparticles that provides a "relaxation switch" for detecting cellular endosomal activation. *Magn. Reson. Imaging* **2011**, *34*, 653−661. (c) Kislukhin, A. A.; Xu, H.; Adams, S. R.; Narsinh, K. H.; Tsien, R. Y.; Ahrens, E. T. Paramagnetic fluorinated nanoemulsions for sensitive cellular fluorine-19 magnetic resonance imaging. *Nat. Mater.* **2016**, *15*, 662−668.

(12) (a) Senanayake, P. K.; Kenwright, A. M.; Parker, D.; van der Hoorn, S. Responsive fluorinated lanthanide probes for ^{19}F magnetic resonance spectroscopy. *Chem. Commun.* **2007**, 2923−2925. (b) Kenwright, A. M.; Kuprov, I.; De Luca, E.; Parker, D.; Pandya, S. U.; Senanayake, P. K.; Smith, D. G. ^{19}F NMR based pH probes: lanthanide(III) complexes with pH-sensitive chemical shifts. *Chem. Commun.* **2008**, 2514−2516. (c) Chalmers, K. H.; De Luca, E.; Hogg, N. H. M.; Kenwright, A. M.; Kuprov, I.; Parker, D.; Botta, M.; Wilson, J. I.; Blamire, A. M. Design principles and theory of paramagnetic fluorine-labelled lanthanide complexes as probes for ^{19}F magnetic resonance: A proof-of-concept study. *Chem. - Eur. J.* **2010**, *16*, 134−148. (d) Chalmers, K. H.; Botta, M.; Parker, D. Strategies to enhance signal intensity with paramagnetic fluorine-labelled lanthanide complexes as probes for ^{19}F magnetic resonance. *Dalton Trans.* **2011**, *40*, 904−913. (e) Harvey, P.; Kuprov, I.; Parker, D. Lanthanide

complexes as paramagnetic probes for ^{19}F magnetic resonance. *Eur. J. Inorg. Chem.* **2012**, *2012*, 2015−2022. (f) Harvey, P.; Chalmers, K. H.; De Luca, E.; Mishra, A.; Parker, D. Paramagnetic ^{19}F chemical shift probes that respond selectively to calcium or citrate levels and signal ester hydrolysis. *Chem. - Eur. J.* **2012**, *18*, 8748−8757. (g) De Luca, E.; Harvey, P.; Chalmers, K. H.; Mishra, A.; Senanayake, P. K.; Wilson, J. I.; Botta, M.; Fekete, M.; Blamire, A. M.; Parker, D. Characterisation and evaluation of paramagnetic fluorine labelled glycol chitosan conjugates for ^{19}F and ^{1}H magnetic resonance imaging. *JBIC, J. Biol. Inorg. Chem.* **2014**, *19*, 215−227.

(13) (a) Chalmers, K. H.; Kenwright, A. M.; Parker, D.; Blamire, A. M. ^{19}F-Lanthanide complexes with increased sensitivity for ^{19}F MRI: optimization of the MR acquisition. *Magn. Reson. Med.* **2011**, *66*, 931−936. (b) Schmid, F.; Höltke, C.; Parker, D.; Faber, C. Boosting ^{19}F MRI—SNR efficient detection of paramagnetic contrast agents using ultrafast sequences. *Magn. Reson. Med.* **2013**, *69*, 1056−1062.

(14) Cakić, N.; Savić, T.; Stricker-Shaver, J.; Truffault, V.; Platas-Iglesias, C.; Mirkes, C.; Pohmann, R.; Scheffler, K.; Angelovski, G. Paramagnetic lanthanide chelates for multicontrast MRI. *Chem. Commun.* **2016**, *52*, 9224−9227.

(15) Jiang, Z.-X.; Feng, Y.; Yu, Y. B. Fluorinated paramagnetic chelates as potential multi-chromic ^{19}F tracer agents. *Chem. Commun.* **2011**, *47*, 7233−7235.

(16) (a) Xie, D.; King, T. L.; Banerjee, A.; Kohli, T. V.; Que, E. L. Exploiting copper redox for ^{19}F magnetic resonance-based detection of cellular hypoxia. *J. Am. Chem. Soc.* **2016**, *138*, 2937−2940. (b) Yu, M.; Xie, D.; Phan, K. P.; Enriquez, J. S.; Luci, J. J.; Que, E. L. A Co^{II} complex for ^{19}F MRI-based detection of reactive oxygen species. *Chem. Commun.* **2016**, *52*, 13885−13888.

(17) Thorarinsdottir, A. E.; Gaudette, A. I.; Harris, T. D. Spin-crossover and high-spin iron(II) complexes as chemical shift ^{19}F magnetic resonance thermometers. *Chem. Sci.* **2017**, *8*, 2448−2456.

(18) Mizukami, S.; Takikawa, R.; Sugihara, F.; Hori, Y.; Tochio, H.; Wälchli, M.; Shirakawa, M.; Kikuchi, K. Paramagnetic relaxation-based ^{19}F MRI probe to detect protease activity. *J. Am. Chem. Soc.* **2008**, *130*, 794−795.

(19) Srivastava, K.; Weitz, E. A.; Peterson, K. L.; Marjańska, M.; Pierre, V. C. Fe- and Ln-DOTAm-F12 are effective paramagnetic fluorine contrast agents for MRI in water and blood. *Inorg. Chem.* **2017**, *56*, 1546−1557.

(20) Blahut, J.; Hermann, P.; Gálisová, A.; Herynek, V.; Císařová, I.; Tošner, Z.; Kotek, J. Nickel(II) complexes of *N*-CH$_2$CF$_3$ cyclam derivatives as contrast agents for ^{19}F magnetic resonance imaging. *Dalton Trans.* **2016**, *45*, 474−478.

(21) Ward, L. G. L.; Pipa, J. R. *Inorg. Synth.* **1972**, *13*, 154−164.

(22) (a) Kotek, J.; Hermann, P.; Císařová, I.; Rohovec, J.; Lukeš, I. The *cis*/*trans*-isomerism on cobalt(III) complexes with 1,4,8,11-tetraazacyclotetradecane-1,8-bis(methylphosphonic acid). *Inorg. Chim. Acta* **2001**, *317*, 324−330. (b) Havlíčková, J.; Medová, H.; Vitha, T.; Kotek, J.; Císařová, I.; Hermann, P. Coordination properties of cyclam (1,4,8,11-tetraazacyclotetradecane) endowed with two methylphosphonic acid pendant arms in the 1,4-positions. *Dalton Trans.* **2008**, 5378−5386.

(23) Bosnich, B.; Poon, C. K.; Tobe, M. Complexes of cobalt(III) with a cyclic tetradentate secondary amine. *Inorg. Chem.* **1965**, *4*, 1102−1108.

(24) Comparone, A.; Kaden, T. A. Copper(II) and nickel(II) complexes of '*trans*'-difunctionalized tetraaza macrocycles. *Helv. Chim. Acta* **1998**, *81*, 1765−1772.

(25) Batsanov, A. S.; Goeta, A. E.; Howard, J. A. K.; Maffeo, D.; Puschmann, H.; Williams, J. A. G. Nickel(II) complexes of the isomeric tetraazamacrocyclic ligands 1,11- and 1,8-bis(2-pyridylmethyl)-cyclam and of a structurally constrained *N*^{4},*N*^{8}-methylene bridged analogue. *Polyhedron* **2001**, *20*, 981−986.

(26) Choi, K.-Y.; Suh, I.-H.; Kim, J.-G.; Park, Y.-S.; Jeong, S.-I.; Kim, I.-K.; Hong, C.-P.; Choi, S.-N. Synthesis and characterization of copper(II) and nickel(II) complexes of a di-*N*-carboxymethylated tetraaza macrocycle. *Polyhedron* **1999**, *18*, 3013−3018.

(27) (a) Hertli, L.; Kaden, T. A. Metal complexes with macrocyclic ligands, V. Formation and dissociation kinetics of the pentacoordinated Ni^{2+}, Cu^{2+}, Co^{2+} and Zn^{2+} complexes with 1,4,8,11-tetramethyl-1,4,8,11-tetraazacyclotetradecane. *Helv. Chim. Acta* **1974**, *57*, 1328−1332. (b) Billo, E. J. Kinetics of dissociation and isomerization of *cis*-Ni([14]aneN4)(H$_2$O)$_2$$^{2+}$ in aqueous perchloric acid solutions. *Inorg. Chem.* **1984**, *23*, 236−238. (c) Dey, B.; Coates, J. H.; Duckworth, P. A.; Lincoln, S. F.; Wainwright, K. P. Complexation of cobalt(II), nickel(II) and copper(II) by the pendant arm macrocyclic ligand *N*,*N*′,*N*″,*N*‴-tetrakis(2-hydroxyethyl)-l,4,8,11-tetraazacyclotetradecane. *Inorg. Chim. Acta* **1993**, *214*, 77−84. (d) Turonek, M. L.; Duckworth, P. A.; Laurence, G. S.; Lincoln, S. F.; Wainwright, K. P. Equilibrium and kinetic studies of complexes of the pendant donor macrocycles *N*,*N*′,*N*″,*N*‴-tetrakis(2-hydroxyethyl)-1,4,7,10-tetraazacyclododecane (THEC-12) and *N*, *N*′, *N*″, *N*‴-tetrakis(2-hydroxyethyl)-1,4,8,12-tetraazacyclopentadecane (THEC-15). *Inorg. Chim. Acta* **1995**, *230*, 51−57.

(28) Brücher, E.; Tircsó, G.; Baranyai, Z.; Kovács, Z.; Sherry, A. D. In *The Chemistry of Contrast Agents in Medical Magnetic Resonance Imaging*, 2nd ed.; Merbach, A., Helm, L., Tóth, É., Eds.; Wiley: Chichester, United Kingdom, 2013; pp 157−208.

(29) Bertini, I.; Luchinat, C. Relaxation. *Coord. Chem. Rev.* **1996**, *150*, 77−110.

(30) Helm, L. Relaxivity in paramagnetic systems: Theory and mechanisms. *Prog. Nucl. Magn. Reson. Spectrosc.* **2006**, *49*, 45−64.

(31) Belorizky, E.; Fries, P. H.; Helm, L.; Kowalewski, J.; Kruk, D.; Sharp, R. R.; Westlund, P.-O. Comparison of different methods for calculating the paramagnetic relaxation enhancement of nuclear spins as a function of the magnetic field. *J. Chem. Phys.* **2008**, *128*, 052315.

(32) Hennig, J.; Nauerth, A.; Friedburg, H. RARE imaging: a fast imaging method for clinical MR. *Magn. Reson. Med.* **1986**, *3*, 823−833.

(33) Gottlieb, H. E.; Kotlyar, V.; Nudelman, A. NMR chemical shifts of common laboratory solvents as trace impurities. *J. Org. Chem.* **1997**, *62*, 7512−7515.

(34) Pauly, J.; Le Roux, P.; Nishimura, D.; Macovski, A. Parameter relations for the Shinnar-Le Roux selective excitation pulse design algorithm. *IEEE Trans. Med. Imaging* **1991**, *10*, 53−65 and citations therein.

(35) Fabryová, E.; Jirák, D.; Girman, P.; Zacharovová, K.; Gálisová, A.; Saudek, F.; Kříž, J. Effect of mesenchymal stem cells on the vascularization of the artificial site for islet transplantation in rats. *Transplant. Proc.* **2014**, *46*, 1963−1966.

(36) Carvalho, K. A.; Cury, C. C.; Oliveira, L.; Cattaned, R. I.; Malvezzi, M.; Francisco, J. C.; Pachalok, A.; Olandoski, M.; Faria-Neto, J. R.; Guarita-Souza, L. C. Evaluation of bone marrow mesenchymal stem cell standard cryopreservation procedure efficiency. *Transplant. Proc.* **2008**, *40*, 839−841.

Paramagnetic ^{19}F Relaxation Enhancement in Nickel(II) Complexes of *N*-Trifluoroethyl Cyclam Derivatives and Cell Labelling for ^{19}F MRI

Jan Blahut,[a] Karel Bernášek,[b] Andrea Gálisová,[c] Vít Herynek,[c] Ivana Císařová,[a] Jan Kotek,[a] Jan Lang,[b] Stanislava Matějková[d] and Petr Hermann[a]*

[a]Department of Inorganic Chemistry, Faculty of Science, Charles University (Univerzita Karlova), Hlavova 2030, 128 43 Prague 2, Czech Republic. Tel.: +420-221951263, fax: +420-221951253. E-mail: petrh@natur.cuni.cz.

[b]Department of Low Temperature Physics, Faculty of Mathematics and Physics, Charles University (Univerzita Karlova), V Holešovičkách 2, 180 00 Prague 8, Czech Republic.

[c]Department of Radiodiagnostic and Interventional Radiology, Magnetic Resonance Unit, Institute for Clinical and Experimental Medicine, Vídeňská 1958/9, 140 21 Prague 4, Czech Republic.

[d]Institute of Organic Chemistry and Biochemistry, Czech Academy of Sciences, Flemingovo nám. 2, 166 10 Prague, Czech Republic

Crystal structures of organic intermediates and free ligands

Both molecular structures of the benzyl intermediates are centrosymmetric. Due to planarity of the amide group in trifluoroacetyl derivative, the macrocycle has non-regular conformation (Figure S1). In the case of trifluoroethyl derivative, the macrocycle adopts rectangular (3,4,3,4)-B conformation,[1] and pyramidal amino groups are oriented that their free electron pairs point into the macrocycle cavity (Figure S2). The trifluoroethyl groups are bound to the nitrogen atoms present in the shorter sides of the rectangle backbone and the benzyl groups are turned towards these shorter edges, being a source of intermolecular hydrophobic interactions (Figure S3).

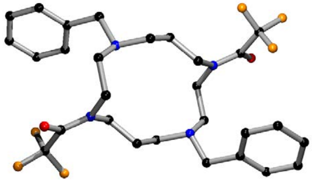

Figure S1: Molecular structure of 1,8-bis(trifluoroacetyl)-4,11-dibenzyl-1,4,8,11-tetraazacyclotetradecane found in its crystal structure. Colour code: C – black, N – blue, O – red, F – orange.

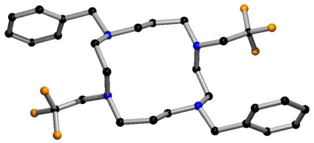

Figure S2: Molecular structure of 1,8-bis(trifluoroethyl)-4,11-dibenzyl-1,4,8,11-tetraazacyclotetradecane found in its crystal structure. Colour code: C – black, N – blue, F – orange.

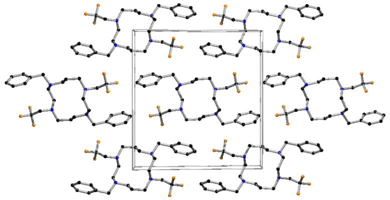

Figure S3: Crystal packing found in the structure of 1,8-bis(trifluoroethyl)-8,11-dibenzyl-1,4,8,11-tetraazacyclotetradecane. View down along the *a* axis. Colour code: C – black, N – blue, F – orange.

The centrosymmetric molecule of intermediate **1** adopts (3,4,3,4)-D conformation[1] of the macrocyclic unit with trifluoroethyl groups bound to the nitrogen atom lying in the corners of the rectangle (Figure S4). All pendant arms lie perpendicular to the longer edge of the macrocycle rectangle, and in the crystal packing, form hydrophobic layers oriented in the *xy* plane (Figure S5).

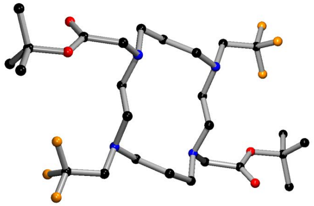

Figure S4: Molecular structure of the intermediate **1** found in its crystal structure. Colour code: C – black, N – blue, O – red, F – orange.

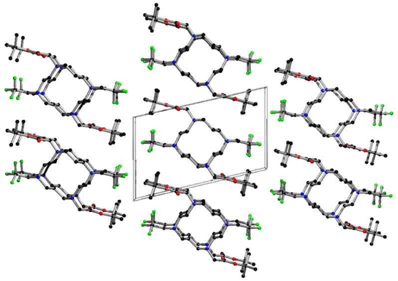

Figure S5: Crystal packing found in the structure of the intermediate **1**. View down along the *a* axis. Colour code: C – black, N – blue, O – red, F – orange.

The macrocyclic ligand cation (H_6**te2f2a**)$^{4+}$ found in crystal structure of (H_6**te2f2a**)Cl_4 adopts (3,4,3,4)-A conformation (Figure S6) which is the most common one for macrocycles those all amino groups are protonated. This conformation minimizes electrostatic repulsions of the positively charged amine groups.[1] Chloride counter-ions serve as acceptors of the hydrogen atoms in 2-D system of medium-to-strong hydrogen bonds with heavy-atom distances d(N,O⋯Cl) = 3.0 Å (Figure S7).

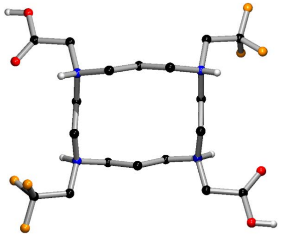

Figure S6: Molecular structure of the (H_6**te2f2a**)$^{4+}$ cation found in the crystal structure of (H_6**te2f2a**)Cl_4. Colour code: C – black, N – blue, O – red, H – white, F – orange.

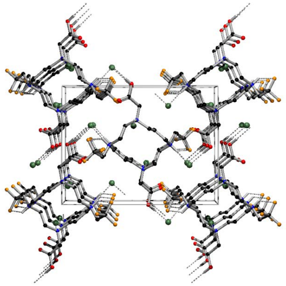

Figure S7: Crystal packing found in the structure of (H_6**te2f2a**)Cl_4. View down along the *a* axis. Colour code: C – black, N – blue, O – red, H – white, F – orange, Cl – dark green.

The macrocycle of intermediate **2** adopts centrosymmetric (3,4,3,4)-B conformation[1] with the trifluoroethyl groups bound to the nitrogen atoms in the longer sides of the backbone rectangle. Two phthalimidoethyl moieties point above and below the macrocyclic plane and the aromatic groups are oriented as dish cover above and below the macrocycle, respectively, with angle between the aromatic and macrocyclic planes ~26°.

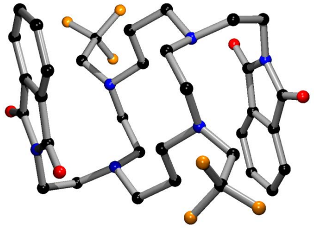

Figure S8: Molecular structure of the intermediate **2** found in its crystal structure. Colour code: C – black, N – blue, O – red, F – orange.

The ligand **te2f2py** adopts the same molecular conformation as 1,8-bis(trifluoroethyl)-8,11-dibenzyl-1,4,8,11-tetraazacyclotetradecane, see Figure S9.

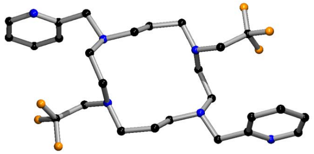

Figure S9: Molecular structure of **te2f2py** found in its crystal structure. Colour code: C – black, N – blue, F – orange.

Course of complexation of Ni(II) with H_2te2f2a

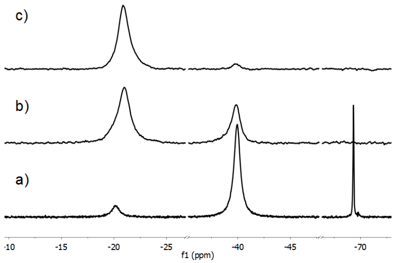

Figure S10: Time-dependence of ^{19}F NMR spectra during course of complexation of Ni(II) with H_2**te2f2a** in 5 % aq. NH_3: (**a**) after heating at 60 °C for 24 h, (**b**) after additional heating at 60 °C for 2 days and (**c**) after additional heating at 120 °C for another 4 days in sealed ampoule.

Crystal structures of Ni(II) complexes

Table S1: Selected distances found in the studied nickel(II) complexes (Å).

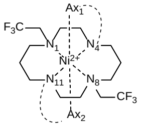

Parameter	**_trans_-[Ni(te2f2a)] ·2EtOH**	**_trans_-[Ni(te2f2ae)](ClO_4)$_2$ ·2MeOH**	**_trans_-[Ni(te2f2py)](ClO_4)$_2$**		**_trans_-(NH_4)[Ni(Hte2f2p)] ·4H_2O**		**_trans_-[Ni(te2f)(H_2O)$_2$]Cl_2**	**_trans_-[Ni(te2f)](ClO_4)$_2$** [ref. 2]	**_trans_-(NH_4)[Ni(Hte2f2p)] ·3.25H_2O** [ref. 2]	**_cis_-[Ni(te2f)(H_2O)](TsO)$_2$** [ref. 2]
			Molecule 1	Molecule 2	Molecule 1	Molecule 2				
						Bond lengths (Å)				
Ni–N1	2.233(2)	2.297(2)	2.212(3)	2.220(3)	2.222(2)	2.231(2)	2.192(2)	1.992(5)	2.221(2)	2.217(3)
Ni–N4	2.070(2)	2.067(2)	2.098(3); 2.104(19) [b]	2.111(4); 2.105(24) [b]	2.098(2)	2.092(2)	2.040(2)	1.946(5)	2.108(2)	2.087(3)
Ni–N8	2.234(2)	2.297(2) [a]	2.212(3) [a]	2.220(3) [a]	2.226(2)	2.234(2)	2.192(2) [a]	1.992(5) [a]	2.229(2)	2.254(3)
Ni–N11	2.070(2)	2.067(2) [a]	2.098(3) [a]; 2.104(19) [a,b]	2.111(4) [a]; 2.105(24) [a,b]	2.095(2)	2.094(2)	2.040(2) [a]	1.946(5) [a]	2.093(2)	2.072(3)
Ni–Ax1	2.042(1)	2.157(2)	2.260(3)	2.223(3)	2.066(1)	2.085(1)	2.132(2)	2.833(5) [c]	2.063(1)	2.072(2) [e]
Ni–Ax2	2.043(1)	2.157(2) [a]	2.260(3) [a]	2.223(3) [a]	2.104(1)	2.082(1)	2.132(2) [a]	2.833(5) [a,c]	2.102(1)	2.100(2) [e]
						Bond angles (°)				
Ax1-Ni-N1	89.23(5)	91.06(6)	90.4(1)	91.4(1)	89.95(5)	88.83(5)	86.45(6)	83.4(2)	91.02(6)	– [d]
Ax1-Ni-N4	83.20(6)	82.48(6)	78.8(1); 73.2(5) [b]	79.6(2); 78.9(8) [b]	87.02(5)	86.08(5)	88.29(8)	81.4(2)	86.62(6)	– [d]
Ax1-Ni-N8	91.07(5)	88.94(6) [a]	89.6(1) [a]	88.6(1) [a]	89.97(5)	91.57(5)	93.55(6) [a]	96.6(2) [a,c]	88.59(6)	– [d]
Ax1-Ni-N11	96.83(6)	97.52(6) [a]	101.2(1) [a]; 106.8(5) [a,b]	100.4(2) [a]; 101.1(8) [a,b]	92.18(5)	94.21(5)	91.71(8) [a]	98.6(2) [a,c]	91.63(6)	– [d]
Ax2-Ni-N1	91.38(5)	88.94(6) [a]	89.6(1) [a]	88.6(1) [a]	90.83(5)	90.74(5)	93.55(6) [a]	96.6(2) [a,c]	91.37(6)	– [d]
Ax2-Ni-N4	96.87(6)	97.52(6) [a]	101.2(1) [a]; 106.8(5) [a,b]	100.4(2) [a]; 101.1(8) [a,b]	94.53(5)	93.14(5)	91.71(8) [a]	98.6(2) [a,c]	95.97(6)	– [d]
Ax2-Ni-N8	88.32(5)	91.06(6) [a]	90.4(1) [a]	91.4(1) [a]	89.26(5)	88.86(5)	86.45(6) [a]	83.4(2) [a,c]	89.04(6)	– [d]
Ax2-Ni-N11	83.10(6)	82.48(6) [a]	78.8(1) [a]; 73.2(5) [a,b]	79.6(2) [a]; 78.9(8) [a,b]	86.27(5)	86.56(5)	88.29(8) [a]	81.4(2) [a,c]	85.82(6)	– [d]
Ax1-Ni-Ax2	179.39(5)	180 [a]	180 [a]	180 [a]	178.31(5)	179.13(5)	180 [a]	180 [a,c]	176.61(5)	– [d]
N1-Ni-N4	86.33(6)	86.99(6)	87.2(1); 90.0(5) [b]	87.4(1); 91.0(6) [b]	86.50(6)	87.09(6)	85.12(9)	87.9(2)	85.35(6)	– [d]
N1-Ni-N8	179.65(6)	180 [a]	180 [a]	180 [a]	179.53(6)	179.42(5)	180 [a]	180 [a]	179.24(6)	– [d]
N1-Ni-N11	93.22(6)	93.01(6) [a]	92.8(1) [a]; 90.0(5) [a,b]	92.6(1) [a]; 89.0(6) [a,b]	93.61(6)	93.13(6)	94.88(9) [a]	92.1(2) [a]	93.77(6)	– [d]
N4-Ni-N8	93.90(6)	93.01(6) [a]	92.8(1) [a]; 90.0(5) [a,b]	92.6(1) [a]; 89.0(6) [a,b]	93.03(6)	93.35(6)	94.88(9) [a]	92.1(2) [a]	93.98(6)	– [d]
N4-Ni-N11	179.54(6)	180 [a]	180 [a]; 180 [a,b]	180 [a]; 180 [a,b]	179.19(6)	179.63(6)	180 [a]	180 [a]	178.02(6)	– [d]
N8-Ni-N11	86.56(6)	86.99(6) [a]	87.2(1) [a]; 90.0(5) [a,b]	87.4(1) [a]; 91.0(6) [a,b]	86.86(6)	86.42(6)	85.12(9) [a]	87.9(2) [a]	86.89(6)	– [d]
						Non-bonding distances (Å)				
Ni···F1	5.424(1)	5.581(1)	5.481(3)	5.461(2)	5.470(1)	5.388(1)	5.345(2)	5.033(3)	5.360(1)	5.297(2)
Ni···F2	5.161(1)	5.226(1)	5.158(3)	5.135(2)	5.150(1)	5.167(1)	5.098(2)	4.872(4)	5.152(1)	5.107(3)
Ni···F3	5.135(1)	5.202(1)	5.124(3)	5.130(2)	5.108(1)	5.086(1)	5.097(2)	4.848(4)	5.113(1)	5.046(2)
Ni···F4	5.423(1)	– [a]	– [a]	– [a]	5.437(1)	5.429(1)	– [a]	– [a]	5.458(1)	5.325(3)
Ni···F5	5.148(1)	– [a]	– [a]	– [a]	5.136(1)	5.144(1)	– [a]	– [a]	5.127(1)	5.114(3)
Ni···F6	5.022(1)	– [a]	– [a]	– [a]	5.124(1)	5.104(1)	– [a]	– [a]	5.118(1)	5.087(3)
Ø(Ni···F)	5.219	5.337	5.254	5.242	5.237	5.220	5.180	4.918	5.221	5.163

[a] Centrosymmetric structure (N1 = N8, N4 = N11, Ax1 = Ax2). [b] Disordered nitrogen atom. [c] "Pseudo"-coordination of perchlorate anion in the axial positions. [d] Non-relevant due to different macrocycle conformation (*cis*-stereochemistry). [d] Coordinated water molecules in mutual *cis*-positions.

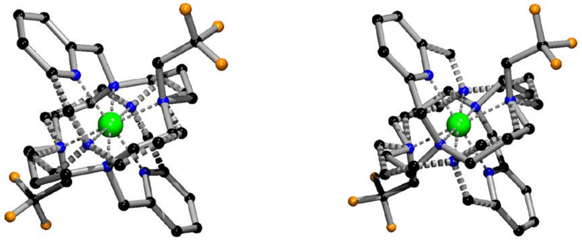

Figure S11: Molecular structure of the *trans*-[Ni(**te2f2py**)]$^{2+}$ ion found in the crystal structure of *trans*-[Ni(**te2f2py**)](ClO$_4$)$_2$. Both independent centrosymmetric units show pseudo-C_s disorder of the macrocyclic ring and the pivot atom bearing the methylpyridine pendant group. Colour code: C – black, N – blue, F – orange, Ni – green.

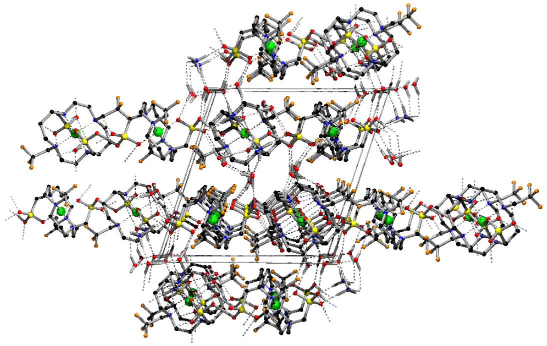

Figure S12: Crystal packing found in the structure of *trans*-(NH$_4$)[Ni(H**te2f2p**)]·4H$_2$O. View down along the *x* axis. Colour code: C – black, N – blue, O – red, H – white, F – orange, Ni – green, P – yellow.

UV-Vis spectra of nickel complexes

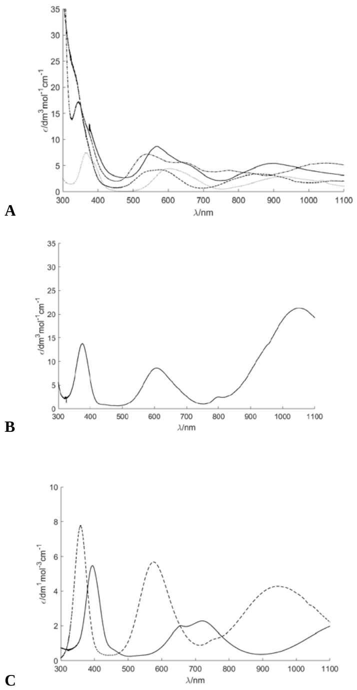

Figure S13. UV-Vis spectra of (**A**): *trans*-[Ni(**te2f2py**)]$^{2+}$ (full line), *trans*-[Ni(**te2f2ae**)]$^{2+}$ (dot-dashed), *trans*-[Ni(**te2f2p**)]$^{2-}$ (dotted) and *trans*-[Ni(**te2f2a**)] (dashed line); (**B**): *cis*-[Ni(**te2f**)(H$_2$O)$_2$]$^{2+}$; and (**C**): [Ni(H$_2$O)$_6$]$^{2+}$ (full line) and [Ni(NH$_3$)$_6$]$^{2+}$ (dashed line).

Table S2. UV-Vis absorption spectra of the discussed nickel(II) complexes in solution.

Complex	Solvent	λ_{max} / nm (ε / mol^{-1}·dm^3·cm^{-1})
trans-[Ni(**te2f2a**)]	H_2O	330 sh, 541 sh, 574(4), 862(3)
trans-[Ni(**te2f2py**)]$^{2+}$	CH_3NO_2	568(9), 645 sh, 901(5)
trans-[Ni(H**te2f2p**)]$^{2-}$	H_2O	366(7), 390 sh, 605(4), 927(3)
trans-[Ni(**te2f2ae**)]$^{2+}$	DMSO	346(17), 376 sh, 542(7), 648(6), 771(4), 1060(5)
cis-[Ni(**te2f**)(H$_2$O)$_2$]$^{2+}$	H_2O	375(14), 608(9), 797(2), 1050(21)

Dissociation kinetics of nickel complexes

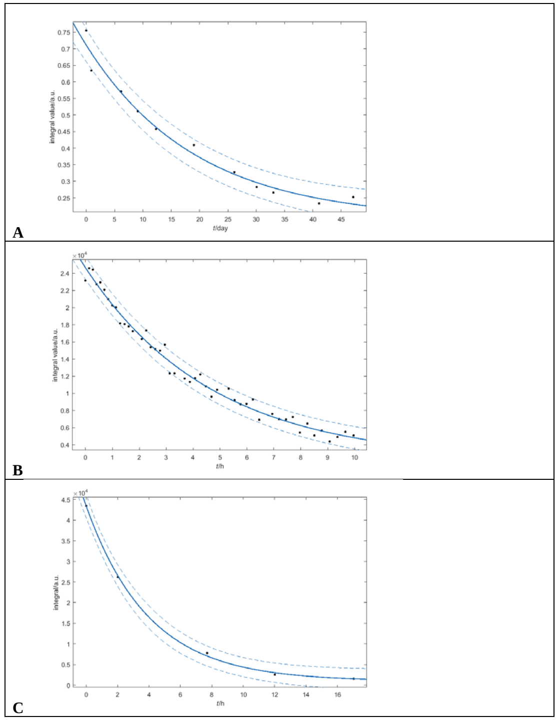

Figure S14. Dissociation of the studied complexes: (**A**): *trans*-[Ni(**te2f2a**)] (80 °C, 12 M aq. HCl), (**B**): *trans*-[Ni(**te2f2py**)]$^{2+}$ (80 °C, 1 M aq. HCl) and (**C**): *trans*-[Ni(**te2f2ae**)]$^{2+}$ (25 °C, pH 7.8). Dashed lines correspond to 95 % confidence interval.

Cell labelling study

Table S3: Viability of mesenchymal stem cells (MSCs) after labelling with *trans*-[Ni(**te2f2p**)]$^{2-}$.

Contrast agent	CA molar concentration in media / mM	Molar concentration of ^{19}F in media / mM	Cell viability / %	Cell gain / %	Ni uptake pg / cell
trans-[Ni(**te2f2p**)]$^{2-}$	4.2	25	98(3)	77(17)	2.94×10^{-1}
trans-[Ni(**te2f2p**)]$^{2-}$	8.3	50	99(2)	99(3)	4.23×10^{-1}
trans-[Ni(**te2f2p**)]$^{2-}$	16.7	100	96(1)	69(13)	9.25×10^{-1}
trans-[Ni(**te2f2p**)]$^{2-}$	25.0	150	94(1)	44(5)	1.85×10^{0}
Control	0	0	98(1)	100	1.49×10^{-4} [a]
Control	0	0	99(1)		5.51×10^{-4} [a]

[a] Measured natural nickel background.

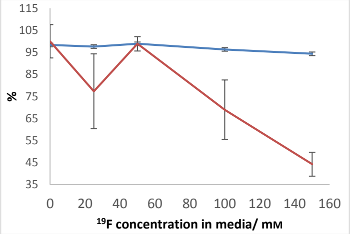

Figure S15. Cell viability (blue) and gain (red) as a function of ^{19}F concentration in cultured medium.

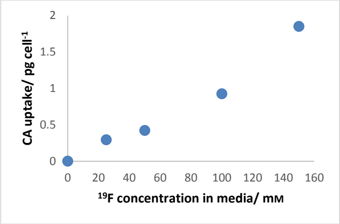

Figure S16. Cell uptake of the CA as a function of ^{19}F concentration in cultured medium.

Ligand syntheses

Synthesis of compound 1

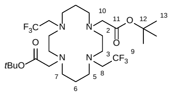

Extraction of 1,8-bis(2,2,2-trifluoroethyl)cyclam hydrochloride (**te2f**·4HCl, 500 mg, 0.98 mmol) dissolved in 5 % aq. NaOH (50 mL) by $CHCl_3$ (3×50 mL) gave the amine as free base. The organic phases were combined, dried by anhydrous Na_2SO_4 and the solvent was evaporated. The resulted viscous oil was dissolved in of anhydrous acetonitrile (50 mL) and *t*-butyl bromoacetate (470 mg, 2.41 mmol) and flame-dried K_2CO_3 (700 mg, 5.07 mmol) were added. The reaction mixture was stirred at room temperature overnight. Any solids were filtered off and volatiles were removed on rotary evaporator. Product was purified by crystallization from boiling MeOH yielding compound **1** (430 mg, ≈68 %).

TLC: R_f = 0.9 (MeOH). NMR: ^{1}H (300 MHz; $CDCl_3$): 1.45 (s, 18H, H13); 1.62 (p, 4H, H6, $^{3}J_{HH}$ = 6.1 Hz); 2.74 (t, 8H, $^{5}J_{HH}$ = 6.7 Hz, H5, H7); 2.80 (m, 8H, H2, H3); 3.09 (q, 4H, H8, $^{3}J_{HF}$ = 9.7 Hz); 3.25 (s, 4H, H10). $^{13}C\{^{1}H\}$ (151 MHz; $CDCl_3$): 25.2 (s, C6); 28.2 (s,C13); 51.3 (s, C2 or C3); 51.4 (s, C5 or C7); 52.0 (s, C5 or C7); 55.3 (s, C2 or C3); 55.2 (q, C8, $^{2}J_{CF}$ = 28.6 Hz); 55.9 (s, C10); 81.2 (s, C12); 126.1 (q, C9, $^{1}J_{CF}$ = 282.5 Hz); 170.5 (s, C11). ^{19}F (282 MHz; $CDCl_3$): –69.2 (bs). MS: 592.3 (calc. 593.7, $[4+H]^+$); 590.3 (calc. 591.7, $[5–H]^–$). Elem. anal. (%): found C 52.74; H 7.7; N 9.46 (calc. **1**, M_r = 592.69; C, 52.69; H, 7.82; N, 9.45). Single-crystals suitable for X-ray diffraction analysis of **1** were isolated during bulk synthesis after final recrystallization.

Synthesis of H_2te2f2a

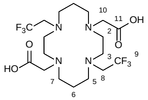

The entire amount of the compound **1** (430 mg, 0.73 mmol) from the previous step was dissolved in the TFA/$CHCl_3$ mixture (1/1 v/v, 80 ml) and stirred at room temperature overnight. The reaction mixture was evaporated to dryness and product was isolated after chromatography on strong cation exchanger (30 ml, H^+-form). Impurities (mainly residual TFA) ware washed out by water (≈500 ml) till neutrality of the eluate and the product was eluted by 10 % aq. pyridine. The eluate was evaporated to dryness, crude product was dissolved in water and evaporated again to remove residual pyridine (three times) and the zwitterionic form of the ligand was isolated by lyophilization. Yield 260 mg (69 %) of H_2**te2f2a**·$2H_2O$.

NMR: ^{1}H (600 MHz; D_2O; pH 7.9): 2.84 (s, 4H, H6); 2.84 (t, 4H, H5, $^{3}J_{HH}$ = 6.4 Hz); 3.12 (t, 4H, H3, $^{3}J_{HH}$ = 5.4 Hz), 3.32 (q, 4H, H8, $^{3}J_{HF}$ = 9.7 Hz); 3.45 (t, 4H,H2, $^{3}J_{HH}$ = 5.4 Hz); 3.48 (s, 4H, H7); 3.77 (s, 4H, H10). $^{13}C\{^{1}H\}$ (151 MHz; D_2O; pH 7.9): 23.3 (s,C6); 50.3 (s, C3); 51.9 (s, C5); 53.4 (s, C2); 53.95 (s, C7); 54.17 (q, C8, $^{2}J_{CF}$ = 29.8 Hz); 57.17 (s, C10); 126.45 (q, C9, $^{1}J_{CF}$ = 281.0 Hz); 171.29 (s, C11). ^{19}F (376 MHz; D_2O; pH 7.9): –68.31 (t, $^{3}J_{HF}$ = 9.8 Hz). MS: 480.9 (calc. 480.2, [**te2f2a**+H]$^+$); 502.9 (calc. 503.2, [**te2f2a**+Na]$^+$); 478.7 (calc. 479.2, [**te2f2a**–H]$^–$). Elem. anal. (%): found C 41.95; H 6.11; N 10.69 (calc. **te2f2a**·$2H_2O$, M_r = 516.48; C, 41.86; H, 6.64; N, 10.85).

Single-crystals of (H_6**te2f2a**)Cl_4 suitable for X-ray diffraction were isolated during acid-assisted decomplexation of *trans*-[Ni(**te2f2a)**] in ~12 M aq. HCl at 80 °C.

Synthesis of compound 2

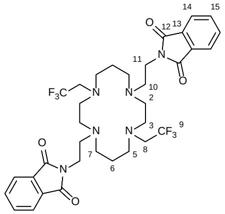

1,8-Bis(2,2,2-trifluoroethyl)cyclam hydrochloride (**te2f**·4HCl, 500 mg, 0.98 mmol) was dissolved in 5 % aq. NaOH (50 mL) and extracted into $CHCl_3$ (3×50 mL). The organic phases were combined, dried by anhydrous Na_2SO_4 and the solvent was evaporated. Resulted viscous oil (**te2f** as free base) was dissolved in anhydrous acetonitrile (50 mL), and *N*-(2-bromoethyl)phthalimide (800 mg, 3.15 mmol) and powdered flame-dried anhydrous K_2CO_3 (1.5 g, 10.9 mmol) were added. The reaction mixture was stirred at 60 °C for 4 d while the alkylation agent (1.5 g, 5.9 mmol) and anhydrous K_2CO_3 (2.75 g, 20 mmol) were added successively (half on the beginning and half after 2 days. A reaction progress was followed by TLC (SiO_2; conc. Aq. NH_3/EtOH (1/20, v/v), R_f = 0.9). The solids were filtered off and washed by $CHCl_3$ to dissolve any solid product. The organic phases were combined and volatiles were removed. Product **2** was crystallized from boiling EtOH to give colourless crystals (620 mg, 0.87 mmol, 89 %).

TLC: R_f = 0.9 (MeOH). NMR: ^{1}H (600 MHz; D_2O; pH 7.9): 1.46 (bm, 4H, H4); 2.52 (bm, 4H, H5 or H7); 2.53 (bm, 4H, H2 or H3); 2.59 (bm, 4H, H5 or H7); 2.65 (bm, 4H, H3 or H2); 2.68 (bm, 4H, H10), 3.0 (q, 4H, H8, $^{3}J_{HF}$ = 9.7 Hz); 3.74 (bm, 4H, H11); 7.73 (bm, 4H, H15); 7.85 (bm, 4H, H14). $^{13}C\{^{1}H\}$ (151 MHz; $CDCl_3$): 24.5 (s, C6); 35.9 (s, C11); 51.2 (s, C5 or C7); 51.4 (s, C2 or C3); 51.9 (s, C7 or C5); 52.0 (s, C10); 52.2 (s, C3 or C2); 55.4 (q, C8, $^{2}J_{CF}$ = 31 Hz); 123.1 (s, C14); 131.8 (s, C13); 125.9 (q, C9, $^{1}J_{CF}$ = 282 Hz); 133.9 (s, C15); 168.3 (s, C12). ^{19}F (376 MHz; CDCl3): –69.21 (t, $^{3}J_{HF}$ = 9.6 Hz). MS: 711.6 (calc. 711.3, [**1**+H]$^+$).

Single-crystals suitable for X-ray diffraction analysis of **2** were isolated during bulk synthesis after final recrystallization

Synthesis of te2f2ae

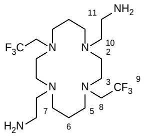

The entire amount of **2** obtained in the previous step (620 mg, 0.87 mmol) was dissolved in mixture of 60 % aq. N_2H_4 and EtOH (1/1 v/v; 60 mL) and the solution was stirred at 90 °C overnight. The reaction mixture was evaporated to dryness, the residue was dissolved in a mixture of 5 % aq. NaOH and EtOH (1/1 v/v; 60 ml) and the solution was stirred at 90 °C overnight. The reaction mixture was evaporated to dryness, the residue was dissolved in 5 % aq. NaOH (10 mL) and the solution was extracted by $CHCl_3$ (3×10 mL). The organic phases were combined, dried by anhydrous Na_2SO_4 and the volatiles were evaporated off. The crude product was purified by chromatography (SiO_2, conc. aq. NH_3/EtOH 1/5 v/v). The product-containing fractions were combined and solvents were evaporated off, the residue was dissolved in 15 % aq. HCl and volatiles were evaporated off. To remove excess of HCl, the remaining solid material was repeatedly dissolved in water and the solvent was evaporated. The product was isolated as a **te2f2ae**·4HCl·$4H_2O$ from its MeOH solution by precipitation using Et_2O (290 mg (41 %).

NMR: ^{1}H NMR (600 MHz, MeOH-d_4): 1.67 (p, $^{3}J_{HH}$ = 7.0 Hz, 4H, H6); 2.47 (t, 3H, H10, $^{3}J_{HH}$ = 6.2 Hz), 2.55 (t, 4H, H7, $^{3}J_{HH}$ = 6.8 Hz), 2.59 (t, 3H, H2, $^{3}J_{HH}$ = 6.4 Hz), 2.67 (t, 3H, H11, $^{3}J_{HH}$ = 6.2 Hz), 2.74 (t, 4H, H5, $^{3}J_{HH}$ = 7.1 Hz), 2.77 (t, 4H, H3, $^{3}J_{HH}$ = 6.4 Hz), 3.14 (q, 4H, H8, $^{3}J_{HF}$ = 9.8 Hz). $^{13}C\{^{1}H\}$ NMR (151 MHz, MeOH-d_4): 25.65 (s, C6); 39.95 (s, C11); 52.71 (s, C2); 52.83 (s, C7); 53.49(s, C3); 53.82(s, C5); 56.62 (q, C8, $^{2}J_{CF}$ = 29.9 Hz, 8); 57.77(s, C10); 127.60 (q, C9, $^{1}J_{CF}$ = 280.2 Hz). ^{19}F NMR (282 MHz, MeOH-d_4): –69.35 (t, $^{3}J_{HF}$ = 9.8 Hz). MS: 551.2 (calc.

551.5, [**te2f2ae**+H]$^+$). Elem. anal. (%): found C 32.90; H 6.71; N 12.14 (calc. **te2f2ae**·4H_2O·4HCl, M_r = 668.41; C 32.35; H 7.24; N 12.57).

Synthesis of te2f2py

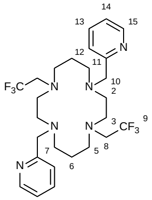

1,8-Bis(2,2,2-trifluoroethyl)cyclam hydrochloride (**te2f**·4HCl, 500 mg, 0.98 mmol) was dissolved in 5 % aq. NaOH (50 mL) and extracted into $CHCl_3$ (3×50 mL). The organic phases were combined, dried by anhydrous Na_2SO_4 and the solvent was evaporated. Resulted viscous oil (**te2f** as a free base) was dissolved of anhydrous acetonitrile (50 mL), and 2-(chloromethyl)pyridine hydrochloride (520 mg, 3.17 mmol) and powdered flame-dried anhydrous K_2CO_3 (1.2 g, 8.70 mmol) were added. After stirring at 60 °C for 24 h, 250 mg (1.52 mmol) of the alkylation agent was added and mixture was stirred for another 24 h. Reaction progress was followed by TLC (SiO_2, MeOH, R_f = 0.8). A crude product was isolated after chromatography on strong cation exchanger (100 mL, H$^+$-form). Impurities were washed off by pyridine/EtOH/water mixture (1/10/10 v/v/v, 500 mL) and the product was eluted by conc. aq. NH_3/EtOH/water mixture (1/5/5 v/v/v, 500 mL). The crude product was further purified by column chromatography (SiO_2; MeOH, R_f = 0.8) affording product as a colourless oil. The oil was dissolved in 15 % aq. HCl, solution was evaporated to dryness and the residue was triturated with anhydrous EtOH. The next portion of the product was obtained from the mother liquor by precipitation with Et_2O. Combined yield of **te2f2py**·3H_2O·6HCl was 376 mg (47 %).

NMR: ^{1}H NMR (600 MHz, MeOH-d_4): 1.71 (p, $^3J_{HH}$ = 6.7 Hz, 4H, H6); 2.57 (t, $^3J_{HH}$ = 6.6 Hz, 4H, H7); 2.65 (t, $^3J_{HH}$ = 6.5 Hz, 4H, H2); 2.67 (t, $^3J_{HH}$ = 8.0 Hz, 4H, H5); 2.80 (t, $^3J_{HH}$ = 6.3 Hz, 4H, H3); 3.03 (q, $^3J_{HF}$ = 9.8 Hz, 4H, H8); 3.68 (s, 4H, H10); 7.24–7.35 (m, 2H, H14); 7.66 (d, $^3J_{HH}$ = 7.9 Hz, 2H, H12); 7.81 (td, J_{HH} = 1.9, 7.7 Hz, 2H, H13); 8.43 (dd, J_{HH} = 1.8, 5.3 Hz, 2H, H15). ^{13}C{^{1}H} NMR (151 MHz, MeOH-d_4): 25.76 (s, C6); 52.47 (s, C2); 52.85 (s, C7); 53.40 (s, C3); 53.43 (s, C5); 56.32 (q,2*J*CF = 30.0 Hz, C8); 61.26 (s, C10); 123.69 (s, C14); 125.39 (s, C12); 127.53 (q, 1*J*CF = 280.2 Hz, C9); 138.47 (s, C13); 149.07 (s, C15); 161.28 (s, C11). ^{19}F NMR (282 MHz, MeOH-d_4): –69.49 (t, 3*J*HF = 9.8 Hz). TLC: R_f = 0.7 (MeOH). MS: 547.2 (calc. 547.3, [**te2f2py**+H]$^+$). Elem. anal. (%): found C 38.05; H 5.63; N 10.03 (calc. for **te2f2py**·3H_2O·6HCl, M_r = 819.40; C 38.11; H 5.90; N 10.26).

Single crystals suitable for X-ray analysis were obtained by crystallisation of **te2f2py** (in a form of free amine) from boiling acetonitrile on cooling.

Experimental for X-ray diffraction study

The diffraction data were collected at 150 K (Cryostream Cooler, Oxford Cryosystem) by Nonius KappaCCD diffractometer equipped with Bruker APEX-II CCD detector using monochromatized Mo-K_α radiation (λ = 0.71073 Å), or with Bruker D8 VENTURE Kappa Duo PHOTON100 diffractometer with IμS micro-focus sealed tube using Mo-Kα (λ = 0.71073 Å) or Cu-Kα (λ = 1.54178 Å). Data were analyzed by SAINT V8.27B (Bruker AXS Inc., 2012) program package. Data were corrected for absorption effects using the multi-scan method (SADABS). The structures were solved by direct methods (SHELXS97)[3] and refined by full-matrix least-squares techniques (SHELXL2014).[4] In general, all non-hydrogen atoms were refined anisotropically except of disordered parts of the molecules having low occupancy. All hydrogen atoms were found in the difference map of electron density. Those belonging to carbon atoms were fixed in theoretical (C–H) positions using thermal parameters U_{eq}(H) = 1.2 U_{eq}(C), and those belonging to heteroatoms (N–H, O–H) were fully refined.

X-ray diffraction study of organic intermediates and free ligands

Single crystals of 1,8-bis(2,2,2-trifluoroacetyl)-4,11-dibenzyl-1,4,8,11-tetraazacyclotetradecane were obtained by crystallisation from boiling MeOH. Single crystals of 1,8-bis(2,2,2-trifluoroethyl)-4,11-dibenzyl-1,4,8,11-tetraazacyclotetradecane were obtained by crystallisation from boiling $CHCl_3$. Preparations of single crystals of other crystallographically characterized organic compounds are given in synthetic part.

In the crystal structures of 1,8-bis(2,2,2-trifluoroacetyl)-4,11-dibenzyl-1,4,8,11-tetraazacyclotetradecane, 1,8-bis(2,2,2-trifluoroethyl)-4,11-dibenzyl-1,4,8,11-tetraazacyclotetradecane, intermediate **1** (= bis(*tert*-butyl) ester of H_2**te2f2a**), (H_6**te2f2a**)Cl_4, intermediate **2** (bis(phthaloyl-protected) **te2f2ae**) and **te2f2py**, the independent units were formed by one half of the formula units, and all macrocyclic molecules possess centre of symmetry. Table S4 brings relevant experimental data.

Table S4. Experimental data of the reported crystal structures of organic intermediates and ligands.

Compound	Intermediate **A**[a]	Intermediate **B**[a]	Intermediate **1**	(H_6**te2f2a**)Cl_4	Intermediate **2**	**te2f2py**
Formula	$C_{28}H_{34}F_6N_4O_2$	$C_{28}H_{38}F_6N_4$	$C_{26}H_{46}F_6N_4O_4$	$C_{18}H_{34}Cl_4F_6N_4O_4$	$C_{34}H_{40}F_6N_6O_4$	C26 H36 F6 N6
M_r	572.59	544.62	592.67	626.29	710.72	546.61
Colour	colourless	colourless	colourless	colourless	colourless	colourless
Shape	prism	prism	plate	prism	prism	prism
Dimensions (mm)	0.27×0.44×0.80	0.29×0.37×0.42	0.07×0.35×0.97	0.09×0.17×0.21	0.11×0.12×0.19	0.14×0.20×0.23
Crystal system	monoclinic	monoclinic	triclinic	monoclinic	monoclinic	triclinic
Space group	$P2_1/c$	$P2_1/c$	P–1	$P2_1/n$	$C2/c$	P–1
a (Å)	8.9905(4)	5.8630(1)	5.5875(2)	7.2293(3)	11.4592(3)	5.8781(2)
b (Å)	11.8310(5)	15.9929(4)	9.0805(5)	15.7011(6)	17.1698(4)	10.7977(4)
c (Å)	13.3786(5)	15.1270(3)	15.1931(8)	11.8830(5)	17.3181(4)	10.8366(4)
α (°)	–	–	102.255(2)	–	–	93.118(1)
β (°)	104.297(2)	98.613(1)	100.202(2)	92.810(1)	93.185(1)	99.001(1)
γ (°)	–	–	92.517(2)	–	–	92.490(1)
V (Å^3)	1379.0(1)	1402.41(5)	738.71(6)	1347.19(9)	3402.1(1)	677.38(4)
Z	2	2	1	2	4	1
D_c (g cm^{-3})	1.379	1.290	1.332	1.544	1.388	1.340
F(000)	600	576	316	648	1488	288
Radiation	Mo-Kα	Mo-Kα	Mo-Kα	Mo-Kα	Cu-Kα	Cu-Kα
μ (mm^{-1})	0.115	0.105	0.114	0.513	0.979	0.943
Diffractions unique; observed ($I_o > 2\sigma(I)$)	3166; 2532	3223; 2790	3129; 2622	3099; 2846	3364; 2934	2659; 2382
Parameters	181	172	184	175	226	172
G-o-f on F^2	1.034	1.036	1.066	1.077	1.042	1.053
R; R' (all data)	0.0375; 0.0520	0.0380; 0.0447	0.0406; 0.0483	0.0254; 0.0279	0.0374; 0.0443	0.0348; 0.0397
wR; wR' (all data)	0.0894; 0.0984	0.0955; 0.1008	0.1060; 0.1126	0.0650; 0.0667	0.0899; 0.0941	0.0850; 0.0883
Difference max; min (e Å^{-3})	0.252; –0.230	0.264; –0.255	0.278; –0.256	0.379; –0.285	0.211; –0.270	0.259; –0.202
CCDC number	1558415	1558414	1558411	1558412	1558410	1558786

[a] Intermediate **A =** 1,8-bis(2,2,2-trifluoroacetyl)-4,11-dibenzyl-1,4,8,11-tetraazacyclotetradecane; Intermediate **B =** 1,8-bis(2,2,2-trifluoroethyl)-4,11-dibenzyl-1,4,8,11-tetraazacyclotetradecane.

X-ray diffraction study of Ni(II)-complexes

Few single crystals of *trans*-(NH_4)[Ni(H**te2f2p**)]·4H_2O were obtained on a slow evaporation of the mother liquor after bulk synthesis of *trans*-(NH_4)[Ni(H**te2f2p**)]·3.25H_2O.[2] Few violet single crystals of *trans*-[Ni(**te2f**)(H_2O)$_2$]Cl_2 were isolated as a low-abundant by-product from reaction of **te2f**·4HCl with Ni(ClO_4)$_2$, where blue-green *cis*-[Ni(**te2f**)Cl_2] complex was formed as a major product.[2] Preparation of single crystals of other Ni(II)-complexes is given in the synthetic part.

In the structure of *trans*-[Ni(**te2f2a**)]·2EtOH, independent unit is identical with the formula unit, although the complex molecule is near-to-centrosymmetry. One of ethanol solvate molecules is slightly disordered and the disorder was best modelled by splitting of methylene group into two positions with occupancies 72%:28%. The structure of *trans*-[Ni(**te2f2ae**)](ClO_4)$_2$·2MeOH is centrosymmetric, and contains in the independent unit half formula unit. The molecule of methanol was best refined disordered (using EADP command) in two positions sharing acidic hydrogen atom, which is involved in hydrogen bond to one of perchlorate oxygen atoms. Such refinement led to relative occupancy 71%:29%. In the crystal structure of *trans*-[Ni(**te2f2py**)](ClO_4)$_2$, two independent halves of the formula unit (*i.e.* two halves of centrosymmetric complex molecules and two perchlorate anions) form the independent unit. Macrocyclic parts of each of the complex molecules were found to be disordered in two positions (83%:17% and 85%:15% for both independent molecules, respectively), swapping the positions of five- and six-membered macrocycle chelate rings and keeping positions of the trifluoroethyl groups with corresponding nitrogen pivot atom and the pyridine moieties common for both possibilities (Figure S10). One of perchlorate anions was best refines with oxygen atoms disordered in two positions, and the second perchlorate was refined non-disordered. However, there are still some difference maxima of electron density, the biggest one (1.76 e Å^{-3}) very close (0.79 Å) to the chlorine atom of non-disordered and the second one (1.29 e Å^{-3}) near to disordered anion. The crystals of *trans*-(NH_4)[Ni(H**te2f2p**)]·4H_2O have different crystal-packing than previously reported phase *trans*-(NH_4)[Ni(H**te2f2p**)]·3.25H_2O.[2] Asymmetric unit contains two complex anions with protonated phosphonate pendants, two ammonia cations and eight water molecules. One of trifluoromethyl groups was best refined staggered in two positions with relative occupancy 90%:10%. The highest difference maximum of electronic density (1.05 e Å^{-3}) is located very close to central Ni(II) ion (0.80 Å) in direction to apical oxygen donor atom. In the crystal structure of *trans*-[Ni(**te2f**)(H_2O)$_2$]Cl_2, the independent moiety contains one half of the centrosymmetric complex molecule and one chloride anion. Table S5 brings relevant experimental data.

Table S5. Experimental data of the reported crystal structures of the Ni(II) complexes.

Compound	*trans*-[Ni(**te2f2a**)] ·2EtOH	*trans*-[Ni(**te2f2ae**)]$(ClO_4)_2$ ·2MeOH	*trans*-[Ni(**te2f2py**)]$(ClO_4)_2$	*trans*-(NH_4)[Ni(H**te2f2p**)] ·$4H_2O$	*trans*-[Ni(**te2f**)$(H_2O)_2$]Cl_2
Formula	$C_{22}H_{40}F_6N_4NiO_6$	$C_{20}H_{44}Cl_2F_6N_6NiO_{10}$	$C_{26}H_{36}Cl_2F_6N_6NiO_8$	$C_{16}H_{41}F_6N_5NiO_{10}P_2$	$C_{14}H_{30}Cl_2F_6N_4NiO_2$
M_r	629.29	772.22	804.22	698.19	530.03
Colour	light violet	light blue	light violet	light blue	light violet
Shape	plate	prism	prism	prism	prism
Dimensions (mm)	0.04×0.11×0.28	0.09×0.16×0.19	0.10×0.14×0.16	0.29×0.40×0.53	0.08×0.20×0.21
Crystal system	monoclinic	triclinic	triclinic	triclinic	triclinic
Space group	$P2_1/n$	P–1	P–1	P–1	P–1
a (Å)	8.6960(3)	8.9314(3)	9.9682(5)	11.1896(2)	7.5579(13)
b (Å)	16.2679(8)	10.2263(3)	10.2247(5)	15.7105(3)	8.9176(16)
c (Å)	18.8283(8)	10.6001(4)	17.9233(9)	16.4468(3)	8.9261(15)
α (°)	–	64.004(1)	75.724(2)	71.6682(7)	92.549(7)
β (°)	94.442(2)	89.465(1)	81.111(2)	87.4434(9)	111.394(7)
γ (°)	–	66.770(1)	61.931(2)	87.2703(8)	111.083(7)
V (Å^3)	2655.6(2)	783.83(5)	1560.55(14)	2740.07(9)	511.85(16)
Z	4	1	2	4	1
D_c (g·cm^{-3})	1.574	1.636	1.711	1.692	1.719
F(000)	1320	402	828	1456	274
Radiation	Mo-Kα	Mo-Kα	Mo-Kα	Mo-Kα	Mo-Kα
μ (mm^{-1})	0.818	0.885	0.889	0.924	1.281
Diffractions unique; observed ($I_o > 2\sigma(I)$)	6128; 5301	3607; 3304	7184; 6177	1190; 10259	2352; 2038
Parameters	366	226	516	835	146
G-o-f on F^2	1.026	1.040	1.068	1.035	0.982
R; R' (all data)	0.0342; 0.0425	0.0302; 0.0339	0.0533; 0.0630	0.0304; 0.0369	0.0337; 0.0415
wR; wR' (all data)	0.0844; 0.0889	0.0757; 0.0780	0.1331; 0.1395	0.0807; 0.0847	0.0518; 0.0539
Difference max; min (e Å^{-3})	0.934; –0.401	0.729; –0.545	1.762; –1.082	1.052; –0.502	0.858; –0.935
CCDC number	1558417	1558418	1558419	1558416	1558413

References

---

1 M. Meyer, V. Dahaoui-Ginderey, C. Lecomte and R. Guilard, *Coord. Chem. Rev.*, **1998**, *178–180*, 1313–1405.

2 J. Blahut, P. Hermann, A. Gálisová, V. Herynek, I. Císařová, Z. Tošner, J. Kotek, *Dalton Trans.* **2016**, *45*, 474–478.

3 G. M. Sheldrick, SHELXS97. Program for Crystal Structure Solution from Diffraction Data. University of Göttingen, Göttingen, 1997.

4 G. M. Sheldrick, SHELXL-2014/7. Program for Crystal Structure Refinement from Diffraction Data. University of Göttingen: Göttingen, 2014.

Appendix C

A combined NMR and DFT study of conformational dynamics in lanthanide complexes of macrocyclic DOTA-like ligands

- J. Blahut, P. Hermann, Z. Tošner, C. Platas-Iglesias, *Phys. Chem. Chem. Phys.* 2017, **19**, 26662–71. (2017 PCCP HOT Articles Collection)

PCCP

PAPER

View Article Online
View Journal | View Issue

Check for updates

Cite this: Phys. Chem. Chem. Phys., 2017, 19, 26662

A combined NMR and DFT study of conformational dynamics in lanthanide complexes of macrocyclic DOTA-like ligands†

Jan Blahut,[a] Petr Hermann,*[a] Zdeněk Tošner[b] and Carlos Platas-Iglesias[c]

Received 4th August 2017,
Accepted 6th September 2017

DOI: 10.1039/c7cp05296k

rsc.li/pccp

The solution dynamics of the Eu(III) complexes of H_4**dota** (1,4,7,10-tetraazacyclododecane-1,4,7,10-tetracarboxylic acid) and H_5**do3ap** (1,4,7,10-tetraazacyclododecane-4,7,10-tris(carboxymethyl)-1-methyl-phosphonic acid, bound in both monoprotonated and fully deprotonated forms) were investigated by using a combination of NMR measurements and DFT calculations. In solution, an equilibrium between the square antiprismatic (SAP) and twisted-square antiprismatic isomers (TSAP) of these complexes is present. These two isomers interconvert by rotation of the pendant arms or inversion of the cyclen chelate rings. 1D EXSY NMR spectra were used to determine these exchange rates with unprecedented accuracy. It was found that the two processes occur at different rates. Additional variable-temperature measurements allowed determination of the corresponding activation parameters for the two processes. DFT calculations were then used to obtain mechanistic information at the molecular level. The results show that the cyclen inversion pathway involves stepwise inversion of the four chelate rings formed upon metal ion coordination. However, the arm rotation process may operate through a synchronous rotation of the pendant arms or a stepwise mechanism depending on the system. A mixed cluster-continuum approach was required to improve the agreement between experimental and calculated activation parameters for the arm rotation process. The obtained results will aid the design of MRI contrast agents. Furthermore, the methodology developed in this work can be further applied for the investigation of other dynamic paramagnetic systems, *e.g.* peptides with Ln(III) probes or natively paramagnetic metalloproteins.

1 Introduction

Since the early 1980s, when the first lanthanide(III) complexes of H_4**dota** were prepared (H_4**dota** = 1,4,7,10-tetraazacyclododecane-1,4,7,10-tetraacetic acid),[1] great efforts have been made to understand and describe the conformational properties and dynamics of these and structurally related compounds in solution. The efforts have been mainly driven by the wide range of applications of the complexes in different fields, especially in biology and medicine in various techniques of molecular imaging. In the [Ln(**dota**)]$^-$ complexes and related systems, the metal ion is coordinated to the four nitrogen atoms of the macrocycle, which define the N_4 plane, and four oxygen atoms of the pendant arms (referred to as the O_4 plane). Usually, an additional coordination position is occupied by a water molecule which caps the O_4 plane (Fig. 1).[2] The relative torsion of the N_4

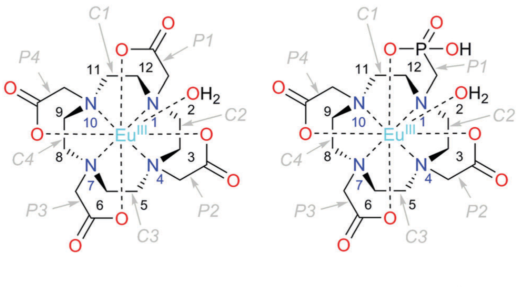

[Eu(**dota**)(H_2O)]$^-$ [Eu(H**do3ap**)(H_2O)]$^-$

Fig. 1 Structure of the complexes discussed in this work with an atom and cyclen chelate/pendant arm numbering scheme. The TSAP isomers are depicted in both cases.

---

[a] Department of Inorganic Chemistry, Faculty of Science, Charles University, Hlavova 2030/8, Prague 2, 128 43, Czech Republic. E-mail: petrh@natur.cuni.cz

[b] Faculty of Science, Charles University, Hlavova 2030/8, Prague 2, 128 43, Czech Republic

[c] Centro de Investigaciones Científicas Avanzadas (CICA) and Departamento de Química, Facultade de Ciencias, Universidade da Coruña, 15071 A Coruña, Galicia, Spain

† Electronic supplementary information (ESI) available. See DOI: 10.1039/c7cp05296k

and O_4 planes results in two possible orientations of the pendant arms (Δ or Λ) while the chelate rings of the macrocyclic cyclen unit may adopt two different conformations (δδδδ or λλλλ). As a result, four conformational isomers are possible which are observed as two enantiomeric pairs. One enantiomeric pair [Δ(λλλλ)/Λ(δδδδ)] presents a square antiprismatic (SAP) coordination geometry, whereas the Λ(λλλλ)/Δ(δδδδ) enantiomeric pair adopts a twisted-square antiprismatic (TSAP) coordination geometry. The exchange between the SAP and TSAP forms can occur *via* pendant arm rotation or macrocycle chelate ring inversion, while the combination of these two processes results in interconversion between the enantiomers.[3] While direct enantiomerization has also been postulated,[4] there is no experimental evidence supporting such a concerted arm-rotation and ring-inversion pathway and, likely, a high activation energy barrier disables it.[5]

The relative abundance of the SAP and TSAP isomers is affected by both the lanthanide(III) ion and the nature of the ligand. Generally, abundance of the SAP isomers increases on going to the right across the lanthanide series while an increase in the steric demand of the pendant arms increases the abundance of the TSAP form.[6,7] A rational control of the TSAP/SAP ratio in solution favoring one isomer or another is of key importance for many applications of these types of complexes. For instance, TSAP isomers present much faster exchange rates of the coordinated water molecule which, in the case of the $[Gd(\mathbf{dotam})(H_2O)]^{3+}$ complex (**dotam** = tetraamide of H_4**dota**), was shown to be ~50 times faster than that for the SAP form.[8–10] The water exchange rate of the coordinated water molecule is an important parameter that affects the efficiency of gadolinium-based contrast agents (CAs) for magnetic resonance imaging (MRI).[11] A slow water exchange is also critical for the design of MRI contrast agents based on the chemical exchange saturation transfer (CEST) approach.[12] Because two isomeric forms are present in solution, it is also problematic to use lanthanide complexes with dota-like ligands as paramagnetic probes in protein structure studies,[13] for the determination of drug binding sites,[14] and in the design of CEST[12,15] and PARASHIFT[16,17] MRI CAs. Other properties are expected to be influenced by this isomerism as well, such as the magnetic anisotropy and symmetry axis orientation in Dy^{3+} complexes,[18] or the nuclear relaxation rate of ^{89}Y complexes for application in dynamic nuclear polarization.[19] Last but not least, isomeric composition affects luminescence properties[9] and the enantioselectivity of organic reactions using dota-like complexes as catalysts.[20]

NMR spectroscopy is a powerful method that allows determination of isomer composition as well as their interconversion dynamics even in the steady-state. The application of NMR to Ln^{3+} complexes was reviewed by Babilov,[21] and the most important methods and their limitations are briefly discussed below. First, the dynamics of the system can be followed by analyzing changes in the line-shape with temperature. Activation energies can be determined either by simple estimation of exchange rates from the coalescence temperature or by more rigorous line-shape fitting. While this method is straightforward and relatively sensitive, it requires a reasonable estimate of the temperature dependence of chemical shifts and transverse relaxation rates. This can be relatively simple for diamagnetic systems but, for paramagnetic complexes, the paramagnetically induced shift and relaxation rates complicate the analysis. Other problems arise from signal overlap and complicated signal behaviour when the exchange process involves more than two sites, which is often the case in dota-like systems. Nevertheless, this technique has been relatively successfully applied for diamagnetic La^{3+} and Lu^{3+} complexes and/or employing ^{13}C and ^{31}P NMR spectra which are less affected by paramagnetic effects and are less crowded.[7,21–26]

A second group of NMR techniques is based on selective inversion[4,5,24] or selective saturation[27] of a selected NMR resonance and following signal intensities after a delay during which the exchange takes place. These approaches also suffer from signal overlap, especially in complexes of dota derivatives with low symmetry. This problem can be alleviated by using 2D pulse sequences such as 2D-EXSY.[28,29] While being very useful for a qualitative description of the dynamics of the system, it is difficult to obtain quantitative results due to the problematic integration of 2D cross-peaks suffering from phase and baseline distortions.

Theoretical calculations can provide detailed information about the mechanism of dynamic processes at the molecular level experienced by lanthanide(III) complexes in solution. Both classical[30] and *ab initio*[31–33] molecular dynamics (AIMD) have been used to investigate lanthanide(III) complexes. However, the parametrization of force fields to be used for *f*-block elements is not a trivial task. In contrast, AIMD offer a robust tool to investigate lanthanide(III) complexes in solution, but their high computational cost rarely allows simulations exceeding a hundred picoseconds. Pollet *et al.*[34] used metadynamics to gain information on the water exchange rates of a gadolinium(III) complex, a process that occurs at the time scale of hundreds of nanoseconds. However, conformational dynamics of dota-like complexes take place at the time scale of tens of milliseconds at room temperature, which cannot be reached with the currently available computational resources. Thus, information on the conformational dynamics of lanthanide(III) complexes has been generally obtained by exploring the potential energy surface of the system of interest, which provides the relevant energy minima and transition states and the associated energy profile.[35] While this approach suffers from some limitations, in particular related to the treatment of solvent effects, it has been shown to provide useful information at the molecular level complementary to experimental studies.[36]

Herein we report thorough NMR analysis of the conformational dynamics of the Eu^{3+} complexes with the $(\mathbf{dota})^{4-}$ anion and with protonated and deprotonated forms of the $(\mathbf{do3ap})^{5-}$ anion (Fig. 1), which provides exchange rates and activation parameters with unprecedented accuracy. DFT calculations will subsequently be presented to reveal details of the mechanisms responsible for the isomer interconversion.

2 Results and discussion

2.1 ^1H MNR spectra

The ^1H NMR spectrum of $[Eu(\mathbf{dota})(D_2O)]^-$ recorded at 5 °C (Fig. 2) is in agreement with that reported previously.[28] The spectrum

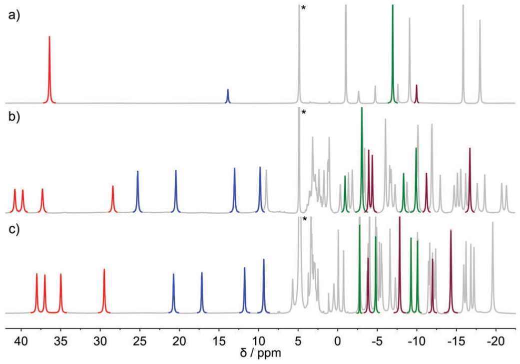

Fig. 2 ^{1}H-NMR spectra of: (a) [Eu(**dota**)(D_2O)]$^-$ (pD = 7.0) (b) [Eu(**do3ap**)(D_2O)]$^{2-}$ (pD = 8.5) and (c) [Eu(H**do3ap**)(D_2O)]$^-$ (pD = 3.6) as recorded in D_2O solution at 5 °C. The signals of the cyclen protons used for ^{1}H 1D-EXSY studies are highlighted in red (SAP axial protons), green (SAP equatorial protons), blue (TSAP axial protons), and purple (TSAP equatorial protons).

consists of two sets of six signals with different intensities, which correspond to the SAP and TSAP isomers, each showing an effective C_4 symmetry. The equilibrium constant characterizing the isomer equilibrium reaction SAP $\leftrightarrows$ TSAP was determined by integration of signals at $\delta(^1\mathrm{H})$ = 36.32 and 13.76 ppm yielding K_{integral} = 0.21. This value is in good agreement with the values reported previously.[3] The synthesis and NMR spectra of [Eu(**do3ap**)(D_2O)]$^{2-}$ were also published previously;[6] however no spectral assignments were provided. The phosphonate group of the SAP and TSAP isomers were found to experience protonation processes characterized by pK_a values of 6.0 (TSAP) and 5.5 (SAP).[6] Thus, ^{1}H NMR spectra at two pD values were recorded to investigate the conformational dynamics of both the protonated and non-protonated forms of the complex. The C_1 symmetry of the two isomers present in solution results in two sets of 24 ^{1}H NMR signals and two ^{31}P NMR resonances.

The conformational dynamics of [Eu(**dota**)(D_2O)]$^-$ was investigated by focusing on two signals in its ^{1}H NMR spectrum, namely on the macrocyclic chelate ring axial protons that are directed opposite to the pendant arms, and the corresponding geminal equatorial protons (SAP: 36.3 ppm (axial) and −7.0 ppm (equatorial); TSAP: 13.8 ppm (axial) and −10.1 ppm (equatorial)).[28,37] For the [Eu(H**do3ap**)(D_2O)]$^-$ and [Eu(**do3ap**)(D_2O)]$^{2-}$ complexes, the analogous proton signals were identified using a combination of 2D ^{1}H EXSY and ^{1}H–^{1}H COSY experiments (Table S1 and Fig. S2, ESI†). The four signals of axial protons of the cyclen unit that point opposite to the pendant arms are observed in the range ∼28–40 ppm for the SAP isomers, and between 10 and 25 ppm for the TSAP isomers. These spectral ranges are typical for Eu^{3+} complexes of H_4**dota** and dota-tetraamide derivatives.[38] The equilibrium constants K_{integral} obtained from the integration of the ^{1}H NMR axial proton resonances (red and blue in Fig. 2) are 0.88 and 1.42 for the [Eu(H**do3ap**)(D_2O)]$^-$ and [Eu(**do3ap**)(D_2O)]$^{2-}$ complexes, respectively. The increase in the population of the TSAP isomer upon replacing carboxylate group(s) by bulkier phosphonate arm(s) is well documented, and has been attributed to steric effects.[6,7]

2.2 1D-EXSY experiments

The conformational dynamics of [Eu(**dota**)(D_2O)]$^-$, [Eu(H**do3ap**)(D_2O)]$^-$ and [Eu(**do3ap**)(D_2O)]$^{2-}$ were investigated using an optimized variant of the 1D EXSY experiment. The pulse sequence starts with a selective excitation block realized using a selective refocusing pulse during a spin echo. It is followed by an exchange period τ_M during which the magnetization is stored along the z-axis and a spectrum is recorded after the final 90° pulse (eqn (1)).

$$90^\circ - \delta - 180^\circ(\mathrm{sel}) - \delta - 90^\circ - \tau_M - 90^\circ - \mathrm{FID} \qquad (1)$$

Relatively fast relaxation and exchange rates, especially at high temperature, impose a strong requirement to minimize both the duration of an echo, 2δ, and the mixing period τ_M. For slowly relaxing diamagnetic systems, z gradients are used to improve the performance of the selective 180° pulse, and an inversion pulse (accompanied with gradients) is used during the mixing in order to suppress unwanted magnetization pathways.[39] For the title paramagnetic samples, the gradients were replaced by a phase cycle that combines EXORCYCLE on the 180°(sel) pulse, EXORCYCLE on the last 90° pulse, and a two-step cycle of the first pulse in order to reduce T_1 relaxation effects by $\pm z$ alternation of the selected magnetization before mixing. In total, the phase cycle has 32 steps that presents no complication for systems with short T_1 relaxation, allowing fast repetition. Note that the measured magnetization effectively evolves to zero for long mixing times.[39]

Additional considerations should be taken into account when designing the selective refocusing pulse, as both the chemical exchange and relaxation processes take place during the pulse. While the exact description is beyond the scope of this paper, one can qualitatively state that in order to avoid significant loss of signal intensity, the pulse length should be shorter than the characteristic exchange and/or relaxation times. In the present case, the characteristic exchange and relaxation times are approximately 2×10^{-2} s, and thus pulses longer than ≈5 ms should be avoided. On the other hand, short pulses are less selective. Using a Gauss pulse length of 5 ms results in re-focusing of all resonances within the range of ≈200 Hz. This problem is particularly relevant in EXSY experiments when proximate signals are involved in chemical exchange (*e.g.* undesired partial refocusation of the signal of TSAP axial protons when applying the 180°(sel) pulse to the resonance of SAP axial protons). Due to this restriction in signal separation, the 1D-EXSY experiments in [Eu(**do3ap**)(D_2O)]$^{2-}$ and [Eu(H**do3ap**)(D_2O)]$^-$ at all temperatures and in [Eu(**dota**)(D_2O)]$^-$ at temperatures above 5 °C were performed selecting axial proton signals (6–40 ppm), which are well isolated (Fig. 2). In the case of [Eu(**dota**)(D_2O)]$^-$ at 5 °C, equatorial signals were also used. The same set of experiments was performed for ^{31}P TSAP and SAP signals of [Eu(**do3ap**)(D_2O)]$^{2-}$, and [Eu(H**do3ap**)(D_2O)]$^-$ at 5 °C as well.

2.3 Data analysis

The exchange rates characterizing the conformational dynamics of the complexes investigated in this work were determined by analyzing the evolution of the signal integral as a function of τ_M through numerical solution of Bloch-McConnell eqn (2),

$$\frac{d\boldsymbol{M}}{dt} = -\boldsymbol{R}\left(\boldsymbol{M}(t) - \boldsymbol{M}_{eq}\right) + \boldsymbol{k}\boldsymbol{M}(t) \qquad (2)$$

$$\boldsymbol{k} = \begin{pmatrix} -k_{PendSAP} - k_{CycleSAP} & 0 & k_{PendTSAP} & k_{CycleTSAP} \\ 0 & -k_{PendSAP} - k_{CycleSAP} & k_{CycleTSAP} & k_{PendTSAP} \\ k_{PendSAP} & k_{CycleSAP} & -k_{PendTSAP} - k_{CycleTSAP} & 0 \\ k_{CycleSAP} & k_{PendSAP} & 0 & -k_{PendTSAP} - k_{CycleTSAP} \end{pmatrix} \qquad (3)$$

where $\boldsymbol{M}(t)$ is a vector consisting of z-magnetization of SAP$_{ax}$, SAP$_{eq}$, TSAP$_{ax}$ and TSAP$_{eq}$ hydrogen atoms; $\boldsymbol{M}_{eq}$ is its equilibrium value, and $\boldsymbol{R}$ is a diagonal matrix of R_1 relaxation rates at each site. The exchange matrix $\boldsymbol{k}$ describes all exchange processes that occur in our system and is expressed by eqn (3). In eqn (3), exchange rates $k_{PendSAP}$, $k_{CycleSAP}$, $k_{PendTSAP}$ and $k_{CycleTSAP}$ describe pendant arm rotation and macrocycle inversion experienced by either the SAP or TSAP isomers.

The exchange rates and relaxation times of [Eu(**dota**)(D$_2$O)]$^-$ were obtained at 5 °C from a simultaneous fitting of four datasets measured starting from selected magnetization at the frequencies of the SAP$_{ax}$ (36.3 ppm), TSAP$_{ax}$ (13.8 ppm), SAP$_{eq}$ (−7.1 ppm) and TSAP$_{eq}$ (−10.1 ppm) protons. The four rate constants and the four relaxation rates were used as global variables during the fitting procedure, while $\boldsymbol{M}_{eq}$ and $\boldsymbol{M}(0)$ were used as local variables for each dataset. Fig. 3 shows the ^{1}H NMR spectra used to obtain one of these datasets by applying the 180°(sel) pulse at the frequency of the SAP$_{ax}$ resonance (36.3 ppm). At short τ_M values only the signal of the SAP axial protons is observed while the signals of the remaining three protons gradually emerge upon increasing τ_M as the chemical exchange progresses. The signal evolution of the three resonances encodes kinetic information of a different exchange pathway, as illustrated in Fig. 3. The interconversion between SAP$_{ax}$ and TSAP$_{ax}$ protons occurs by rotation of the pendant arms. Interconversion between SAP$_{ax}$ ⇆ TSAP$_{eq}$ requires the inversion of the cyclen unit, while the SAP$_{ax}$ ⇆ SAP$_{eq}$ exchange requires both arm rotation and ring inversion. The intensity of the three signals observed due to chemical exchange fades away at long τ_M values due to T_1 relaxation and the applied phase cycle.

Fig. 4 shows four datasets used to determine the exchange rates and relaxation times in [Eu(**dota**)(D$_2$O)]$^-$. A nice fit of the experimental data was obtained by analyzing these four data sets simultaneously. The same procedure was applied to the [Eu(**do3ap**)(D$_2$O)]$^{2-}$ and [Eu(H**do3ap**)(D$_2$O)]$^-$ systems at 5 °C by using eight datasets. In these cases, the four axial protons of the SAP isomer and the four axial protons of the TSAP isomer were selectively excited (these resonances are well isolated from the remaining ^{1}H NMR signals, see blue and red signals in Fig. 2). The resulting fits are presented in the ESI† (Fig. S4a and S5a). All the exchange and relaxation rates determined from the analysis of the 1D EXSY data are compiled in Table 1.

In agreement with the literature,[6] the dominant isomer of [Eu(**dota**)(D$_2$O)]$^-$ is the SAP isomer while the TSAP isomer is the dominant species for [Eu(**do3ap**)(D$_2$O)]$^{2-}$ and the population of SAP and TSAP isomers is very similar for [Eu(H**do3ap**)(D$_2$O)]$^-$. Therefore, the TSAP → SAP interconversion is faster than the SAP → TSAP interconversion in [Eu(**dota**)(D$_2$O)]$^-$, while the situation is reversed for [Eu(**do3ap**)(D$_2$O)]$^{2-}$ and the two processes are characterized by similar rates for [Eu(H**do3ap**)(D$_2$O)]$^-$. The equilibrium constants for the SAP ⇆ TSAP equilibrium

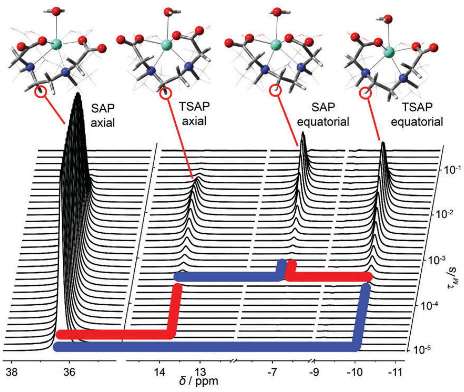

Fig. 3 Series of 1D-EXSY spectra of [Eu(**dota**)(D$_2$O)]$^-$ recorded by using increasing τ_M values (10 μs–250 ms). The refocusing selective 180° pulse was applied to the SAP axial resonance. Blue and red lines highlight ring inversion and arm rotation pathways, respectively.

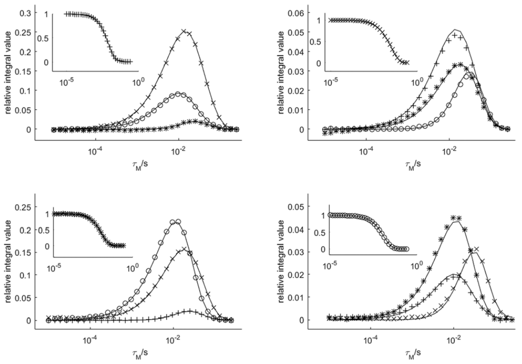

Fig. 4 Relative areas of the four signals of [Eu(**dota**)(D$_2$O)]$^-$ as a function of the mixing time obtained from 1D-EXSY experiments at 5 °C. The insets show the evolution of the magnetization of the signal to which the refocusing selective 180° pulse was applied. Symbols: TSAP$_{ax}$ (+), SAP$_{eq}$ (×), TSAP$_{eq}$ (*), SAP$_{ax}$ (○). The solid lines represent the simultaneous fit of all four data sets using eqn (2).

Table 1 Exchange and relaxation rates and equilibrium constants of the Eu^{3+} complexes determined by the nonlinear fit of ^1H 1D-EXSY experimental data at 5 °C in D_2O^a

Parameter	Anion **dota**$^{4-}$	H**do3ap**$^{4-}$	**do3ap**$^{5-}$
k_{PendSAP}	5.58(6)	23.2(5)	99.7(3)
k_{CycleSAP}	10.60(7)	19.6(6)	21.0(3)
k_{PendTSAP}	25.80(7)	25.0(5)	71.7(3)
$k_{\mathrm{CycleTSAP}}$	52.30(8)	23.0(6)	15.5(2)
K_{EXSY}	0.207(5)	0.89(9)	1.39(4)
K_{integral}	0.21	0.88	1.42
$R_{1\mathrm{Ax.\ SAP}}$	69.1(1)	69.4(9)	73.2(4)
$R_{1\mathrm{Eq.\ SAP}}$	22.53(7)	20(3)	16(2)
$R_{1\mathrm{Ax.\ TSAP}}$	47.6(2)	54.1(9)	58.9(3)
$R_{1\mathrm{Eq.\ TSAP}}$	18.3(1)	22(3)	23(2)

[a] k/s^{-1} are exchange rates, R_1/s^{-1} are longitudinal relaxation rates, and K denotes equilibrium constants calculated as $K_{\mathrm{EXSY}} = (k_{\mathrm{PendSAP}} + k_{\mathrm{CycleSAP}})/(k_{\mathrm{PendTSAP}} + k_{\mathrm{CycleTSAP}})$ or determined from integration of the ^1H proton signals of TSAP/SAP axial protons (K_{integral}).

reaction obtained from the exchange rates ($K_{\mathrm{EXSY}} = (k_{\mathrm{PendSAP}} + k_{\mathrm{CycleSAP}})/(k_{\mathrm{PendTSAP}} + k_{\mathrm{CycleTSAP}})$) are in excellent agreement with those obtained from ^1H spectral integration (Table 1) and confirms the accuracy of our analysis.

In the case of $[Eu(\mathbf{dota})(D_2O)]^-$, the TSAP ⇆ SAP interconversion processes are dominated by the ring inversion mechanism which is approximately twice as fast as the arm rotation (Table 1). The arm rotation and ring inversion processes proceed with comparable rates for $[Eu(H\mathbf{do3ap})(D_2O)]^-$. Deprotonation of the phosphonate pendant arm does not have an important effect on the rates characterizing the ring inversion pathway; however, it dramatically accelerates the arm rotation pathway for the TSAP → SAP interconversion (from 25.0 s^{-1} to 71.7 s^{-1}), and even more for the reverse process (from 23.2 s^{-1} to 99.7 s^{-1}, Table 1). These results are in a good agreement with the results of ^{31}P 1D-EXSY experiments where only the sum of arm rotation and ring inversion can be principally detected (see Fig. S6, S7 and Table S5, ESI†).

The SAP_{ax} ⇆ SAP_{eq} exchange process represents the mutual interconversion of the SAP enantiomers and requires both arm rotation and inversion of the cyclen chelate rings. Fig. 3 shows that magnetization transfer to SAP_{eq} protons occurs with some delay with respect to the $TSAP_{ax}$ and $TSAP_{eq}$ protons. The same effect can be observed in Fig. 4 for all protons exchanging by racemization with those chosen for the 180°(sel) pulse. These results indicate that enantiomerization follows concatenated arm rotation and ring inversion mechanisms.

As the EXSY experiments were not designed to measure relaxation rates (their effect is partially suppressed by phase cycling), they were determined with lower accuracy than exchange rates. Nevertheless, in all cases the axial protons present faster relaxation rates than the equatorial ones, which is caused by their shorter distance from the Eu^{3+} central ion compared to the equatorial protons.[40] The relaxation rates determined for axial protons of SAP geometries are faster than those observed for TSAP isomers while equatorial protons show comparable relaxation rates in both isomers. This can be attributed, at least in part, to shorter $Eu\cdots H_{ax}$ distances in the SAP isomers (3.849 and 3.931 Å for the SAP and TSAP isomers of $[Eu(\mathbf{dota})(D_2O)]^-$ respectively, according to the DFT calculations presented below), and quite similar distances for the equatorial protons (4.550 and 4.579 Å for the same SAP and TSAP isomers, respectively).

2.4 Activation parameters

Variable-temperature ^1H 1D-EXSY experiments were also conducted at 15, 25 and 35 °C by applying the same procedures described in the previous section for 5 °C. Measurements at lower temperature were not possible due to hardware and solvent limitations while, at higher temperatures, extensive signal broadening occurs due to chemical exchange. The exchange rates determined at four temperatures (5, 15, 25 and 35 °C) were used to determine the activation enthalpy $\Delta H^{\ddagger}$ and activation entropy $\Delta S^{\ddagger}$ of each exchange process using the Eyring equation (4), where all symbols have their usual meaning.

$$k(T) = \frac{k_B T}{h} e^{-\frac{\left(\Delta H^{\ddagger} - T\Delta S^{\ddagger}\right)}{RT}} \tag{4}$$

The activation parameters obtained for the TSAP/SAP exchange processes indicate that arm rotation is driven mainly by enthalpy factors, since entropic contribution is close to zero.

The $\Delta S^{\ddagger}$ values characterizing the arm rotation path of the SAP isomers take values lower than 10 J K^{-1} mol^{-1}. The reverse process in $[Eu(\mathbf{do3ap})(D_2O)]^{2-}$ is characterized by a negative activation entropy ($\Delta S^{\ddagger}_{\mathrm{PendTSAP}} = -17(2)$ J K^{-1} mol^{-1}) that deviates from this trend. Although this difference could be associated with a different mechanism, it can also be associated with an enthalpy–entropy compensation effect due to the simplified model applied, and/or an insufficient temperature range accessible in our experiments.[41]

The activation entropies obtained for the ring inversion process are consistently negative. However, a comparison with data reported for related systems is not straightforward. This is either because of the high uncertainty of the data,[29] or the different hydration numbers of the SAP and TSAP isomers in the case of the Lu^{3+}-**dota** complex, which determines the entropy of the transition state.[23] Despite this, the activation entropy reported for the La^{3+}-**dota** complex ($\Delta S^{\ddagger}_{\mathrm{CycleTSAP}}$ −21.4 J K^{-1} mol^{-1}) is consistent with our results.[7] The strong negative values obtained herein in some cases ($\Delta S^{\ddagger}_{\mathrm{CycleSAP}} = -54(11)$ J K^{-1} mol^{-1} for $[Eu(\mathbf{do3ap})(D_2O)]^{2-}$ and $\Delta S^{\ddagger}_{\mathrm{CycleTSAP}} = -43(4)$ J K^{-1} mol^{-1} for $[Eu\ (H\mathbf{do3ap})(D_2O)]^-$) are associated with rather low activation enthalpies ($\Delta H^{\ddagger}_{\mathrm{CycleSAP}} = 45(3)$ kJ mol^{-1} for $[Eu(\mathbf{do3ap})(D_2O)]^{2-}$ and $\Delta H^{\ddagger}_{\mathrm{CycleTSAP}} = 49(1)$ kJ mol^{-1} for $[Eu(H\mathbf{do3ap})(D_2O)]^-$), which again suggests an enthalpy–entropy compensation effect.

2.5 DFT calculations

DFT calculations were used to gain an insight into the mechanisms responsible for the conformational dynamics of $[Eu(\mathbf{dota})(H_2O)]^-$, $[Eu(\mathbf{do3ap})(H_2O)]^{2-}$ and $[Eu(H\mathbf{do3ap})(H_2O)]^-$ at the molecular level. Following previous studies, we employed the large core relativistic effective pseudopotential of Dolg,[42,43] which includes 46 + $4f^6$ electrons of Eu^{3+} in the core, in combination with Pople's 6-31+G(d,p) basis set to describe the ligand atoms. The hybrid meta-GGA functional M06 was used throughout.[44] Bulk solvent effects were considered by using a polarized continuum model (see computational details below). The two pathways responsible for TSAP/SAP exchange (arm rotation and cyclen inversion) were studied separately as there is no experimental evidence of the composite mechanism.

Geometry optimizations of the $[Eu(\mathbf{dota})(H_2O)]^-$, $[Eu(\mathbf{do3ap})(H_2O)]^{2-}$ and $[Eu(H\mathbf{do3ap})(H_2O)]^-$ complexes provided the expected SAP and TSAP isomers as local energy minima. The structure calculated for the SAP isomer of $[Eu(\mathbf{dota})(H_2O)]^-$ presents average Eu–$O_{carboxylate}$ and Eu–N distances of 2.390 and 2.725 Å, respectively, which compare well with the average experimental values obtained from X-ray diffraction measurements (Eu–O = 2.394 and Eu–N = 2.680 Å).[45] The ring-inversion process responsible for the SAP → TSAP interconversion pathway calculated for the three systems is a four-step process; it involves the stepwise inversion of each of the five-membered chelate rings, resulting from the coordination of the macrocyclic unit. This stepwise mechanism is in line with previous studies performed on cyclen-based complexes using HF and DFT methods.[5,35,46]

Several pathways are possible for the inversion of the cyclen unit of $[Eu(\mathbf{dota})(H_2O)]^-$ depending on the sequence of ethylenediamine units that change conformation from δ to λ. The lowest energy path corresponds to the inversion of cyclen chelate rings following the sequence C2 → C3 → C4 → C1 (see Fig. 1 for labeling). The calculated activation free energy, as estimated for the transition state (TS) with the highest energy along the minimum energy pathway ($\Delta G^{\ddagger}_{calc}$ = 61.9 kJ mol^{-1}, Table 3), is in excellent agreement with the experimental value ($\Delta G^{\ddagger}_{CycleSAP}$ = 62.7 ± 0.9 kJ mol^{-1}). For $[Eu(\mathbf{do3ap})(H_2O)]^{2-}$ and $[Eu(H\mathbf{do3ap})(H_2O)]^-$, the paths with the lowest energy correspond to the sequences C3 → C1 → C4 → C2 and C2→ C3 → C4 → C1, respectively, with the inversion of C2 ($\Delta G^{\ddagger}_{calc}$ = 66.6 kJ mol^{-1}) and C3 ($\Delta G^{\ddagger}_{calc}$ = 60.6 kJ mol^{-1}) being the steps with the highest activation energies (Fig. 5). The agreement between the experimental and calculated activation free energies is very good in both cases. However, one should bear in mind that our calculations provide several pathways with very similar activation energies, with 3, 12 and 7 paths having activation free energies within 5 kJ mol^{-1} for $[Eu(\mathbf{dota})(H_2O)]^-$, $[Eu(\mathbf{do3ap})(H_2O)]^{2-}$ and $[Eu(H\mathbf{do3ap})(H_2O)]^-$, respectively. Thus, it is likely that several of them can play a role in the SAP → TSAP interconversion process (Fig. 5 and ESI†).

Our calculations provide negative $\Delta S^{\ddagger}$ values, in agreement with the experimental data (Table 3). An analysis of the different contributions to the total $\Delta S^{\ddagger}$ (ESI†) indicates that the vibrational contribution is the main factor leading to negative values due to the reduction of intramolecular vibrational frequencies. Inspection of the geometries of the SAP isomers and the transition states responsible for the SAP → TSAP interconversion shows that the inversion of the cyclen chelate rings provokes an important lengthening of the Eu–N distances. Thus, the largest contribution to the negative $\Delta S^{\ddagger}$ values can be attributed to a reduction of the vibrational frequencies of low-frequency modes involving the relative displacement of the lanthanide(III) ion and the nitrogen atoms of the cyclen chelate rings.[47]

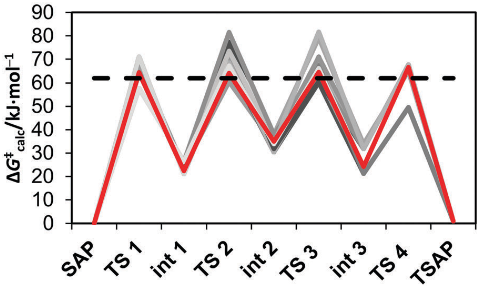

Fig. 5 Energy profile calculated for the cyclen chelate ring inversions in $[Eu(\mathbf{do3ap})(H_2O)]^{2-}$ at 25 °C. The lowest energy pathway is highlighted in red, while the experimental activation free energy is represented by a black dashed line.

According to the calculations, the arm rotation process is synchronous (*i.e.* the process involves only one transition state) in both $[Eu(\mathbf{dota})(H_2O)]^-$ and $[Eu(H\mathbf{do3ap})(H_2O)]^-$ but follows a stepwise pathway for $[Eu(\mathbf{do3ap})(H_2O)]^{2-}$. The synchronous mechanisms of $[Eu(\mathbf{dota})(H_2O)]^-$ and $[Eu(H\mathbf{do3ap})(H_2O)]^-$ involve the simultaneous rotation of all four pendant arms. The activation free energies obtained from these calculations are 71.4 ($[Eu(\mathbf{dota})(H_2O)]^-$) and 85.5 ($[Eu(H\mathbf{do3ap})(H_2O)]^-$) kJ mol^{-1}. These values considerably exceed the experimental values of 64 and 61 kJ mol^{-1} (Table 3), respectively. Nevertheless, the value calculated for $[Eu(\mathbf{dota})(H_2O)]^-$ represents a significant improvement with respect to that obtained for $[Lu(\mathbf{dota})]^-$ in the gas phase (82.0 kJ mol^{-1}).[7] Thus, the introduction of bulk solvent effects with a polarized continuum appears to bring the calculated activation energies closer to the experimental values.

Table 2 Activation parameters calculated for TSAP/SAP exchange for the Eu^{3+} complexes in D_2O^a

	Anion		
Parameter	**dota**$^{4-}$	H**do3ap**$^{4-}$	**do3ap**$^{5-}$
$\Delta H^{\ddagger}_{PendSAP}$	66.0(6)	61.8(7)	58.3(5)
$\Delta H^{\ddagger}_{CycleSAP}$	58.8(4)	54(1)	45(3)
$\Delta H^{\ddagger}_{PendTSAP}$	57(1)	61.1(6)	53.4(7)
$\Delta H^{\ddagger}_{CycleTSAP}$	55(1)	49(1)	59(2)
$\Delta S^{\ddagger}_{PendSAP}$	7(2)	4(2)	4(2)
$\Delta S^{\ddagger}_{CycleSAP}$	−13(1)	−26(4)	−54(11)
$\Delta S^{\ddagger}_{PendTSAP}$	−9(5)	2(2)	−17(2)
$\Delta S^{\ddagger}_{CycleTSAP}$	−14(4)	−43(4)	−10(7)
$\Delta G^{\ddagger}_{PendSAP}$	64(1)	61(1)	57(1)
$\Delta G^{\ddagger}_{CycleSAP}$	62.7(9)	62(2)	62(7)
$\Delta G^{\ddagger}_{PendTSAP}$	61(3)	60(1)	58(1)
$\Delta G^{\ddagger}_{CycleTSAP}$	59(2)	62(2)	62(4)

[a] $\Delta H^{\ddagger}$/kJ mol^{-1}, $\Delta S^{\ddagger}$/J K^{-1} mol^{-1} and $\Delta G^{\ddagger}$ (25 °C)/kJ mol^{-1} are activation enthalpy, activation entropy and Gibbs energy (calculated from $\Delta H^{\ddagger}$ and $\Delta S^{\ddagger}$ at 25 °C), respectively.

Table 3 Activation parameters calculated for the ring-inversion process responsible for the SAP → TSAP interconversion process of the Eu^{3+} complexes at 25 °C[a]

Anion	$\Delta G^{\ddagger}_{\mathrm{CycleSAP}}$	$\Delta S^{\ddagger}_{\mathrm{CycleSAP}}$	$\Delta H^{\ddagger}_{\mathrm{CycleSAP}}$
dota^{4-}	61.9 (62.7)	−3.3 (−13)	63.8 (58.8)
H**do3ap**$^{4-}$	60.6 (62.0)	−8.8 (−26)	57.9 (54)
do3ap^{5-}	66.6 (62.0)	−15 (−54)	62.2 (45)

[a] $\Delta H^{\ddagger}$/kJ mol^{-1}, $\Delta S^{\ddagger}$/J K^{-1} mol^{-1} and $\Delta G^{\ddagger}$ (25 °C)/kJ mol^{-1}. The experimental values are provided in parentheses.

This suggests that solvent effects play an important role in the arm rotation process of negatively charged pendant arms.

The polarized continuum model used in this work represents an improvement with respect to previous studies, but it still shows some limitations to account for specific solute–solvent interactions (*i.e.* hydrogen bonds involving second-sphere water molecules and the negatively charged pendant arms). For instance, it has been shown previously that the explicit inclusion of a few second-sphere water molecules was critical to compute accurate Ln–O_{water} bond distances and ^{17}O hyperfine coupling constants in lanthanide(III) complexes.[48,49] To test the effect of an explicit second hydration shell, the arm-rotation process on the $[Eu(\mathbf{dota})(H_2O)]^{-}\cdot 2H_2O$ system was investigated. It includes two explicit second-sphere water molecules involved in hydrogen bonds with the coordinated water molecule and oxygen atoms of the carboxylate groups (Fig. S12, ESI†). The inclusion of two second-sphere water molecules results in a significant shortening of the calculated Eu–O_{water} bond distance from 2.583 to 2.491 Å for the SAP isomer, the latter value being in good agreement with the value observed in the solid state (2.480 Å).[45] The synchronous transition state obtained for this system provides a calculated $\Delta G^{\ddagger}$ value of 60.0 kJ mol^{-1}, which is in close agreement with the experimental value of 64(1) kJ mol^{-1} (Table 3). For $[Eu(H\mathbf{do3ap})(H_2O)]^{-}$, the inclusion of the explicit water molecules also results in the decrease in the arm rotation activation energy (81.9 kJ mol^{-1}), but the effect is not as large as for $[Eu(\mathbf{dota})(H_2O)]^{-}$. However, a similar trend in the Eu–O_{water} bond distance of the SAP isomer was followed; the distances are 2.584 and 2.492 Å for the $[Eu(H\mathbf{do3ap})(H_2O)]^{-}$ complex and the $[Eu(H\mathbf{do3ap})(H_2O)]^{-}\cdot 2H_2O$ system, respectively.

The energy profile calculated for the stepwise rotation of the pendant arms in $[Eu(\mathbf{do3ap})(H_2O)]^{2-}$ is shown in Fig. 6 and Table 4. The first step of the pathway corresponds to the rotation of the phosphonate pendant arm, which changes its coordination mode from mono – to bidentate (Fig. 7). Subsequent rotation of the three acetate pendant arms results in SAP → TSAP interconversion. The activation free energy estimated from the energy of the transition state with the highest energy is 42.6 kJ mol^{-1} (Table 5). This value is somewhat lower than the experimental one (57(1) kJ mol^{-1}, Table 2). We attribute this discrepancy to an overestimation of the stability of the intermediates with the bidentate phosphonate group; this is related to the limitations of continuum solvation models to provide an adequate description of the hydration of the negatively double-charged phosphonate groups. In order to understand this effect, the rate determining step was re-optimized with two second-sphere water molecules. The corresponding activation energy (51.2 kJ mol^{-1}) is in reasonable agreement with the experiment. The Eu–O_{water} bond distance of the SAP isomer is 2.633 and 2.593 Å for $[Eu(\mathbf{do3ap})(H_2O)]^{2-}$ and $[Eu(\mathbf{do3ap})(H_2O)]^{2-}\cdot 2H_2O$ respectively, which is consistent with the trends discussed above.

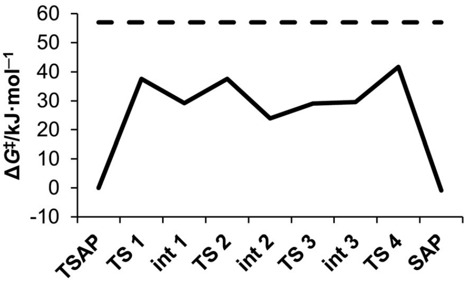

Fig. 6 Calculated energy profile of successive arm rotation of $[Eu(\mathbf{do3ap})(H_2O)]^{2-}$ at 25 °C (full line); compared to experimental activation energy $\Delta G^{\ddagger}_{\mathrm{PendTSAP}}$ (dashed line). For geometry of each intermediate (Int #) and transition state (TS #), see the ESI.†

Table 4 Calculated energy profile of successive pendant flipping of $[Eu(\mathbf{do3ap})(H_2O)]^{2-}$ at 25 °C

Step/intermediate[a]	$\Delta G^{\ddagger}_{\mathrm{calc}}$/kJ mol^{-1}
TSAP	0.0
TS 1	37.5
Int 1	29.2
TS 2	37.5
Int 2	23.9
TS 3	29.0
Int 3	29.6
TS 4	41.7
SAP	−0.9

[a] For each step description, see text and ESI; **Int** # indicates a stable intermediate between two-step transition states (**TS** #).

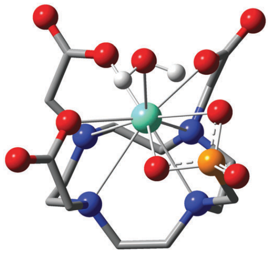

Fig. 7 Calculated molecular structure of the $[Eu(\mathbf{do3ap})(H_2O)]^{2-}$ intermediate (**Int 1**) with the bidentate phosphonate group. Color code: black – carbon; white – hydrogen; blue – nitrogen; red – oxygen; orange – phosphorus; green – europium. Macrocycle hydrogen atoms are omitted for clarity.

The results obtained for the arm rotation mechanism show that adding second-sphere water molecules results in a more accurate description of the system. In principle, the model

Table 5 Calculated free energy of arm rotation ($\Delta G^{\ddagger}_{\text{calc}}$/kJ mol^{-1}) compared to the related experimental value ($\Delta G^{\ddagger}_{\text{PendSAP}}$/kJ mol^{-1}) with n second-sphere water molecules (the free energies are related to the SAP isomers)

	Anion		
Parameter	**dota**$^{4-}$	H**do3ap**$^{4-}$	**do3ap**$^{5-}$
$\Delta G^{\ddagger}_{\text{PendSAP}}$	64(1)	61(1)	57(1)
$\Delta G^{\ddagger}_{\text{calc}}$ $n = 0$	71.4[b]	85.5[b]	42.6[c]
$\Delta G^{\ddagger}_{\text{calc}}$ $n = 2$	60.0[b]	81.9[b]	51.2[c]
[Lu(**dota**)]$^{-}$without PCM[a]	82.0	—	—

[a] Ref. 7. [b] Synchronous process. [c] Rate-determining step of successive arm rotation.

could be further improved by increasing the number of explicit second-sphere water molecules. However, our attempts in this direction failed because the increasing number of soft degrees of freedom disables transition state geometry optimization. However, alternative molecular dynamics or metadynamics simulations[34,50] are not effective enough to reach the long (ms) trajectories required to describe the TSAP ↔ SAP interconversion.

2.6 Conclusions

The dynamics of lanthanide(III) complexes with ligands structurally related to H$_4$**dota** in solution is critical for the behaviour of these systems if they are applied as MRI CAs. One of the most important dynamic processes occurring in complexes of the **dota**-like ligands is the exchange between the SAP and TSAP geometries of the coordination polyhedron. This exchange can occur *via* pendant arm rotation or cyclen inversion. Though many publications have focused on the description of this complicated motion, the rates of these processes were not measured accurately.

In this work, we determined arm rotation and cyclen inversion rates separately by utilization of a modified EXSY NMR pulse sequence in combination with full Bloch-McConnell-based data analysis. In addition, we also reported the corresponding activation barriers. A detailed insight into the mechanisms of these motions at the molecular level was obtained using DFT calculations.

The calculated activation parameters for the cyclen-inversion process are in excellent agreement with the experimental ones, including the activation entropies. The activation barriers computed with DFT for the arm rotation pathway present larger deviations from the experimental values. However, we showed that this is mainly due to deficient modelling of solvent effects by PCM as the arm rotation process involves flipping of the negatively charged pendant arms. Propitiously, using a mixed cluster-continuum model that includes two explicit second-sphere water molecules results in activation parameters which are in better agreement with the experiment for the arm rotation process. We believe that the results reported here represent an important contribution to a better understanding the dynamics of these important complexes.

Furthermore, the NMR methodology described here could be, in principle, applied to investigations of the dynamics of complex paramagnetic systems (*i.e.* proteins with open-shell ions) thanks to the paramagnetically-induced shifts which avoid extensive signal overlap and increase the range of observable exchange rates.

3 Experimental and computational section

3.1 Reagents and materials

The ligands, H$_4$**dota** and H$_5$**do3ap**, were prepared according the literature procedures.[1,6] Samples of the Eu^{3+} complexes for NMR studies were obtained by dissolving the corresponding ligand (100 mg) in water (4 mL) and adding 0.95 equiv. of EuCl$_3$·6H$_2$O. Then, 5% aq. LiOH was slowly added to reach pH 11 and the mixture was stirred overnight at 60 °C. The absence of free Eu^{3+} ions was tested by reaction with xylenol orange in acetate buffer at pH 6.7.[51] The solution was then evaporated to dryness and the residue was re-dissolved in D$_2$O (Euriso-top, 99.96% D) for the NMR measurements. The pD of the samples was adjusted by addition of dilute solutions of DCl or LiOD in D$_2$O.

3.2 NMR spectroscopy

NMR experiments were performed on a Bruker AVANCE III 600 and 400 MHz spectrometers, the former equipped with a cryoprobe. The temperature of the sample was calibrated using pure MeOH (below 15 °C) and ethylene glycol (above 15 °C) by measuring the chemical shift differences between the two ^{1}H NMR signals.[52,53] Particular care was taken to ensure that the sample reached thermal equilibrium before the data acquisition started. The acquired FID data were then analyzed using MestReNova software.[54] A 50 Hz exponential apodization was applied prior to the Fourier transform, followed by phase and baseline corrections. The signals of axial and equatorial protons of both isomers were integrated for the data analysis. In the case of signal overlap, the signal pattern was deconvoluted into Lorenzian–Gaussian curves using MestReNova tools. The dependence of signal integral values with mixing time was fitted using self-written procedures in the MATLAB R2015b®[55] environment. The activation enthalpies and entropies ($\Delta H^{\ddagger}$ and $\Delta S^{\ddagger}$) were determined using MATLAB by fitting the temperature dependence of exchange rates using the Eyring equation (4).

3.3 Computational details

All calculations presented in this work were performed using Gaussian 09 (Revision D.01).[56] Full geometry optimizations of transition states and energetic minima were performed employing DFT within the meta-GGA approximation using M06[57] exchange–correlation functional. For all atoms except Eu^{3+}, the 6-31+G(d,p) basis set was employed. The large core effective core potential of the Stuttgart family (including 46 + 4f^6 electrons in core, ECP52MWB)[43] and the associated (7s6p5d)/[5s4p3d] basis set were used for Eu^{3+}. An UltraFine integration grid and the default SCF energy convergence threshold (10^{-8}) were used in all calculations. All the calculations were performed employing a polarization continuum model to account for bulk solvent effects (water) and the solvent accessible surface to define the solute cavity. The identities of all stationary points (0 imaginary frequencies) and transition states (1 imaginary frequency) were confirmed by frequency analysis.

Conflicts of interest

There are no conflicts of interest to declare.

Acknowledgements

The investigations were supported by the Czech Science Foundation (16-03156S; to J. B.), by the Grant Agency of Charles University (1076016, to J. B.) and the Ministry of Education of the Czech Republic (LTC 170607, to J. B. and P. H.; project is connected to the EU COST CA15209 Action). Computational resources were provided by the CESNET LM2015042 and the CERIT Scientific Cloud LM2015085, provided under the program "Projects of Large Research, Development, and Innovations Infrastructures". C. P.-I. thanks Ministerio de Economía y Competitividad (CTQ2013-43243-P) for generous financial support.

Notes and references

1 J. F. Desreux, *Inorg. Chem.*, 1980, **19**, 1319–1324.
2 D. Parker, R. S. Dickins, H. Puschmann, C. Crossland and J. A. K. Howard, *Chem. Rev.*, 2002, **102**, 1977–2010.
3 S. Aime, M. Botta, M. Fasano, M. P. M. Marques, C. F. G. C. Geraldes, D. Pubanz and A. E. Merbach, *Inorg. Chem.*, 1997, **36**, 2059–2068.
4 F. A. Dunand, S. Aime and A. E. Merbach, *J. Am. Chem. Soc.*, 2000, **122**, 1506–1512.
5 L. S. Natrajan, N. M. Khoabane, B. L. Dadds, C. A. Muryn, R. G. Pritchard, S. L. Heath, A. M. Kenwright, I. Kuprov and S. Faulkner, *Inorg. Chem.*, 2010, **49**, 7700–7709.
6 J. Rudovský, P. Cígler, J. Kotek, P. Hermann, P. Vojtíšek, I. Lukes, J. A. Peters, L. Vander Elst and R. N. Muller, *Chem. – Eur. J.*, 2005, **11**, 2373–2384.
7 M. Purgel, Z. Baranyai, A. de Blas, T. Rodríguez-Blas, I. Bányai, C. Platas-Iglesias and I. Tóth, *Inorg. Chem.*, 2010, **49**, 4370–4382.
8 S. Aime, A. Barge, M. Botta, A. S. De Sousa and D. Parker, *Angew. Chem., Int. Ed.*, 1998, **37**, 2673–2675.
9 B. C. Webber and M. Woods, *Inorg. Chem.*, 2012, **51**, 8576–8582.
10 M. Woods, S. Aime, M. Botta, J. A. K. Howard, J. M. Moloney, M. Navet, D. Parker, M. Port and O. Rousseaux, *J. Am. Chem. Soc.*, 2000, **122**, 9781–9792.
11 *The Chemistry of Contrast Agents in Medical Magnetic Resonance Imaging*, ed. A. Merbach, L. Helm and É. Tóth, John Wiley & Sons, Ltd, Chichester, UK, 2013.
12 S. Viswanathan, Z. Kovacs, K. N. Green, S. J. Ratnakar and A. D. Sherry, *Chem. Rev.*, 2010, **110**, 2960–3018.
13 W. M. Liu, M. Overhand and M. Ubbink, *Coord. Chem. Rev.*, 2014, **273–274**, 2–12.
14 U. Brath, S. I. Swamy, A. X. Veiga, C.-C. Tung, F. Van Petegem and M. Erdélyi, *J. Am. Chem. Soc.*, 2015, **137**, 11391–11398.
15 T. Krchová, A. Gálisová, D. Jirák, P. Hermann and J. Kotek, *Dalton Trans.*, 2016, 3486–3496.
16 T. Krchová, V. Herynek, A. Gálisová, J. Blahut, P. Hermann and J. Kotek, *Inorg. Chem.*, 2017, **56**, 2078–2091.
17 P. Harvey, A. M. Blamire, J. I. Wilson, K.-L. N. A. Finney, A. M. Funk, P. Kanthi Senanayake and D. Parker, *Chem. Sci.*, 2013, **4**, 4251–4258.
18 G. Cucinotta, M. Perfetti, J. Luzon, M. Etienne, P. E. Car, A. Caneschi, G. Calvez, K. Bernot and R. Sessoli, *Angew. Chem., Int. Ed.*, 2012, **51**, 1606–1610.
19 L. Lumata, A. K. Jindal, M. E. Merritt, C. R. Malloy, A. D. Sherry and Z. Kovacs, *J. Am. Chem. Soc.*, 2011, **133**, 8673–8680.
20 R. S. Dickins, S. Gaillard, S. P. Hughes and A. Badari, *Chirality*, 2005, **17**, 357–363.
21 S. P. Babailov, *Prog. Nucl. Magn. Reson. Spectrosc.*, 2008, **52**, 1–21.
22 F. K. Kálmán, Z. Baranyai, I. Tóth, I. Bányai, R. Király, E. Brücher, S. Aime, X. Sun, A. D. Sherry and Z. Kovács, *Inorg. Chem.*, 2008, **47**, 3851–3862.
23 S. Aime, A. Barge, M. Botta, M. Fasano, J. Danilo Ayala and G. Bombieri, *Inorg. Chim. Acta*, 1996, **246**, 423–429.
24 F. A. Dunand, R. S. Dickins, D. Parker and A. E. Merbach, *Chem. – Eur. J.*, 2001, **7**, 5160–5167.
25 M. Elhabiri, S. Abada, M. Sy, A. Nonat, P. Choquet, D. Esteban-Gómez, C. Cassino, C. Platas-Iglesias, M. Botta and L. J. Charbonnière, *Chem. – Eur. J.*, 2015, **21**, 6535–6546.
26 M. Mato-Iglesias, T. Rodríguez-Blas, C. Platas-Iglesias, M. Starck, P. Kadjane, R. Ziessel and L. Charbonniére, *Inorg. Chem.*, 2009, **48**, 1507–1518.
27 S. P. Babailov, A. G. Coutsolelos, A. Dikiy and G. A. Spyroulias, *Eur. J. Inorg. Chem.*, 2001, 303–306.
28 S. Hoeft and K. Roth, *Chem. Ber.*, 1993, **126**, 869–873.
29 V. Jacques and J. F. Desreux, *Inorg. Chem.*, 1994, **33**, 4048–4053.
30 O. V. Yazyev, L. Helm, V. G. Malkin and O. L. Malkina, *J. Phys. Chem.*, 2005, **109**, 10997–11005.
31 A. Lasoroski, R. Vuilleumier and R. Pollet, *J. Chem. Phys.*, 2014, **141**, 14201.
32 A. Lasoroski, R. Vuilleumier and R. Pollet, *J. Chem. Phys.*, 2013, **139**, 104115.
33 A. Ramírez-Solís, J. I. Amaro-Estrada, J. Hernández-Cobos and L. Maron, *J. Phys. Chem. A*, 2017, **121**, 2293–2297.
34 R. Pollet, N. N. Nair and D. Marx, *Inorg. Chem.*, 2011, **50**, 4791–4797.
35 U. Cosentino, A. Villa, D. Pitea, G. Moro, V. Barone and A. Maiocchi, *J. Am. Chem. Soc.*, 2002, **124**, 4901–4909.
36 C. Platas-Iglesias, *Eur. J. Inorg. Chem.*, 2012, 2023–2033.
37 M. P. M. Marques, C. F. G. C. Geraldes, A. D. Sherry, A. E. Merbach, H. Powell, D. Pubanz, S. Aime and M. Botta, *J. Alloys Compd.*, 1995, **225**, 303–307.
38 C. Kumas, W. S. Fernando, P. Zhao, M. Regueiro-Figueroa, G. E. Kiefer, A. F. Martins, C. Platas-Iglesias and A. D. Sherry, *Inorg. Chem.*, 2016, **55**, 9297–9305.

39 K. Stott, J. Stonehouse, J. Keeler, T.-L. Hwang and A. J. Shaka, *J. Am. Chem. Soc.*, 1995, **117**, 4199–4200.

40 S. Aime, L. Barbero, M. Botta and G. Ermondi, *J. Chem. Soc., Dalton Trans.*, 1992, 225–228.

41 L. Liu and Q. X. Guo, *Chem. Rev.*, 2001, **101**, 673–695.

42 M. Dolg, H. Stoll and H. Preuss, *Theor. Chim. Acta*, 1993, **85**, 441–450.

43 M. Dolg, H. Stoll, A. Savin and H. Preuss, *Theor. Chim. Acta*, 1989, **75**, 173–194.

44 A. Roca-Sabio, M. Regueiro-Figueroa, D. Esteban-Gómez, A. de Blas, T. Rodríguez-Blas and C. Platas-Iglesias, *Comput. Theor. Chem.*, 2012, **999**, 93–104.

45 M. R. Spirlet, J. Rebizant, J. F. Desreux and M. F. Loncin, *Inorg. Chem.*, 1984, **23**, 359–363.

46 M. Regueiro-Figueroa, B. Bensenane, E. Ruscsák, D. Esteban-Gómez, L. J. Charbonnière, G. Tircsó, I. Tóth, A. de Blas, T. Rodríguez-Blas and C. Platas-Iglesias, *Inorg. Chem.*, 2011, **50**, 4125–4141.

47 G. Brehm, M. Reiher and S. Schneider, *J. Phys. Chem. A*, 2002, **106**, 12024–12034.

48 D. Esteban-Gómez, A. de Blas, T. Rodríguez-Blas, L. Helm and C. Platas-Iglesias, *ChemPhysChem*, 2012, **13**, 3640–3650.

49 M. Regueiro-Figueroa and C. Platas-Iglesias, *J. Phys. Chem. A*, 2015, **119**, 6436–6445.

50 R. Pollet, C. S. Bonnet, P. Retailleau, P. Durand and É. Tóth, *Inorg. Chem.*, 2017, **56**, 4317–4323.

51 A. Barge, G. Cravotto, E. Gianolio and F. Fedeli, *Contrast Media Mol. Imaging*, 2006, **1**, 184–188.

52 C. Ammann, P. Meier and A. Merbach, *J. Magn. Reson.*, 1982, **46**, 319–321.

53 M. L. Kaplan, F. A. Bovey and H. N. Cheng, *Anal. Chem.*, 1975, **47**, 1703–1705.

54 MestReNova, Version 11.0.1-17801, Mestrelab Research S.L., Santiago de Compostela, 2016.

55 MATLAB and Optimisation Toolbox 7.3 Release R2015b, The MathWorks, Inc., Natick, Massachusetts, United States, DERIVESTsuite, available *via* www.mathworks.com.

56 *Gaussian 09, Revision D.01*, Gaussian, Inc., Wallingford, CT, 2016.

57 Y. Zhao and D. G. Truhlar, *Theor. Chem. Acc.*, 2008, **120**, 215–241.

Electronic Supplementary Material (ESI) for Physical Chemistry Chemical Physics.

Combined NMR and DFT study of conformational dynamics in lanthanide DOTA-like complexes

Jan Blahut, Petr Hermann, Zdeněk Tošner, and Carlos Platas-Iglesias,

Electronic supplementary information

Content:

For all calculated Cartesian coordinates and related energies of intermediates see folder in coordinatesArchive.rar archive.

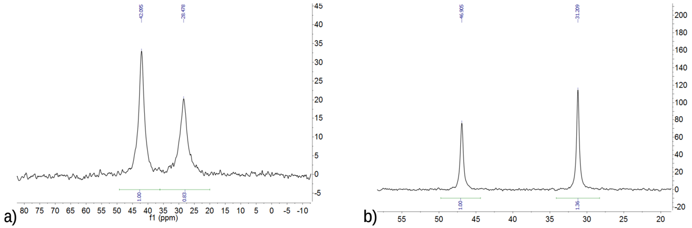

Figure S1: ^{31}P spectra of a) $[Eu(Hdo3ap)(D_2O)]^-$ (pD = 3.6) and b) $[Eu(Hdo3ap)(D_2O)]^{2-}$ (pD = 8.5) at 5 °C and 162 MHz.

Table S1: ^{1}H chemical shifts at 5 °C of axial and equatorial hydrogen nuclei used in 1D-EXSY studies. Supplement to Figure 2 in the main text.

δ/ppm	dota	Hdo3ap	do3ap
SAP axial 1	36.32	38.02	40.68
SAP axial 2	–	37.00	39.68
SAP axial 3	–	34.98	37.20
SAP axial 4	–	29.50	28.30
TSAP axial 1	13.78	20.74	25.16
TSAP axial 2	–	17.17	20.34
TSAP axial 3	–	11.76	12.93
TSAP axial 4	–	9.34	9.70
SAP equatorial 1	–7.04	–2.78	–1.04
SAP equatorial 2	–	–4.02	–3.15
SAP equatorial 3	–	–10.07	–10.01
SAP equatorial 4	–	–9.26	–8.43
TSAP equatorial 1	–10.06	–3.84	–4.48
TSAP equatorial 2	–	–7.83	–4.03
TSAP equatorial 3	–	–11.98	–11.32
TSAP equatorial 4	–	–14.3	–16.81

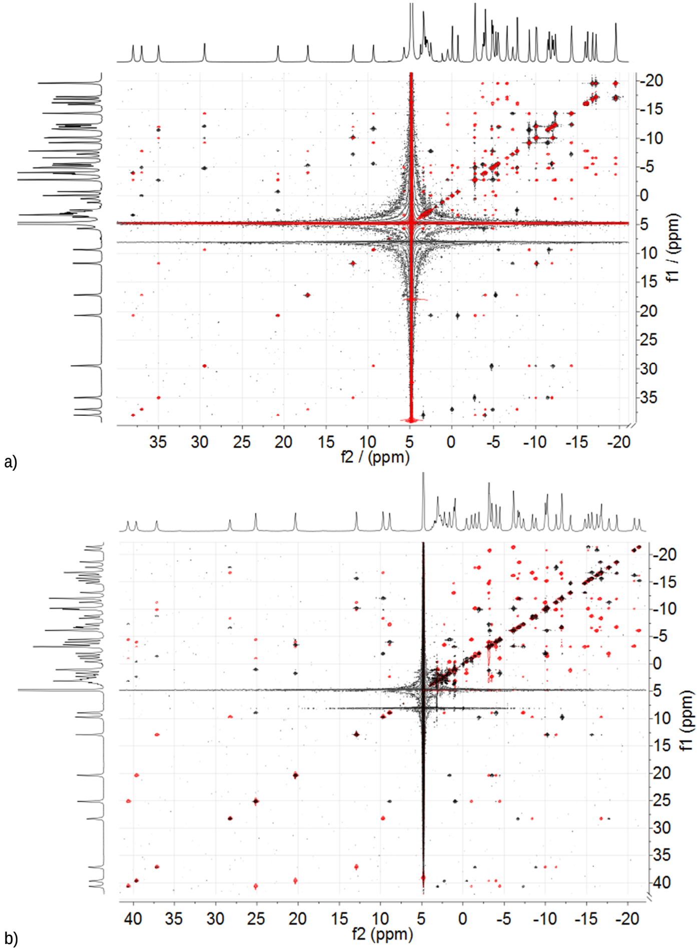

Figure S2: ^{1}H-^{1}H 2D-COSY (black) and ^{1}H 2D-EXSY spectra (red) of a) [Eu(Hdo3ap)(D$_2$O)]$^-$ (pD = 3.6) and b) [Eu(do3ap)(D$_2$O)]$^{2-}$ (pD = 8.5); 5 °C, 600 MHz, mixing time 5 ms for (a) and 10 ms for (b).

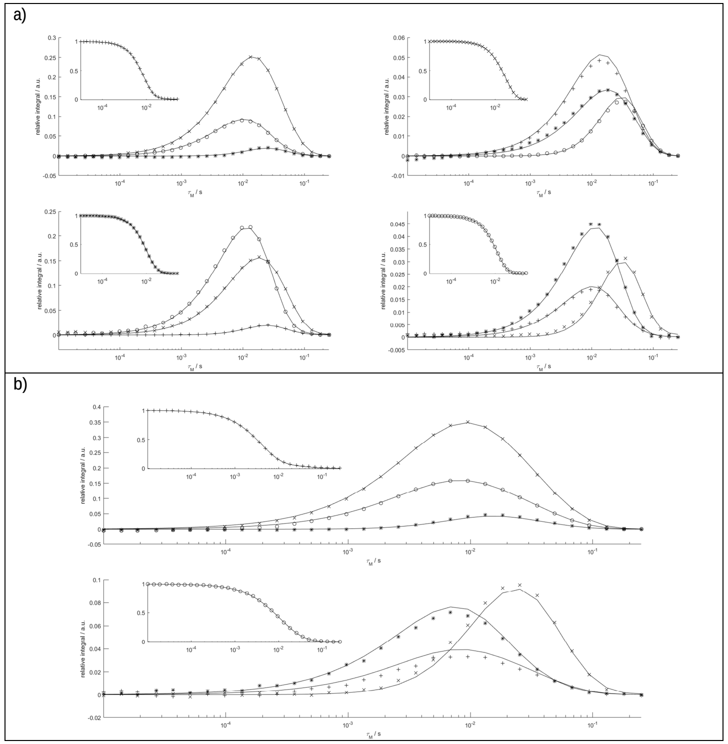

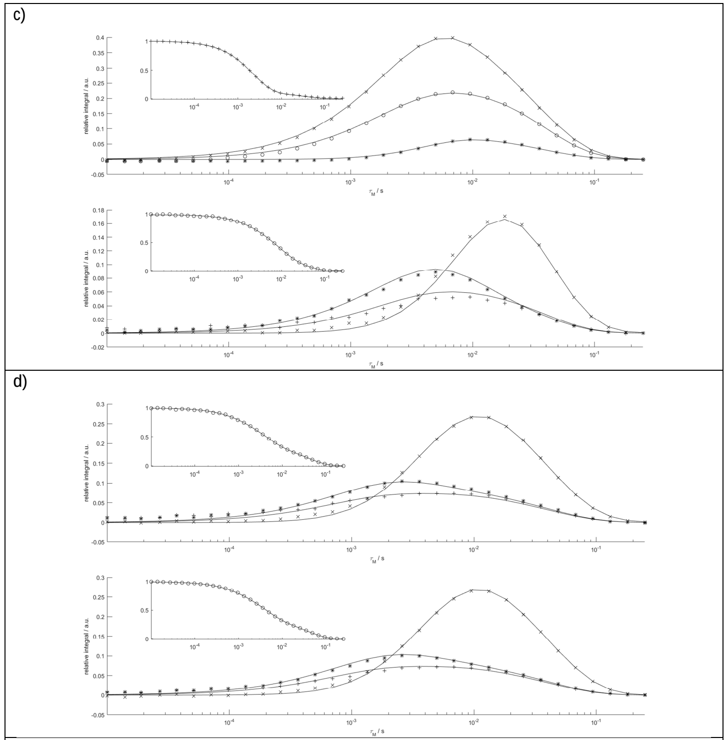

Figure S3. Relative areas of proton NMR signals of $[Eu(dota)(D_2O)]^-$ as a function of the mixing time obtained from 1D-EXSY experiments at a) 5 °C b) 15 °C c) 25 °C and d) 35 °C at pD = 7.0. The insets show the evolution of the magnetisation of the signal to which the refocusing selective 180° pulse was applied. Symbols: $TSAP_{ax}$ (+), SAP_{eq} (×), $TSAP_{eq}$ (*), SAP_{ax} (○). The solid lines represent the simultaneous fit of all four data sets using Equation [2].

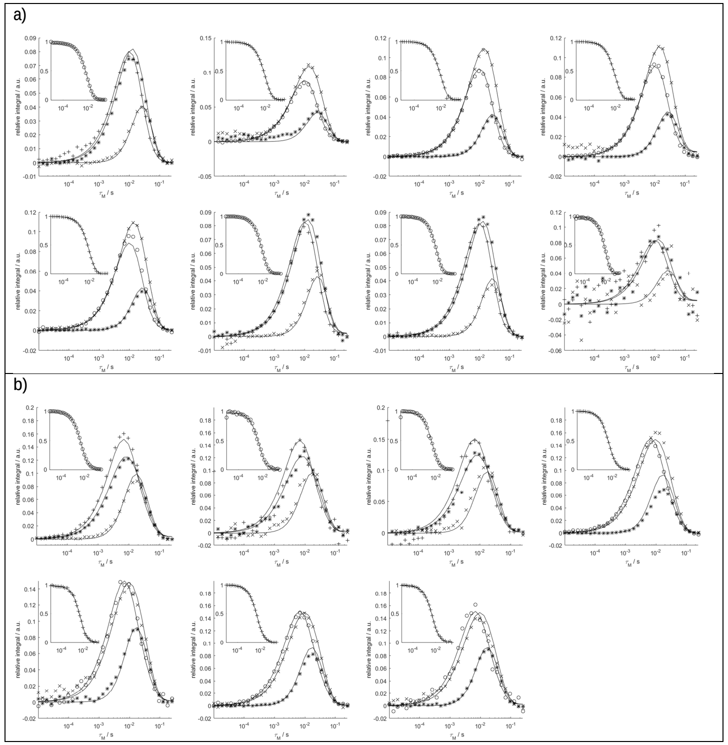

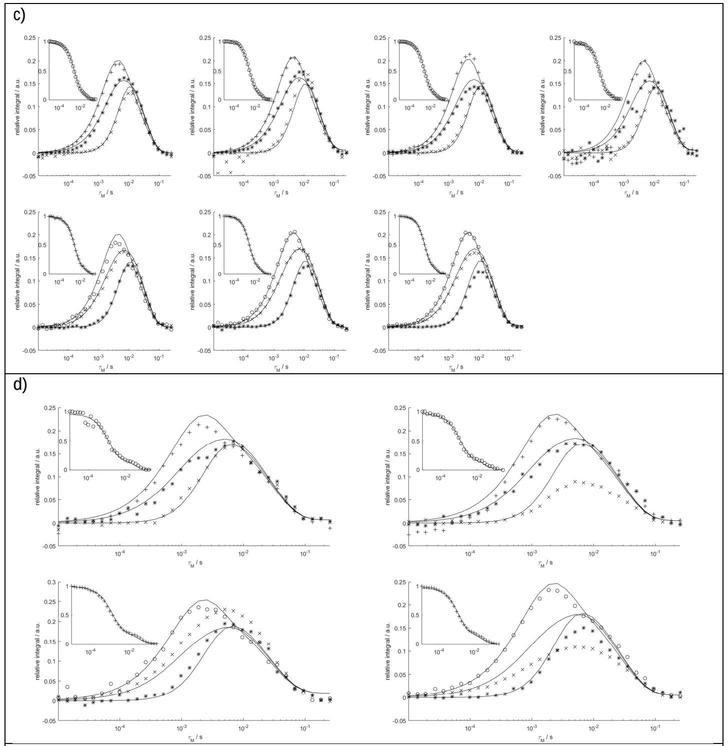

Figure S4. Relative areas of proton NMR signals of $[Eu(Hdo3ap)(D_2O)]^-$ as a function of the mixing time obtained from 1D-EXSY experiments at a) 5 °C b) 15 °C c) 25 °C and d) 35 °C at pD = 3.6. The insets show the evolution of the magnetisation of the signal to which the refocusing selective 180° pulse was applied. Symbols: $TSAP_{ax}$ (+), SAP_{eq} (×), $TSAP_{eq}$ (*), SAP_{ax} (○). The solid lines represent the simultaneous fit of all four data sets using Equation [2].

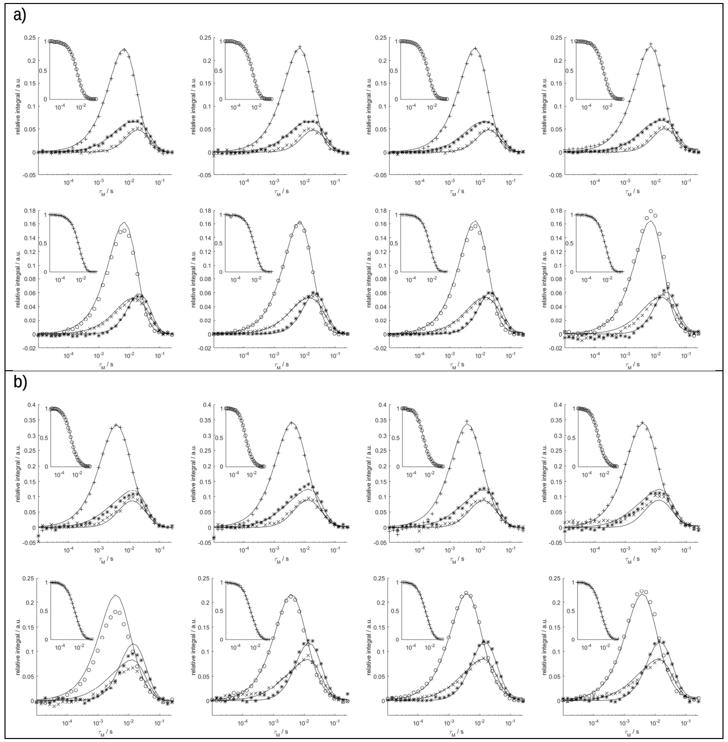

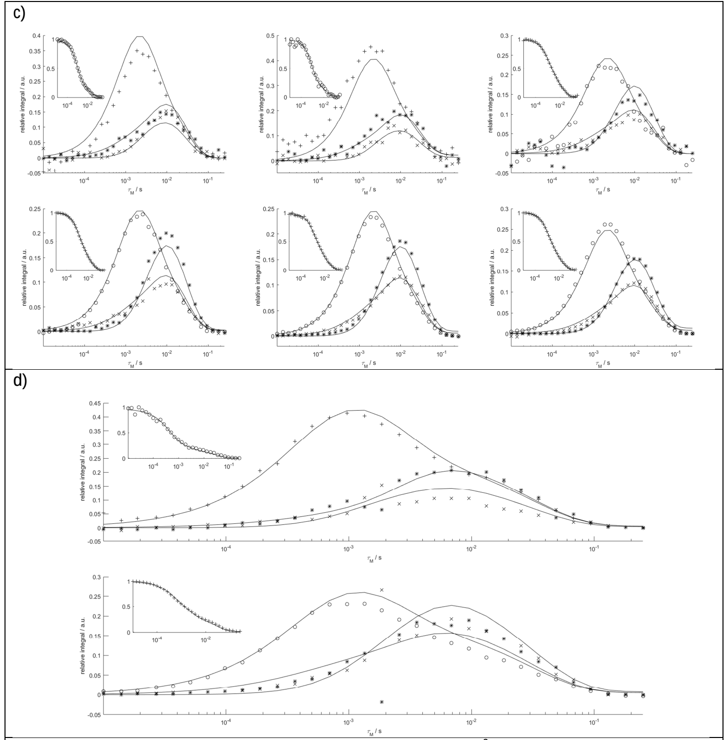

Figure S5. Relative areas of proton NMR signals of $[Eu(do3ap)(D_2O)]^{2-}$ as a function of the mixing time obtained from 1D-EXSY experiments at a) 5 °C b) 15 °C c) 25 °C and d) 35 °C at pD = 8.5. The insets show the evolution of the magnetisation of the signal to which the refocusing selective 180° pulse was applied. Symbols: $TSAP_{ax}$ (+), SAP_{eq} (×), $TSAP_{eq}$ (*), SAP_{ax} (○). The solid lines represent the simultaneous fit of all four data sets using Equation [2].

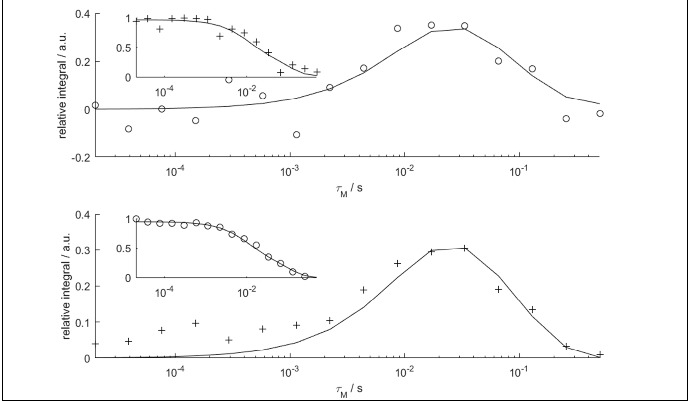

Figure S6. Relative areas of signals of $[Eu(Hdo3ap)(D_2O)]^{2-}$ as a function of the mixing time obtained from ^{31}P 1D-EXSY experiments at 5 °C; pD(25 °C) = 3.6 . The insets show the evolution of the magnetisation of the signal to which the refocusing selective 180° pulse was applied. Symbols: TSAP (+), SAP (○). The solid lines represent the simultaneous fit of both data sets using Equation [2] modified for two-site exchange.

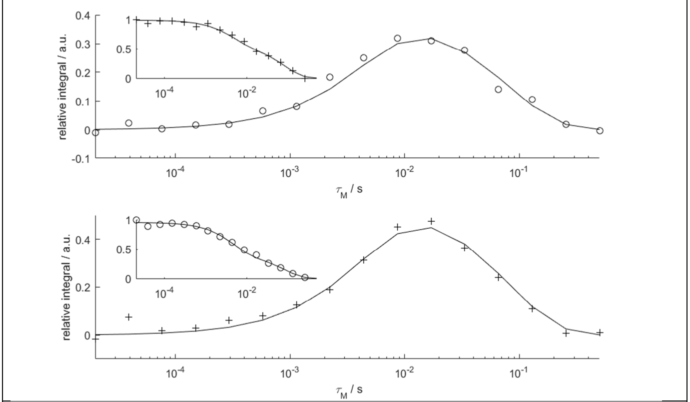

Figure S7. Relative areas of signals of $[Eu(do3ap)(D_2O)]^{2-}$ as a function of the mixing time obtained from ^{31}P 1D-EXSY experiments at 5 °C; pD(25 °C) = 8.5. The insets show the evolution of the magnetisation of the signal to which the refocusing selective 180° pulse was applied. Symbols: TSAP (+), SAP (○). The solid lines represent the simultaneous fit of both data sets using Equation [2] modified for two-site exchange.

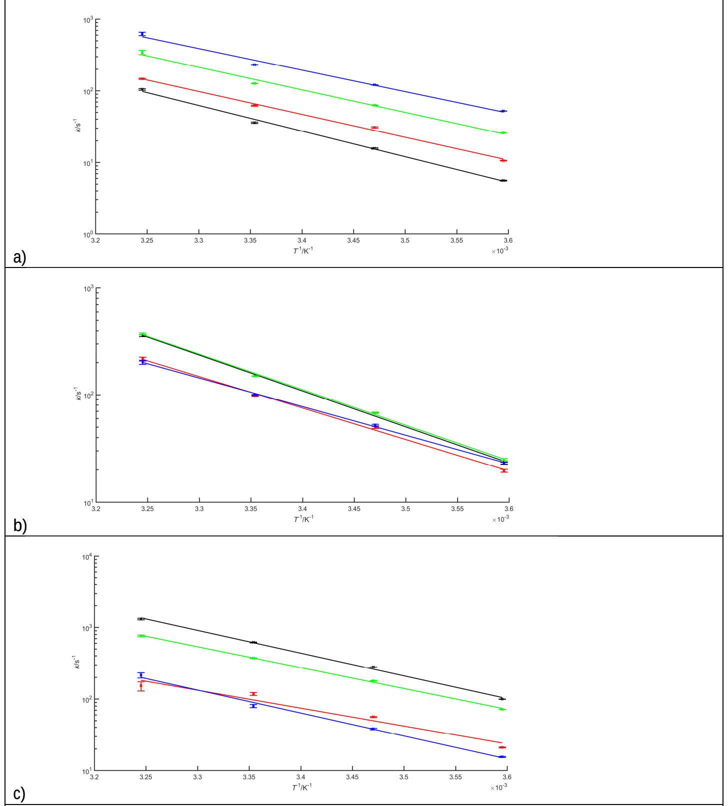

Figure S8: Temperature dependence of exchange rates $k_{PendSAP}$ (black), $k_{CycleSAP}$ (red) , $k_{PendTSAP}$ (green) and $k_{CycleTSAP}$ (blue) of a) $[Eu(dota)(D_2O)]^-$ b) $[Eu(Hdo3ap)(D_2O)]^-$ c) $[Eu(do3ap)(D_2O)]^{2-}$ fitted using Eyring equation (black line) [4].

Table S2: Exchange and relaxation rates of $[Eu(dota)(D_2O)]^{-}$ [a]

Parameter	Temperature / °C			
	5	15	25	35
$k_{PendSAP}$	5.58(6)	15.6(3)	35.8(6)	104(3)
$k_{CycleSAP}$	10.60(7)	30.8(5)	62(1)	147(3)
$k_{PendTSAP}$	25.81(7)	63.0(4)	126.6(9)	345(24)
$k_{CycleTSAP}$	52.30(8)	120.4(5)	231(1)	624(31)
K_{EXSY}	0.207(5)	0.25(1)	0.27(1)	0.26(4)
$R_{1Ax.\ SAP}$	69.1(1)	55.1(6)	43(1)	30(3)
$R_{1Eq.\ SAP}$	22.53(7)	16.2(5)	11(1)	0(5)
$R_{1Ax.\ TSAP}$	47.6(2)	45.9(7)	41(1)	130(25)
$R_{1Eq.\ TSAP}$	18.3(1)	34(4)	54(8)	17(15)

[a] k / s^{-1} are exchange rates, R_1 / s^{-1} are longitudinal relaxation rates and K_{EXSY} is equilibrium constants calculated as $K_{EXSY} = (k_{PendSAP} + k_{CycleSAP})/ (k_{PendTSAP} + k_{CycleTSAP})$.

Table S3: Exchange and relaxation rates of $[Eu(Hdo3ap)(D_2O)]^{-}$ [a]

Parameter	Temperature / °C			
	5	15	25	35
$k_{PendSAP}$	23.2(5)	68(1)	150(1)	357(7)
$k_{CycleSAP}$	19.6(6)	50(1)	98(1)	216(9)
$k_{PendTSAP}$	25.0(5)	67.6(8)	150(1)	374(8)
$k_{CycleTSAP}$	23.0(6)	52.3(9)	100(1)	202(9)
K_{EXSY}	0.89(9)	0.98(7)	0.99(4)	1.0(1)
$R_{1Ax.\ SAP}$	69.4(9)	63(1)	57(1)	68(9)
$R_{1Eq.\ SAP}$	20(3)	8(3)	9(3)	43(29)
$R_{1Ax.\ TSAP}$	54.1(9)	55(1)	52(1)	37(9)
$R_{1Eq.\ TSAP}$	22(3)	32(4)	22(3)	0(28)

[a] k / s^{-1} are exchange rates, R_1 / s^{-1} are longitudinal relaxation rates and K_{EXSY} is equilibrium constants calculated as $K_{EXSY} = (k_{PendSAP} + k_{CycleSAP})/ (k_{PendTSAP} + k_{CycleTSAP})$.

Table S4: Exchange and relaxation rates of $[Eu(do3ap)(D_2O)]^{2-}$ [a]

Parameter	Temperature / °C			
	5	15	25	35
$k_{PendSAP}$	99.7(3)	280(1)	619(8)	1305(30)
$k_{CycleSAP}$	21.0(3)	56(1)	118(5)	152(22)
$k_{PendTSAP}$	71.7(3)	180(1)	374(5)	762(23)
$k_{CycleTSAP}$	15.5(2)	38.2(9)	80(4)	215(18)
K_{EXSY}	1.39(5)	1.54(8)	1.6(2)	1.5(4)
$R_{1Ax.\ SAP}$	73.2(4)	59(1)	42(7)	122(24)
$R_{1Eq.\ SAP}$	16(2)	0(6)	0(29)	0(110)
$R_{1Ax.\ TSAP}$	59.0(3)	63(1)	58(4)	0(19)
$R_{1Eq.\ TSAP}$	23(2)	35(4)	40(18)	32(72)

[a] k / s^{-1} are exchange rates, R_1 / s^{-1} are longitudinal relaxation rates and K_{EXSY} is equilibrium constants calculated as $K_{EXSY} = (k_{PendSAP} + k_{CycleSAP})/ (k_{PendTSAP} + k_{CycleTSAP})$.

Table S5: Exchange and relaxation rates of $[Eu(Hdo3ap)(D_2O)]^{2-}$ and $[Eu(do3ap)(D_2O)]^{2-}$ as determined by ^{31}P 1D-EXSY at 5 °C [a]

Parameter	$[Eu(Hdo3ap)(D_2O)]^{2-}$	$[Eu(do3ap)(D_2O)]^{2-}$
k_{SAP}	42(3)	120(3)
k_{TSAP}	45(3)	82(3)
K_{EXSY}	0.93(6)	1.46(4)
R_{SAP}	12(3)	7(2)
R_{TSAP}	9(3)	16(2)

[a] k_{SAP} / s^{-1}, k_{TSAP} / s^{-1} are exchange rates of exchange from SAP $\longrightarrow$ TSAP and backward respectively, R_1 / s^{-1} are longitudinal relaxation rates and K_{EXSY} equilibrium constants calculated as $K_{EXSY} = k_{SAP}/k_{TSAP}$. It should be highlighted that arm rotation and cycle inversion cannot be separated by ^{31}P 1D-EXSY as a sum of both processes is observed.

Table S6: Calculated energy profile of cyclen inversion of $[Eu(dota)(H_2O)]^{-}$. The most favourable pathway is in bold and the rate-determining step is underlined.

Sequence of chelate ring inversions				$\Delta G^{\ddagger}_{calc}$(25 °C) / kJ mol^{-1}								
				SAP	TS 1	int 1	TS 2	int 2	TS 3	int 3	TS 4	TSAP
2	3	4	1	0.00	60.54	19.05	61.99	28.91	57.87	24.77	60.08	–2.84
3	2	4	1	0.00	60.54	21.37	66.90	28.91	57.87	24.77	60.08	–2.84
2	4	3	1	0.00	60.54	19.05	64.48	27.28	63.28	24.77	60.08	–2.84
4	2	3	1	0.00	60.54	21.88	68.08	27.28	63.28	24.77	60.08	–2.84
4	3	2	1	0.00	60.54	21.87	67.01	30.37	72.08	24.77	60.08	–2.84
3	4	2	1	0.00	60.54	21.37	67.42	30.37	72.08	24.77	60.08	–2.84

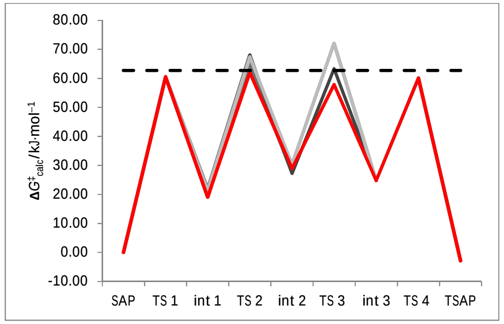

Figure S9: Energy profile calculated for the cyclen inversion of $[Eu(dota)(H_2O)]^{-}$ at 25 °C. The lowest energy pathway is highlighted in red while the experimental activation free energy is represented by a black dashed line.

Table S7: Calculated energy profile of cyclen inversion of $[Eu(Hdo3ap)(H_2O)]^{-}$. The most favourable pathway is in bold and the rate-determining step is underlined.

Sequence of chelate ring inversion				$\Delta G^{\ddagger}_{calc}$(25 °C) / kJ mol^{-1}								
				SAP	TS 1	int 1	TS 2	int 2	TS 3	int 3	TS 4	TSAP
1	2	3	4	0	63.6	19.8	64.7	26.9	55.5	19.2	56.8	–2.6
2	1	3	4	0	51.5	19.4	66.2	26.9	55.5	19.2	56.8	–2.6
1	3	2	4	0	63.6	19.8	72.6	32.4	55.0	19.2	56.8	–2.6
3	1	2	4	0	63.7	21.7	69.8	32.4	55.0	19.2	56.8	–2.6
3	2	1	4	0	63.7	21.7	57.5	24.6	65.9	19.2	56.8	–2.6
2	3	1	4	0	51.5	19.4	60.6	24.6	65.9	19.2	56.8	–2.6
1	2	4	3	0	63.6	19.8	64.7	26.9	69.5	23.0	62.3	–2.6
2	1	4	3	0	51.5	19.4	66.2	26.9	69.5	23.0	62.3	–2.6
1	4	2	3	0	63.6	19.8	62.9	25.7	63.0	23.0	62.3	–2.6
4	1	2	3	0	59.6	21.8	71.6	25.7	63.0	23.0	62.3	–2.6
4	2	1	3	0	59.6	21.8	62.8	29.6	66.4	23.0	62.3	–2.6
2	4	1	3	0	51.5	19.4	65.0	29.6	66.4	23.0	62.3	–2.6
1	4	3	2	0	63.6	19.8	62.9	25.7	71.8	27.9	51.7	–2.6
4	1	3	2	0	59.6	21.8	71.6	25.7	71.8	27.9	51.7	–2.6
1	3	4	2	0	63.6	19.8	72.6	32.4	65.7	27.9	51.7	–2.6
3	1	4	2	0	63.7	21.7	69.8	32.4	65.7	27.9	51.7	–2.6
3	4	1	2	0	63.7	21.7	65.5	34.6	67.4	27.9	51.7	–2.6
4	3	1	2	0	59.6	21.8	68.0	34.6	67.4	27.9	51.7	–2.6
4	2	3	1	0	59.6	21.8	62.8	29.6	62.9	20.0	59.4	–2.6
2	4	3	1	0	51.5	19.4	65.0	29.6	62.9	20.0	59.4	–2.6
4	3	2	1	0	59.6	21.8	68.0	34.6	64.0	20.0	59.4	–2.6
3	4	2	1	0	63.7	21.7	65.5	34.6	64.0	20.0	59.4	–2.6
3	2	4	1	0	63.7	21.7	57.5	24.6	56.4	20.0	59.4	–2.6
2	3	4	1	0	51.5	19.4	60.6	24.6	56.4	20.0	59.4	–2.6

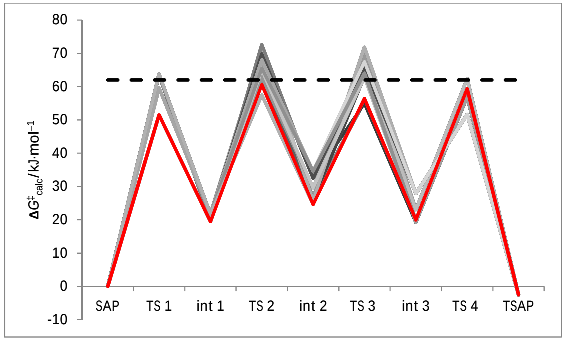

Figure S10: Energy profile calculated for the cyclen inversion of $[Eu(Hdo3ap)(H_2O)]^{-}$ at 25 °C. The lowest energy pathway is highlighted in red, while the experimental activation free energy is represented by a black dashed line.

Table S8: Calculated energy profile of cyclen inversion of $[Eu(do3ap)(H_2O)]^{2-}$. The most favourable pathway is in bold and the rate-determining step is underlined.

Sequence of chelate ring inversion				$\Delta G^{\ddagger}_{calc}$(25 °C) / kJ mol^{-1}								
				SAP	TS 1	int 1	TS 2	int 2	TS 3	int 3	TS 4	TSAP
4	3	2	1	0.0	68.1	23.9	67.1	30.5	60.2	21.3	49.6	0.9
4	3	1	2	0.0	68.1	23.9	67.1	30.5	62.9	24.1	66.6	0.9
4	2	3	1	0.0	68.1	23.9	71.8	31.8	67.4	21.3	49.6	0.9
4	2	1	3	0.0	68.1	23.9	71.8	31.8	61.1	31.8	67.7	0.9
4	1	2	3	0.0	68.1	23.9	60.5	33.9	81.7	31.8	67.7	0.9
4	1	3	2	0.0	68.1	23.9	60.5	33.9	66.2	24.1	66.6	0.9
3	4	2	1	0.0	64.4	22.4	70.4	30.5	60.2	21.3	49.6	0.9
3	4	1	2	0.0	64.4	22.4	70.4	30.5	62.9	24.1	66.6	0.9
3	2	4	1	0.0	64.4	22.4	67.7	30.4	71.0	21.3	49.6	0.9
3	2	1	4	0.0	64.4	22.4	67.7	30.4	67.8	33.8	65.1	0.9
3	1	2	4	0.0	64.4	22.4	64.1	34.9	70.9	33.8	65.1	0.9
3	1	4	2	0.0	64.4	22.4	64.1	34.9	64.6	24.1	66.6	0.9
2	3	4	1	0.0	71.1	21.1	68.7	30.4	71.0	21.3	49.6	0.9
2	3	1	4	0.0	71.1	21.1	68.7	30.4	67.8	33.8	65.1	0.9
2	4	3	1	0.0	71.1	21.1	77.5	31.8	67.4	21.3	49.6	0.9
2	4	1	3	0.0	71.1	21.1	77.5	31.8	61.1	31.8	67.7	0.9
2	1	4	3	0.0	71.1	21.1	73.5	37.9	63.9	31.8	67.7	0.9
2	1	3	4	0.0	71.1	21.1	73.5	37.9	79.1	33.8	65.1	0.9
1	3	2	4	0.0	57.7	26.3	73.5	34.9	70.9	33.8	65.1	0.9
1	3	4	2	0.0	57.7	26.3	73.5	34.9	64.6	24.1	66.6	0.9
1	2	3	4	0.0	57.7	26.3	81.5	37.9	79.1	33.8	65.1	0.9
1	2	4	3	0.0	57.7	26.3	81.5	37.9	63.9	31.8	67.7	0.9
1	4	2	3	0.0	57.7	26.3	67.2	33.9	81.7	31.8	67.7	0.9
1	4	3	2	0.0	57.7	26.3	67.2	33.9	66.2	24.1	66.6	0.9

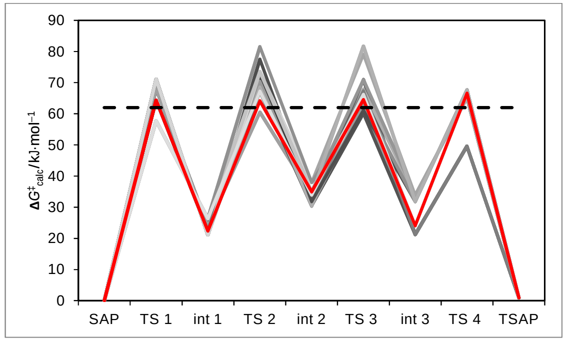

Figure S11: Energy profile calculated for the cyclen inversion of $[Eu(do3ap)(H_2O)]^{2-}$ at 25 °C. The lowest energy pathway is highlighted in red, while the experimental activation free energy is represented by a black dashed line.

Table S9: Contributions to the activation entropy (in J K^{-1} mol^{-1}) for the ring inversion process responsible for the SAP → TSAP interconversion process (at 25 °C).

Anion	$\Delta S^{\ddagger}_{CycleSAP}$		
	Overall	Rotation	Vibration
dota	–3.28	–0.054	–3.23
Hdo3ap	–8.77	0.033	–8.80
do3ap	–14.6	0.12	–14.7

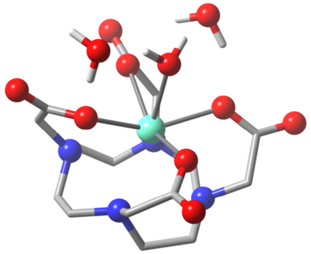

Figure S12. Calculated molecular structure of $[Eu(dota)(H_2O)]^{-}\cdot 2H_2O$ in SAP geometry. Hydrogen atoms bonded to carbon atoms are omitted for the sake of clarity.

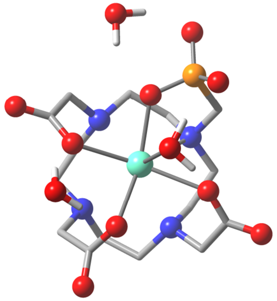

Figure S13. Calculated molecular structure of $[Eu(do3ap)(H_2O)]^{2-}\cdot 2H_2O$ in SAP geometry. Hydrogen atoms bonded to carbon atoms are omitted for the sake of clarity.

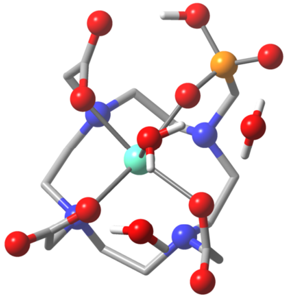

Figure S14. Calculated molecular structure of $[Eu(Hdo3ap)(H_2O)]^- \cdot 2H_2O$ in SAP geometry. Hydrogen atoms bonded to carbon atoms are omitted for the sake of clarity.

Appendix D

Complexes of $Co^{2+/3+}$

In this Appendix, syntheses of cobalt(II) and cobalt(III) complexes of the ligands H_4**te2f2p** and H_2**te2f2a** are described as well as the corresponding magnetometric measurements.

Commercial chemicals (Fluka, Aldrich, CheMatech, Lachema) were used as obtained. Anhydrous solvents were obtained by established procedures or purchased. Syntheses of H_4**te2f2p** and H_2**te2f2a** are described in Appendixes A and B, respectively. Preparation of $[Co^{II}(NH_3)_6]Cl_2$ was performed as published in Ref. 72 and the product was stored in a flame-sealed ampoule or in a form of stock solution (dissolved in ≈10% oxygen-free NH_3 aq.) under argon atmosphere. Other general experimental procedures and used instruments are described in Appendix B.

D.1 Synthesis of complex

NH_4**{*trans*-[Co^{II}(Hte2f2p)]}**

H_4**te2f2p** (200 mg, 360 µmol) was dissolved in 5% oxygen-free NH_3 (20 ml) and stock solution of $[Co^{II}(NH_3)_6]Cl_2$ (10 ml, 86 mM, i.e. 860 µmol, 2.4 eq.) was added. The reaction mixture was refluxed under ammonia atmosphere overnight. An absence of the free ligand was tested by ^{19}F-NMR. Product was purified by column chromatography (SiO_2, 6×3 cm) with EtOH/NH_3 (aq.) v/v = 5/1 as mobile phase. Fractions containing pure product were combined, evaporated to dryness and the product was crystallised from minimal amount of water, with a drop of 5% aq. NH_3, by vapour diffusion of acetone. Yield 174 mg (79 %).

Single crystals of (NH_4)\{*trans*[Co^{II}(H**te2f2p**])]\}·3.25H_2O were obtained by vapour diffusion of acetone into aqueous solution of the complex containing slight excess of ammonia.

For BMS measurement, 10.1 mg of (NH_4)\{*trans*-[Co^{II}(H**te2f2p**])]\}·3.25H_2O was dissolved in water (0.3 ml) with 0.25% NH_3 (aq.), 0.1 % *t*-BuOH and 0.5 % TFE. The stock solution was diluted to 3 concentration (37.7, 28.0 and 21.5 mM). Average differences in chemical shift of *t*BuOH (^{1}H) and TFE (^{1}H and ^{19}F) between sample and coaxial insert were used. Exact content of Co^{2+} was determined by AAS. Average magnetic dipole moment was calculated.[49], to be $\mu_{\text{eff}} = 4.9(2)\mu_B$.

trans-[Co^{III}(Hte2f2p)]

The (NH_4)\{*trans*-[Co^{II}(H**te2f2p**])]\}·3.25H_2O (8 mg, 13 µmol) was dissolved in D_2O (0.7 ml) with 10 µL conc. aq. NH_3 (pD 10.9) and *meta*-chloroperoxybenzoic acid (MCPBA) (13 mg 70–75 %, i.e. ≈ 53 µmol; ≈4 eq.) was added. The reaction proceeds for 10 min and excess of MCPBA and by-products were then filtered off. NMR experiments were performed directly with this sample.

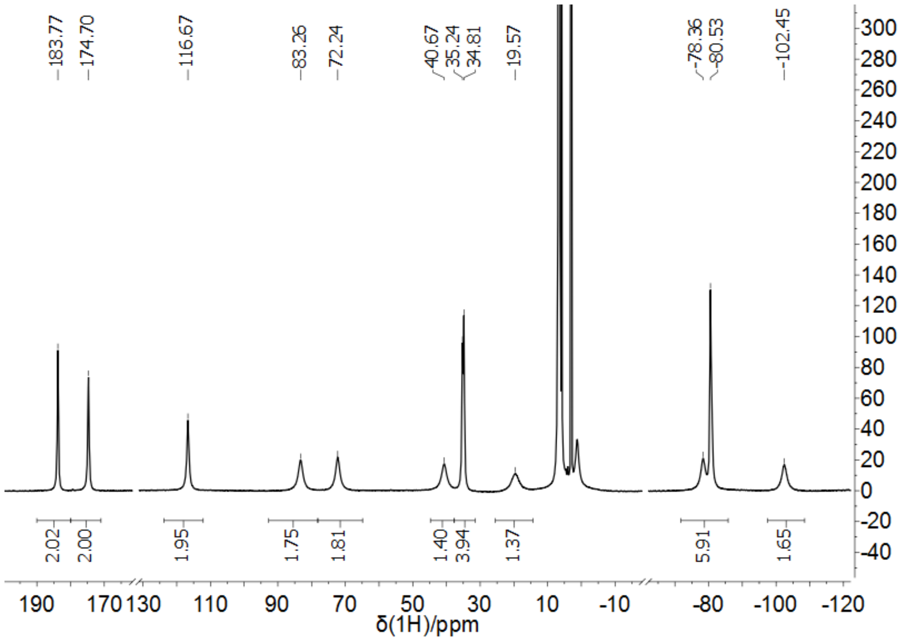

Figure 5.1: ^{1}H-NMR (300 MHz, D_2O, pD 10.9) spectrum of *trans*-$[\mathrm{Co^{II}}(\mathbf{te2f2p})]^{2-}$

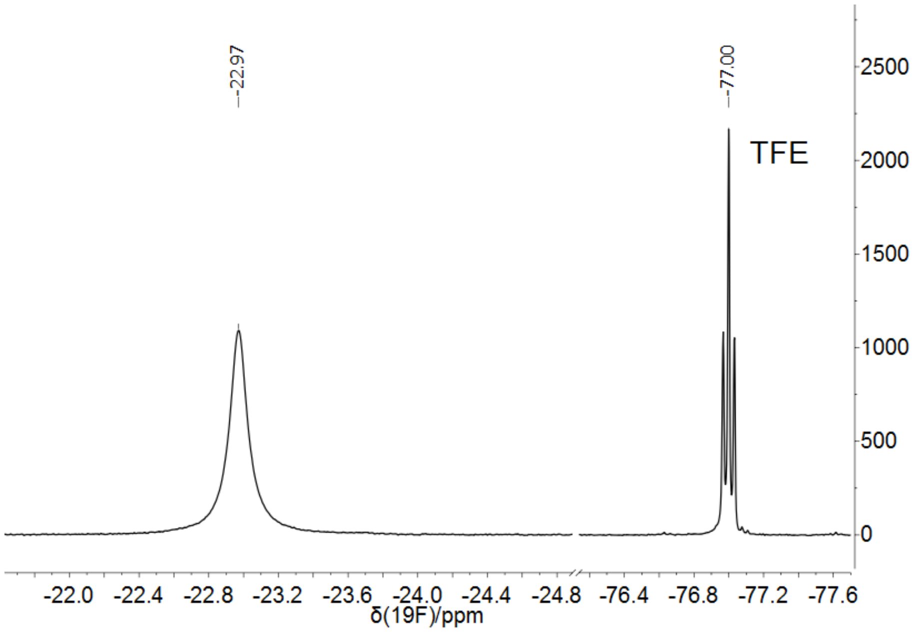

Figure 5.2: ^{19}F-NMR (282 MHz, D_2O, pD 10.9) spectrum of *trans*-$[\mathrm{Co^{II}}(\mathbf{te2f2p})]^{2-}$

^{19}F NMR (282 MHz, D2O, pD 9.7): −59.23 (t, $^3J_{\mathrm{HF}}$ = 9.4 Hz); ^{31}P NMR (121 MHz, D2O, pD 9.7): 38.3 (bs);

Single crystals of *trans*-[Co$^{\mathrm{III}}$(H**te2f2p**)] were prepared by acetone vapour diffusion into aq. solution of the complex.

trans-[Co$^{\mathrm{II}}$(te2f2a)]

H$_2$**te2f2a** (100 mg, 420 µmol) was mixed with 60 mM stock solution of [Co$^{\mathrm{II}}$(NH$_3$)$_6$]Cl$_2$ in oxygen-free NH$_3$ (aq) (10 ml, 600 µmol, 1.4 eq.). The reaction was refluxed under an ammoniac atmosphere overnight. Resulting [Co$^{\mathrm{II}}$(**te2f2a**)] precipitates from the reaction mixture in a form of small crystals during the reaction and was isolated by filtration after disappearance of the free ligand signal in ^{19}F-NMR of the solution. Complex is hardly soluble in water. Yield 60 mg (60 %).

Single crystals of *trans*-[Co$^{\mathrm{II}}$(**te2f2a**)]·MeOH were obtained by slow cooling of boiling saturated [Co$^{\mathrm{II}}$(**te2f2a**)] solution in EtOH/MeOH mixture.

[Co$^{\mathrm{III}}$(te2f2a)]Cl

The *trans*-[Co$^{\mathrm{II}}$(**te2f2a**)] (10 mg, 19 µmol) was suspended in D$_2$O (0.7 ml, pD 9.2) and MCPBA (18 mg, 70–75%; ≈ 78 µmol; ≈4 eq.) was added. The reaction proceeds for 10 min and excess of MCPBA and by-products were filtered off. NMR experiments were performed directly with this sample.

^{19}F NMR (282 MHz, D2O, pD 4.2): −59.47 (t, $^3J_{\mathrm{HF}}$ = 8.6 Hz);

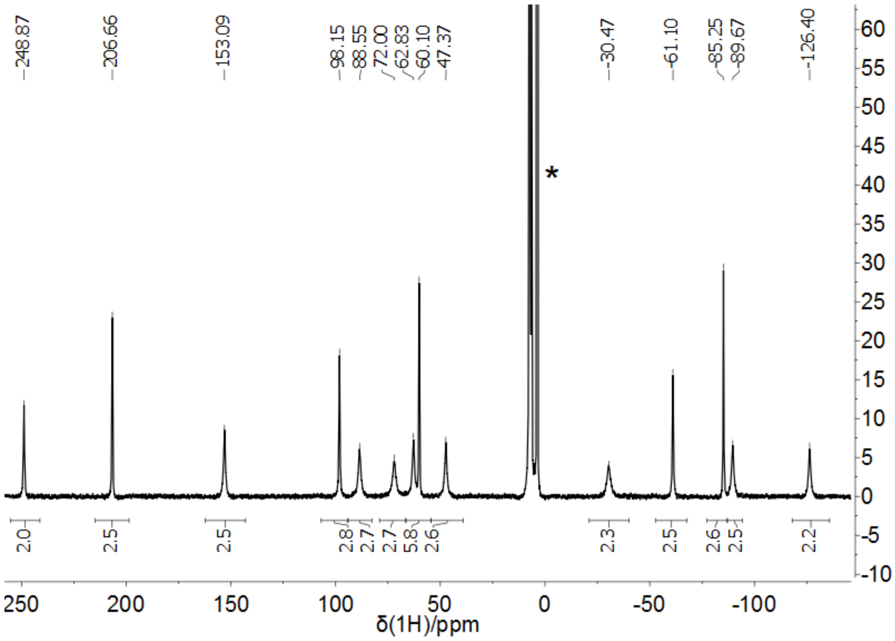

Figure 5.3: ^{1}H-NMR (300 MHz, D_2O, pD 9.2) spectrum of [Co^{II}(**te2f2a**)]

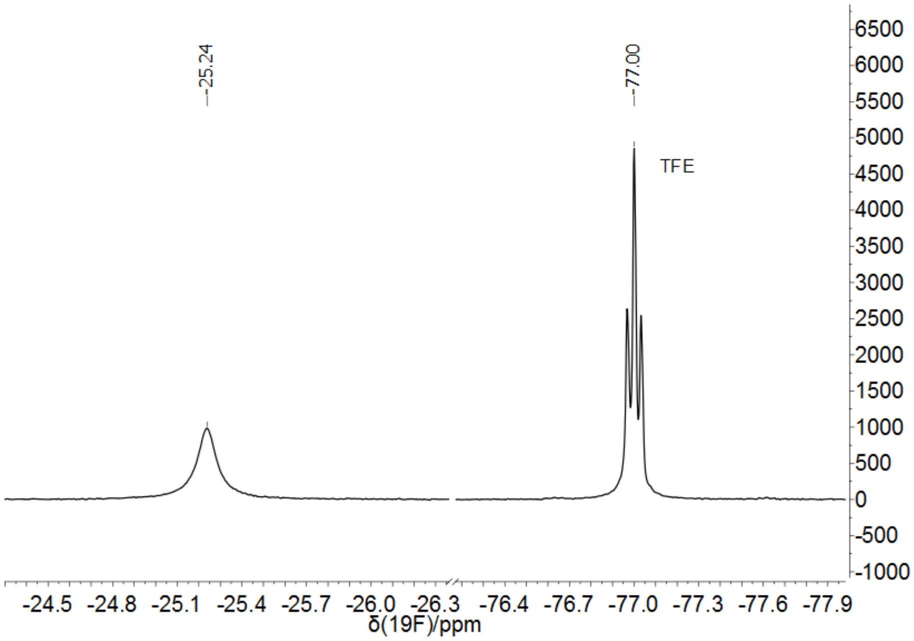

Figure 5.4: ^{19}F-NMR (282 MHz, D_2O, pD 9.2) spectrum of [Co^{II}(**te2f2a**)]

Bibliography

[1] D. Le Bihan, J.-F. Mangin, C. Poupon, C. Clark, S. Pappata, N. Molko and H. Chabriat, *J. Magn. Reson. Imaging*, 2001, **13**, 534–546.

[2] P. Collaboration, *Astron. Astrophys.*, 2016, **594**, A13.

[3] M. H. Levitt, *Spin dynamics: Basics of Nuclear Magnetic Resonance*, Wiley, Chichester, UK, 2nd edn., 2008.

[4] M. Bertmer, *Solid State Nucl. Magn. Reson.*, 2016, **81**, 1–7.

[5] Y. Inada, H. H. Loeffler and B. M. Rode, *Chem. Phys. Lett.*, 2002, **358**, 449–458.

[6] M. P. Hartung, T. M. Grist and C. J. François, *J. Cardiovasc. Magn. Reson.*, 2011, **13**, 19.

[7] A. D. Bain, *Prog. Nucl. Magn. Reson. Spectrosc.*, 2003, **43**, 63–103.

[8] V. Římal, H. Štěpánková and J. Štěpánek, *Concepts Magn. Reson. Part A*, 2011, **38A**, 117–127.

[9] J. Kowalewski and L. Maler, *Nuclear Spin Relaxation in Liquids: Theory, Experiments, and Applications*, Taylor & Francis, New York, 2006.

[10] I. Bertini, C. Luchinat, G. Parigi and E. Ravera, *NMR of Paramagnetic Molecules*, Elsevier, Amsterdam, 2nd edn., 2017.

[11] T. Krchová, V. Herynek, A. Gálisová, J. Blahut, P. Hermann and J. Kotek, *Inorg. Chem.*, 2017, **56**, 2078–2091.

[12] J. Kowalewski, L. Nordenskiöld, N. Benetis and P.-O. Westlund, *Prog. Nucl. Magn. Reson. Spectrosc.*, 1985, **17**, 141–185.

[13] T. Nilsson, J. Svoboda, P. O. Westlund and J. Kowalewski, *J. Chem. Phys.*, 1998, **109**, 6364–6375.

[14] E. Wiberg and A. F. Holleman, *Inorganic chemistry*, Academic Press, Berlin, 2001, p. 1233.

[15] D. F. Evans, *J. Chem. Soc.*, 1959, 2003.

[16] M. Kaupp and F. H. Köhler, *Coord. Chem. Rev.*, 2009, **253**, 2376–2386.

[17] L. Benda, J. Mareš, E. Ravera, G. Parigi, C. Luchinat, M. Kaupp and J. Vaara, *Angew. Chem. Int. Ed.*, 2016, **55**, 14713–14717.

[18] A. J. Pell and G. Pintacuda, *Prog. Nucl. Magn. Reson. Spectrosc.*, 2015, **84-85**, 33–72.

[19] L. Di Bari, G. Pintacuda, S. Ripoli and P. Salvadori, *Magn. Reson. Chem.*, 2002, **40**, 396–405.

[20] E. Belorizky, P. H. Fries, L. Helm, J. Kowalewski, D. Kruk, R. R. Sharp and P.-O. Westlund, *J. Chem. Phys.*, 2008, **128**, 052315.

[21] K. Du and T. D. Harris, *J. Am. Chem. Soc.*, 2016, **138**, 7804–7807.

[22] L. Nordenskiöld, A. Laaksonen and J. Kowalewski, *J. Am. Chem. Soc.*, 1982, **104**, 379–382.

[23] A. S. Merbach, L. Helm and E. Toth, *The Chemistry of Contrast Agents in Medical Magnetic Resonance Imaging, 2nd Edition*, John Wiley & Sons, Ltd., Chichester, UK, 2013, p. 512.

[24] J. R. Morrow and É. Tóth, *Inorg. Chem.*, 2017, **56**, 6029–6034.

[25] P. Harvey, A. M. Blamire, J. I. Wilson, K.-L. N. A. Finney, A. M. Funk, P. K. Senanayake and D. Parker, *Chem. Sci.*, 2013, **4**, 4251.

[26] *Fluorine Magnetic Resonance Imaging*, ed. U. Flogel and E. Ahrens, CRC Press, Boca Raton (Florida), 2016.

[27] I. Tirotta, V. Dichiarante, C. Pigliacelli, G. Cavallo, G. Terraneo, F. B. Bombelli, P. Metrangolo and G. Resnati, *Chem. Rev.*, 2015, **115**, 1106–29.

[28] H. Amiri, M. Srinivas, A. Veltien, M. J. van Uden, I. J. M. de Vries and A. Heerschap, *Eur. Radiol.*, 2015, **25**, 726–735.

[29] C. Giraudeau, J. Flament, B. Marty, F. Boumezbeur, S. Mériaux, C. Robic, M. Port, N. Tsapis, E. Fattal, E. Giacomini, F. Lethimonnier, D. Le Bihan and J. Valette, *Magn. Reson. Med.*, 2010, **63**, 1119–1124.

[30] J. Hennig, A. Nauerth and H. Friedburg, *Magn. Reson. Med.*, 1986, **3**, 823–833.

[31] K. H. Chalmers, M. Botta and D. Parker, *Dalton Trans.*, 2011, **40**, 904–13.

[32] F. Schmid, C. Höltke, D. Parker and C. Faber, *Magn. Reson. Med.*, 2013, **69**, 1056–62.

[33] M. J. Goette, J. Keupp, J. Rahmer, G. M. Lanza, S. A. Wickline and S. D. Caruthers, *Magn. Reson. Med.*, 2015, **74**, 537–543.

[34] M. D. Robson, P. D. Gatehouse, M. Bydder and G. M. Bydder, *J. Comput. Assist. Tomogr.*, 2003, **27**, 825–846.

[35] I. Tirotta, A. Mastropietro, C. Cordiglieri, L. Gazzera, F. Baggi, G. Baselli, M. G. Bruzzone, I. Zucca, G. Cavallo, G. Terraneo, F. Baldelli Bombelli, P. Metrangolo and G. Resnati, *J. Am. Chem. Soc.*, 2014, **136**, 8524–7.

[36] A. A. Kislukhin, H. Xu, S. R. Adams, K. H. Narsinh, R. Y. Tsien and E. T. Ahrens, *Nat. Mater.*, 2016, **15**, 662–668.

[37] K. Srivastava, E. A. Weitz, K. L. Peterson, M. Marjańska and V. C. Pierre, *Inorg. Chem.*, 2017, **56**, 1546–1557.

[38] D. Xie, T. L. King, A. Banerjee, V. Kohli and E. L. Que, *J. Am. Chem. Soc.*, 2016, **138**, 2937–2940.

[39] M. Yu, D. Xie, K. P. Phan, J. S. Enriquez, J. J. Luci and E. L. Que, *Chem. Commun.*, 2016, **52**, 13885–13888.

[40] S. Mizukami, R. Takikawa, F. Sugihara, Y. Hori, H. Tochio, M. Wälchli, M. Shirakawa and K. Kikuchi, *J. Am. Chem. Soc.*, 2008, **130**, 794–795.

[41] A. Sarkar, I. E. Biton, M. Neeman and A. Datta, *Inorg. Chem. Commun.*, 2017, **78**, 21–24.

[42] A. Bianchi, M. Micheloni and P. Paoletti, *Coord. Chem. Rev.*, 1991, **110**, 17–113.

[43] J. Blahut, *Diplomová práce - Regiospecifické deriváty cyklamu pro radiomedicínské a MRI aplikace*, Univerzita Karlova v Praze, Praha, 2013.

[44] B. Bosnich, C. K. Poon and M. L. Tobe, *Inorg. Chem.*, 1965, **4**, 1102–1108.

[45] S. J. Dorazio, A. O. Olatunde, J. A. Spernyak and J. R. Morrow, *Chem. Commun.*, 2013, **49**, 10025–10027.

[46] J. Drabowicz, F. Jordan, M. Kudzin, Z. Kudzin, C. Stevens and P. Urbaniak, *Dalton Trans.*, 2016, **45**, 2308–2317.

[47] D. Kruk, T. Nilsson and J. Kowalewski, *Phys. Chem. Chem. Phys.*, 2001, **3**, 4907–4917.

[48] L. Helm, *Prog. Nucl. Magn. Reson. Spectrosc.*, 2006, **49**, 45–64.

[49] D. M. Corsi, C. Platas-Iglesias, H. van Bekkum and J. A. Peters, *Magn. Reson. Chem.*, 2001, **39**, 723–726.

[50] D. Parker, R. S. Dickins, H. Puschmann, C. Crossland and J. a. K. Howard, *Chem. Rev.*, 2002, **102**, 1977–2010.

[51] S. Aime, M. Botta, M. Fasano, M. P. M. Marques, C. F. G. C. Geraldes, D. Pubanz and A. E. Merbach, *Inorg. Chem.*, 1997, **36**, 2059–2068.

[52] S. Aime, A. Barge, M. Botta, A. S. De Sousa and D. Parker, *Angew. Chem. Int. Ed.*, 1998, **37**, 2673–2675.

[53] B. C. Webber and M. Woods, *Inorg. Chem.*, 2012, **51**, 8576–8582.

[54] M. Woods, S. Aime, M. Botta, J. A. K. Howard, J. M. Moloney, M. Navet, D. Parker, M. Port and O. Rousseaux, *J. Am. Chem. Soc.*, 2000, **122**, 9781–9792.

[55] W.-M. Liu, M. Overhand and M. Ubbink, *Coord. Chem. Rev.*, 2014, **273-274**, 2–12.

[56] S. Hoeft and K. Roth, *Chem. Ber.*, 1993, **126**, 869–873.

[57] V. Jacques and J. F. Desreux, *Inorg. Chem.*, 1994, **33**, 4048–4053.

[58] C. Platas-Iglesias, *Eur. J. Inorg. Chem.*, 2012, 2023–2033.

[59] M. Purgel, Z. Baranyai, A. de Blas, T. Rodríguez-Blas, I. Bányai, C. Platas-Iglesias and I. Tóth, *Inorg. Chem.*, 2010, **49**, 4370–82.

[60] F. K. Kálmán, Z. Baranyai, I. Tóth, I. Bányai, R. Király, E. Brücher, S. Aime, X. Sun, A. D. Sherry and Z. Kovács, *Inorg. Chem.*, 2008, **47**, 3851–3862.

[61] S. Aime, A. Barge, M. Botta, M. Fasano, J. Danilo Ayala and G. Bombieri, *Inorg. Chim. Acta*, 1996, **246**, 423–429.

[62] F. A. Dunand, R. S. Dickins, D. Parker and A. E. Merbach, *Chem. Eur. J.*, 2001, **7**, 5160–5167.

[63] M. Elhabiri, S. Abada, M. Sy, A. Nonat, P. Choquet, D. Esteban-Gómez, C. Cassino, C. Platas-Iglesias, M. Botta and L. J. Charbonnière, *Chem. Eur. J.*, 2015, **21**, 6535–6546.

[64] M. Mato-Iglesias, T. Rodríguez-Blas, C. Platas-Iglesias, M. Starck, P. Kadjane, R. Ziessel and L. Charbonnière, *Inorg. Chem.*, 2009, **48**, 1507–1518.

[65] K. Stott, J. Stonehouse, J. Keeler, T.-L. Hwang and a. J. Shaka, *J. Am. Chem Soc.*, 1995, **117**, 4199–4200.

[66] K. Stott, J. Keeler, Q. Van and A. Shaka, *J. Magn. Reson.*, 1997, **324**, 302–324.

[67] T. D. Claridge, *High-Resolution NMR Techniques in Organic Chemistry*, Elsevier, Amsterdam, 2nd edn., 2016.

[68] J. E. Power, M. Foroozandeh, R. W. Adams, M. Nilsson, S. R. Coombes, A. R. Phillips and G. A. Morris, *Chem. Commun.*, 2016, **52**, 2916–2919.

[69] A. Roca-Sabio, M. Regueiro-Figueroa, D. Esteban-Gómez, A. de Blas, T. Rodríguez-Blas and C. Platas-Iglesias, *Comput. Theor. Chem.*, 2012, **999**, 93–104.

[70] M. Dolg, H. Stoll and H. Preuss, *Theor. Chim. Acta*, 1993, **85**, 441–450.

[71] M. Dolg, H. Stoll, A. Savin and H. Preuss, *Theor. Chim. Acta*, 1989, **75**, 173–194.

[72] G. B. Kauffman, N. Sugisaka, K. Emerson, L. A. Bares and C. C. Houk, in *Inorg. Synth. vol. 9*, ed. S. Y. Tyree, 1967, pp. 157–160.

Abbreviation list

$\boldsymbol{A}$	Hyperfine-coupling tensor
A	Hyperfine-coupling constant
$\boldsymbol{B_0}$	External magnetic field (T)
B_0	Size of external magnetic field (T)
BMS	Bulk magnetic susceptibility
CA	Contrast agent
$\boldsymbol{\chi}$	Magnetic susceptibility tensor
χ_M	Molar magnetic susceptibility ($\mathrm{m^3\,mol^{-1}}$)
$\boldsymbol{D}$	ZFS tensor
D	ZFS tensor axiality
$\Delta\nu_0$	Difference in resonance frequencies (Hz)
DFT	Density functional theory
E	ZFS tensor rhombicity
η	Viscosity ($\mathrm{kg\ m^{-1}\ s^{-1}}$)
EXSY	Exchange spectroscopy
FID	Free induction decay
$\boldsymbol{g}$	g-tensor
γ_I	Nuclear gyromagnetic ratio ($\mathrm{rad\ s^{-1}\ T^{-1}}$)
γ_S	Electron gyromagnetic ratio ($\mathrm{rad\ s^{-1}\ T^{-1}}$)

g_e	Electron g factor, $g_e = 2.0023$
g_I	Nuclear g factor
h	Planc constant ($6.626\,070\,040 \times 10^{-34}\,\mathrm{J\,s}$)
$\boldsymbol{I}$	Operator of nuclear angular momentum
I	Nuclear spin angular momentum quantum number
I^2	Square of electron spin angular momentum operator, related eigenvalue I
$\boldsymbol{J}$	Overall angular momentum operator
$\mathcal{J}$	Spectral density function
J	Overall angular momentum quantum number
$\boldsymbol{\kappa}$	Direction of external magnetic field
k_B	Boltzmann constant ($1.38064852\times10^{-23}\mathrm{m}^2$ kg s^{-2} K^{-1})
$\boldsymbol{L}$	Orbital angular momentum operator
L	Orbital angular momentum quantum number
L^2	Square of overall orbital angular momentum operator, related eigenvalue L
$\boldsymbol{M}$	Magnetisation
M_I	Operator of nuclear angular momentum projection to z axis, related eigenvalue M_I
M_L	Operator of overall orbital angular momentum projection to z axis, related eigenvalue M_L
M_m	Molar mass (kg mol^{-1})
MRI	Magnetic resonance imaging
M_S	Operator of electron spin angular momentum projection to z axis, related eigenvalue M_S
$\langle\boldsymbol{\mu}\rangle$	Induced electron magnetic dipole moment
$\langle\mu\rangle$	Size of induced electron magnetic dipole moment

μ_B	Bohr magneton: $9.2740 \times 10^{-24}\,\mathrm{J\,T^{-1}}$
μ_{eff}	Effective electron magnetic dipole moment
μ_n	Nuclear magneton: $5.0508 \times 10^{-27}\,\mathrm{J\,T^{-1}}$
N_A	Avogadro constant ($6.022\,140\,857 \times 10^{23}\,\mathrm{mol^{-1}}$)
NMDR	Nuclear magnetic resonance dispersion
NMR	Nuclear Magnetic Resonance
ν_0	Larmor frequency in Hz
$\nu_{1/2}$	Line-width at the half of the signal maxima (Hz)
ω	Angular velocity in rad $\mathrm{s^{-1}}$
PARACEST	Chemical Exchange Saturation Transfer in paramagnetic systems[21]
PCM	Polarized continuum model (of solvatation)
pNMR	Paramagnetic NMR
$R_{1,2}$	Longitudinal, transversal relaxation rate respectively
RF	radiofrequency (pulses)
ρ_v	Density (kg $\mathrm{m^{-3}}$)
RT	Room temperature
$\boldsymbol{S}$	Operator of electron spin angular momentum
S^2	Square of nuclear angular momentum operator, related eigenvalue S
SAP	square antiprismatic (geometry)
SBMR	Solomon-Bloembergen-Morgan-Redfield theory
SNR	Signal-to-noise ratio
$\langle S_z \rangle$	Expectation value of S_z operator
T	Absolute temperature in Kelvin
t	Time

$T_{1/2}$	Longitudinal/transversal nuclear relaxation time
τ_c	Total correlation time (s)
τ_M	Exchange time (s)
τ_R	Rotation correlation time (s)
T_e	Electron relaxation time (s)
TFE	2,2,2-trifluoroethanol
TSAP	twisted square antiprismatic (geometry)
UTE	Ultra short echo-time (MRI pulse sequence)
VT	Variable temperature

The document was set up using LaTeX
`<http://www.latex-project.org>`
Used font: *Computer Modern* (Donald Knuth)
Prague, 2017